



## 저작자표시 2.0 대한민국

이용자는 아래의 조건을 따르는 경우에 한하여 자유롭게

- 이 저작물을 복제, 배포, 전송, 전시, 공연 및 방송할 수 있습니다.
- 이차적 저작물을 작성할 수 있습니다.
- 이 저작물을 영리 목적으로 이용할 수 있습니다.

다음과 같은 조건을 따라야 합니다:



저작자표시. 귀하는 원저작자를 표시하여야 합니다.

- 귀하는, 이 저작물의 재이용이나 배포의 경우, 이 저작물에 적용된 이용허락조건을 명확하게 나타내어야 합니다.
- 저작권자로부터 별도의 허가를 받으면 이러한 조건들은 적용되지 않습니다.

저작권법에 따른 이용자의 권리는 위의 내용에 의하여 영향을 받지 않습니다.

이것은 [이용허락규약\(Legal Code\)](#)을 이해하기 쉽게 요약한 것입니다.

[Disclaimer](#) 

August 2011

Ph.D. Dissertation

**Photovoltaic Characterization of  
Nanocrystalline TiO<sub>2</sub> Electrode Controlled  
by Aging Process for  
High Efficient Dye-Sensitized Solar Cells**

**Graduate School of Chosun University**

**Department of Chemical Engineering**

**Kyung-Jun Hwang**

# Photovoltaic Characterization of Nanocrystalline TiO<sub>2</sub> Electrode Controlled by Aging Process for High Efficient Dye-Sensitized Solar Cells

高效率 染料感應型 太陽電池에서 熟成工程으로 製造된  
나노 TiO<sub>2</sub> 電極의 光起電 特性

August 25, 2011

Graduate School of Chosun University

Department of Chemical Engineering

Kyung-Jun Hwang

# **Photovoltaic Characterization of Nanocrystalline TiO<sub>2</sub> Electrode Controlled by Aging Process for High Efficient Dye-Sensitized Solar Cells**

Supervised by Professor Jae-Wook Lee

This dissertation is submitted to the Graduate School of  
Chosun University in partial fulfillment of the requirements for  
the Degree of Doctor of Philosophy in Engineering

April 2011






Graduate School of Chosun University

Department of Chemical Engineering

Kyung-Jun Hwang



# Kyung-Jun Hwang's dissertation is certified

Committee Chair	Chonnam Nat'l University	Prof. Hee Moon 
Member	Chosun University	Prof. Sun-Il Kim 
Member	Seonam University	Prof. Seung-Joon Yoo 
Member	Linkline I&C Co., Ltd.	CTO Kyung-Hee Park 
Member	Chosun University	Prof. Jae-Wook Lee 

June 2011

Graduate School of Chosun University

## Acknowledgment

The thesis was funded by the Korea Research Foundation Grant from Korean Government (KRF-2007- H00023; Development and Evaluation of Highly Efficient Dye-Sensitized Solar Cells).

Firstly, I would like to thank Professor Jae-Wook Lee for giving me an interesting research topic and for supervising the thesis as well as for his guidance in selecting the guidelines for the work. I am extremely grateful to Professor Jae-Wook Lee for his excellent guidance, advice, consistent motivation and unstinted enthusiasm, patience and the degree of freedom that he gave, made me to explore, adopt innovative learning and develop a scientific temper. Also, supported through several discussions, various conferences, works shop, especially during our meal times, all the way through this project and shaped me as an intelligent person.

I wish to express gratitude to Professor Seung-Joon Yoo, Dr. Wang-Geum Shim, and Dr. Kyung-Hee Park, who really inspired me by their caring nature and ingenuity. I am also, grateful to them for providing the pleasant atmosphere, fruitful co-operation, numerous memorable events, which makes me to smile.

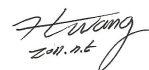
It is my privilege to thank Professor Dong-Heui Kwak, Professor Se-Il Lee, Dr. Chan Kim, and Dr. Tae-Young Kim. They always gives me a moral support and valuable solutions whenever I faced some problem in my Ph. D work and my personal life. I really admire their way of solving problems and showing kindness.

I am grateful to my thesis committee members, Professor Sun-Il Kim, who monitored my works and put efforts in reading and providing me with valuable comments on this thesis. Especially, I must thank Professor Hee Moon for his special care, helpful advises and support, which were really helped me to made a better form of final version of thesis.

My sincere thanks to Dr. Soon-Do Yoon, Dr. Dong-Won Park, Dr. Do-Young Choi, Dr. Jeong-Sun Sohn, and Dr. Yoo-Sung Choi for their friendliness, suggestions and timely help in my Ph. D works.

I wish to thank my laboratory members, Adsorption and Separation Laboratory members, Chemical Engineering Laboratory members, Acrosol Co. Ltd. staff for their helping hands whenever it was needed. They supported me in a several critical situations and also gave me a special care on every occasion.

Finally, I am in paucity of words to express my inner feeling for my parents and my wife Mrs. Hyun-Joung Kim, whose constant encouragement and moral support always helped me to smile at the difficult times to achieve the goal. They always sacrificed their own wishes and happiness towards the upliftment of my career. Without their care, love, sacrifice, support, prayers, wishes and motivation, it would have not been possible to finish my Ph. D course.



**Kyung-Jun Hwang**

July 5, 2011

*Dedicated to my beloved family*

세상에서 소중한 사람이 되길 바라면서,  
사랑과 열정만큼 아름다운 길이 있다는 것을 알게 해준 사람들에게 감사의 말을 전합니다.

# Table of Contents

<b>List of Tables</b> .....	v
<b>List of Figures</b> .....	viii
<b>Abbreviations and Symbols</b> .....	xiv
<b>Abstract in Korean</b> .....	xvi
 <b>Chapter 1. Introduction</b> .....	 <b>1</b>
1.1 Renewable Energy .....	1
1.2 Photovoltaics .....	3
<i>1.2.1 Current Status of Photovoltaics</i> .....	3
<i>1.2.2 Photovoltaic Technologies</i> .....	5
1.2.2.1 Single Crystal and Polycrystalline Silicon Solar Cells .....	5
1.2.2.2 Thin Film Solar Cells .....	6
1.2.2.3 III-V Semiconductors .....	7
1.2.2.4 Dye-Sensitized Solar Cells .....	8
1.2.2.5 Organic Solar Cells .....	8
1.3 Literature Review .....	10
<i>1.3.1 Current Situation of Dye-sensitized Solar Cells</i> .....	10
1.3.1.1 Comparison of Solar Cell Materials .....	10
1.3.1.2 Major Research Institutes of Dye-Sensitized Solar Cells .....	11
<i>1.3.2 Research and Development Trends of Dye-Sensitized Solar Cells</i> .....	13
1.3.2.1 Photo Electrode .....	13
1.3.2.2 Dye .....	14
1.3.2.3 Electrolyte .....	15
1.3.2.4 Counter Electrode .....	16
1.3.2.5 Cell Encapsulation/Modularization .....	16
1.4 Outline of This Dissertation .....	17

1.4.1 Summary of Research Background .....	17
1.4.2 Purpose and Outline of This Dissertation .....	19
<b>Chapter 2. Theoretical Background .....</b>	<b>22</b>
2.1 Basics of Photovoltaic Energy Conversion .....	22
2.1.1 Solar Irradiation and Availability of Solar Electricity .....	22
2.1.2 Photovoltaic Cell Performance .....	23
2.1.2.1 Basic Solar Cell Parameters .....	23
2.1.2.2 Operating Principle of the Standard Silicon Solar Cell .....	26
2.2 Operating Principle of Dye-Sensitized Solar Cell .....	29
2.3 Theoretical Issues of Dye-Sensitized Solar Cell Operation .....	31
2.3.1 Light Absorption .....	32
2.3.1.1 Adsorption of the Dye Molecule .....	32
2.3.1.2 Light Absorption via MLCT Excitation .....	33
2.3.1.3 Effect of the Sensitization .....	34
2.3.2 Charge Separation .....	34
2.3.2 Charge Transport .....	35
2.3.2.1 Electron Transport in the Nanostructured Semiconductor Electrode .....	35
2.3.2.2 Ion Transport in the Redox Electrolyte .....	37
2.3.4 Recombination .....	38
2.3.5 Interfacial Kinetics .....	39
2.4 Materials of Dye-Sensitized Solar Cell .....	40
2.4.1 TiO <sub>2</sub> Thin Film .....	40
2.4.2 Dye .....	44
2.4.3 Electrolyte .....	45
2.4.4 Counter Electrode .....	46
2.4.5 Substrate .....	47
2.5 Fabrication of Dye-Sensitized Solar Cell .....	47

2.6 Simple Electrical Model of the Dye-Sensitized Solar Cell .....	48
--	----

### **Chapter 3. Photovoltaic Properties of TiO<sub>2</sub> Electrode Prepared by Sol-Gel Method .....**

3.1 Introduction .....	50
3.2 Experimental .....	51
3.2.1 Synthesis of Nanocrystalline TiO <sub>2</sub> Particle .....	51
3.2.2 Fabrication of TiO <sub>2</sub> Electrode for Dye-sensitized Solar Cell .....	52
3.2.3 Characterization of TiO <sub>2</sub> Electrode for Dye-sensitized Solar Cell .....	53
3.2.4 Adsorption Properties of SG-TiO <sub>2</sub> Electrode for Dye-sensitized Solar Cell .....	54
3.3 Results and Discussion .....	55
3.3.1 Characteristics of Nanocrystalline SG-TiO <sub>2</sub> Particle and SG-TiO <sub>2</sub> Electrode .....	55
3.3.2 Adsorption Study of N719 Dye on SG-TiO <sub>2</sub> Electrode .....	67
3.4 Summary .....	79

### **Chapter 4. Photovoltaic Properties of TiO<sub>2</sub> Electrode Prepared by Mesoporous Silica Template .....**

4.1 Introduction .....	81
4.1.1 Mesoporous Materials .....	84
4.1.2 Nanoporous TiO <sub>2</sub> Replicas from Mesoporous Silica .....	87
4.2 Experimental .....	88
4.2.1 Synthesis of Nanoporous TiO <sub>2</sub> Materials .....	88
4.2.2 Fabrication of Nanoporous TiO <sub>2</sub> Electrode for Dye-Sensitized Solar Cells .....	90
4.2.3 Characterization of Nanoporous TiO <sub>2</sub> Electrode for Dye-Sensitized Solar Cells .....	91
4.3 Results and Discussion .....	92
4.3.1 Characterization of Nanoporous TiO <sub>2</sub> Particles .....	92

4.3.2 Characterization of Nanoporous TiO <sub>2</sub> Electrode .....	98
4.3.3 Adsorption Properties of N719 on Nanoporous TiO <sub>2</sub> Thin Films .....	101
4.3.4 Improvement of Photovoltaic Performance for Dye-Sensitized Solar Cell .....	108
4.4 Summary .....	111
<b>Chapter 5. Enhanced Photovoltaic Properties of TiO<sub>2</sub> Electrode Prepared by Polycondensation in Sol Reaction .....</b>	<b>113</b>
5.1 Introduction .....	113
5.1.1 Sol-Gel Process for Synthesis of TiO <sub>2</sub> .....	114
5.2 Experimental .....	117
5.2.1 Synthesis of TiO <sub>2</sub> Sols and TiO <sub>2</sub> Particles .....	117
5.2.2 Fabrication of TiO <sub>2</sub> Electrode .....	119
5.2.3 Fabrication of Dye-Sensitized Solar Cells .....	120
5.2.4 Characterization of TiO <sub>2</sub> Sol Particles and TiO <sub>2</sub> Electrode .....	120
5.2.5 Adsorption and Photovoltaic Properties of TiO <sub>2</sub> Electrode .....	121
5.3 Results and Discussion .....	122
5.3.1 Physicochemical Properties of TiO <sub>2</sub> Sol Particles by Aging .....	122
5.3.2 Structure Properties of TiO <sub>2</sub> Electrode by Aging .....	138
5.3.3 Adsorption Properties of TiO <sub>2</sub> Electrode by Aging .....	147
5.3.4 Photovoltaic Performance of TiO <sub>2</sub> Electrode by Aging .....	166
5.4 Summary .....	172
<b>Chapter 6. Overall Conclusions .....</b>	<b>174</b>
<b>Literature Cited .....</b>	<b>178</b>
<b>Abstract in English .....</b>	<b>188</b>
<b>Research Activities .....</b>	<b>191</b>

# List of Tables

## Chapter 1

Table 1.1. Types and characteristics of solar cell materials .....	9
--	---

## Chapter 2

Table 2.1. The comparison of properties of rutile and anatase .....	41
---	----

## Chapter 3

Table 3.1. Surface characteristics of TiO <sub>2</sub> film .....	59
Table 3.2. Physical properties of TiO <sub>2</sub> film .....	60
Table 3.3. Photovoltaic performance of dye-sensitized solar cell .....	67
Table 3.4. Sips parameters of N719 adsorption on SG-TiO <sub>2</sub> for different temperatures ...	70
Table 3.5. The pseudo-second-order kinetic parameter of N719 adsorption on SG-TiO <sub>2</sub> ..	74
Table 3.6. Characteristics values of dye-sensitized solar cell depending on adsorption amount .....	78
Table 3.7. Determination of 1-diode model parameters of dye-sensitized solar cell depending on the adsorption quantity .....	79

## Chapter 4

Table 4.1. Physical properties of various mesoporous silicate used in this works .....	87
Table 4.2. Textural properties of nanoporous TiO <sub>2</sub> replicas obtained from mesoporous silica .....	94
Table 4.3. Surface characteristics of various TiO <sub>2</sub> films. ....	101
Table 4.4. Langmuir-Freundlich isotherm equation (a), adsorption energy distribution function (b), and Langmuir-Freundlich isotherm parameters (c) .....	104



Table 4.5. Photovoltaic performance of dye-sensitized solar cell using nanoporous TiO <sub>2</sub> films. ....	108
Table 4.6. Photovoltaic performance for various TiO <sub>2</sub> electrode of dye-sensitized solar cell with multi-layer coating. ....	111

## Chapter 5

Table 5.1. Turbidity and average particle size of six TiO <sub>2</sub> sol according to different aging conditions .....	124
Table 5.2. Physical properties of six TiO <sub>2</sub> sol particles according to different aging conditions .....	129
Table 5.3. Photocurrent-voltage of TiO <sub>2</sub> thin films electrode depending on KYJ-6 powder content in TiO <sub>2</sub> paste .....	138
Table 5.4. Photocurrent-voltage of TiO <sub>2</sub> thin films electrode depending on the concentration of HPC binder in TiO <sub>2</sub> paste .....	139
Table 5.5. Physical properties of TiO <sub>2</sub> film with different aging conditions .....	141
Table 5.6. Surface roughness of TiO <sub>2</sub> thin film with different aging conditions .....	142
Table 5.7. Textural properties of TiO <sub>2</sub> thin film prepared according to the different aging conditions .....	146
Table 5.8. Langmuir isotherm parameters of N719 dye on various TiO <sub>2</sub> films at three different temperatures .....	148
Table 5.9. Langmuir-Freundlich isotherm parameters of N719 dye on various TiO <sub>2</sub> films at three different temperatures .....	149
Table 5.10. Langmuir isotherm parameters of N719 dye on various TiO <sub>2</sub> films in terms of pH at 333.15 K .....	153
Table 5.11. Langmuir-Freundlich isotherm parameters of N719 dye on various TiO <sub>2</sub> films in terms of pH at 333.15 K .....	156
Table 5.12. Thermodynamic parameters .....	157

Table 5.13. Thermodynamic parameters of N719 dye (Gibbs energy, enthalpy and entropy)	158
Table 5.14. AED parameters of N719 dye on various TiO <sub>2</sub> films in terms of pH	159
Table 5.15. AED parameters of N719 dye on various TiO <sub>2</sub> films in terms of temperature	163
Table 5.16. Photovoltaic performance of DSSC for KYJ-TiO <sub>2</sub> film series under different aging conditions	167

# List of Figures

## Chapter 1

Figure 1.1. Evolution of the world annual PV market. ....	4
Figure 1.2. Market shares of different photovoltaic technologies by the year 2009. ....	5
Figure 1.3. Prototype models of dye-sensitized solar cell panels. ....	11
Figure 1.4. Numbers of papers on dye-sensitized solar cells and all solar cells. ....	12
Figure 1.5. Cell structure of dye-sensitized solar cell. ....	13
Figure 1.6. Action spectrum of dye-sensitized cells with different ruthenium (Ru) dyes. ·	15
Figure 1.7. Plastic substrate module (left) and large module for outdoor use (right). ....	17
Figure 1.8. Overall layout. ....	20

## Chapter 2

Figure 2.1. The standard AM 1.5 global solar spectrum. ....	22
Figure 2.2. A typical $I$ - $V$ curve of a solar cell. ....	24
Figure 2.3. A solar simulation system. ....	25
Figure 2.4. The standard $pn$ -junction solar cell configuration from the 1960s. ....	27
Figure 2.5. Formation of the abrupt semiconductor $pn$ -junction. ....	28
Figure 2.6. The working principle of the dye-sensitized solar cell. ....	30
Figure 2.7. Charge transfer processes between dye and the $\text{TiO}_2$ lattice .....	33
Figure 2.8. State diagram representation of kinetics of dye-sensitized solar cell's function. .....	40
Figure 2.9. (a) The typical preparation protocol for $\text{TiO}_2$ paste (b) the various coating method for the fabrication of nanocrystalline $\text{TiO}_2$ thin film. ....	43
Figure 2.10. Fabrication method of dye-sensitized solar cell. ....	47
Figure 2.11. (a) A solar cell, (b) A simple electrical model of a solar cell (equivalent circuit using a 1-diode model). ....	48

## Chapter 3

Figure 3.1. Fabrication procedure of SG-TiO <sub>2</sub> electrode. ....	51
Figure 3.2. Thermal gravity analysis of SG-TiO <sub>2</sub> film and HPC powder. ....	53
Figure 3.3. X-ray diffraction spectra of SG-TiO <sub>2</sub> and P25-TiO <sub>2</sub> . ....	55
Figure 3.4. HR-TEM images and electron diffraction pattern of anatase SG-TiO <sub>2</sub> at (a) low and (b) high resolution. ....	56
Figure 3.5. XPS survey spectra of (a) SG-TiO <sub>2</sub> , (b) Ti 2p core level (c) O 1s core level. .	57
Figure 3.6. FE-SEM images of (a) P25-TiO <sub>2</sub> (b) SG-TiO <sub>2</sub> film. ....	58
Figure 3.7. AFM images of (a) P25-TiO <sub>2</sub> (b) SG-TiO <sub>2</sub> film. ....	59
Figure 3.8. (a) N <sub>2</sub> gas adsorption and desorption isotherms (b) pore size distributions of SG-TiO <sub>2</sub> and P25-TiO <sub>2</sub> films. ....	61
Figure 3.9. The flow chart for the general calculation of adsorption energy distribution functions. ....	63
Figure 3.10. Adsorption energy distributions of SG-TiO <sub>2</sub> and P25-TiO <sub>2</sub> films. ....	64
Figure 3.11. FT-IR spectra of N719 dye adsorbed on TiO <sub>2</sub> films compared to the signals of the N719 dye powder. ....	65
Figure 3.12. Photocurrent-voltage ( <i>I-V</i> ) curves of SG-TiO <sub>2</sub> and P25-TiO <sub>2</sub> films. ....	66
Figure 3.13. Adsorption isotherms of N719 on SG-TiO <sub>2</sub> particles at different temperatures. ....	68
Figure 3.14. Isosteric heat of adsorption for N719 on SG-TiO <sub>2</sub> particles. ....	71
Figure 3.15. Adsorption kinetics of N719 on SG-TiO <sub>2</sub> particles depending on the concentrations (0.05 and 0.5 mM). ....	73
Figure 3.16. (a) Adsorption capacity of N719 in terms of solution pH (b) zeta potential of SG-TiO <sub>2</sub> particles (b). ....	75
Figure 3.17. Flow chart for the calculation of 1-diode model. ....	76
Figure 3.18. <i>I-V</i> curves of SG-TiO <sub>2</sub> films depending on the N719 adsorption amount .....	77

## Chapter 4

Figure 4.1. (a) Molecular structure of N719 (b) coordination types of physisorption (c) chemisorption. ....	83
Figure 4.2. Pore size distributions for different types of porous silica materials. ....	85
Figure 4.3. Synthesis process of common mesoporous silica. ....	85
Figure 4.4. (a) XRD pattern of KIT-6, (b) SBA-15 and MSU-H. ....	86
Figure 4.5. Synthesis process of nanoporous TiO <sub>2</sub> replicas from mesoporous silica. ....	89
Figure 4.6. Manufacture process of nanoporous TiO <sub>2</sub> electrode. ....	90
Figure 4.7. XRD patterns of nanoporous TiO <sub>2</sub> particle: (a) MK-TiO <sub>2</sub> , (b) MS-TiO <sub>2</sub> , (c) MU-TiO <sub>2</sub> . ....	93
Figure 4.8. Electron diffraction image of nanoporous TiO <sub>2</sub> particle: (a) MK-TiO <sub>2</sub> , (b) MS-TiO <sub>2</sub> , (c) MU-TiO <sub>2</sub> . ....	94
Figure 4.9. HR-TEM images of nanoporous TiO <sub>2</sub> particle: (a) MK-TiO <sub>2</sub> , (b) MS-TiO <sub>2</sub> , (c) MU-TiO <sub>2</sub> . ....	95
Figure 4.10. N <sub>2</sub> adsorption and desorption isotherms for nanoporous TiO <sub>2</sub> particle. ....	96
Figure 4.11. Pore size distributions of nanoporous TiO <sub>2</sub> particles. ....	97
Figure 4.12. Adsorption energy distributions of nanoporous TiO <sub>2</sub> particles. ....	98
Figure 4.13. FE-SEM image of various TiO <sub>2</sub> thin films: (a) P25-TiO <sub>2</sub> , (b) MK-TiO <sub>2</sub> , (c) MS-TiO <sub>2</sub> , (d) MU-TiO <sub>2</sub> . ....	99
Figure 4.14. AFM image analysis of (a) P25-TiO <sub>2</sub> , (b) MK-TiO <sub>2</sub> , (c) MS-TiO <sub>2</sub> , (d) MU-TiO <sub>2</sub> film. ....	100
Figure 4.15. FT-IR spectra of N719 adsorbed on nanoporous TiO <sub>2</sub> film compared with the signals of the N719 dye powder. ....	102
Figure 4.16. Adsorption equilibrium amount of N719 on nanoporous TiO <sub>2</sub> films at 333.15 K. ....	103
Figure 4.17. Pore volumes in comparison with N719 adsorption as a function of nanoporous TiO <sub>2</sub> films. ....	105

Figure 4.18. Adsorption energy distributions of N719 on nanoporous TiO <sub>2</sub> films. ....	106
Figure 4.19. <i>I-V</i> curves of nanoporous TiO <sub>2</sub> films. ....	107
Figure 4.20. FE-SEM image for multi-layer coating: (a) P25-TiO <sub>2</sub> /MK-TiO <sub>2</sub> , (b) P25-TiO <sub>2</sub> /MS-TiO <sub>2</sub> , (c) P25-TiO <sub>2</sub> /MU-TiO <sub>2</sub> . ....	109
Figure 4.21. <i>I-V</i> curves of nanoporous TiO <sub>2</sub> films by using multi-layer coating. ....	110

## Chapter 5

Figure 5.1. Typical sol-gel process. ....	115
Figure 5.2. Experimental apparatus for synthesis of TiO <sub>2</sub> sol. ....	117
Figure 5.3. Experimental flowchart for synthesis of TiO <sub>2</sub> . ....	118
Figure 5.4. Average particle size of TiO <sub>2</sub> sol particles according to concentration of peptization agent (HNO <sub>3</sub> ). ....	119
Figure 5.5. Turbidity and photograph (inlet) of TiO <sub>2</sub> sol samples according to aging conditions. ....	122
Figure 5.6. Particle size distributions of TiO <sub>2</sub> sol particles according to the different aging conditions. ....	123
Figure 5.7. Zeta potential curves of TiO <sub>2</sub> sol particle with various aging time at (a) 313.15 K (b) 363.15 K. ....	125
Figure 5.8. HR-TEM image of TiO <sub>2</sub> sol particles according to the aging times [0 h (a, d), 24 h (b, e) and 72 h (c, f)] at 313.15 K (left side) and at 363.15 K (right side). ....	127
Figure 5.9. N <sub>2</sub> adsorption and desorption isotherm of TiO <sub>2</sub> sol particles with various aging time at 313.15 K (a) and 363.15 K (b). ....	128
Figure 5.10. BJH pore size distribution of TiO <sub>2</sub> sol particles with various aging time at 313.15 K (a) and 363.15 K (b). ....	130
Figure 5.11. TGA curves of TiO <sub>2</sub> sol particles with various aging time at (a) 313.15 K (b) at 363.15 K. ....	132

Figure 5.12. FT-IR spectra of $\text{TiO}_2$ sol particles with various aging time at (a) 313.15 K (b) 363.15 K. ....	133
Figure 5.13. XRD patterns of $\text{TiO}_2$ sol particles with various aging time at 313.15 K (a) and at 363.15 K (b). ....	135
Figure 5.14. XRD patterns of calcined $\text{TiO}_2$ sol particles with various aging time at 313.15 K (a) and at 363.15 K (b). ....	136
Figure 5.15. FE-SEM images of calcined $\text{TiO}_2$ powder's morphology according to the different aging conditions: 0 h (a, d); 24 h (b, e); 72 h (c, f) at 313.15 K (left side) and at 363.15 K (right side). ....	137
Figure 5.16. XRD patterns of prepared $\text{TiO}_2$ film from $\text{TiO}_2$ sol according to the different aging conditions. ....	140
Figure 5.17. 3-dimensional AFM images of $\text{TiO}_2$ thin film according to different aging conditions. ....	143
Figure 5.18. FE-SEM surface images of $\text{TiO}_2$ thin film according to different aging conditions ....	145
Figure 5.19. Photographs of photo electrode layers with a background of stripe. ....	146
Figure 5.20. Adsorption isotherms of N719 on KYJ- $\text{TiO}_2$ film series at three different temperatures (Langmuir equation). ....	150
Figure 5.21. Adsorption isotherms of N719 on KYJ- $\text{TiO}_2$ film series at three different temperatures (Langmuir-Freundlich equation). ....	151
Figure 5.22. Adsorption isotherms of N719 on KYJ- $\text{TiO}_2$ film series at three different pH (Langmuir equation). ....	154
Figure 5.23. Adsorption isotherms of N719 on KYJ- $\text{TiO}_2$ film series at three different pH (Langmuir-Freundlich equation). ....	155
Figure 5.24. Calculated adsorption energy distribution curves for KYJ-1F, KYJ-2F and KYJ-3F at three different pHs. ....	160
Figure 5.25. Calculated adsorption energy distribution curves for KYJ-4F, KYJ-5F and KYJ-6F at three different pHs. ....	161

Figure 5.26. Calculated adsorption energy distribution curves for KYJ-1F, KYJ-2F and KYJ-3F at three different temperatures. ....	164
Figure 5.27. Calculated adsorption energy distribution curves for KYJ-4F, KYJ-5F and KYJ-6F at three different temperatures. ....	165
Figure 5.28. <i>I-V</i> curves of KYJ-TiO <sub>2</sub> film series under different aging conditions. ....	167
Figure 5.29. Nyquist plots of KYJ-TiO <sub>2</sub> film series with various aging time at 313.15 K (a) and 363.15 K (b). ....	168
Figure 5.30. Correlation plot between crystallite size-adsorption (a) and crystallite size-photovoltaic properties (b). ....	169
Figure 5.31. FE-SEM image of KYJ-6F: (a) surface, (b) thickness, and (c) thickness of repetitive dry coating. ....	170
Figure 5.32. <i>I-V</i> curves of TiO <sub>2</sub> thin film with repetitive dry coating method fabricated using TiO <sub>2</sub> sol prepared under optimal aging conditions of 363.15 K and 72 h. ....	171

## Chapter 6

Figure 6.1. Commercial applications of the photo electrode. ....	176
--	-----



## Abbreviations and Symbols

<b>ACN</b>	: acetonitrile	<b>FT-IR</b>	: fourier transform infrared spectrophotometer
<b>AED</b>	: adsorption energy distribution	<b>FTO</b>	: fluorine-doped tin oxide
<b>AFM</b>	: atomic force microscope	<b><i>h</i></b>	: initial adsorption rate
<b>AIST</b>	: advanced industrial science and technology	<b><i>h</i><sup>+</sup></b>	: hole
<b>Amosil 4</b>	: Adhesives	<b>HOMO</b>	: highest occupied molecular orbital
<b>APD</b>	: average pore width	<b>HPC</b>	: hydropropylcellulose
<b><i>a</i>-Si</b>	: amorphous silicon	<b>HR-TEM</b>	: high resolution transmission electron microscope
<b><i>b</i></b>	: adsorption intensity or langmuir coefficient	<b><i>I<sub>A</sub></i></b>	: X-ray diffraction intensities at 2 theta= 25.3° for anatase main peak ( <i>d</i> <sub>101</sub> )
<b>BET</b>	: Brunauer, Emmett, and Teller	<b>IEP</b>	: isoelectric point
<b>BIPV</b>	: building-integrated photovoltaic	<b><i>I<sub>i,cal</sub></i></b>	: experimental and calculated current at <i>i</i> -th point
<b>BJH</b>	: Barrett, Joyner, and Halenda	<b><i>I<sub>max</sub></i></b>	: current at maximum power point
<b><i>C</i></b>	: concentration of adsorbate in solution at equilibrium	<b><i>I<sub>o</sub></i></b>	: diode saturation current
<b>CB</b>	: conduction band	<b>IPCE</b>	: incident photon to current conversion efficiency
<b>CdTe</b>	: cadmium telluride	<b><i>I<sub>ph</sub></i></b>	: photo-generated current
<b>CdTe</b>	: copper indium gallium diselenide	<b><i>I<sub>R</sub></i></b>	: X-ray diffraction intensities at 2 theta= 27.5° for rutile main peak ( <i>d</i> <sub>110</sub> )
<b>CMK-1</b>	: mesoporous carbon	<b><i>I<sub>sc</sub></i></b>	: short circuit current
<b><i>D</i></b>	: crystalline size of the particles, fractal dimension	<b>IUPAC</b>	: international union of pure and applied chemistry
<b>DFT</b>	: density functional theory	<b><i>I-V</i> curves</b>	: current-voltage curves
<b>DSSC</b>	: dye-sensitized solar cells	<b><i>K</i></b>	: absolute temperature, Langmuir constant, and apparatus constant
<b><i>e</i><sup>-</sup></b>	: electron	<b><i>k</i><sub>2</sub></b>	: Pseudo-second-order rate constant
<b><i>E</i></b>	: adsorption energy	<b><i>k<sub>B</sub></i></b>	: Boltzmann constant
<b><i>E</i>(%)</b>	: average percent deviation between experimental and predicted results	<b>KIT-6, SBA-15, and MSU-H</b>	: mesoporous silica template
<b><i>E</i><sub>12</sub></b>	: energy difference between the solute and water	<b><i>K<sub>a</sub></i>(<i>T</i>)</b>	: pre-exponential factor expressing the partition functions for an isolated molecule
<b><i>E<sub>A</sub></i></b>	: acceptor level	<b>KYJ-TiO<sub>2</sub></b>	: synthesized TiO <sub>2</sub> in chapter 5
<b><i>E<sub>c</sub></i></b>	: conduction band edge	<b>LF</b>	: Langmuir-Freundlich isotherm model
<b><i>E<sub>D</sub></i></b>	: donor level	<b>LHE</b>	: light-harvesting efficiency
<b><i>E<sub>F</sub></i></b>	: fermi level	<b>LUMO</b>	: lowest unoccupied molecular orbital
<b><i>E<sub>g</sub></i></b>	: energy band gap of a semiconductor	<b><i>M</i></b>	: molar mass
<b>EIS</b>	: electrochemical impedance spectroscopy	<b>M41S family</b>	: MCM-41, MCM-48, and MCM-50
<b><i>E<sub>max</sub></i></b>	: maximum adsorption energy	<b>MAN</b>	: methoxyacetonitrile
<b><i>E<sub>min</sub></i></b>	: minimum adsorption energy	<b>MK-, MS-, MU-TiO<sub>2</sub></b>	: nanoporous TiO <sub>2</sub> materials
<b>EPFL</b>	: federal institute of technology, lausanne	<b>MLCT</b>	: metal to ligand charge transfer
<b><i>E<sub>v</sub></i></b>	: valence band edge	<b>MPN</b>	: methoxypropionitrile
<b><i>F</i>(<i>E</i>) or <i>F</i>(<i>E</i><sub>12</sub>)</b>	: adsorption energy distribution function		
<b><i>F<sub>A</sub></i></b>	: ratio of anatase crystalline phase		
<b>FE-SEM</b>	: field-emission scanning electron microscope		
<b>FF</b>	: fill factor		

<b>MPU</b>	: maximum power unit
<b><i>n</i></b>	: diode quality factor in 1-diode model equation, number of experimental data, and parameter of system heterogeneity in Sip and LF equation
<b>OMS</b>	: ordered mesoporous silicas
<b><i>p</i></b>	: equilibrium pressure
<b><i>P</i></b>	: equilibrium pressures during the gas adsorption
<b>P123</b>	: EO <sub>20</sub> PO <sub>70</sub> EO <sub>20</sub>
<b>P25-TiO<sub>2</sub></b>	: commercially available TiO <sub>2</sub>
<b><i>P<sub>in</sub></i></b>	: power of the incident irradiation
<b><i>P<sub>o</sub></i></b>	: saturation pressures during the gas adsorption
<b><i>P<sub>out</sub></i></b>	: output power of a solar cell
<b>PSA</b>	: particle size analysis
<b>PSC</b>	: photoelectrochemical solar cells
<b>PV</b>	: photovoltaic
<b><i>q</i></b>	: adsorption equilibrium capacity
<b><i>Q</i></b>	: N719 dye adsorption amount
<b><i>q<sub>c</sub></i></b>	: elementary electric charge
<b><i>q<sub>cal,k</sub></i></b>	: calculated adsorption capacity
<b><i>q<sub>e</sub></i></b>	: equilibrium adsorption capacity
<b><i>q<sub>exp,k</sub></i></b>	: experimental adsorption capacity
<b><i>q<sub>m</sub></i></b>	: maximum amount of adsorbate bonded to adsorbent when a monolayer is formed
<b><i>q<sub>st</sub></i></b>	: isosteric enthalpy
<b><i>R</i></b>	: gas constant, resistance
<b><i>R<sup>2</sup></i></b>	: correlation coefficients
<b><i>R<sub>a</sub></i></b>	: mean roughness
<b><i>R<sub>ct</sub></i></b>	: charge transfer resistance
<b><i>R<sub>q</sub></i></b>	: root mean square roughness
<b><i>R<sub>s</sub></i></b>	: series resistance
<b><i>R<sub>sh</sub></i></b>	: parallel resistance
<b><i>S</i></b>	: sensitizer
<b><i>S<sup>*</sup></i></b>	: excited energy state of the sensitizer
<b><i>S<sup>+</sup></i></b>	: oxidized state of the sensitizer
<b><i>S<sub>BET</sub></i></b>	: specific BET surface area ( $P/P_o=0.1-0.2$ )
<b>SG-TiO<sub>2</sub></b>	: synthesized TiO <sub>2</sub> in chapter 3
<b><i>S<sup>o</sup></i></b>	: molecular ground state of the sensitizer
<b><i>T</i></b>	: absolute temperature in adsorption energy distribution equation, temperature
<b>TCO</b>	: transparent conducting oxide
<b>TEOS</b>	: tetraethyl orthosilicate

<b>TGA</b>	: thermal gravity analysis
<b>TTIP</b>	: titanium-tetraisopropoxide
<b><i>u</i></b>	: unknown parameters
<b><i>V</i></b>	: volume, voltage
<b><i>V<sub>B</sub></i></b>	: valence band
<b><i>V<sub>DFT</sub></i></b>	: DFT pore volume
<b><i>V<sub>max</sub></i></b>	: voltage at maximum power unit
<b><i>V<sub>oc</sub></i></b>	: open circuit voltage
<b><i>V<sub>t</sub></i></b>	: total pore volume at $P/P_o=0.99$
<b><i>w</i></b>	: interaction energy between the two nearest neighboring molecules
<b>XPS</b>	: X-ray photo electron spectroscopy
<b>XRD</b>	: X-ray diffractometer
<b><i>z</i></b>	: number of closest adjacent molecules in the monolayer
<b>3-MPN</b>	: 3-methoxypropionitrile
<b>4-TBP</b>	: 4-tert-butylpyridine

### Greek Symbols

<b><math>\beta</math></b>	: full width at half-maximum of the diffraction peak
<b><math>\Delta G^o</math></b>	: adsorption free energy
<b><math>\Delta H^o</math></b>	: adsorption enthalpy
<b><math>\Delta S^o</math></b>	: adsorption entropy
<b><math>\eta_{eff}</math></b>	: energy conversion efficiency
<b><math>\eta_{el}</math></b>	: charge collection efficiency
<b><math>\theta</math></b>	: Bragg's angle
<b><math>\theta(c)</math></b>	: total fraction coverage of solute
<b><math>\theta(p)</math></b>	: experimental adsorption isotherm data
<b><math>\theta(p,E)</math></b>	: local adsorption isotherm with an adsorption energy
<b><math>\lambda</math></b>	: wavelength
<b><math>\Phi</math></b>	: model dependent function
<b><math>\Phi_{h\nu}</math></b>	: photon flux
<b><math>\Phi_{inj}</math></b>	: charge injection yield
<b><math>\chi</math></b>	: $c/c_{sol}$ , where $c_{sol}$ is the solubility of the solute in water

## 高效率 染料感應型 太陽電池에서 熟成工程으로 製造된 나노 $\text{TiO}_2$ 電極의 光起電 特性

황 경 준

지도교수 : 이재욱

화학공학과

조선대학교 대학원

최근의 세계 경제는 에너지 수요의 폭발적인 증가와 동시에 빠른 성장을 하고 있으며, 세계의 에너지 소비량 중 석유와 천연가스의 비중이 2010년 65%에 이르고 있다. 이는 에너지 관련 지출 비용에 대한 소비 증가 및 지구 온난화라는 당면 과제를 야기하게 되어 환경 규제라는 제약이 대두되었다. 이로 인하여 최근 친환경에너지 정책이 세계 각국에서 앞 다투어 발표되고 핵 발전 및 태양광, 수력, 풍력, 조력, 지열 등의 연구가 다방면으로 진행되고 있다.

본 논문에서는 친환경 신재생에너지원으로서 태양전지를 다루었다. 태양전지는 광기전 효과에 의해 태양빛 에너지를 전기로 직접 변화시키는 전기 발생 장치이다. 1991년 스위스의 그라첼 교수가 'Nature'에 소개한 차세대 태양전지로 각광받고 있는 염료감응형 태양전지는 반도체가 접합되어 있는 기존의 태양전지와는 달리 높은 에너지 변환 효율과 저렴한 제조단가로 인하여 산업계의 비상한 관심을 모으고 있으며, 태양전지의 효율향상을 위해 주로  $\text{TiO}_2$  나노결정 소재 및 전극구조, 염료 개발, 전해질 및 홀전도체, 광전자 전달, 봉합기술 그리고 전도성 기판 등에 관한 핵심 연구들이 수행되어 오고 있다.

본 연구에서는 고효율 광전극 제조를 위해 염료감응형 태양전지의 광전자의 전달 및 전류 발생에 중요한 역할을 하는  $\text{TiO}_2$  전극을 다양한 방법으로 제조하고 광기전 특성을 조사하였다. 이를 위해  $\text{TiO}_2$  나노입자 (SG- $\text{TiO}_2$ )를 가수분해에 의한 졸-겔 방법으로 합성하였다. 이렇게 얻은 다결정 나노입자는 염료감응형 태양전지에서 효과적인 아나타제의 결정상과 약 15 nm 입자 크기를 보였다. 제조된  $\text{TiO}_2$ 를 이용하여 광전극을 제조한 후, AFM, BET, FE-SEM, FT-IR, HR-TEM, XPS 및 XRD 등의 기기분석을 통해

상업적으로 널리 이용되는 P25-TiO<sub>2</sub>로 제작된 광전극과 비교 평가하였다. P25-TiO<sub>2</sub>에 비해 작은 TiO<sub>2</sub>의 입자 크기와 대부분의 결정상이 아나타제로 이루어진 SG-TiO<sub>2</sub> 전극의 경우 높은 에너지 변환 효율을 보였다. 그리고, 합성된 TiO<sub>2</sub> 나노입자 상에서 N719 염료의 흡착특성이 염료감응형 태양전지 효율에 미치는 영향을 체계적으로 조사하였다. 이를 위해 SG-TiO<sub>2</sub> 전극 상에서 온도, 시간, pH 변화에 따른 N719 염료의 흡착 평형 및 속도론적 특성을 고찰한 결과, 염료의 흡착량은 온도, 시간 및 pH 변화에 따라 크게 달라짐을 확인할 수 있었다. 특히, N719 염료의 흡착 시간에 따른 흡착량 차이는 염료감응형 태양전지의 효율에도 크게 영향을 미쳤다. 본 연구에서 얻은 *I-V* 곡선 데이터를 1-Diode 모델을 이용하여, 등가 회로 모델의 저항 값을 얻었다.

TiO<sub>2</sub> 전극에서 염료의 흡착량을 증가시키기 위해 규칙적인 세공 구조를 이루고 있는 KIT-6, SBA-15 및 MSU-H 메조포러스 구조체를 이용하여 나노포러스 TiO<sub>2</sub> (MK-TiO<sub>2</sub>, MS-TiO<sub>2</sub>, MU-TiO<sub>2</sub>)를 제조하였다. AFM, BET, FE-SEM, HR-TEM, XPS 및 XRD 등의 기기분석을 통해 제조된 나노포러스 TiO<sub>2</sub> 전극을 평가하였다. 나노포러스 TiO<sub>2</sub> 전극은 FT-IR, 흡착 평형 실험, 흡착 에너지 분포 및 DFT 세공 분석을 통하여 TiO<sub>2</sub> 전극 표면에서 일어나는 N719 염료와의 흡착 특성을 관찰하였다. 높은 표면적을 가진 나노포러스 TiO<sub>2</sub> 전극은 염료의 높은 흡착량을 보였다. 특히, 4 nm 이상의 메조세공은 나노포러스 TiO<sub>2</sub> 전극과 염료와의 흡착에 높은 영향을 미쳤다. 그러나 나노포러스 TiO<sub>2</sub> 전극 내부에서 광전자 전달시 발생하는 구조적인 문제점은 염료감응형 태양전지에서 높은 에너지 효율을 보이지 못하였다. 이러한 문제를 200 nm 이상으로 TiO<sub>2</sub> 입자가 규칙적으로 응집된 나노포러스 TiO<sub>2</sub> 전극을 빛의 산란층으로 이용하여 해결하였다. 나노포러스 TiO<sub>2</sub>를 나노 TiO<sub>2</sub> 전극위에 다중코팅을 하여 높은 전류 밀도와 에너지 변환 효율을 얻었다.

높은 광기전 특성을 가지는 TiO<sub>2</sub> 전극 제조를 위해 TiO<sub>2</sub> 졸 합성 공정 중 축중합 반응 (숙성공정)을 조절하여 TiO<sub>2</sub> 전극을 제조하였다. TiO<sub>2</sub> 졸의 합성은 출발물질인 티타늄 알콕사이드를 이용하여 가수분해 및 축중합 반응을 숙성 과정을 통해 제어 한 후 제조 하였다. 숙성 공정 조건은 TiO<sub>2</sub> 졸과 TiO<sub>2</sub> 입자의 입자 크기 및 미세구조까지 조절하였다. 이러한 TiO<sub>2</sub> 졸을 이용하여 염료감응형 태양전지용 TiO<sub>2</sub> 전극 (KYJ-TiO<sub>2</sub>)을 제조하였다. 특히, 숙성 조건 (시간, 온도)의 영향에 따른 KYJ-TiO<sub>2</sub> 전극의 물리 화학적 특성의 변화를 체계적으로 조사하였다. 그 결과 TiO<sub>2</sub> 졸 합성 시 숙성 조건 조절을 통하여 KYJ-TiO<sub>2</sub> 전극의 결정성, 입자크기, 거칠기, 표면적, 투명도 등을 성공적으로 조절 할 수 있었다. 또한 숙성 조건에 따라 제조된 KYJ-TiO<sub>2</sub> 전극의 N719 염료와의 흡

작 특성 (흡착 등온선, 흡착열, 흡착 에너지 분포)을 연구하였다. 숙성 조건에 따라 제조되어진  $\text{TiO}_2$  전극의 물리 화학적 특성은 염료감응형 태양전지의 광기전 특성 (전류 밀도, 에너지 변환 효율)에도 많은 영향을 미쳤다. 본 연구를 통해 얻은 최적화된  $\text{TiO}_2$  졸 입자와 최적화된 조건으로 제조된  $\text{TiO}_2$  페이스트를 이용하여 높은 태양에너지 변환 효율 (10.2%)을 가지는 염료감응형 태양전지용 광전극을 제조할 수 있었다. 본 논문에서 수행한 다양한  $\text{TiO}_2$  전극의 제조와 광기전 특성에 관한 체계적인 연구 결과는 향후 상업용 고효율 염료감응형 태양전지 모듈을 제작하는데 중요한 정보로 활용될 것이다.

## **This dissertation was based on**

### ***Research funds:***

1. The Korea Research Foundation Grant funded by the Korean Government (KRF-2007-H00023; Development and Evaluation of Highly Efficient Dye-Sensitized Solar Cells).

### ***International Scientific Journals:***

1. Jae-Wook Lee, Kyung-Jun Hwang, Wang-Geun Shim, Kyung-Hee Park, Hal-Bon Gu, Kyu-Hyuk Kwun, **Energetic Surface Heterogeneity of Nanocrystalline Dye-Sensitized Solar Cells**, *Korean J. Chem. Eng.*, **2007**, 24(5), 847 (SCIE), ISSN: 0256-1115.
2. Jae-Wook Lee, Kyung-Jun Hwang, Dong-Won Park, Kyung-Hee Park, Wang-Geun Shim, Sang-Chai Kim, **Photocurrent-Voltage of a Dye-Sensitized Nanocrystalline TiO<sub>2</sub> Solar Cells Influenced by N719 Dye Adsorption Properties**, *J. Nanosci. Nanotechnol.*, **2007**, 7(11), 3717 (SCI), ISSN: 1533-4880.
3. Kyung-Jun Hwang, Seung-Joon Yoo, Sung-Soo Kim, Ji-Man Kim, Wang-Geun Shim, Sun-Il Kim, Jae-Wook Lee, **Photovoltaic Performance of Nanoporous TiO<sub>2</sub> Replicas Synthesized from Mesoporous Materials for Dye-Sensitized Solar Cells**, *J. Nanosci. Nanotechnol.*, **2008**, 8(10), 4976 (SCI), ISSN: 1533-4880.
4. Kyung-Jun Hwang, Seung-Joon Yoo, Sung-Hoon Jung, Dong-Won Park, Sun-Il Kim, Jae-Wook Lee, **Synthesis and Characterization of Nanostructured Titania Films for Dye-Sensitized Solar Cells**, *Bull. Korean Chem. Soc.*, **2009**, 30(1), 172 (SCI), ISSN: 0253-2964.
5. Kyung-Jun Hwang, Jae-Wook Lee, Ho-Sung Yoon, Hee-Dong Jang, Jin-Geol Kim,, Jin-Suk Yang, Seung-Joon Yoo, **Photoelectric Characteristics of Nanocrystalline TiO<sub>2</sub> Film Prepared from TiO<sub>2</sub> Colloid Sol for Dye-Sensitized Solar Cell**, *Bull. Korean Chem. Soc.*, **2009**, 30(10), 2365 (SCI) ISSN: 0253-2964.
6. Kyung-Jun Hwang, Sung-Hoon Jung, Dong-Won Park, Seung-Joon Yoo, Jae-Wook Lee, **Heterogeneous Ruthenium Dye Adsorption on Nanostructured TiO<sub>2</sub> Films for Dye-Sensitized Solar Cells**, *Curr. Appl. Phys.*, **2010**, 10, S184 (SCI), ISSN: 1567-1739.
7. Kyung-Jun Hwang, Wang-Geun Shim, Sung-Hoon Jung, Seung-Joon Yoo, Jae-Wook Lee, **Analysis of Adsorption Properties of N719 Dye Molecules on Nanoporous TiO<sub>2</sub> Surface for Dye-Sensitized Solar Cell**, *Appl. Surf. Sci.*, **2010**, 256, 5428 (SCI), ISSN: 0169-4332.

# Chapter 1. Introduction

## 1.1 Renewable Energy

Since the industrial revolution in the 18<sup>th</sup> century, the demand for energy has increased exponentially. The energy demand which increased concurrently with the development of technology, has been taken for granted, except for shortages that arose during local crises. For example, during the World War II, shortage of petrol in Germany resulted in the invention of wood fired car, which was propelled by wood gases, obtained through distillation of the wood. The petrol crisis was not recognized until the 1970's when the oil crisis struck the world and almost over night the price for crude oil tripled. Although this was a political decision rather than a natural catastrophe, it simulated people's thoughts about energy resources. Government around the world also stepped in to find solutions to the energy resources problem. Considerable efforts were undertaken to identify the limits of current energy resources. At that stage, it was realized that the availability of crude oil and other fossil fuel would last till the turn of the millennium. However, recent advances in exploration technology have extended this threshold.

The first task was to identify alternative form of renewable energy. Of course, nuclear fission was one of the first energy carriers identified and strongly sponsored. However, today we know the problems associated with this kind of energy source and its long-term dangers (such as nuclear disposal issues). The nuclear accidents of Three miles island 1979, Chernobyl 1986 and recently Fukushima 2011 has compelled countries around the world to rethink of obtaining energy from nuclear resources.

At, present, human world energy consumption is made up of about 76% fossil fuels, 14% biomass, 6% hydroelectric power, and 4% nuclear and a tiny fraction from other solar energy sources.<sup>1</sup> Renewable energy has become a fashionable term and is unalterably attached to the phrase "Renewable Energy". The term "Renewable Energy Resource" is used for energy flows which are replenished at rates comparable to which they are used.<sup>2</sup>

Fossil energy (petrol and the likes) is not a renewable energy resource. The crude oil (Fossil fuels) found on our planet was formed over periods of several tens of thousands of years. However, it has been used by mankind within only a few decades which suggests that fossils fuels cannot fall in the category of renewable energy. Nuclear energy obtained from nuclear fusion is also not a renewable energy because its main resources such as uranium were formed during the birth of our planet and therefore is in limited supply.

Similarly, nuclear fusion is also not a renewable energy resource, since it depends on the availability of deuterium. However, these fusion reactions are similar to those that occur in the sun and other stars, and provide a much greater energy potential than nuclear fission. In a fusion process deuterium, a hydrogen isotope reacts to give helium and hydrogen atoms and simultaneously releases the heat. Although the quantity of starting material is finite in a fusion process, it is abundantly available in seawater. The potential nuclear energy that could be released by nuclear fusion of deuterium contained in one cubic meter seawater is  $1,013 \text{ J/m}^3$ . Nevertheless, radioactive substances are formed as side products (nuclear wastes) and the technology will not be available in time for this generation to make fusion an important energy resource.

The quantity of solar energy absorbed by the earth is about equal to the amount of heat reradiated back into space. Utilization of solar energy usually means temporary storage of energy in a usable form (battery or another natural process like photosynthesis). However, solar energy is eventually reconverted into heat upon utilization, so that the renewable cycle is completed. The same renewable cycle is true for wind, tidal and hydrodynamic energy resources. Wood as an energy resource is more complicated to categorize and demonstrates that the definition of renewable energy cannot be sufficiently rigid to allow the adoption of a universal black and white classification scheme. Timber needs on average 60-70 years for regrowth, although some species grow to full size within 10-20 years. In the wood energy cycle, a tree is felled and burnt for energy conversion within a maximum of a few months, and this cycle occurs on a timescale which is significantly shorter than its "energy flow rate". However, if proper forestry management techniques are employed to ensure forest regrowth (such as crop rotation), wood can be considered as a renewable energy source.

The above discussion however, does not take into account the environmental impact of



the energy cycle, such as the greenhouse effect, the release of toxic fumes and undesirable chemical or dangerous radiation into the atmosphere. Ideally, the environment must include the biosphere of the earth as well as all other resources required for our existence. Consequently, a positive attitude toward renewable energy resources is essential and ultimately the use of this kind of energy will be helpful and beneficial.

## **1.2 Photovoltaics**

### **1.2.1 Current Status of Photovoltaics**

After the development of the first silicon solar cell in 1954, the solar cells were used primarily in space applications until about the mid 70s.<sup>3</sup> Since then the solar cells have found applications in consumer electronics, small scale remote residential power systems, as well as in communication and signaling. However, it is only in the second half of last decade that grid connected photovoltaic (PV) systems entered the market with significant contribution as a result of the intensive roof programs in Japan, Germany and US. Today's PV market has exceeded 5,000 MW per year and the market growth has been between 20% and 30% in the last decade as shown in **Figure 1.1**. In 2010 the Production of PV panels exceeded 15,000 MW, and has been forecasted to surpass 20,000 MW in 2013. According to market forecasts predicting an average growth of about 20% world PV market could reach 30,000 MW in 2014.<sup>4</sup>

In order to be a fully sustainable energy resource and technology, photovoltaics has to qualify in certain indicators of viability such as: the energy payback time; the CO<sub>2</sub> emissions and the end-of-life management and recycling. The energy payback time of the PV systems depends not only on the energy content of the entire PV system, but also on the local irradiation conditions. An energy payback time of 2.5-3 years has been estimated for present day grid connected rooftop installations in Southern Europe conditions.<sup>5</sup> This should be compared to the expected life times of over 30 years of the present PV systems.<sup>6</sup> Quite opposite to the fossil energy sources, the CO<sub>2</sub> emissions associated with photovoltaic energy conversion occur almost entirely during system manufacturing instead of

system operation. Therefore the CO<sub>2</sub> emissions depend on the CO<sub>2</sub> emission factor of the local energy utility system, which provides the energy for the manufacture of the PV system.

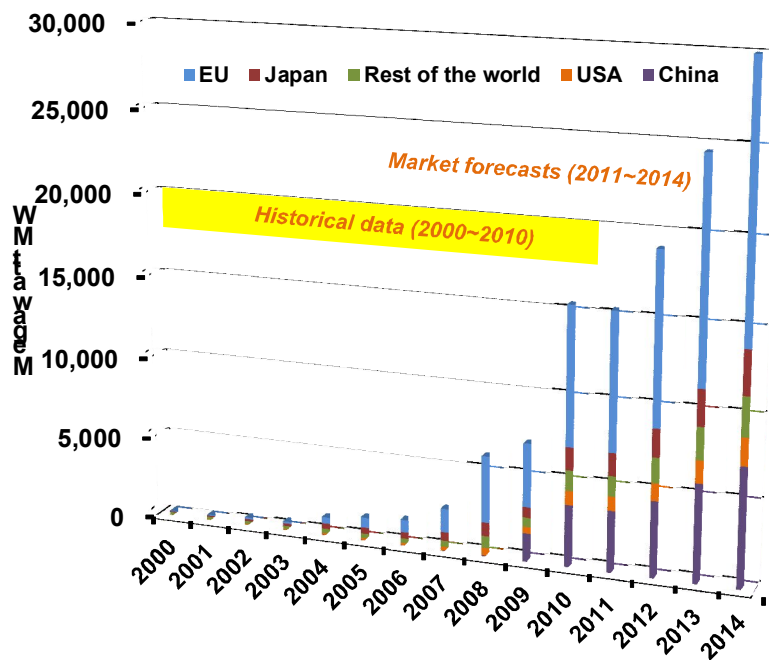


**Figure 1.1.** Evolution of the world annual PV market.

The CO<sub>2</sub> emissions (g/kWh) of the present grid connected rooftop systems have been estimated to be significantly lower than those of fossil fuel power plants, but somewhat higher than those of biomass, wind energy and nuclear energy.<sup>5</sup> The requirement of substantiality of photovoltaic energy conversion extends beyond the operating lifetime of a PV system. Depending on the PV technology the cells contain small amounts of different hazardous and regulated materials, such as Cd, Pb, and Se, which raises concerns about their disposal into municipal landfills. However, the technology for recycling the solar cells already exists and it can be considered also economically feasible.<sup>7</sup>

## 1.2.2 Photovoltaic Technologies

### 1.2.2.1 Single Crystal and Polycrystalline Silicon Solar Cells

The first silicon solar cell was developed by Chapin, Fuller and Pearson at the Bell Telephone Laboratories in the mid 1950's, and could convert solar energy (to electric energy) by 6%.<sup>3</sup> Today, the silicon solar cells dominate the PV market by 86% (**Figure 1.2**) and the record conversion efficiency for a laboratory cell is 24.7%,<sup>8</sup> while the efficiency of the commercial crystalline silicon solar panels in the best case is about 15%.<sup>9</sup> The main reason why Si has dominated the PV market is due to the production of high quality Si in large quantities by the semiconductor industry. The processing of crystalline silicon wafers for high level semiconductor technology is expensive and very capital intensive. The cost of processed silicon wafers contribute to fifty per cent of the total manufacturing cost of the module.<sup>10</sup>

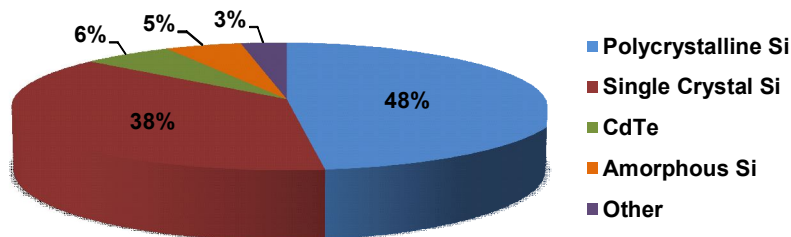


**Figure 1.2.** Market shares of different photovoltaic technologies by the year 2009.

The main hurdle for the success of Si PV technology is the availability of highly purified Si. The PV industry has been using mainly high cost material from the semiconductor industry. This has created a problematic dependence on the volatile semiconductor market causing fluctuations also in the cost of Si material for the solar cells. In fact, it is generally seen that the dominance of the standard Si PV technology in the growing PV market can be realized only by production of a special solar cell grade

silicon. Yet the first efforts to produce such material has been unsuccessful because of the high purity requirements and the small market for the special silicon at the moment.<sup>10</sup> While the crystalline silicon technology is relatively mature, it still has a large cost reduction potential. The cost reduction can be achieved by increasing manufacturing volume.

#### 1.2.2.2 Thin Film Solar Cells

The crystalline silicon is often referred to as the first generation photovoltaic technology, while the second generation photovoltaics consists of thin film solar cell materials such as amorphous silicon (*a*-Si), cadmium telluride (CdTe), copper indium gallium diselenide (CIGS), and thin film crystalline silicon. The driving force for the development of thin film solar cells stems from their potential for the reduction of manufacturing costs. While silicon solar panels are assembled from individual cells processed from about 100 cm<sup>2</sup> silicon wafers, thin film semiconductor materials can be deposited onto large surfaces, which is beneficial for volume production. Also as direct band gap semiconductors the thin film semiconductor materials have much higher absorption coefficient than silicon, and therefore typically less than 1 mm thick semiconductor layer is required, which is 100-1,000 times less than for Si. The amount of expensive semiconductor material is thus reduced, or on the other hand, more expensive semiconductors can be used in the thin films.

*CdTe*: Cadmium telluride has a nearly optimal band gap and is easily deposited with thin film techniques. Over 16% efficiencies have been demonstrated in the laboratory.<sup>8</sup> An often discussed issue of the CdTe technology is the cadmium content of the cells. While this question can be most certainly solved by recycling the Cd if necessary, the public acceptance of the technology may be somewhat trickier question. Solar electricity, usually marketed as an environmentally benign energy form, may not be tolerated to imply environmental concerns about hazardous metals used for the manufacture of the solar cells. However, production plants for commercial presentation of the CdTe cells are being built, the expected module efficiencies are in the range of 8 to 9%.<sup>9</sup>

*CIGS*: Copper indium diselenide (CIS) or CIGS, when gallium is added, is perhaps the most promising thin film material at the moment. It holds the record laboratory efficiency of 18.8% among thin film materials<sup>8</sup> and shows excellent stability. Actually the efficiency

of the CIS cells tend to rise during the first 10-30 minutes of light exposure.<sup>3</sup> First pilot line products are now being marketed by Siemens with efficiencies above 10%.<sup>10</sup> Small amount of cadmium and selenium are also present in the CIGS solar cell hence the concerns associated with the CdTe also apply to the CIGS technology.

*a-Si*: The amorphous silicon (*a-Si*) solar cells have been commercially available since many years and hold 13% of the worlds PV market. The special market for *a-Si* cells has been low power sources for consumer electronics where process ability weights more than the absolute solar conversion efficiency. The problem with *a-Si* has been the degradation of efficiency by the Stabler-Wronski effect and stabilized efficiencies only in the range of 4-5% have been obtained for single junction cells.<sup>11</sup> However, decreasing the thickness of the active *a-Si* layer can enhance the stability of the *a-Si* cells. The best commercial *a-Si* cells utilizes a stacked three-layer structure with stabilized efficiencies of 6.4%.<sup>11</sup> The three-junction concept also enables tuning the band gap of individual layers to achieve higher efficiencies. A three-junction *a-Si* tandem-cell technology utilizing *a-SiGe* alloys in the two lower junctions holds the record confirmed module efficiency of 10.4%.<sup>8</sup>

*Thin Film Si*: One way to reduce the usage of amount of Si in the solar cell is to use optical confinement (light trapping). This idea is utilized in the thin film crystalline silicon technology. When crystalline Si layer with flat surface is deposited on a Lambertian reflector surface the thickness of the Si layer can be reduced, typically to 5-50 mm. Such a thin Si layer needs a supporting substrate which can be either low grade silicon or foreign materials like graphite or glass. Presently the crystalline thin film Si technology is actively developed in the laboratories and the first crystalline silicon thin film product with 12.2% efficiency is about to be made available commercially by Astropower.<sup>10</sup>

### 1.2.2.3 III-V Semiconductors

Semiconductors such as GaAs, GaAlAs, GaInAsP, InAs, InSb, and InP are interesting solar cell materials because they have near optimal band gaps. These materials are extremely expensive, and have found applications only in the space solar cells, where performance is more important criteria than cost, and to some extent in concentrating systems where the active surface area of the cells can be reduced significantly and therefore expensive materials be used.

#### 1.2.2.4 Dye-Sensitized Solar Cells

Historically the dye-sensitization dates back to the 19<sup>th</sup> century, when photography was invented. The work of Vogel in Berlin after 1873 can be considered the first significant study of dye-sensitization of semiconductors, where silver halide emulsions were sensitized by dyes to produce black and white photographic films.<sup>12</sup> The use of dye-sensitization in photovoltaics however remained rather unsuccessful until a breakthrough at the early 1990's in the Laboratory of Photonics and Interfaces in the Federal Institute of Technology, Lausanne (EPFL) Switzerland. By the successful combination of nanostructured electrodes and efficient charge injection dyes professor Grätzel and his co-workers developed a solar cell with energy conversion efficiency exceeding 7% in 1991<sup>13</sup> and 10% in 1993, respectively.<sup>14</sup> This solar cell is called the Dye-Sensitized Solar Cells (DSSC) or the Grätzel cell after its inventor.

In contrast to the all-solid conventional semiconductor solar cells, the dye-sensitized solar cell is a photo electrochemical solar cell and uses a liquid electrolyte or other ion-conducting phase as a charge transport medium. Due to the high efficiencies and good long-term stability reported for the dye-sensitized solar cells, the research interest in this technology grew rapidly during the 1990's. While the patent holders and the licensees developed the original patented concepts towards practical products, numerous research groups explored the replacement of the original materials with new ones.

#### 1.2.2.5 Organic Solar Cells

Synthetic organic materials such as plastics are used literally everywhere in our daily life in coatings and packing materials and in form of plastic consumer products, cloth fibers, coatings, paints, etc. It is therefore not a big surprise, that ever since the discovery of semiconducting polymers, great possibilities and new avenues have been foreseen for the replacement of the inorganic semiconductors, the core materials of the present electronics, with their organic counterparts. One of the possible future applications of these new organic electronic materials is an organic solar cell.

The potential of organic solar cells is related to the idea of low cost photovoltaic materials such as polymers (plastics), which could be easily manufactured as large area films, cut from rolls and installed onto permanent structures. Inspired by the significant

progress in solar cell efficiencies with some organic materials such as dyes in the case of DSSCs and the discovery of efficient charge transfer between certain organic electron donor and acceptor molecules, the research on organic photovoltaic materials has grown rapidly during the last decade and is very active at the moment.

Organic materials used presently in solar cells include for example conducting polymers, dyes, pigments, and liquid crystals. Among these, the conductive polymers are perhaps the best known for their photo physical properties, and some reviews have published on the subject.<sup>15</sup>

**Table 1.1.** Types and characteristics of solar cell materials

Type	Material	Structure/process	Measured conversion efficiency, %	Cost competitiveness	Advantages	Disadvantages (Necessary improvements)
Si-based	Single-crystal Si (SC-Si)	<i>n</i> -type Si layer doped on single-crystal <i>p</i> -type Si layer	25.0	low	High efficiency, high reliability	Not suited for mass production; High cost, variable raw material price, little room for improvement in conversion efficiency
	Polycrystalline Si (MC-Si)	<i>n</i> -type Si layer doped on polycrystalline <i>p</i> -type Si layer	20.4	middle	Lower cost than single-crystal Si; High efficiency, high reliability	Lower efficiency than single-crystal Si; Variable raw material price
	Amorphous Si ( $\alpha$ -Si)	<i>p</i> -layer, <i>i</i> layer, and <i>n</i> layer deposited by CVD process	9.5	middle	Relatively small use of Si material; Lower cost than single-crystal Si	Lower efficiency than single-crystal Si; Light degradation
Compound-based	GaAs	Metal-organic CVD	26.1	low	High efficiency; Endure radiations in space	Low deposition rate; Using toxic As; High cost
	CdTe	<i>p</i> -type CdTe polycrystalline layer on <i>n</i> -type CdS layer	16.7	middle	A variety of production methods; Optimum band gap for generation; Lower cost than single-crystal Si	Using highly toxic Cd; Dependent on the amount of Te resources
	CIS/CIGS	Vapor deposition of CIS/CIGS layers	19.4	middle	High optical absorbance	Dependent on In resources
Dye-sensitized	Dye, semiconductor, electrolyte	Place dye-absorbed TiO <sub>2</sub> electrode in electrolyte	10.4	high	Capable of production by simple process in open air; Colorable, transparent; Maintain generation characteristics under room light etc.	Ultraviolet degradation
Organic thin film based	Fullerene, polymer	Apply mixture of <i>p</i> -type polymer and <i>n</i> -type fullerene etc.	5.2	high	Little thickness; Capable of manufacturing by inexpensive application process	Ultraviolet degradation; Low efficiency

## **1.3 Literature Review**

### **1.3.1 Current Situation of Dye-sensitized Solar Cells**

#### **1.3.1.1 Comparison of Solar Cell Materials**

**Table 1.1** shows the types and characteristics of solar cell materials for comparison.<sup>16</sup> In terms of energy conversion efficiency and long-term reliability, the mainstream solar cells at present are silicon-based. For the sake of promoting the extent to which photovoltaic generation is used in the future, the challenge is to reduce the material and process costs significantly from the current 0.56 \$/kWh. Crystalline silicon solar cells are used in large quantities, but have a unstable cost factor, namely price fluctuations due to material supply.

The problem with amorphous silicon solar cells is low energy conversion efficiency. Non-silicon compound semiconductors are under development, however, such materials have essential problems, including resource depletion and toxicity in the long term. Unlike the foregoing cells, dye-sensitized solar cells have the following advantages:

##### **i) Capable of production in a simple way**

No vacuum process is required for manufacturing. The dye-sensitized solar cells and panels can be produced in a simple way in open air. This means a significant cost reduction of 1/5 to 1/10 as compared to silicon solar cells.

##### **ii) Colorable and transparent**

The use of dye and its wide selection allow colored cells and transparent cells.

##### **iii) Flexible thin structure**

Using aggregates of fine particles of photoelectric conversion materials, the solar cells can be formed as flexible thin films.

##### **iv) Generation characteristics insusceptible to the incident angle and intensity of the sunlight**

Generation characteristics can be maintained even in a weak light condition, such as under faint light in the morning and evening and when indoors.

##### **v) Light weight**

Plastic substrates can be used to reduce the weight of solar cells and panels. With



these advantages, dye-sensitized solar cells can be installed in locations where appearance is important and other solar cells are hardly applicable, such as the glass panels on inner and outer walls of a building (building-integrated photovoltaic, BIPV), the sunroof and outer panels of an automobile and the enclosure of a cellular phone. This allows the creation of new markets with expanded demand.



**Figure 1.3.** Prototype models of dye-sensitized solar cell panels.

**Figure 1.3** shows examples of prototype models for dye-sensitized solar cell panels. Such panels can be installed on the roof of a transit shelter, taking advantage of the excellent design. The panels can be freely and differently decorated for room walls, windows, and interior use.

#### 1.3.1.2 Major Research Institutes of Dye-Sensitized Solar Cells

In this field of research and development, EPFL, led by Professor Grätzel and several Japanese research institutes are leading the world. EPFL excels at approaches based on basic research methods, such as a laser spectroscopic analysis, semiconductor theories, and dye molecular orbital calculation. The Japanese research institutes are successful in pursuing applied research methods, such as the development of dyes and cell devices in collaboration with private companies, universities, and independent administrative institutions. At present, Japanese research achievements provide the world's highest records both in the cell and module conversion efficiencies. Japan is also leading the world in developing

quasi-solid electrolytes and plastic substrates, which are major technological challenges for the future.<sup>17,18</sup>

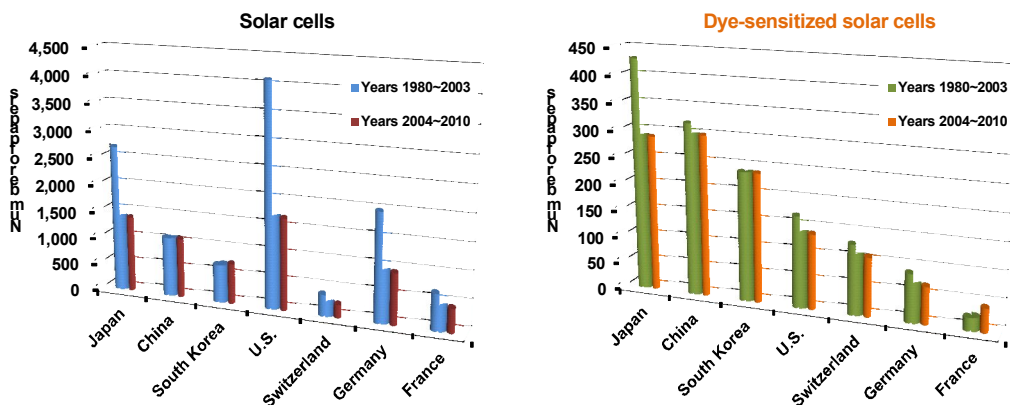


**Figure 1.4.** Numbers of papers on dye-sensitized solar cells and all solar cells.

**Figure 1.4** shows the number of papers on dye-sensitized solar cells and all solar cells from each major country from 1980 to 2010 and since 2004. These results were obtained from the Thomson Reuters' ISI Web of Knowledge database with the search keyword "dye-sensitized solar cell" and "solar cell." Japan has more papers on dye-sensitized solar cell than on any other solar cells. The reason is that more than one university, public research organization and private company were involved in publishing the papers. In recent years, papers from China and South Korea have been increasing sharply.

In regard to commercialization, G24i Innovations (U.K.) and Solaronix SA (Switzerland) have already released commercial products. Dyesol (Australia) has been making efforts toward commercial production including the delivery of modules to public organizations. Konarka Technologies Inc. (U.S.) aims to prepare flexible products for the market. Nissha Printing Co. Ltd. (Japan) has announced that it will ship out samples in 2010, but has yet to reach commercialization. Prototype models have been released by many Japanese company (Aisin Seiki Co. Ltd., Toyota Central R&D Labs. Inc., Fujikura Ltd., Sony

Corporation, TDK Corporation, Rohm Co. Ltd., Hitachi Maxwell Ltd., and Peccell Technologies Inc.). The development for practical use is continuing. Because Grätzel's basic patent (Switzerland) expired on April 12, 2008, efforts toward commercialization and practical use are expected to be more active in the future.

### 1.3.2 Research and Development Trends of Dye-Sensitized Solar Cells

Research and development of the respective technologies of dye-sensitized solar cells will be described by photo electrode, dye, electrolyte, and counter electrode of the cell structure shown in **Figure 1.5**.

#### 1.3.2.1 Photo Electrode

The Grätzel cell is that the photo electrode is made of nanoparticles of titanium oxide ( $\text{TiO}_2$ ) with a porous structure as a support for dye absorption. Layers of  $\text{TiO}_2$  with different particle sizes can be stacked to provide a light confinement effect.

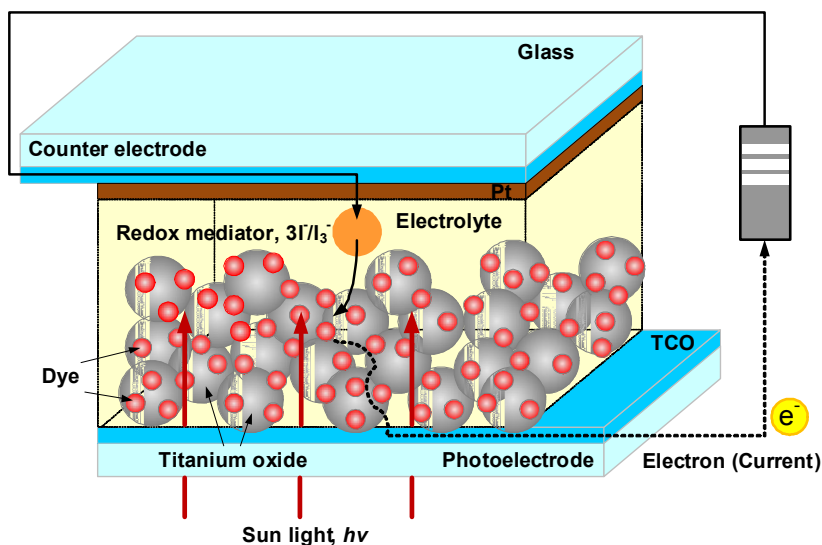


**Figure 1.5.** Cell structure of dye-sensitized solar cell.

This has been combined with the light scattering from star-shaped particles of  $\text{TiO}_2$  to provide a cell conversion efficiency of above 10% (Sumitomo Osaka Cement Co. Ltd.).<sup>19,20</sup> Research has also been made conducted to improve the conductivity of  $\text{TiO}_2$  through morphological control such as the formation of nanotubes as well as to coat the surface of  $\text{TiO}_2$  with a different type of oxide such as niobium oxide ( $\text{Nb}_2\text{O}_5$ ) thereby suppressing electron leakage from the  $\text{TiO}_2$  to the electrolyte solution. Research papers have been published for oxide semiconductor materials other than  $\text{TiO}_2$  and composite materials with other oxide semiconductors to improve charge separation efficiency. Such efforts, however, have not been successful in providing characteristics superior to those of simple  $\text{TiO}_2$ . As for the method of manufacturing the photo electrode, the uniform formation of the electrode is essential in mass production. After various attempts, screen printing is considered to be suitable for mass production.

#### 1.3.2.2 Dye

Dye-sensitized solar cells use the dye to expand the available range of wavelengths in the spectrum of sunlight. The dye therefore plays the essential role in visible region. The dye that was first used in the Grätzel cell was a ruthenium (Ru) bipyridine complex with a carboxyl group. This dye can efficiently absorb visible light in a wavelength range of up to 800 nm. The carboxyl group provides chemical bonding to the surfaces of titanium oxide particles. The resulting advantage was the smooth injection of electrons from the dye to the titanium oxide.<sup>21</sup> **Figure 1.6** shows the action spectrum of dye-sensitized cells with different ruthenium (Ru) dyes. Professor Grätzel et al.<sup>22</sup> then changed the substituent group and found a dye commonly called black dye (N749) which absorbs the light up to a wavelength of 900 nm with a photoelectric conversion efficiency as high as 80% for incident monochromatic light. The cell using this dye records the highest performance at present. Since ruthenium is an expensive metal, ruthenium-free dyes have also been developed. However, no dye has been reported to surpass ruthenium in performance. It should be noted that National Institute of Advanced Industrial Science and Technology (AIST) presented a coumarin organic dye that contains no metallic element and exhibits a conversion efficiency of around 8%.<sup>19</sup> A carbazole dye presented by AIST senior researcher Hara et al. provides an improved cell conversion efficiency and longer life.<sup>23</sup> Studies have

also been made on the stability of the dye. Ruthenium dyes have a turnover (the possible number of photovoltaic conversions per dye molecule) of above ten million, which compares with ten years of light irradiation.

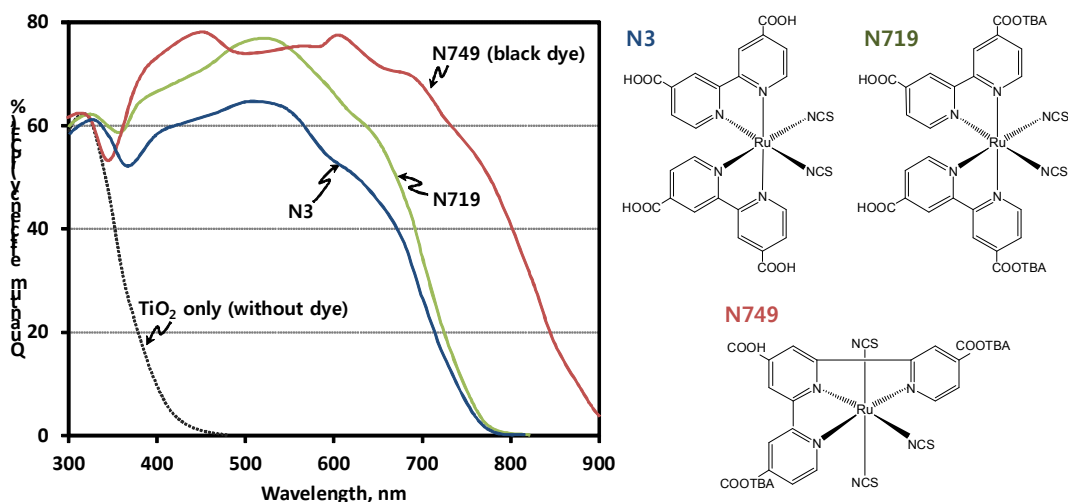


**Figure 1.6.** Action spectrum of dye-sensitized cells with different ruthenium (Ru) dyes.

### 1.3.2.3 Electrolyte

The electrolyte in a dye-sensitized solar cell and its redox potential determines the potential of the cell's positive electrode. The electrolyte is indispensable for the sake of electron transfer in the electrolyte, based on the physical diffusion of redox pairs. The highest conversion efficiency has been achieved by an electrolyte solution of acetonitrile in which iodine ions and iodine are dissolved. Due to low evaporating pressure, acetonitrile is prone to evaporation and drops in the conversion efficiency at high temperatures or with long-term use. Therefore, techniques for sealing the electrolyte in the cell have been developed. The solidification of the electrolyte is also required due to concern about

physical damage to the cell. A quasi-solid electrolyte made of a combination of a nonvolatile ionic liquid and a gel with a conversion efficiency of above 7% was reported at Kyushu Institute of Technology.<sup>24</sup> Aiming at a fully solid electrolyte, there have been research on the use of inorganic compounds such as CuI and CuSCN, conductive polymers such as polypyrrole, low-molecular materials such as triphenyldiamine, and amorphous organic compounds such as OMe-TAD [2,2',7,7'-tetrakis-(*N,N*-di-*p*-methoxyphenyl-amine)9,9'-spirobifluorene].<sup>25</sup>

#### 1.3.2.4 Counter Electrode

The counter electrode plays the role of returning electrons that are generated at the photo-electrode back to the electrolyte through the external circuit. Since the electrolyte is corrosive, the counter electrode requires high corrosion resistance as well as a high reaction rate when reducing iodine in the electrolyte to an iodide ion. Considering the balance between these factors, a conductive glass electrode coated with platinum (Pt) has been used. Carbon electrodes and conductive polymers have been examined as an alternative to expensive Pt, however, such materials do not come up to Pt in terms of the reduction rate.

#### 1.3.2.5 Cell Encapsulation/Modularization

For a better dye-sensitized solar cell, it is understandably necessary to improve the overall performance of the cell device. Dr. Hans of Sharp Corporation et al.<sup>26</sup> clarified the losses in the respective components of a cell by an internal resistance analysis, and achieved the world's highest performance (at present) through loss-reducing approaches. AIST successfully improved the conversion efficiency up to 11% by stacking a plurality of cells in tandem.<sup>27</sup> Attempts to improve efficiency were also made to encapsulate a cell with optical nanofibers.<sup>28,29</sup>

The glass substrate can be replaced with plastic to add flexibility to the cell. For higher output, solar cells need to have an increased area for light reception. A single cell of a greater size however, typically has a higher substrate resistance with a significant drop in output per unit area. This requires more than one cell to be connected for upsizing (modularization). Various methods have been examined to connect cells to each other. A module with connecting grids achieved a conversion efficiency of 9.0% (Tokyo University

of Science).<sup>30</sup> For cell and module stabilities, a single small cell that is stable under simulated solar light for more than 7,000 hours was reported. **Figure 1.7** shows prototype examples of a module with a plastic substrate (Konarka Technologies Inc.) and a large module for outdoor use (Toyota Central R&D Labs. Inc.).<sup>31</sup>



**Figure 1.7.** Plastic substrate module (left) and large module for outdoor use (right).

## 1.4 Outline of This Dissertation

### 1.4.1 Summary of Research Background

Photo electrochemical solar cells (PSC), consisting of a photo electrode, a redox electrolyte, and a counter electrode, have been studied extensively. Several semiconductor materials, including single crystal and polycrystal forms of *n*- and *p*-Si, *n*- and *p*-GaAs, *n*- and *p*-InP, and *n*-CdS, have been used as photo electrodes. These materials, when used with a suitable redox electrolyte, can produce solar light-to-current conversion efficiency of approximately 10%. However, under irradiation photocorrosion of the electrode in the electrolyte solution frequently occurs, resulting in poor stability of the cell hence, efforts

have been made worldwide to develop more stable PSC.

Oxide semiconductor materials have good stability under irradiation in solution. However, stable oxide semiconductor cannot absorb visible light because they have relatively wide band gaps. Sensitization of wide band gap oxide semiconductor materials, such as  $\text{TiO}_2$ ,  $\text{ZnO}$ , and  $\text{SnO}_2$  with photosensitizers such as organic dyes that can adsorb visible light has been extensively studied in relation to the development of photography technology since the late nineteenth century. In the sensitization process, photosensitizers adsorbed onto the semiconductor surface absorb visible light and excited electrons are injected into the conduction band of the semiconductor electrodes. Dye-sensitized oxide semiconductor photo electrode have been used for PSC.

Gerischer and Tributsch studied a  $\text{ZnO}$  electrode sensitized by organic dyes including rose bengal, fluorescein, and rhodamine.<sup>32</sup> In early studies, single crystal and polycrystal materials which cannot adsorb a large amount of dye were used for the photo electrode that resulted in low light-harvesting efficiency (LHE) and consequently low photon to current conversion efficiencies. Additionally, the organic dyes that were used had a narrow absorption range in visible light, which also contributed to low solar cell performance. Therefore, to improve light-harvesting efficiencies and cell performance, researchers used two approaches: developing photo electrodes with larger surface areas that could adsorb large amount of dye and synthesizing dyes with broader absorption ranges. Significant improvements in the performance of a dye-sensitized solar cell (DSSC) have been mainly due to the development of high performance nanoporous  $\text{TiO}_2$  thin film electrodes that have a large surface area capable of adsorbing a large amount of photosensitizer, and due to the synthesis of new Ru complex photosensitizers capable of adsorbing in the wide visible and near-IR region from 400 to 800 or 900 nm.

Ru bipyridyl complexes are suitable photosensitizers because the excited state of the complexes have long lifetimes and oxidized Ru (III) has long-term chemical stability. Therefore, Ru bipyridyl complexes have been studied intensively as photosensitizers for homogeneous photocatalytic reactions and dye-sensitization systems. An Ru bipyridyl complex, bis(2,2'-bipyridine)(2,2'-bipyridine-4,4'-dicarboxylate)ruthenium(II), having carboxy groups as anchors to adsorb onto the semiconductor surface, was synthesized and single crystal  $\text{TiO}_2$  photo electrodes sensitized by the Ru complex were developed and studied in



1797 to 1980.<sup>33</sup>

Recent drastic improvements in the performance of DSSC have been made by Grätzel and coworkers at the EPFL. They achieved a solar energy efficiency ( $\eta_{eff}$ ) of 7 to 10% under air mass (AM) 1.5 irradiation using a DSSC consisting of a nanocrystalline TiO<sub>2</sub> thin film electrode having a nanoporous structure with large surface area, a novel Ru bipyridyl complex, and an iodine redox electrolyte.<sup>14</sup> The DSSC is an attractive and promising device for solar cell application that have been intensively investigated worldwide, and its PV mechanism is well understood.<sup>34,35</sup> Recently, commercial applications of the DSSC have been under intensive investigation. The cost of commercially fabricating DSSC is expected to be relatively low because the cells are made of low cost materials and assembly is simple and easy.

#### **1.4.2 Purpose and Outline of This Dissertation**

The thesis is arranged into six Chapters, the first chapter contains an introduction to the thesis and describes the history of development of renewable energy, the current situation of photovoltaics technologies, and literature review of dye-sensitized solar cells as well as the outline of this study. The overall layout of the thesis is shown in **Figure 1.8**.

**Chapter 2** deals with the theoretical background of DSSC. The basics of photovoltaic energy conversion is described. The parameters related to photovoltaic cell performance are also listed in a separate sections. The operating principle of the DSSC is presented along with the mechanism of this process. In addition, theoretical issues of DSSC operation is systematically explained. The fundamental physical and chemical processes of the cell operation is discussed. The materials of the DSSC are introduced. The components of the cell are treated one by one each time making a cut through to the literature by examining the used materials, their key properties and the related preparation methods. The fabrication of DSSC is described in this work. The manufacturing begins with: the making of TiO<sub>2</sub> particle and TiO<sub>2</sub> film; followed by dyeing of the films; producing counter electrode; preparing the electrolyte; and finally assembling the cell. Finally, simple electrical model of the DSSC is introduced.

**Chapter 3** describes photovoltaic properties of TiO<sub>2</sub> electrode prepared by sol-gel method. In this chapter, the preparation of SG-TiO<sub>2</sub> (synthesized TiO<sub>2</sub> in chapter 3)

electrode by typical sol-gel method and its various characterizations are investigated for the application of DSSC. The prepared SG-TiO<sub>2</sub> was also used for investing dye (N719) for adsorption properties. The influence of adsorption amount of N719 on the energy conversion efficiency of DSSC was investigated on the basis of photocurrent-potential curves. Finally, an equivalent circuit analysis using the one-diode model by a nonlinear least-square optimization method was used to evaluate the influences of adsorption quantity on the energy conversion efficiency of DSSC.

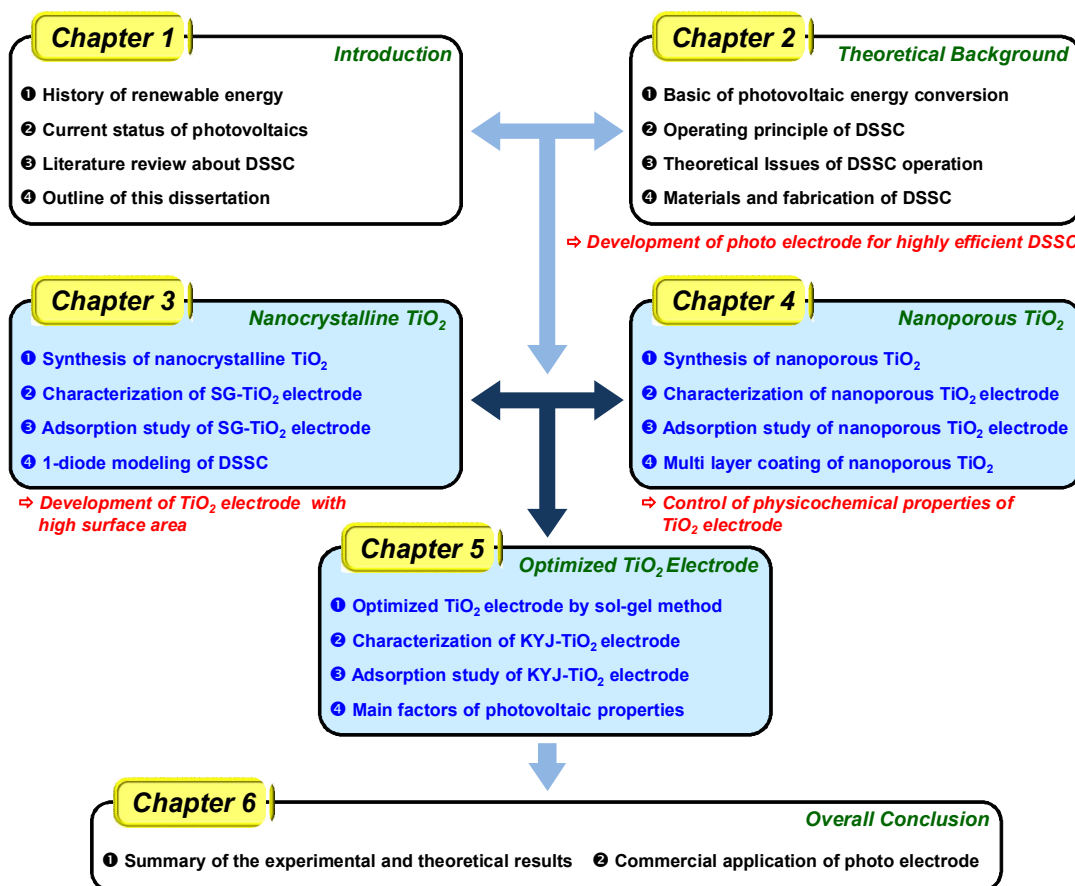


**Figure 1.8.** Overall layout.

**Chapter 4** investigates photovoltaic properties of TiO<sub>2</sub> electrode prepared by mesoporous silica template. In this chapter, nanoporous TiO<sub>2</sub> with high surface area and uniform pore

network for DSSCs were synthesized to increase the surface area of the photo electrode. Highly ordered nanoporous  $\text{TiO}_2$  materials (MK- $\text{TiO}_2$ , MS- $\text{TiO}_2$ , and MU- $\text{TiO}_2$ ) with crystalline frameworks were successfully synthesized from different silica templates including SBA-15, KIT-6, and MSU-H. The as-synthesized samples were characterized by various instrumental analysis. The influence of the adsorption properties between N719 molecules and nanoporous  $\text{TiO}_2$  thin film surfaces on the energy conversion efficiency of DSSC was also systematically investigated on the basis of photovoltaic performance calculated from the  $I-V$  curves.

**Chapter 5** deals enhanced photovoltaic properties of  $\text{TiO}_2$  electrode prepared by polycondensation in sol reaction. The fabrication of DSSC using the KYJ- $\text{TiO}_2$  (synthesized  $\text{TiO}_2$  in chapter 5) from modified sol-gel method were discussed in this chapter. KYJ- $\text{TiO}_2$  sol was prepared by the process of aging accompanied hydrolysis/polycondensation using titanium-tetraisopropoxide (TTIP) as a starting material. The aging conditions were adjusted to control the particle size and crystalline structure of  $\text{TiO}_2$  sol and  $\text{TiO}_2$  particle. A  $\text{TiO}_2$  thin film on photo electrode of DSSC was fabricated using  $\text{TiO}_2$  sol. In especial, the effect of aging times and temperatures on physical and chemical properties of KYJ- $\text{TiO}_2$  thin film was systematically investigated. Moreover, the adsorption properties of N719 dye molecules on the prepared KYJ- $\text{TiO}_2$  thin film were also investigated.

Finally, overall conclusions are drawn in **Chapter 6** on the basis of the experimental and theoretical results. The thesis includes 187 pages, 91 figures and 31 tables and 188 references.

## Chapter 2. Theoretical Background

### 2.1 Basics of Photovoltaic Energy Conversion

#### 2.1.1 Solar Irradiation and Availability of Solar Electricity

The intensity of solar radiation in the earth's distance from the sun is approximately  $1,353 \text{ kW/m}^2$ , a number also called the solar constant. The solar radiation is emitted from the sun's photosphere at  $6,000 \text{ K}$  temperature, which gives it a spectral distribution resembling closely that of a black body at the corresponding temperature.

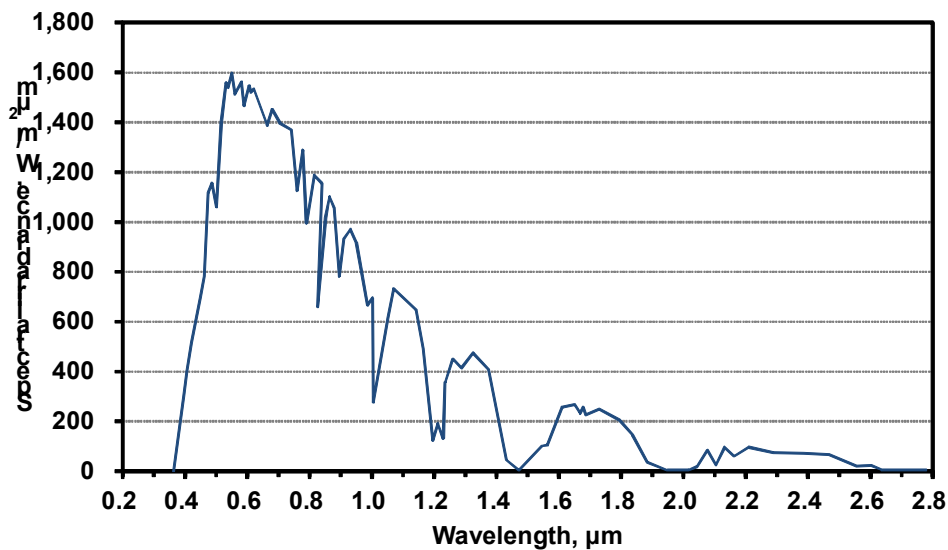


Figure 2.1. The standard AM 1.5 global solar spectrum.

Passing through the earth's atmosphere the solar radiation is attenuated by scattering from the air molecules, aerosols and dust particles, as well as by absorption by the air

molecules, in particular oxygen, ozone, water vapor, and carbon dioxide. **Figure 2.1** gives a characteristic fingerprint to the solar radiation spectrum on the earth's surface.

The available solar irradiation at a certain place depends on the latitude, the altitude and the climatic type, on the season, the time of day and the weather conditions in a specific time. The total yearly solar irradiation on horizontal surface is 700-1,000 kWh/m<sup>2</sup> in North Europe, 900-1,300 kWh/m<sup>2</sup> in Middle Europe, 1,300-1,800 kWh/m<sup>2</sup> in South Europe, 1,800-2,300 kWh/m<sup>2</sup> in the equator, and 2,000-2,500 kWh/m<sup>2</sup> in the so called "solar belt" i.e. between 20° and 30° latitude respectively. An order of magnitude estimate of the usefulness of these yearly solar energy densities, converted to electricity with a grid-connected PV system, can be made by comparing these to an area related yearly electricity consumption of a typical detached house. In Finland, a typical electricity consumption for a 4 person family living in a detached house with floor area of 120 m<sup>2</sup> and using electric heating is 18,500 kWh/year.<sup>36</sup>

The yearly solar irradiation falling to the same horizontal area in North Europe conditions (about 1,000 kWh/m<sup>2</sup>/year), converted to solar electricity with total PV system efficiency of 10% amounts to about 12,000 kWh/m<sup>2</sup>, i.e. about 65% of the yearly electricity consumption of the examined typical Finnish family. In a large scale, the determination of the actual practical grid-connected PV potential is of course a far more complicated task, since factors such as type of the buildings, roof shapes, tilt angles, shading questions, ages of the buildings, and other technical questions has to be accounted.

By an analysis of the building stock Gutschner et al.<sup>36</sup> estimated that 16% of the electricity consumption of a urban area (city of Zurich) and almost half of the consumption of a rural area (canton of Fribourg) could replace by solar electricity generated by BIPV covering the available roof-top area having a good solar yield (more than 80% of the maximum annual solar irradiation).

## **2.1.2 Photovoltaic Cell Performance**

### **2.1.2.1 Basic Solar Cell Parameters**

When a solar cell is illuminated, a current and voltage are generated. The current

depends on voltage and a plot of current versus voltage is called the  $I$ - $V$  curve of the cell. The characteristics of an  $I$ - $V$  curve depends on illumination as well as the temperature. A typical  $I$ - $V$  curve is shown in **Figure 2.2**.

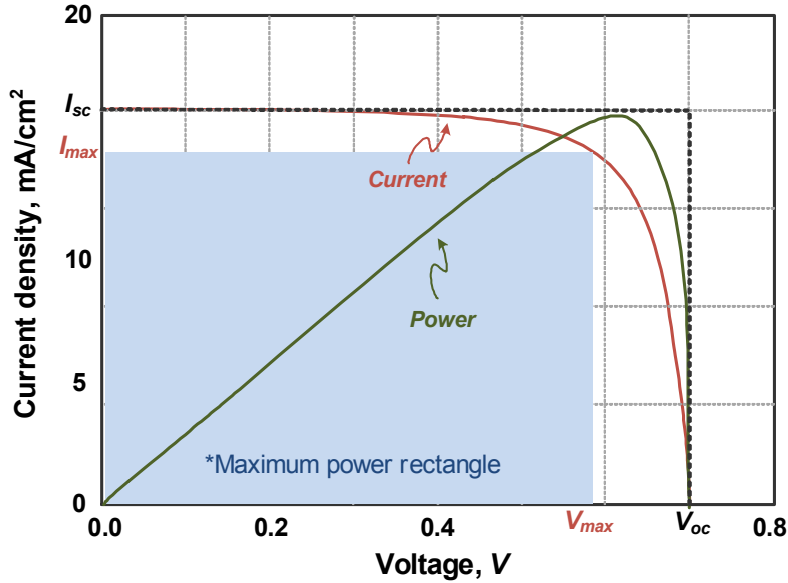


**Figure 2.2.** A typical  $I$ - $V$  curve of a solar cell.

If the voltage is zero, i.e. the cell is short circuited, then the short circuit current  $I_{sc}$  is generated. On the other hand, if there is no current in the cell, the voltage over the cell will be the open circuit voltage  $V_{oc}$ . The generated power equals current times voltage, and the power-voltage dependence corresponding to the  $I$ - $V$  curves as shown in the **Figure 2.2**. The maximum of the power-voltage curve is called the maximum power unit (MPU). The voltage, current and power at MPU are  $V_{max}$ ,  $I_{max}$  and  $P_{max}$ , respectively.<sup>37,38</sup> The energy conversion efficiency  $\eta_{eff}$  (%) of a solar cell is depend as ratio of the output of the cell and incident irradiance as shown in **Equation 2.1**.

$$\eta_{eff}(\%) = \frac{P_{out}}{P_{in}} \times 100 = \frac{V_{max} I_{max}}{P_{in}} \times 100 = \frac{V_{oc} I_{sc} FF}{P_{in}} \times 100 \quad (\text{Eq. 2.1})$$

where  $FF$  is the fill factor which can be defined by **Equation 2.2**.

$$FF = \frac{V_{\max} I_{\max}}{V_{oc} I_{sc}} \quad (\text{Eq. 2.2})$$

The fill factor is an important part of the efficiency of the cell. High open circuit voltage and short circuit current are essential in achieving high efficiencies. However, the overall efficiency of the cell with a low fill factor will remain low. In the standard condition used for testing of terrestrial solar cells the light intensity is  $1,000 \text{ W/m}^2$ , the spectral distribution of the light source is that of AM 1.5 global standard solar spectrum (**Figure 2.1**) and temperature of the cell is  $298.15 \text{ K}$ . In practice, special solar simulator light sources are used for the standard measurements. **Figure 2.3** shows the solar simulation system installed in our laboratory. In this thesis, the current-voltage ( $I$ - $V$ ) curves are measured using a source measure unit under irradiation of white light from a  $1,000 \text{ W}$  Xenon lamp (Thermo Oriel Instruments Co.). The incident light intensity and the active unit cell area are  $100 \text{ mW/cm}^2$  and  $0.25 \text{ cm}^2$  respectively.

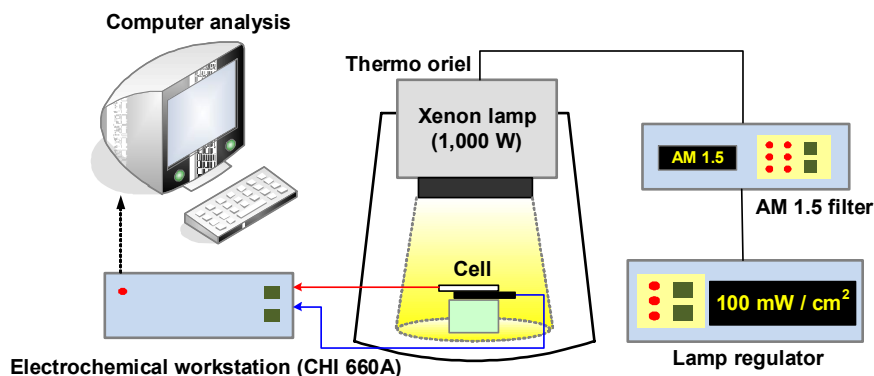


**Figure 2.3.** A solar simulation system.

Incident photon to current conversion efficiency (IPCE) is another important parameter when determining the performance of a solar cell. IPCE is defined as the number of

electrons flowing through the external circuit divided by the number of photons incident on the solar cell surface at particular wave length  $\lambda$ .<sup>37</sup> In the case of DSSC, it is defined as the ratio between the observed photocurrent (short circuit current) and the incident photon flux uncorrected for reflective losses during optical excitation through the conducting glass electrode. It can also be considered as a product of three components as give by **Equation 2.3**.

$$IPCE(\lambda) = LHE(\lambda) \Phi_{inj} \eta_{el} = 1,240 \frac{I_{sc}(\lambda)}{\lambda \Phi_{hv}(\lambda)} \quad (\text{Eq. 2.3})$$

where, the light harvesting efficiency (LHE) depends on the spectral properties of the dye, the charge injection yield ( $\Phi_{inj}$ ) which depends on the excited state redox potential and life time, and charge collection efficiency ( $\eta_{el}$ ) that depends on the structure and morphology of the TiO<sub>2</sub> layer. The right part of the **Equation 2.3** is the general definition of IPCE which can be applied to all solar cells [ $\lambda$  is the wavelength and  $\Phi_{hv}(\lambda)$  is the photon flux]. Further explanation of the different factors of **Equation 2.3** can be found in Nazeeruddin et al.<sup>14</sup> IPCE is often referred to as photocurrent action spectrum or spectral response or (external) quantum efficiency. A standard example of IPCE is shown in **Figure 1.6** (left side).

#### 2.1.2.2 Operating Principle of the Standard Silicon Solar Cell

The standard silicon solar cell is based on a semiconductor *pn*-junction. The cell consists of *n*-doped and *p*-doped semiconductor layers forming the *pn*-junction, an antireflection coating, current collectors and a metal substrate for the collection of photogenerated charge carriers from *n*-type (electrons) and *p*-type (holes) layers respectively (**Figure 2.4**). *N*-type semiconductors are obtained by doping with impurity atoms (from group V in the case of silicon) having an excess valence electron with respect to the surrounding host atoms. *P*-type semiconductors on the other hand are obtained by doping with impurity atoms (from group III in the case of silicon) with one valence electron less than the surrounding atoms. The *n*-type doping results in localized energy states just below



the conduction band edge of the host semiconductor lattice and occupied by the excess electrons from the impurity atoms, while  $p$ -type doping results in (Figure 2.5a) localized empty states with energy slightly above the valence band edge of the semiconductor.<sup>39</sup>

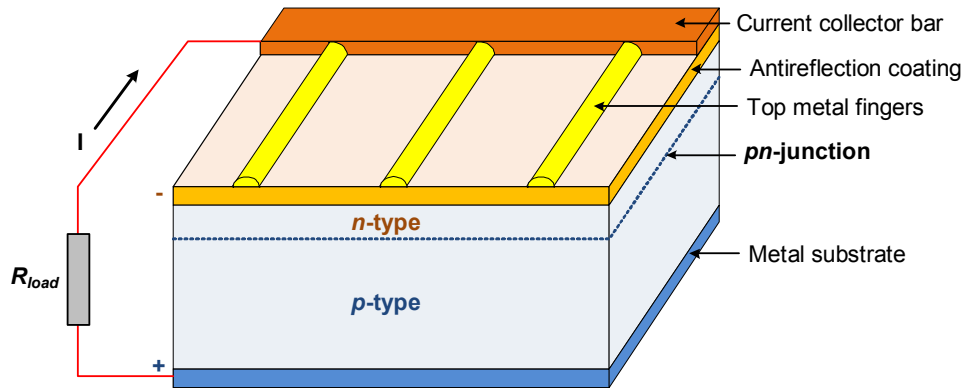


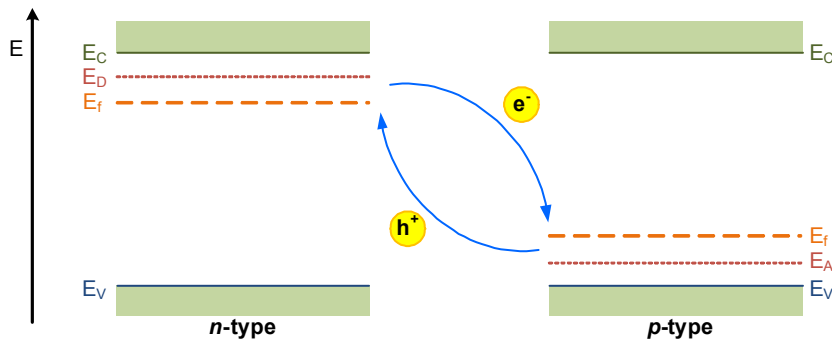
**Figure 2.4.** The standard  $pn$ -junction solar cell configuration from the 1960s.

The donor atoms in the  $n$ -type material are easily ionized by thermal excitation due to the closeness of the donor states and the conduction band edge. The ionization of the donor atoms generates free electrons to the conduction band and leaves immobile empty donor states behind. For the same reason in the  $p$ -type material the originally empty acceptor states are partly filled by electrons from the valence band leaving mobile holes to the valence band. Bringing an  $n$ -type and  $p$ -type semiconductor in contact leads to a transport of electrons and holes across the junction until equilibrium is reached. This can be described as equalization of the Fermi-level in the both materials in thermal equilibrium with each other, and this process sets up a depletion zone near the junction where there are practically no free charges, but an electric field (potential difference) across the region.

The formation of the  $pn$ -junction is pictured schematically in Figure 2.5. Upon illumination of the  $pn$ -junction photons are absorbed by excitation of electrons from the valence band to the conduction band leaving holes to the valence band. Due to the high crystallinity of the semiconductor, which is essential for good operation, the electrons and holes are more or less free to move in the material by drift due to potential (or Fermi

energy) gradients and by diffusion due to concentration gradients. The existence of the built-in electric field in the  $pn$ -junction region is the source of photovoltaic activity in the cell. Under illumination, a large number of electrons and holes are generated in the semiconductor material.

- (a) Schematic band structure of an  $n$ -type and a  $p$ -type semiconductor showing conduction and valence band edges  $E_C$  and  $E_V$ , donor level  $E_D$  in  $n$ -type material and acceptor level  $E_A$  in the  $p$ -type material and the Fermi level.



- (b)  $pn$ -junction in thermal equilibrium showing the potential difference  $V_D$  across the junction.

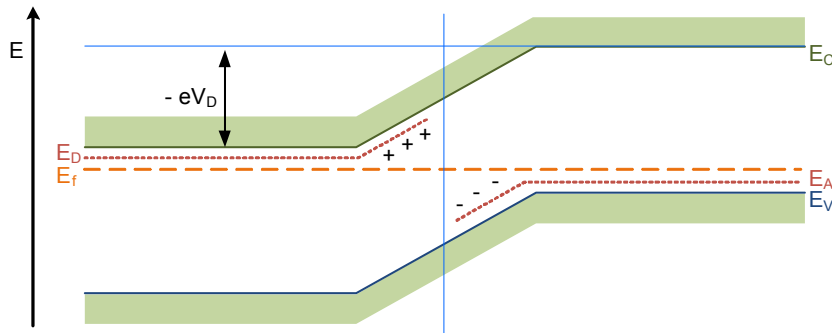


**Figure 2.5.** Formation of the abrupt semiconductor  $pn$ -junction.

Minority charge carriers (holes in the  $n$ -type and electrons in the  $p$ -type layers) generated in the depletion region of the  $pn$ -junction, or within their diffusion length from it, are swept to the opposite side of the junction by the built-in electric field of the junction. Under illumination, electrons are accumulated in the  $n$ -type material and holes in the  $p$ -type

material, generating voltage between the opposite sides of the *pn*- junction and electrical contacts attached to them as well as current through an external load attached between the contacts.<sup>39</sup>

The operation of a photovoltaic cell can be generally divided into three basic steps: i) Light absorption ii) Charge separation iii) Charge collection. The physical or chemical processes behind these principal steps vary between different types of solar cells and photovoltaic materials. The efficiency of a solar cell depends on the efficiency of each of these steps and is maximized by the materials selection and the cell design. In the standard *pn*-junction solar cell, light absorption occurs via band gap excitation of electrons in the bulk of the semiconductor, charge separation in the internal electric field of the *pn*-junction and charge collection by transport of electrons and holes (electric current) through the bulk of the semiconductor to the electrical contacts.

## 2.2 Operating Principle of Dye-Sensitized Solar Cell

At its simplest configuration (**Figure 1.5**), the DSSC is comprised of a transparent conducting glass electrode coated with porous nanocrystalline TiO<sub>2</sub>, dye molecules attached to the surface of the TiO<sub>2</sub>, an electrolyte containing a reduction-oxidation couple such as I<sup>-</sup>/I<sub>3</sub><sup>-</sup> and a catalyst coated counter-electrode. At the illumination the cell produces voltage over and current through an external load connected to the electrodes.

The absorption of light in the DSSC occurs by dye molecules and the charge separation by electron injection from the dye to the TiO<sub>2</sub> at the semiconductor electrolyte interface. A single layer of dye molecules however, can absorb only less than one percent of the incoming light.<sup>13</sup> While stacking dye molecules simply on top of each other to obtain a thick dye layer increases the optical thickness of the layer, only the dye molecules in direct contact to the semiconductor electrode surface can separate charges and contribute to the current generation. A solution to this problem, developed by the Grätzel group, was to use a porous nanocrystalline TiO<sub>2</sub> electrode structure in order to increase the internal surface area of the electrode to allow large amount of dye to be contacted at the same time by the TiO<sub>2</sub> electrode and the electrolyte (**Figure 1.5**).

A TiO<sub>2</sub> electrode typically 10  $\mu$ m thick, with an average particle (as well as pore)

size typically in the order of 20 nm, has an internal surface area thousands of times greater than the geometrical (flat plate) area of the electrode.<sup>22</sup> Essential to the optical operation of this porous electrode structure is the fact that  $\text{TiO}_2$  as a large band gap semiconductor absorbs only below about 400 nm (**Figure 1.6**) letting the major part of the solar spectrum available for the dye molecules.

The regenerative working cycle of the DSSC showing schematically the relative energy levels of a working DSSC is depicted in **Figure 2.6**. The incoming photon is absorbed by the dye molecule adsorbed on the surface on the nanocrystalline  $\text{TiO}_2$  particle and an electron from a molecular ground state  $S^0$  is excited to a higher lying excited state  $S^*$  (reaction 1).

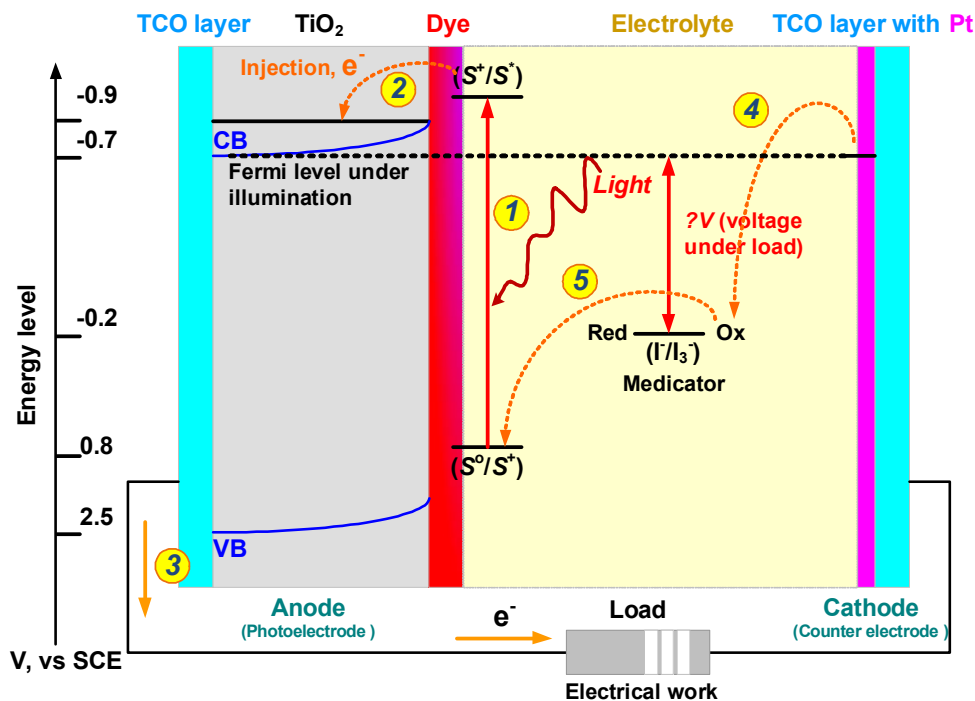
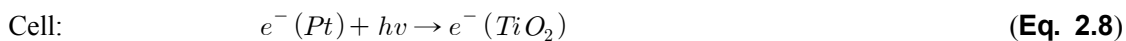
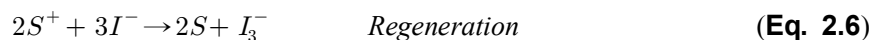


**Figure 2.6.** The working principle of the dye-sensitized solar cell.

The excited electron is injected to the conduction band (CB) of the  $\text{TiO}_2$  particle leaving the dye molecule to an oxidized state  $S^+$  (reaction 2). The injected electron percolates

through the porous nanocrystalline structure to the transparent conducting oxide layer of the glass substrate (negative electrode, anode) and finally through an external load to the counter electrode (positive electrode, cathode) (reaction 3). At the counter electrode the electron is transferred to triiodide in the electrolyte to yield iodine (reaction 4), and the cycle is closed by reduction of the oxidized dye by the iodine in the electrolyte (reaction 5).

The operating cycle can be summarized in chemical reactions as shown from **Equations 2.4-2.8**:<sup>40</sup>



Due to the energy level positioning in the system (**Figure 2.6**), the cell is capable of producing voltage between its electrodes and across the external load. The maximum theoretical value for the photo voltage at open circuit condition is determined by the potential difference between the conduction band edge of the  $TiO_2$  and the redox potential of the  $I/I_3^-$  pair in the electrolyte.<sup>41</sup> The operation of the cell is regenerative in nature, since no chemical substances are neither consumed nor produced during the working cycle, as visualized in the cell reaction (**Equation 2.8**).

## 2.3 Theoretical Issues of Dye-Sensitized Solar Cell Operation

Since the invention of the DSSC, a lot of theoretical and experimental work has been carried out to explain the surprisingly efficient operation of these solar cells. The fundamental differences in the operation between the DSSCs and the traditional semi-

conductor *pn*-junction solar cells are summarized below:

- i) In contrast to the semiconductor *pn*-junction solar cells, where light absorption and charge transport occurs in the same material, the DSSC separate these functions: photons are absorbed by the dye molecules; and transport of charges is carried out in the TiO<sub>2</sub> electrode and electrolyte.
- ii) While the charge separation in the semiconductor *pn*-junction cells is induced by the electric field across the junction, no such long-range electric fields exist in the DSSC. The charge separation occurs via other kinds of kinetic and energetic reasons at the dye-covered semiconductor-electrolyte interface.
- iii) In the semiconductor *pn*-junction cells the generated opposite charges travel in the same material, while in the DSSC, electrons travel in the nanoporous TiO<sub>2</sub> network and holes in the electrolyte. This means that the requirement for a pure and defect free semiconductor material in the case of semiconductor *pn*-junction solar cell is relaxed in the DSSC, where, the recombination can occur only at the semiconductor electrolyte interface.

### **2.3.1 Light Absorption**

While the high efficiency of DSSC arises from a collective effect of numerous well-tuned physical-chemical nano scale properties (as will become apparent later), the key issue is the principle of dye-sensitization of large band-gap semiconductor electrodes. As already mentioned, in the DSSC this is accomplished by coating the internal surfaces of the porous TiO<sub>2</sub> electrode with special dye molecules tuned to absorb the incoming photons. **Figure 1.6** represents the molecular structures of three efficient photosensitizers for DSSCs including the so called N3 dye, N719 dye, and the black dye.

#### **2.3.1.1 Adsorption of the Dye Molecule**

The adsorption of the dye to the semiconductor surface usually takes place via special anchoring groups attached to the dye molecule. In the N3 dye these are the four carboxylic groups (COOH) at the end of the pyridyl rings (**Figure 1.6**). The COOH groups form a bond with the TiO<sub>2</sub> surface by donating a proton to the TiO<sub>2</sub> lattice.<sup>42</sup> The area occupied

by one N3 molecule at the  $\text{TiO}_2$  surface at full monolayer coverage is  $1.65 \text{ nm}^2$ .

### 2.3.1.2 Light Absorption via MLCT Excitation

The absorption of a photon by the dye molecule happens via an excitation between the electronic states of the molecule. For example the N3 dye has two absorption maxima in the visible region at 518 nm and at 380 nm.<sup>42</sup> The excitation of the Ru complexes via photon absorption is of metal to ligand charge transfer (MLCT) type (**Figure 2.7**). This means that the highest occupied molecular orbital (HOMO) of the dye is localized near the metal atom, (Ru in this case) whereas, the lowest unoccupied molecular orbital (LUMO) is localized at the ligand species (in this case at the bipyridyl rings). On excitation, an electron is lifted from the HOMO to the LUMO level.<sup>42</sup> Furthermore, the LUMO level (extending even to the COOH anchoring groups) is spatially close to the  $\text{TiO}_2$  surface, which means that there is significant overlap between the electron wave functions of the LUMO level of the dye and the conduction band of  $\text{TiO}_2$ . This directionality of the excitation is one of the reasons for the fast electron transfer process at the dye- $\text{TiO}_2$  interface.

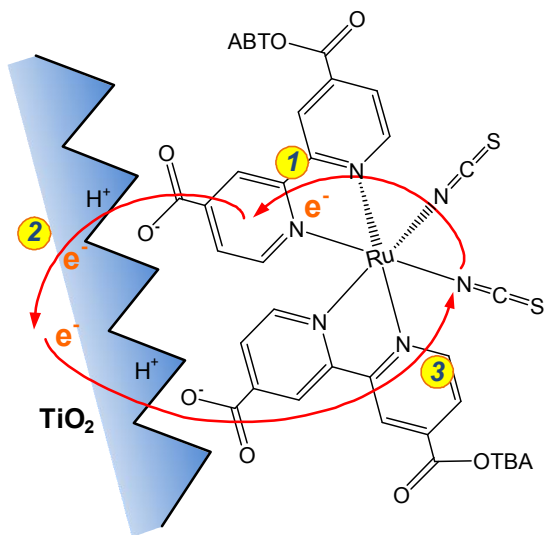


**Figure 2.7.** Charge transfer processes between dye and the  $\text{TiO}_2$  lattice: i) MLCT excitation, ii) Electron injection, and iii) Charge recombination.

### 2.3.1.3 Effect of the Sensitization

The efficient spectral sensitization in the DSSC is made evident in **Figure 1.6**, where the spectral response (IPCE) curves, i.e. the photon to current efficiency curves, for cells sensitized with different dyes is compared with a naked  $\text{TiO}_2$  electrode. The actual sensitization effect can be seen in **Figure 1.6** as a shift of the IPCE curve of the naked  $\text{TiO}_2$  to the higher wave lengths when coated with the dye. The current efficiency of the cell is related to the 'height' of the IPCE curve, which depends on the charge separation and charge collection efficiencies. The IPCE curves in **Figure 1.6** are not corrected for the optical losses in the glass substrate, which only makes the obtained peak IPCE values more significant.

### 2.3.2 Charge Separation

The charge separation in DSSCs is based on an electron transfer process from the dye molecule to  $\text{TiO}_2$  and a hole transport process from the oxidized dye to the electrolyte. The electron transfer mechanism is strongly dependent on the electronic structure of the adsorbed dye molecule and the energy level matching between the excited state of the dye and the conduction band of the  $\text{TiO}_2$ . While charge separation in the semiconductor *pn*-junction arises from the electric field in the space-charge layer in the junction area, the situation in a nanoparticle electrode-electrolyte interface is quite different. The individual particle size in the nanostructured electrode, typically a few tens of nanometers, is too small for the formation of a space charge layer inside the particles.<sup>35</sup> Furthermore, no significant macroscopic electric fields are present between the individual nanoparticles in the bulk of the electrode. In this case, the absence of band bending is a result of the individuality of each nanocrystalline particle. A sufficiently thick nanoparticle film could have a collective space charge, if the film behaved as an ensemble. However, the electrolyte surrounding all the particles effectively decouples the particles and screens any existing electric fields within about a nanometer.<sup>43</sup> While the band bending inside the particles is inhibited, there exists an electric field at the semiconductor-electrolyte interface due to the adsorbed dye molecules. The dye molecules usually have an acid group ( $\text{COOH}$ ) as attachment units and upon binding a proton ( $\text{H}^+$ ) is released to the oxide surface leaving the dye molecule negatively charged (**Figure 2.7**). The potential difference



across the consequently formed Helmholtz's layer is estimated to be approximately 0.3 eV, and it will help to separate the charges and to reduce recombination.<sup>41</sup>

The major mechanism for the charge separation is the energy level positioning (**Figure 2.6**) between the dye molecule and the nanoparticle. The excited state of the dye (the LUMO level) is above the conduction band edge of the TiO<sub>2</sub> and the dye's HOMO level is below the chemical potential of the redox pair iodide/triiodide in the electrolyte both presenting an energetic driving force for the electron and hole separation. In addition to the favorable energetics for the charge separation, also entropic factors arise. The large density of delocalized states in the nanoparticle compared to small number of dye molecules on the particle surface means that the electron injection to the TiO<sub>2</sub> conduction band is associated with an entropy increase presenting a driving force of approximately 0.1 eV for the charge separation.<sup>41</sup>

### **2.3.3 Charge Transport**

In the DSSCs charge transport happens by electron transport in the nanostructured TiO<sub>2</sub> electrode and hole transport in the electrolyte as I<sub>3</sub><sup>-</sup>. Although the electron transport process has attracted an intensive study due to several interesting fundamental questions arising from it, both charge transport mechanisms are equally important for the operation of the solar cell.

#### **2.3.3.1 Electron Transport in the Nanostructured Semiconductor Electrode**

The semiconductor nanoparticle network works not only as a large surface area substrate for the dye molecules but also as a transport media for the electrons injected from the dye molecules. The nature of the highly efficient electron transport in the dye-sensitized electrode is particularly intriguing and has puzzled researchers since the invention of the DSSC. Is the electron transport driven by built-in electric fields or by diffusion? How can the inherently poor conductor TiO<sub>2</sub> perform high photocurrents in the dye cell? Are the electrons travelling in the bulk or on the surface of the particles? These are some of the questions that arise from the better performance of DSSC.

Because of the porous structure of the electrode and the screening effect of the

electrolyte, the electrode can be viewed as a network of individual particles through which electrons percolate by hopping from one particle to the another.<sup>42</sup> As mentioned above, the small size of the particles prevents the formation of a space charge layer and a built-in electric field inside the particles, therefore, the transport of electrons cannot drift in an electric field. Recombination processes being efficiently blocked at the semiconductor electrolyte interface the generation of electrons to the conduction band of the TiO<sub>2</sub> particles under illumination results in an electron concentration gradient in the electrode and the electrons are transferred to the transparent conducting oxide (TCO) back contact layer by diffusion.

Measurements have shown that the diffusion of electrons is characterized by a distribution of diffusion coefficients which have been related to hopping of electrons via surface traps at different depths.<sup>42</sup> These electron traps are localized energy states just below the conduction band edge of the TiO<sub>2</sub> and play a significant role in the electron transport. Because of the nature of the TiO<sub>2</sub> electrode, trapping of electrons in the bulk states does not lead to recombination losses. Instead trapping of electrons at the TiO<sub>2</sub> surface may be a pathway for recombination, resulting in photocurrent losses and also photovoltage losses for kinetic reasons.<sup>35</sup> In addition, the trap states will lead to a lower quasi-Fermi level for the electrons under illumination and thus to a reduced photovoltage.<sup>35</sup>

The diffusion coefficient of electrons depends on the electron quasi-Fermi level under illumination. At low light conditions only deep traps participate in the electron transport causing a low diffusion coefficient. Increasing the light intensity raises the electron quasi-Fermi level and deep traps attain a steady state condition, while, shallow traps contribute to the electron motion resulting in a larger diffusion coefficient.<sup>42</sup> Increasing the illumination level thus increases the conductivity of the TiO<sub>2</sub> electrode by filling the trap states.

It has also been suggested that the motion of the electrons in the semiconductor particles is coupled to the species in the electrolyte at the semiconductor-electrolyte interface.<sup>42</sup> Cahen et al.<sup>41</sup> suggested that the screening by the electrolyte keeps the electrons near the particle surface, consistently with the picture of electron transport via surface electron traps. The electron together with its screening charge in the electrolyte side of the particle surface can be viewed as a polaron moving by the electron diffusion towards the

back contact where the electron is subsequently separated.

The electron transport mechanism in the nanostructured electrode of the DSSC is presently not well understood and a lot of basic research needs to be done. Understanding the mechanisms of charge transport in the nanostructured electrode electrolyte systems is important for the further development of the dye-sensitized nanostructured solar cell concept especially for designing cells with solid polymer or gel electrolytes.

### 2.3.3.2 Ion Transport in the Redox Electrolyte

The electrolyte in the DSSCs is usually an organic solvent containing the redox pair  $I^-/I_3^-$ , which in this case works as a hole-conducting medium. At the  $TiO_2$  electrode the oxidized dye, left behind by the electron injected to the  $TiO_2$ , is regenerated by  $I^-$  in the electrolyte as shown in the reaction (**Equation 2.6**). While at the counter-electrode  $I_3^-$  is reduced to  $I^-$  in the reaction (**Equation 2.7**). In other words,  $I_3^-$  is produced at the  $TiO_2$  electrode and consumed at the counter electrode and hence, diffused across the electrolyte correspondingly.  $I_3^-$  is therefore, often labeled as the hole carrier to draw similarities with the conventional *pn*-junction solar cells. Similarly,  $I^-$  is produced at the counter-electrode and get diffused to the opposite direction in the electrolyte.

The most simple way of dealing with the electrolyte might be to think it as an essentially neutral sink of  $I^-$  and  $I_3^-$  feeding the reactions (**Equation 2.6**) and (**Equation 2.7**) at the electrodes and maintaining the redox potential in the bulk of the electrolyte via the fast redox reaction of the  $I^-/I_3^-$  pair. This redox reaction in the electrolyte is a two-electron reaction as shown in **Equation 2.9**.<sup>43,44</sup>



Which is composed of series of successive reactions given by **Equations 2.10-2.12**.



The redox electrolyte chemistry appears to be standard and established area of chemistry, and rarely discussed in detail than DSSC research reports in the literature.

#### **2.3.4 Recombination**

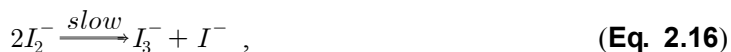
Recombination of the generated electrons with holes in the dye-sensitized nanostructured TiO<sub>2</sub> electrode can in principle occur both after the electron injection or during its migration in the TiO<sub>2</sub> electrode (on its way to the electrical back contact). Illumination of the dye-sensitized electrode initially in equilibrium, (in the dark) generates a transient electric field between the injected electrons in the TiO<sub>2</sub> and the oxidized species in the electrolyte. This electric field could in principle oppose further charge separation and promote recombination. However, in the dye cell, the mobile ions in the electrolyte can easily rearrange and effectively screen the light induced opposing fields (in steady state conditions) throughout the electrode film, and thus enabling an efficient charge separation.<sup>45</sup>

In the silicon solar cells, the recombination of charge carriers in trap states on surfaces, grain boundaries and in the bulk degrades the cell performance easily, therefore, semiconductor material of high crystal purity is required. In the dye-sensitized TiO<sub>2</sub> electrode, on the contrary, there are vast particle boundaries and a huge surface to volume ratio is available. Yet, the DSSC does not seem to suffer from the recombination losses at the grain boundaries. The reason for this is that only electrons are transported through the semiconductor particles, while holes (oxidized ions) are carried by the electrolyte. In other words, the DSSC works as a majority carrier device, similar to a metal-semiconductor junction or a Schottky diode.<sup>46</sup>

In the absence of holes in the semiconductor particles, the recombination occurs mostly by loss of electron to an oxidized dye molecule or to a hole in the electrolyte i.e. the oxidized triiodide. The former process is negligible, as assumed in most electrical models of the cell, but may be important in near open circuit conditions i.e. in the case of the accumulation of electrons into the TiO<sub>2</sub> particles.<sup>47</sup> The latter recombination pathway on the other hand is made inefficient due to reaction kinetics. According to Huang et al. the net recombination reaction at the TiO<sub>2</sub>-electrolyte interface is a two electron reaction as shown in **Equations 2.13-2.16**.<sup>48</sup>



composed of sub-reactions



The reaction shown in **Equation 2.16** is a slow dismutation reaction and rate limiting in the net recombination reaction. The reaction equation (**Equation 2.15**) also suggest that the actual electron acceptor in the recombination reaction is  $I_2$ . Because of the porous structure of the electrode the conducting glass substrate may be partly exposed to the electrolyte setting up a potential recombination pathway between electrons in the conducting substrate and hole carriers in the electrolyte. However, there is experimental evidence that this effect is insignificant, most likely due to low electrocatalytic activity of Pt-free  $\text{SnO}_2\text{:F}$  (FTO, as well as ITO) surface for the iodine/triiodide redox system.<sup>41</sup>

### 2.3.5 Interfacial Kinetics

The DSSC is based on photo electrochemical reactions at the semiconductor-electrolyte interface (as already discussed) and the operation of the cell is therefore, an outcome of competing opposite chemical reactions having different rate constants. A desired direction of the electrochemical reactions is achieved with fast wanted reactions (high rate constants) and slow unwanted reactions (low rate constants). The greater the difference between the rate constants show the higher the efficiency of the system. The kinetics of the DSSC is summarized in a highly simplified manner in **Figure 2.8**. The desired reaction i.e. the electron injection from the excited state of the dye to the conduction band of  $\text{TiO}_2$ , exceeds any unwanted reaction by an order of magnitude or more. In fact, occurring in the femtosecond time scale, the electron injection process between the N3 dye and  $\text{TiO}_2$  in the DSSC is one of the fastest chemical processes known.<sup>42</sup> The other desirable reaction, the

regeneration of the dye by  $I^-$  is also a very fast reaction occurring in 10 ns in the normal conditions in the DSSC. This is important for obtaining high cycle life for the dye, since lack of adequate conditions for the regeneration leads to dye degradation.<sup>42</sup> The electron percolation through the nanostructured  $TiO_2$  has been estimated to occur in the millisecond to second range.<sup>35</sup>

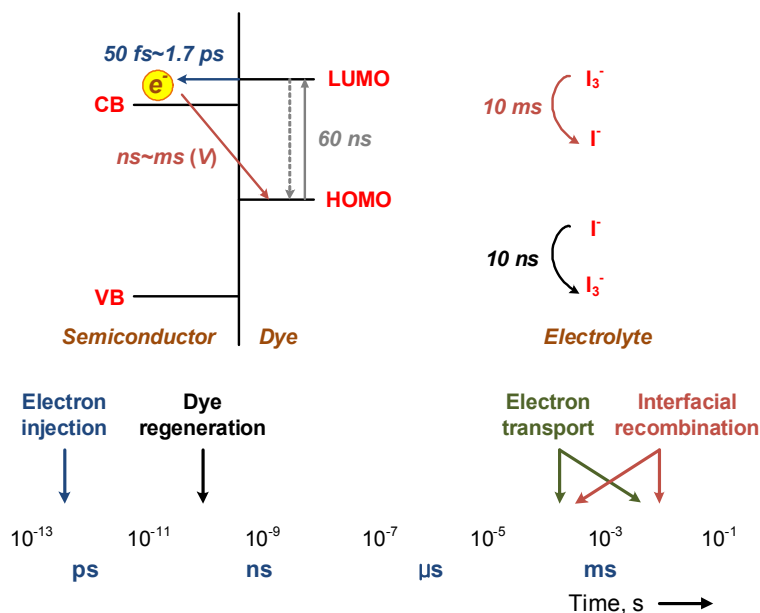


**Figure 2.8.** State diagram representation of the kinetics of dye-sensitized solar cell's function.

## 2.4 Materials of Dye-Sensitized Solar Cell

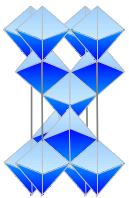
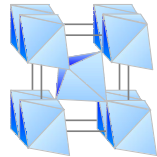
### 2.4.1 $TiO_2$ Thin Film

Oxide semiconductors are preferred in photo electrochemistry because of their exceptional stability against photo-corrosion on optical excitation in the band gap.<sup>37</sup> Furthermore, the large band gap ( $>3$  eV) of the oxide semiconductors is needed in DSSCs for the transparency of the semiconductor electrode for the large part of the solar spectrum.

In addition to  $\text{TiO}_2$ , semiconductors used in porous nanocrystalline electrodes in DSSCs include  $\text{ZnO}$ ,  $\text{CdSe}$ ,  $\text{CdS}$ ,  $\text{WO}_3$ ,  $\text{Fe}_2\text{O}_3$ ,  $\text{SnO}_2$ ,  $\text{Nb}_2\text{O}_5$ , and  $\text{Ta}_2\text{O}_5$ .<sup>35</sup> However,  $\text{TiO}_2$  has been and still is the cornerstone semiconductor material for dye-sensitized nanostructured electrodes for DSSCs.

$\text{TiO}_2$  is a semiconductor which has a wide band gap [in the case of anatase is 3.2 eV ( $E_g$ ) and rutile is 3.0 eV]. It is widely used, as a pigment in paper and paint industry, an excipient in pharmaceuticals and as a raw material for cosmetics. It is very cheap and the preparation of particles with very small size is fairly easy. The crystallite structures of  $\text{TiO}_2$  are anatase, rutile and brookite of which brookite is very difficult to obtain. Rutile absorbs light in the near UV-region. The band-gap excitations lead to generation of hole, and this cause the thermal instability in the solar cell. Anatase is dominant at low temperatures ( $\sim 1,183.15$  K). **Table 2.1** shows crystal structures and the properties of anatase and rutile.

**Table 2.1.** The comparison of properties of rutile and anatase

Property	Anatase	Rutile
Crystal structure		
Crystal system	Tetragonal (stable in low temp.)	Tetragonal (stable in high temp.)
Density, $\text{g/cm}^3$	3.8-3.9	4.2
Refractive index	5.52	2.71
Dielectric constant	31	114
Lattice parameter a, Å	3.78	4.58
Lattice parameter c, Å	9.49	2.96
Volume of unit cell, Å <sup>3</sup>	136.1	62.4
Melting point	Transformation to rutile at 1,183 K	
Band gap, eV	3.2	3.0

Only a few mono-layers of the adsorbed dye can efficiently participate in the charge injection process. If a planar surface of  $\text{TiO}_2$  is used, the small absorption cross section of the dye results in the poor performance. Therefore,  $\text{TiO}_2$  with sponge-like structure and high surface area is necessary. The surface area of the  $\text{TiO}_2$  film increase with decreasing particle size. The particle size cannot be reduced indefinitely because porosity also plays an important role in the performance of the  $\text{TiO}_2$  layer. As the particle size decreases, the pore also gets smaller. The electrolyte has to be able to penetrate the pores and be present where there is adsorbed dye. In addition, larger particles scatter light more effectively, and this has been found to have a positive effect on the performance of the cell.<sup>37</sup> Therefore, the particle size needs to be optimized to maximize the effect of large surface area and the porosity of the  $\text{TiO}_2$  film.

The preparation of nanocrystalline  $\text{TiO}_2$  thin films was first developed by Grätzel's research group.<sup>49</sup> Grätzel and coworkers introduced a preparation method of  $\text{TiO}_2$  nanopowder consisting of sol-gel synthesis and hydrothermal treatment.<sup>50</sup> In a typical sol-gel/hydrothermal experiment, titanium isopropoxide (125 ml) was added drop wise at room temperature to 0.1 M nitric acid solution (750 ml) under vigorous stirring. A white precipitate formed instantaneously. After that, the slurry was heated to 353.15 K and stirred vigorously for 8 h. To achieve peptization (i.e., destruction of the agglomerates and redispersion into primary nanocrystallites), the solution after filtration to remove non-peptized agglomerates was diluted with water to adjust the final solids concentration to ~5%[W/V]. The final step of the process involved hydrothermal treatment in an autoclave for 12 h in the temperature range of ~493.15 K to enhance the crystallinity of the product.

Preparation of the photoanode involves deposition of the  $\text{TiO}_2$  nanoparticles on fluorine-doped tin oxide (FTO) glass, sintering/annealing, post-treatment and sensitization. Nanoparticle deposition most commonly involves preparation of a paste and application by doctor-blade<sup>20</sup> or screen printing.<sup>51</sup> The fabrication scheme for  $\text{TiO}_2$  pastes is shown in **Figure 2.9a**. First the nano  $\text{TiO}_2$  particles are manually ground after mixing with acetic acid, water, and ethanol. The  $\text{TiO}_2$  slurry is transferred with the excess ethanol to a beaker where it is magnetically stirred and then homogenized using a sonicator. This is filled with the addition of a mixture of anhydrous terpineol and a mixture of ethyl cellulose and ethanol by stirring and sonication again. Finally, the contents are concentrated by



evaporation.<sup>52</sup>

In this work, synthesized  $\text{TiO}_2$  powders from  $\text{TiO}_2$  sol, commercial  $\text{TiO}_2$  powder (P25, Degussa Co.), and nanoporous  $\text{TiO}_2$  powder replicas from mesoporous silica template were used. The powder is initially dispersed by grinding with dispersion agent followed by the addition of distilled water and a wetting agent. The binder such as hydroxypropyl cellulose (Aldrich Co.) is also used. The  $\text{TiO}_2$  paste is then spread with doctor blade or screen printing onto the FTO glass ( $10 \Omega/\text{cm}^2$ , Pilkington Co.). A thin  $\text{TiO}_2$  film of  $50 \mu\text{m}$  to  $100 \mu\text{m}$  thickness is formed. Also, the  $\text{TiO}_2$  thin film coated on the FTO glass is  $0.5 \text{ cm} \times 0.5 \text{ cm}$  ( $0.25 \text{ cm}^2$ ) in size. The fabricated  $\text{TiO}_2$  thin film is sintered at  $773.15 \text{ K}$  for  $1 \text{ h}$ . The sintering rate should be very slow. In the temperature interval  $473.15 \text{ K} < T < 623.15 \text{ K}$ , organic materials such as dispersant and organic solvents used during the  $\text{TiO}_2$  film deposition stage decompose.

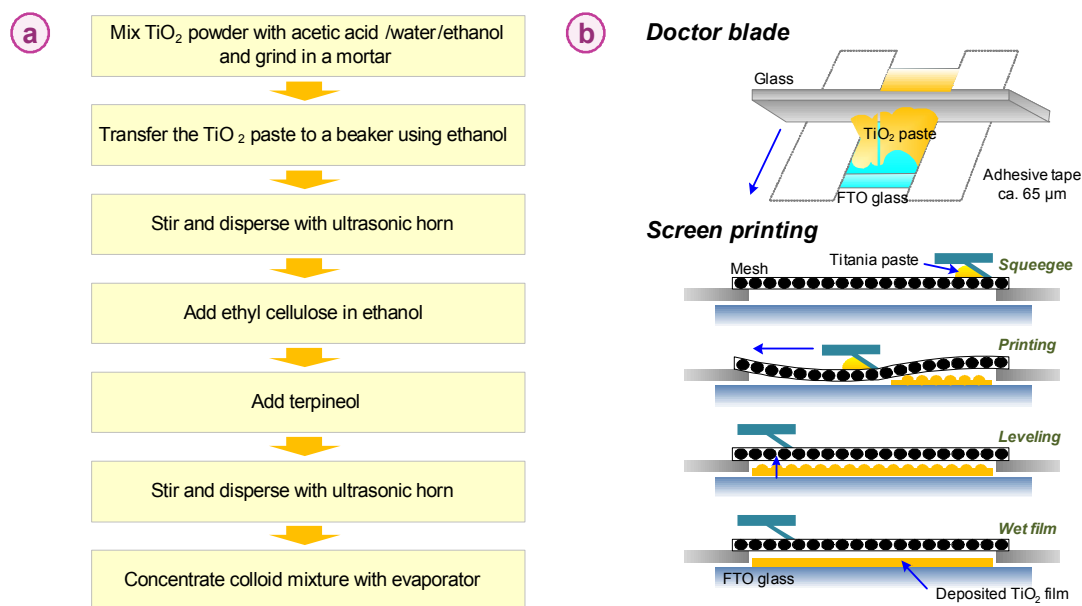


**Figure 2.9.** (a) The typical preparation protocol for  $\text{TiO}_2$  paste (b) the various coating method for the fabrication of nanocrystalline  $\text{TiO}_2$  thin film.

The decomposition process induces mechanical stress into the  $\text{TiO}_2$  layer. If the heating is done too fast, the adhesion to the FTO substrate is not firm. Consequently, cracks form

within the layer and the film becomes brittle. The cooling rate of the sintered TiO<sub>2</sub> electrode also needs to be slow in order to minimize the stress within the TiO<sub>2</sub> layer. Finally, sintered TiO<sub>2</sub> thin film has a thickness of 5  $\mu\text{m}$  to 10  $\mu\text{m}$ . The performance of the TiO<sub>2</sub> layer can be further improved by adding a further layer of TiO<sub>2</sub> after sintering (i.e., multi layer coating).<sup>53</sup> **Figure 2.9b** shows coating method of nanocrystalline TiO<sub>2</sub> thin film by using doctor blade or screen printing.

### 2.4.2 Dye

The absorption of incident light in the DSSCs is realized by specifically engineered dye molecules placed on the semiconductor electrode surface. To achieve a high light to energy conversion efficiency in the DSSC, the properties of the dye molecule attached to the semiconductor particle surface are essential. The desirable properties of the dye can be summarized as:

- i ) **Absorption:** The dye should absorb light at wavelengths up to about 920 nm, i.e. the energy of the excited state of the molecule should be about 1.35 eV above the electronic ground state corresponding to the ideal band gap of a single band gap solar cell.
- ii) **Energetics:** To minimize energy losses and to maximize the photo voltage, the excited state of the adsorbed dye molecule should be only slightly above the conduction band edge of the TiO<sub>2</sub>, but only above enough to present an energetic driving force for the electron injection process. For the same reason, the ground state of the molecule should be only slightly below the redox potential of the electrolyte.
- iii) **Kinetics:** The process of electron injection from the excited state to the conduction band of the semiconductor should be fast enough to outrun competing unwanted relaxation and reaction pathways. The excitation of the molecule should be preferentially of the MLCT-type.
- v ) **Stability:** The adsorbed dye molecule should be stable enough in the working environment (at the semiconductor-electrolyte interface) to sustain at least 10<sup>8</sup> redox turnovers.<sup>42</sup>
- vi) **Interfacial properties:** good adsorption to the semiconductor surface. Dye selection is not a difficult process. One of the first dyes that was introduced with the nanocrystalline solar cell was cis-RuL<sub>2</sub>-(NCS)<sub>2</sub>, where L stand for 2,2'-bipyridyl-4,4'-dicarbox-

ylic acid and the dye is also known as N3. It sensitizes very efficiently wide band-gap oxide semiconductors like titanium oxide up to a wavelength of 750 nm. A two-fold deprotonated form of N3, called N719 [cis-bis(isothiocyanato)bis(2,2'-bipyridyl-4,4'-dicarboxylato)-ruthenium(II)bis-tetrabutylammonium dye, Solaronix Co.], was used in this work (Mw.: 1,185.5 g/mol). It produces somewhat higher photovoltages than N3. The spectral responses of both dyes are presented in **Figure 1.6**.

The dye molecules are adhered onto the nanostructured TiO<sub>2</sub> electrode by immersing the sintered electrode into a dye solution of 0.2 mM in ethanol,<sup>37</sup> for a long period to fully get adsorbed on the electrode. During the adsorption process the electrode is sensitive to water.<sup>54</sup> To minimize water vapor content inside the pores of the electrode, the electrode should be warmed during immersion in the dye solution. The adsorption process lasts from one to several hours depending on the TiO<sub>2</sub> layer thickness and on the temperature of the dye solution. The stability of the dye is intrinsically high, because there is no band gap excitation of the TiO<sub>2</sub> semiconductor substrate and therefore no photo-excited hole generation to oxidize the dye.<sup>36</sup> The dye stability becomes an important factor during manufacturing of the cell and during operation. The humidity and water are to be avoided because of their degrading effect on the dye molecules. In addition, UV-light has some deteriorative effect. If the solar cell is manufactured properly, the dye can last for more than 20 years.<sup>49</sup>

### 2.4.3 Electrolyte

Between the TiO<sub>2</sub> electrode and the counter electrode is the electrolyte solution. The electrolyte used in the DSSCs consists of iodine (I<sup>0</sup>) and triiodide (I<sub>3</sub><sup>-</sup>) as a redox couple in a solvent with possibly other substances added to improve the properties of the electrolyte and the performance DSSC. Since the discovery of the DSSC about ten years ago<sup>13</sup> no redox couple performing better than I<sup>0</sup>/ I<sub>3</sub><sup>-</sup> couple in the DSSC has been discovered.<sup>55</sup> The I<sup>0</sup>/ I<sub>3</sub><sup>-</sup> redox electrolyte is prepared by adding I<sub>2</sub> to the solvent together with some iodine salt such as KI,<sup>13</sup> LiI.<sup>55</sup> A recent report by Wolfbauer et al.<sup>55</sup> clearly highlighted the importance of the cation of the iodine salt to the performance of the DSSC. The photocurrent output was found to increase linearly with decreasing cation radius, the smallest cations Li<sup>+</sup> and K<sup>+</sup> showing the best performance. The results also showed that the

relative concentration of  $I_3^-$  to  $I^-$  in the electrolyte is an important factor to the cell performance.

Examples of the solvents used in the electrolytes in DSSCs are: acetonitrile (ACN)<sup>13</sup>, methoxyacetonitrile (MAN)<sup>55</sup>, methoxypropionitrile (MPN).<sup>56</sup> The solvent ACN used for electrolyte preparation in the early DSSC, seems to be still the best choice when the cell efficiency is to be maximized. However, with respect to the preferred solvent properties listed above, acetonitrile fails at least in two points. Firstly, it is highly volatile with boiling point of 355.15 K, which is about the maximum temperature that a roof-top solar cell can reach at full sunlight,<sup>57</sup> and due to the high volatility it easily escapes from the cell through the sealing. Secondly, acetonitrile is highly toxic and carcinogenic chemical and cannot be used in the commercial DSSC. The choice of solvent is thus always a trade-off between low viscosity with better ion diffusion properties and high viscosity with ease of manufacturing and less stringent sealing requirements.<sup>58</sup> Therefore, the MPN is a potential candidate for the commercial DSSCs. In contrast to ACN it is nontoxic and has a boiling point of 433.15 K.

The 3-methoxypropionitrile (3-MPN, Fluka Co.) was used in this work. In this work, the redox electrolyte used was composed of 0.3 M 1,2-dimethyl-3-propyl imidazolium iodide (Solaronix Co.), 0.5 M LiI (Aldrich Co.), 0.05 M  $I_2$  (Aldrich Co.), and 0.5 M 4-tert-butylpyridine (4-TBP, Aldrich Co.) in 3-MPN as a solvent.

#### **2.4.4 Counter Electrode**

The function of the counter electrode is the reduction of triiodide to iodide. The plain  $SnO_2:F$  (FTO) layer does this rather poorly, so a small amount of platinum (Pt) is deposited on the electrode to catalyze the kinetic reaction. Charge transfer resistance ( $R_{ct}$ ) is a measure of the electrodes performance in an electron transfer process. The platinized counter electrode has a charge transfer resistance of ca.  $1 \Omega/cm^2$ , while the resistance of the plain electrode is of seven orders of larger magnitude.<sup>56,58</sup> In this work, Pt-sol (Pt-catalyst T/SP, Solaronix Co.) was used. Pt counter electrodes were prepared by doctor blade or screen printing of Pt-sol on to FTO glass (TEC 8:  $10 \Omega/cm^2$ , Pilkington Co.) and successive sintering at 723.15 K.

### 2.4.5 Substrate

The electrodes of the standard DSSC are prepared onto TCO coated glass substrates, between which the cell is assembled. The conducting coating of the substrate works as a current collector and the substrate material itself both as a support structure to the cell and as a sealing layer between the cell and the ambient air. Fluorine-doped tin oxide ( $\text{SnO}_2:\text{F}$ ) and indium tin oxide ( $\text{In}_2\text{O}_3:\text{Sn}$  or ITO) are the most frequently used TCOs in thin film photovoltaic cells. The standard preparation procedure of the nanostructured  $\text{TiO}_2$  electrode includes sintering of the deposited  $\text{TiO}_2$  film at 723.15-773.15 K. As the only TCO coating stable at these temperatures,<sup>59</sup> the  $\text{SnO}_2:\text{F}$  (TEC 8: 10  $\Omega/\text{cm}^2$ , Pilkington Co.) has been the material of choice in this work.

## 2.5 Fabrication of Dye-Sensitized Solar Cell

The fabrication method of DSSC in this work is shown in **Figure 2.10**. To fabricate the DSSCs, the prepared nanostructured  $\text{TiO}_2$  thin film electrode was immersed in the N719 dye solution of 0.3 mM at 293.15 K for 12 h, rinsed with anhydrous ethanol and dried.

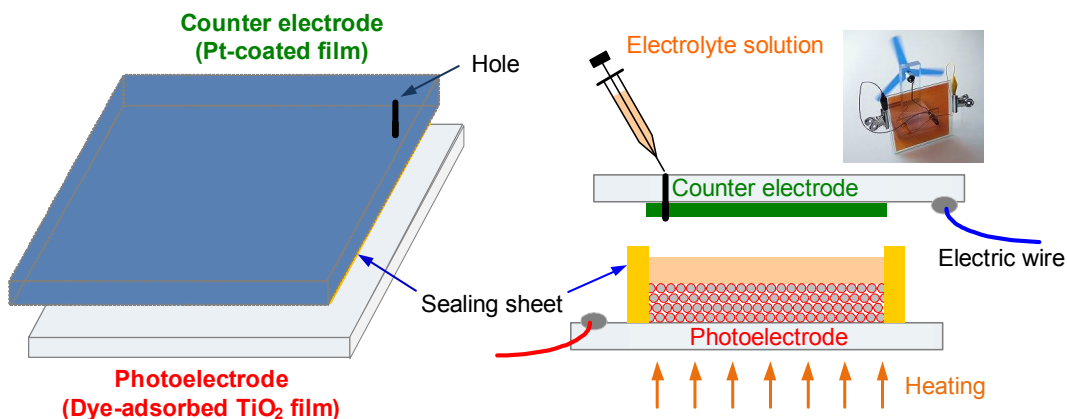


**Figure 2.10.** Fabrication method of dye-sensitized solar cell.

Pt coated FTO glass electrode was prepared as a counter electrode with an active area of  $0.25 \text{ cm}^2$ . The Pt electrode was placed over the dye-adsorbed  $\text{TiO}_2$  electrode, and the edges

of the cell were sealed with 2 mm wide stripers of 60  $\mu\text{m}$  thick sealing sheet (SX 1170-60, Solaronix Co.). Sealing was accomplished by hot-pressing the two electrodes together at 353.15 K. The redox electrolyte filled into the cell through the small holes. Finally, the filling ports were sealed with a sealant glue (Amosil 4, Solaronix Co.), which were let to dry in room temperature for about 24 h, after which the cell was completely sealed and ready for measurements.

## 2.6 Simple Electrical Model of the Dye-Sensitized Solar Cell

A solar cell is a combination of a current source and a diode (see **Figure 2.11a**). An equivalent circuit corresponding to a solar cell is also shown in **Figure 2.11b**. In an ideal cell, the resistance,  $R_s$ , would be zero and the parallel resistance,  $R_{sh}$ , or shunt resistance, would be infinitely large.

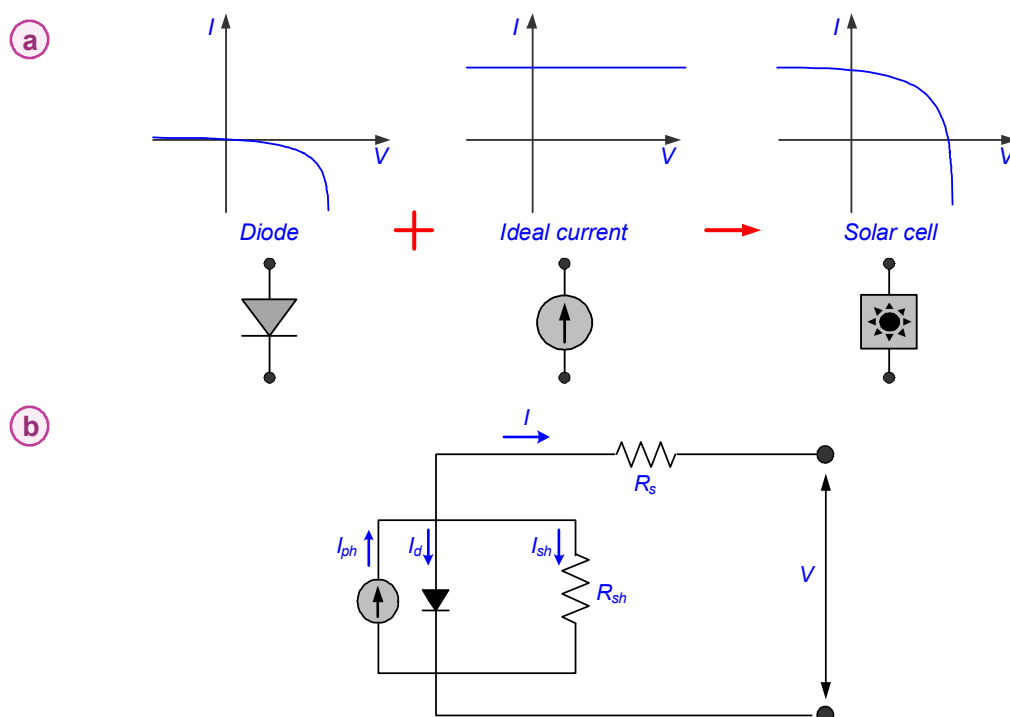


**Figure 2.11.** (a) A solar cell, (b) A simple electrical model of a solar cell (equivalent circuit using a 1-diode model).

In a real situation this is not true. The series resistance is composed of the electrical resistance of the different material in the cell and the interfaces between them. The resistance of the TCO layer has the biggest influence on series resistance.<sup>1</sup> The shunt resistance measures the resistance between the electrodes through undesirable routes for example, from the  $\text{TiO}_2$  film to the electrolyte. It is desired to be as high as possible.

The diode model does not represent the dye solar cell very well. The internal structure of the cell is more complex than that of the conventional silicon solar cell. Thus, all the processes occurring in the DSSC cannot be described with this simple model. Nevertheless, the concepts of series and parallel resistances can also be applied to the dye solar cell.

The resistance can be measured using impedance spectroscopy. In literature, there are several methods for measuring the series resistance.<sup>60</sup> But the applicability of these methods to dye solar cells was found to be poor. The varying from of the  $I$ - $V$  curves caused these methods to produce irrational values for the series resistance. The method is probably suitable for silicon solar cell.

## Chapter 3. Photovoltaic Properties of TiO<sub>2</sub> Electrode Prepared by Sol-Gel Method

### 3.1 Introduction

The nature and morphology of nanostructured TiO<sub>2</sub> thin film play a significant role in determining the overall efficiency of DSSCs.<sup>61,62</sup> This study focused on the synthesis and characterization of nanostructured TiO<sub>2</sub> films for DSSCs. A colloidal TiO<sub>2</sub> (i.e., SG-TiO<sub>2</sub> in this chapter) suspension was prepared by the sol-gel method through the hydrolysis of titanium-tetraisopropoxide. According to many research report, the commercial TiO<sub>2</sub> powders (i.e., P25) is most frequently used.<sup>37,54,63</sup> The crystal structure of P25 which is produced by flame hydrolysis of TiCl<sub>4</sub> is about 70% anatase and 30% rutile.<sup>14</sup> The characteristics of manufactured SG-TiO<sub>2</sub> electrode were compared with P25-TiO<sub>2</sub> electrode by adsorption energy distribution (AED),<sup>64</sup> atomic force microscope (AFM), Brunauer, Emmett, and Teller (BET), field-emission scanning electron microscope (FE-SEM), fourier transform infrared spectrophotometer (FT-IR), high resolution transmission electron microscope (HR-TEM), X-ray photoelectron spectroscopy (XPS), and X-ray diffractometer (XRD) analysis. The solar cell performances of the DSSC were evaluated from the overall conversion efficiency ( $\eta_{eff}$ ), fill factor ( $FF$ ), open-circuit voltage ( $V_{oc}$ ) and short-circuit current ( $I_{sc}$ ).

There have been many studies on the synthesis and characterization of nanostructured TiO<sub>2</sub> electrode as well as the development of dyes for DSSCs.<sup>184,185</sup> However, systematic studies on the influence of adsorption properties between dye molecules and TiO<sub>2</sub> films on the power conversion efficiency of DSSCs are limited. In addition, key point of a continuous process (roll to roll process) for the fabrication of DSSC module is the adsorption process (due to the fact that they need to a long time).<sup>57,65</sup> The second goal of this work is to investigate the influence of Ru (II) dye adsorption properties on the conversion efficiency of DSSC. For this purpose, experimental and theoretical studies on the adsorption equilibrium and kinetic studies as a function of solution pH and temperature were conducted to control the adsorption amount and also to understand the adsorption



mechanism of N719 dye on nanostructured  $\text{TiO}_2$  electrode.<sup>66</sup> The pseudo second order model was used to predict the adsorption kinetic data.<sup>67-69</sup>

The electrical impedance spectroscopy has been often used to analyze electric mechanism and to evaluate the performance of cells.<sup>70</sup> Recently, an alternative method based on the measured current-voltage ( $I$ - $V$ ) characteristics been proposed to determine the series resistance, the ideality factor, the saturation current, and the shunt conductance in DSSCs.<sup>71</sup> Finally, this article evaluates the effect of adsorption quantity using the equivalent circuit analysis.<sup>72,73</sup> A nonlinear least-square Levenberg optimization algorithm was employed to evaluate the five model parameters.<sup>74</sup> In addition, the solar cell performances were investigated in accordance with the adsorption quantity of N719 dye.

## 3.2 Experimental

### 3.2.1 Synthesis of Nanocrystalline $\text{TiO}_2$ Particle

The schematic diagram for the synthesis of nanocrystalline SG- $\text{TiO}_2$  particles and the fabrication of SG- $\text{TiO}_2$  electrode of DSSCs is shown in **Figure 3.1**.

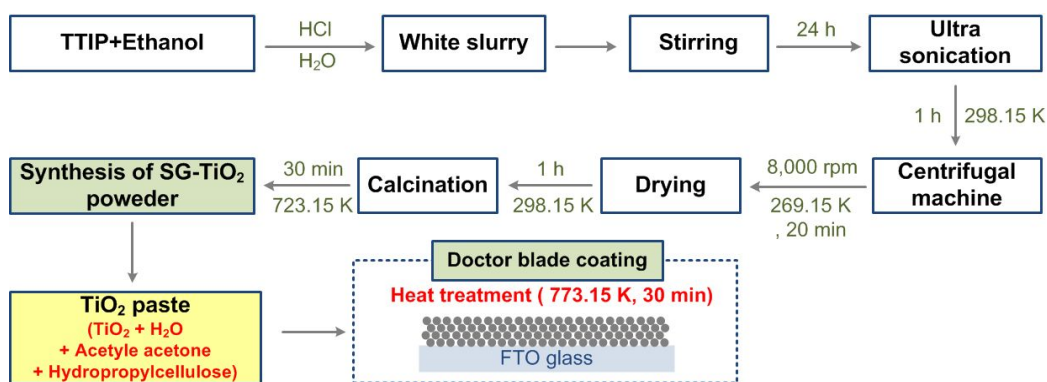


**Figure 3.1.** Fabrication procedure of SG- $\text{TiO}_2$  electrode.

A colloidal  $\text{TiO}_2$  suspension was prepared by the hydrolysis of titanium-tetraispoxide

(TTIP, Junsei Chemical Co., >98%) represented by the reaction shown in **Equation 3.1**.



TTIP was used as a main starting material without further purification. An appreciated amount (20 ml) of TTIP was slowly dropped in ethanol (200 ml) at room temperature for 5 min. Consequently, a drop-wise addition of hydrochloric acid solution (0.05 M) into the TTIP solution was conducted for 24 h under vigorous stirring condition. The suspension was then ultrasonicated at room temperature for 1 h and centrifuged at 8,000 rpm for 20 min at a temperature of 269.15 K. The white precipitate formed was filtered and dried at room temperature for 1 h. Finally, the dried TiO<sub>2</sub> particles were calcined at 723.15 K for 30 min in air gas flow (5 ml/min).

### 3.2.2 Fabrication of TiO<sub>2</sub> Electrode for Dye-sensitized Solar Cell

For the preparation of nanostructured TiO<sub>2</sub> electrode, TiO<sub>2</sub> paste was prepared by mixing 2 g TiO<sub>2</sub> particles, 0.68 ml 10% [V/V] acetyl acetone and 1 g hydroxy-propylcellulose (HPC, Mw. 80,000 g/mol, Aldrich Co.) in 10.68 ml water for 12 h at 300 rpm using a ZrO<sub>2</sub> ball mill (Planetary mono mill, Fritsch Co.). A TiO<sub>2</sub> film was fabricated by coating a precursor paste onto the FTO glass plates (TEC 8: 10 Ω/cm<sup>2</sup>, Pilkington Co.) by using a doctor blade technique (adhesive tape was used as spacer of ca. 65 μm thickness).

Based on the TGA (**Figure 3.2**), the SG-TiO<sub>2</sub> film for the complete removal of HPC was heated at 773.15 K for 2 h. Thus, the SG-TiO<sub>2</sub> film formed on the FTO glass was 4-5 μm thickness and 0.5 cm×0.5 cm in size. To fabricate the DSSCs, the prepared thin film electrode was immersed in the 0.3 mM N719 dye (Solaronix Co.) solution at 293.15 K for 12 h followed by rinsing with an anhydrous ethanol and drying. Pt coated TEC 8 glass electrode was prepared as a counter electrode with an active area of 0.25 cm<sup>2</sup>. The Pt electrode was placed over the dye-adsorbed TiO<sub>2</sub> electrode, and the edges of the cell were sealed with 2 mm wide strippers of 60 μm thick sealing sheet (SX 1170-60,

Solaronix Co.). The sealing was accomplished by hot pressing the two electrodes together at 353.15 K. The redox electrolyte solution was filled into the cell through the small holes and the filling ports were sealed with a sealant glue (Amosil 4, Solaronix Co.). The redox electrolyte was composed of 0.3 M 1,2-dimethyl-3-propyl imidazolium iodide (Solaronix Co.), 0.5 M LiI (Aldrich Co.), 0.05 M I<sub>2</sub> (Aldrich Co.), and 0.5 M 4-TBP (Aldrich Co.) in 3-MPN (Fluka Co.) as a solvent.

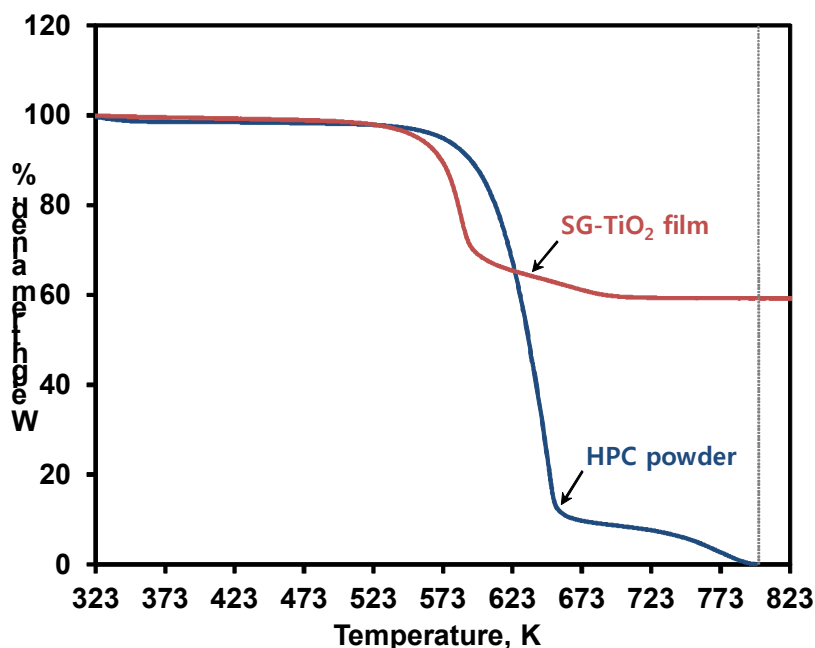


**Figure 3.2.** Thermal gravity analysis of SG-TiO<sub>2</sub> film and HPC powder.

### 3.2.3 Characterization of TiO<sub>2</sub> Electrode for Dye-sensitized Solar Cell

The crystallinity of the synthesized TiO<sub>2</sub> was characterized by HR-TEM (F20, Techai Co.) and an XRD (D/MAX-1200, Rigaku Co.) using a Cu  $k\alpha$  X-ray and Ni filter at 35 kV and 15 mA. The film thickness and surface morphology were measured by FE-SEM (S-4700, Hitachi Co.). XPS analysis was conducted using a photoelectron spectrometer (VG Scientific MultiLab 2000 system) equipped with a non-monochromatic Mg  $k\alpha$  radiation of

1,253.6 eV. The C1s peak (285.0 eV) was used to calibrate the binding energy values. The morphology of the TiO<sub>2</sub> electrode was also examined in an AFM (CP-2, Veeco Co.) in the non-contact model. Nitrogen adsorption isotherms on TiO<sub>2</sub> were measured at 77.15 K using an automatic analyzer (ASAP 2010, Micromeritics Co.). Before the measurements, the samples were out gassed for 2 h in the degas port of the adsorption apparatus. The measurement of the adsorption-desorption isotherms required 1 day. The BET surface areas were determined from the adsorption of isotherms of nitrogen. In addition, the pore size distributions were also calculated by the Barrett, Joyner, and Halenda (BJH) method. Moreover, the FT-IR (DA-8, Bomem Co.) was used for the analysis of the bonding structure between dye molecules and TiO<sub>2</sub> surface.

The current-voltage ( $I$ - $V$ ) curves were measured using a source measure unit under irradiation of white light from a 1,000 W Xenon lamp (Solar simulation system; Thermo oriel instruments Co.). The incident light intensity and the active cell area were 100 mW/cm<sup>2</sup> and 0.25 cm<sup>2</sup>, respectively. The  $I$ - $V$  curves were used to calculate the short-circuit current ( $I_{sc}$ ), open-circuit voltage ( $V_{oc}$ ), fill factor ( $FF$ ), and overall conversion efficiency ( $\eta_{eff}$ ) of DSSC.

### **3.2.4 Adsorption Properties of SG-TiO<sub>2</sub> Electrode for Dye-sensitized Solar Cell**

The Adsorption equilibrium experiments were carried out by contacting a given amount of SG-TiO<sub>2</sub> particle with N719 dye solution of 0.01-0.5 mM in a shaking incubator at different temperatures (293.15, 313.15, and 333.15 K) and pHs (3, 4, 7, and 10). The solution pH was adjusted by using 0.1 M HCl and 0.1 M NaOH. Zeta potentials of SG-TiO<sub>2</sub> particle in the solution were measured using a zeta potential apparatus (ELS-8000, Otsuka electronics Co.). In addition, adsorption kinetic experiments of SG-TiO<sub>2</sub> particles were conducted for low and high concentrations (0.05 mM and 0.5 mM) of N719 dye at 300 rpm. The adsorption capacity ( $q$ ) of SG-TiO<sub>2</sub> particles was determined by measuring the dye concentrations before and after adsorption using a UV/Vis spectrophotometer (UV-160A, Shimadzu Co.) at 528 nm after filtration with a 0.20  $\mu$ m ultra filtration membrane filter.

To investigate the energy conversion efficiency of SG-TiO<sub>2</sub> electrode depending on adsorption amount, the SG-TiO<sub>2</sub> film of 0.8 cm×0.8 cm (0.64 cm<sup>2</sup>) in size was formed on

the FTO glass ( $15 \text{ } \Omega/\text{cm}^2$ , Asahi glass Co.). Also, Pt coated FTO glass ( $15 \text{ } \Omega/\text{cm}^2$ , Asahi glass Co.) electrode was prepared as a counter electrode with an active area of  $0.64 \text{ cm}^2$ . The other fabrication experimental method was described in **section 3.2.2**. At that time, the adsorption amount of N719 was measured by completely desorbing the adsorbed dye molecules from SG-TiO<sub>2</sub> film using 0.1 M NaOH solution/anhydrous ethanol solution (50/50% [V/V]).

### 3.3 Results and Discussion

#### 3.3.1 Characteristics of Nanocrystalline SG-TiO<sub>2</sub> Particle and SG-TiO<sub>2</sub> Electrode

The results of the characterization of the SG-TiO<sub>2</sub> nanoparticles are depicted in **Figure 3.3** to **Figure 3.5**.

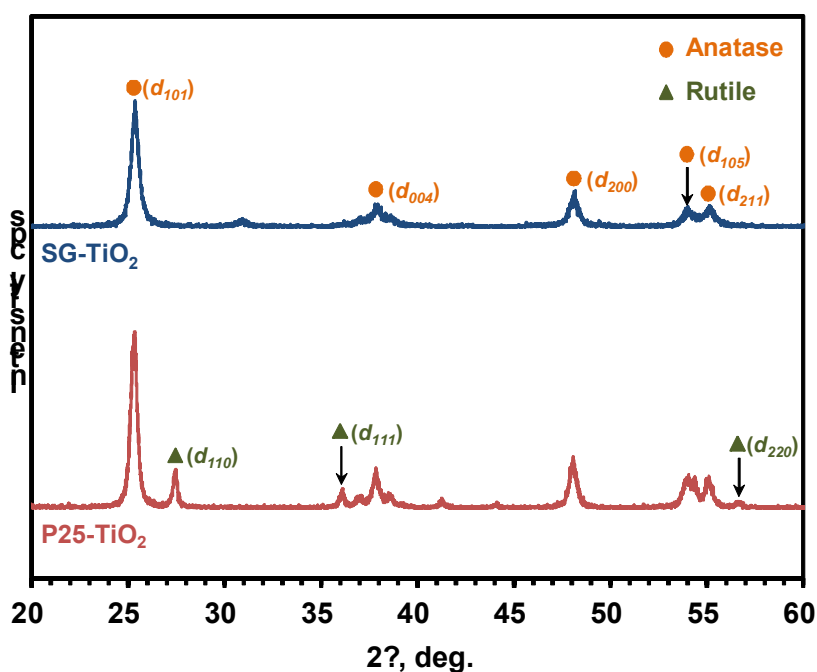


**Figure 3.3.** X-ray diffraction spectra of SG-TiO<sub>2</sub> and P25-TiO<sub>2</sub>.

**Figure 3.3** shows XRD patterns of SG-TiO<sub>2</sub> synthesized in chapter 3 and commercial TiO<sub>2</sub> (P25-TiO<sub>2</sub>, Degussa Co.) with heat treatment at 723.15 K for 30 min. SG-TiO<sub>2</sub> showed almost single-phase anatase nanocrystallites without rutile, while P25-TiO<sub>2</sub> has the mixture of anatase and rutile phases (7:3). **Figure 3.4** shows HR-TEM images and electron diffraction pattern of SG-TiO<sub>2</sub>. The low resolution TEM image in **Figure 3.4a** shows the microstructure of nanocrystalline TiO<sub>2</sub>. The size of TiO<sub>2</sub> particles is approximately 10-20 nm. The electron diffraction of TiO<sub>2</sub> displays the Debye-Scherrer rings of anatase. The lattice fringes corresponding to the (*d*<sub>101</sub>) and (*d*<sub>004</sub>) plane of anatase which can be seen in the high-resolution TEM image (**Figure 3.4b**). The consistent phase of the SG-TiO<sub>2</sub> was also investigated by XRD analysis (**Figure 3.3**). Contrary to the P25-TiO<sub>2</sub>, the synthesized SG-TiO<sub>2</sub> by the sol-gel method consists mainly of anatase phase as shown in the XRD and TEM patterns.

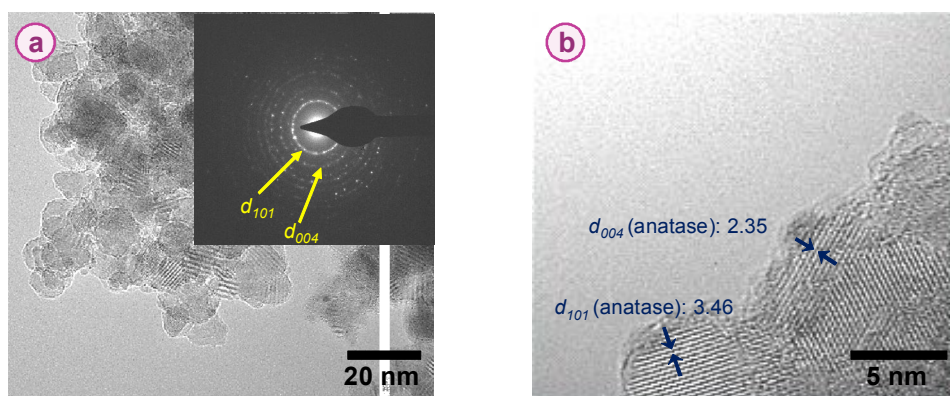


**Figure 3.4.** HR-TEM images and electron diffraction pattern of anatase SG-TiO<sub>2</sub> at (a) low (b) high resolution.

XPS analysis provides important information about physicochemical changes of porous materials. **Figure 3.5** is the quantitative XPS analysis of SG-TiO<sub>2</sub>. The survey spectrum of the SG-TiO<sub>2</sub> (**Figure 3.5a**) contains the Ti 2p and O 1s peaks of the titanium dioxide. The Ti 2p<sub>1/2</sub> and Ti 2p<sub>3/2</sub> spin-orbital splitting photoelectrons are located at binding energies of 464.4 eV and 458.7 eV, respectively (**Figure 3.5b**).

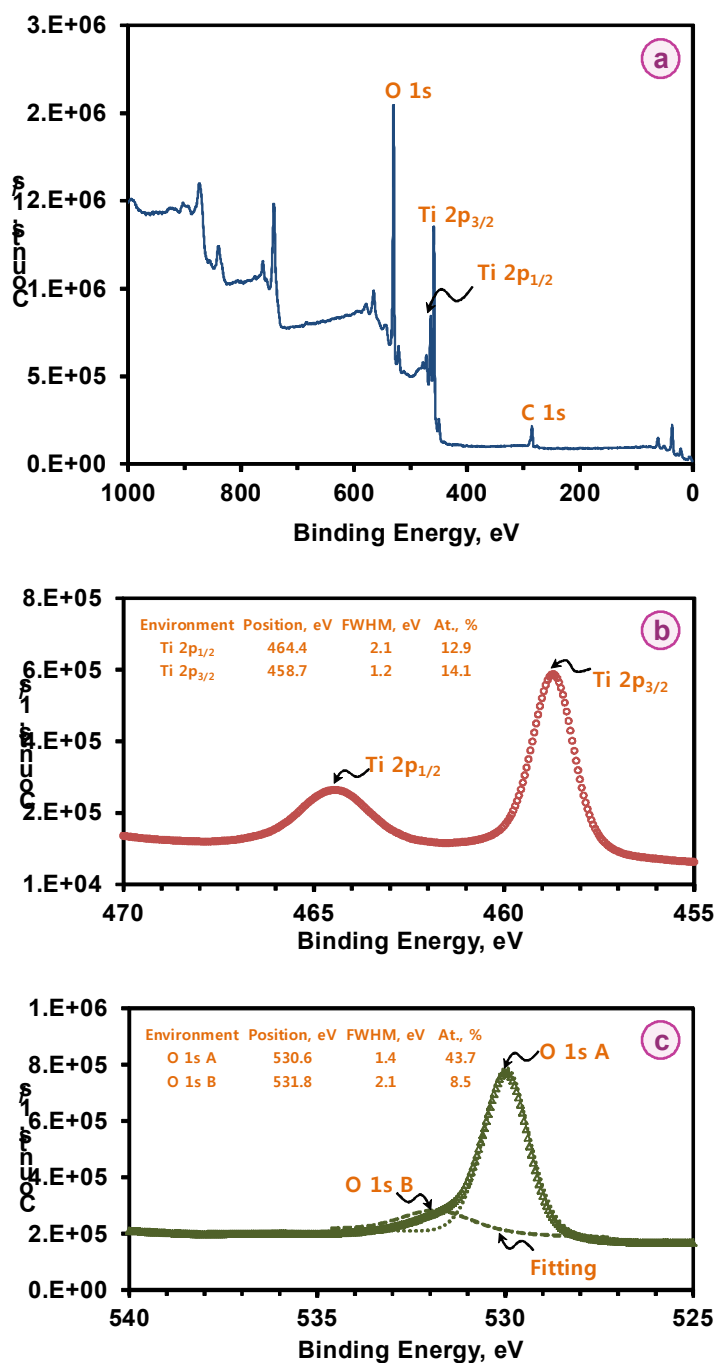


**Figure 3.5.** XPS survey spectra of (a) SG-TiO<sub>2</sub>, (b) Ti 2p core level (c) O 1s core level.

The O 1sA peak of SG-TiO<sub>2</sub> is shown at 530.64 eV and a shoulder located toward the side of higher binding energies (**Figure 3.5c**). The contents of Ti and O of SG-TiO<sub>2</sub> are 27.01% and 52.23% corresponding to closely Ti<sup>4+</sup> state. Similar results are observed in TiO<sub>2</sub> porous materials.<sup>38,75</sup>

To characterize the nanocrystalline SG-TiO<sub>2</sub> film properties, AED, AFM, BET, FE-SEM, and FT-IR measurements were used. **Figure 3.6** exhibits the FE-SEM images of surface morphology and the cross-section of TiO<sub>2</sub> thin films coated on FTO glass.

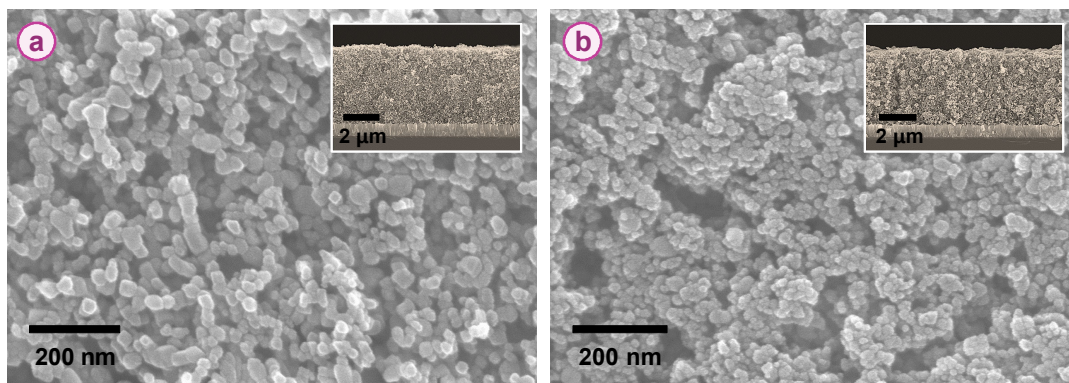


**Figure 3.6.** FE-SEM images of (a) P25-TiO<sub>2</sub> (b) SG-TiO<sub>2</sub> film.

TiO<sub>2</sub> film has a porous structure in which the TiO<sub>2</sub> spherical nanoparticles are all bonded together through a sintering process. The spherical nanoparticles of P25-TiO<sub>2</sub> film (**Figure 3.6a**) and SG-TiO<sub>2</sub> film (**Figure 3.6b**) are well distributed and maintain their original size and shape. The pattern reveals the TiO<sub>2</sub> particles to be composed of a three-dimensional network of interconnected particles. It was also found that the particle size of SG-TiO<sub>2</sub> was smaller than that of P25-TiO<sub>2</sub>. These results are consistent with those estimated from XRD data. From the line width of XRD peak (anatase,  $d_{101}$ ) of the TiO<sub>2</sub> samples, the crystalline sizes of TiO<sub>2</sub> was also roughly estimated by using the Scherrer's equation as shown in **Equation 3.2**.<sup>76</sup>

$$D = \frac{K\lambda}{\beta \cos \theta} \quad (\text{Eq. 3.2})$$



where  $D$  is crystalline size of the particles (nm),  $K$  is the apparatus constant, and taken as 0.89,  $\lambda$  the wavelength of Cu  $k\alpha$  line (0.1542 nm),  $\theta$  the Bragg's angle, and  $\beta$  the full width at half-maximum of the diffraction peak (radian). From the **Equation 3.2**, their crystalline sizes are about 22 nm for P25-TiO<sub>2</sub> and 14 nm for SG-TiO<sub>2</sub>.

**Table 3.1.** Surface characteristics of TiO<sub>2</sub> film

Properties	Unit	P25-TiO <sub>2</sub> film	SG-TiO <sub>2</sub> film
Root mean square roughness ( $R_q$ )	nm	25.1	28.8
Mean roughness ( $R_a$ )	nm	20.3	22.9
Film thickness	$\mu\text{m}$	4.7	4.6
Adsorption amount of N719	mol/cm <sup>2</sup>	$4.982 \times 10^{-8}$	$5.874 \times 10^{-8}$

According to the AFM images of P25-TiO<sub>2</sub> film (**Figure 3.7a**) and SG-TiO<sub>2</sub> film (**Figure 3.7b**), the films have heterogeneous surface with a few separated islands. The surface roughness is summarized in **Table 3.1**. It was found from these results that nanoparticle TiO<sub>2</sub> with a well ordered structure and high surface area can be successfully synthesized. The average surface roughness of SG-TiO<sub>2</sub> films are higher than P25-TiO<sub>2</sub> film.

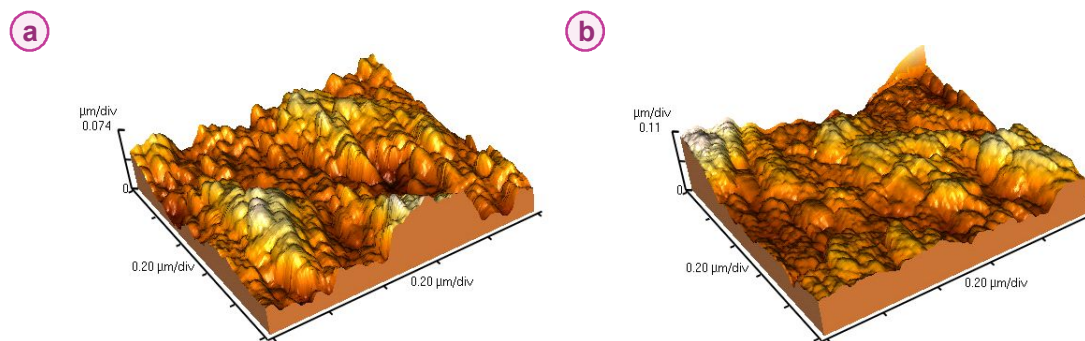


**Figure 3.7.** AFM images of (a) P25-TiO<sub>2</sub> (b) SG-TiO<sub>2</sub> film.

Commonly, if the TiO<sub>2</sub> thin film has a higher surface roughness, the amount of N719 dye adsorbed is drastically increased.<sup>1</sup> It has been known that the anatase TiO<sub>2</sub>-based solar cells exhibit better photovoltaic characteristics compared to the rutile TiO<sub>2</sub>-based solar cells because of higher surface area (i.e., higher amount of dye adsorption).<sup>77</sup> As listed in **Table 3.1**, the obtained results are identical for the adsorption amount of N719 dye on TiO<sub>2</sub> film.

The physical properties of P25-TiO<sub>2</sub> film and synthesized SG-TiO<sub>2</sub> film are listed in **Table 3.2**. The surface area determined by nitrogen adsorption isotherm data of SG-TiO<sub>2</sub> was found to be 63 m<sup>2</sup>/g (**Figure. 3.8a**), and the average pore size calculated by BJH method was 83 Å (**Figure. 3.8b**). From the results of the nitrogen adsorption isotherm, the SG-TiO<sub>2</sub> exhibited the International Union of Pure and Applied Chemistry (IUPAC) type-IV isotherm with a mesoporous structure.<sup>78-80</sup> A slight increase of surface area of SG-TiO<sub>2</sub> fabricated in this work compared to P25-TiO<sub>2</sub> is attributed to the development of mesopores.

**Table 3.2.** Physical properties of TiO<sub>2</sub> film

Properties	Unit	P25-TiO <sub>2</sub> film	SG-TiO <sub>2</sub> film
Surface area (BET)	m <sup>2</sup> /g	50 <sup>a</sup> (40 <sup>b</sup> )	63 <sup>b</sup>
Total pore volume	cm <sup>3</sup> /g	0.19 <sup>b</sup>	0.14 <sup>b</sup>
Average pore size	Å	69 <sup>b</sup>	83 <sup>b</sup>
Average primary particle size	nm	22 <sup>b,c</sup>	14 <sup>b,c</sup>
Density	g/l	130 <sup>a</sup>	248 <sup>b</sup>
Purity	%	>99.5 <sup>a</sup>	-

<sup>a</sup>from the manufacturer's report, <sup>b</sup>measured in this work, <sup>c</sup>the size of the primary particles

As a continuous work, it is essential to understand the energetic and structural heterogeneity of TiO<sub>2</sub> surfaces for the systematic analysis of the adsorption properties between dye molecule and TiO<sub>2</sub> surfaces. It has been known that chemical and geometrical heterogeneities show the unique sorption properties of porous materials. Geometrical hetero-

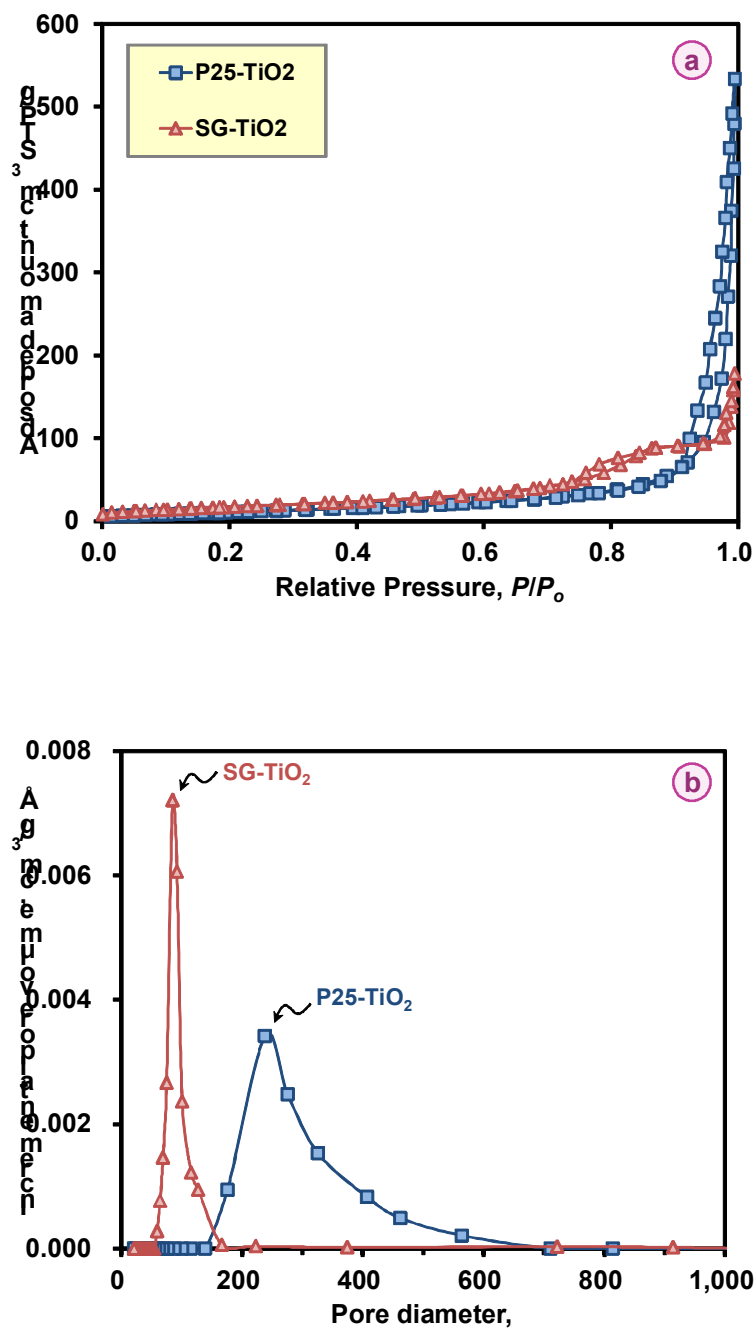


**Figure 3.8.** (a) N<sub>2</sub> gas adsorption and desorption isotherms (b) pore size distributions of SG-TiO<sub>2</sub> and P25-TiO<sub>2</sub> films.

geneity comes from the differences in size and shape of pores while chemical heterogeneity is associated with different functional groups and various surface defects on a surface. The heterogeneity properties of solid adsorbents can be described by their so-called adsorption energy distribution functions.<sup>81</sup>

Adsorption energy distributions have been extensively applied for characterizing the numerous adsorption systems and understanding the surface energy heterogeneities. The fundamental adsorption integral equation for energetically heterogeneous solid surfaces is given in **Equation 3.3**.<sup>82,83</sup>

$$\theta(p) = \int_{E_{\min}}^{E_{\max}} \theta(p, E) \cdot F(E) \cdot dE \quad (\text{Eq. 3.3})$$

Where  $p$  is the equilibrium pressure,  $E$  is the adsorption energy,  $F(E)$  is the adsorption energy distribution function,  $\theta(p, E)$  is a local adsorption isotherm with an adsorption energy, and  $\theta(p)$  is the experimental adsorption isotherm data.

The adsorption integral equation is the well known linear Fredholm integral equation of the first kind, and the calculation of adsorption energy distribution is an ill posed problem.<sup>84,85</sup> For the current work, it was applied the generalized nonlinear regularization method based on smoothness constraint (i.e., Tikhonov regularization) and edge preserving regularization methods. The generalized nonlinear regularization method can avoid the difficulties resulting from the ill-posed nature of an adsorption integral equation.<sup>86,87</sup> **Figure 3.9** shows the flow chart for the general calculation of adsorption energy distribution.

Proper selection of local adsorption isotherm equation for the calculation of energy distribution is very important in analyzing the heterogeneous adsorption systems. In this work, the Fowler and Guggenheim equation is used:

$$\theta(p, E) = \frac{K \cdot p \cdot \exp(zw\Theta/k_B T)}{1 + K \cdot p \cdot \exp(zw\Theta/k_B T)} \quad (\text{Eq. 3.4})$$

Where  $T$  is the absolute temperature,  $p$  is the equilibrium pressure,  $z$  is the number of closest adjacent molecules in the monolayer,  $w$  is the interaction energy between the two nearest neighboring molecules,  $k_B$  is the Boltzmann constant,  $K = K_o(T) \cdot \exp(E/k_B T)$  is the

Langmuir constant, and  $K_o(T)$  is the pre-exponential factor expressing the partition functions for an isolated molecule.

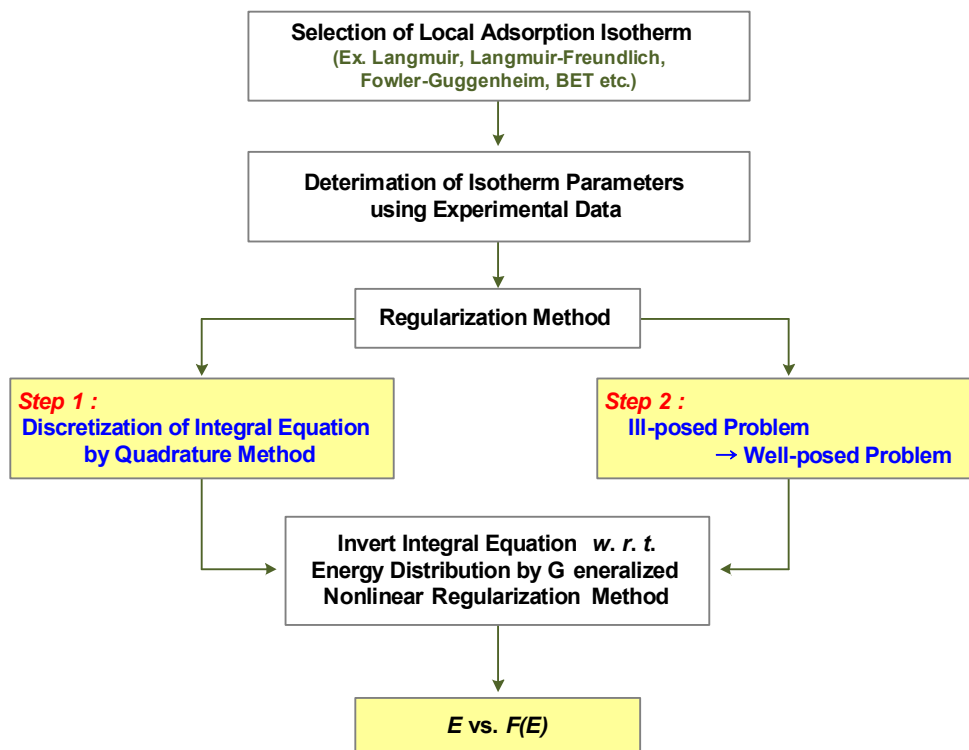


**Figure 3.9.** The flow chart for the general calculation of adsorption energy distribution functions.

**Figure 3.10** shows the adsorption energy distribution functions of  $\text{TiO}_2$  films formed on the FTO glass. The adsorption energy distribution curves of SG- $\text{TiO}_2$  synthesized in chapter 3 exhibited two peaks indicating the existence of energetically two different adsorption sites. The first and second adsorption energy peaks were distributed mainly in the range of 3-9 and 9-16 kJ/mol, respectively. The energy intensity of the first peak is about 2 times higher than that of the second one. However, the second peak of P25- $\text{TiO}_2$  was not evident compared to the synthesized SG- $\text{TiO}_2$  samples. The energy distribution peaks proceeded to

higher energy with the slight increase of surface area because of the micro and mesopore developments on  $\text{TiO}_2$  surfaces as well as  $\text{TiO}_2$  intraparticles (**Table 3.2**). The increase of surface area (i.e., increase in adsorption capacity of dye molecules) will serve for the enhanced energy conversion efficiency of DSSC. It was also found that the shape and the intensity of the adsorption energy distribution curve were highly related with the physical property (i.e., geometrical heterogeneity) and chemical characteristics (i.e., energetic heterogeneity) of nanocrystalline  $\text{TiO}_2$  electrode for DSSC. Therefore, the results can be successfully applied for the design, synthesis and optimization of nanocrystalline  $\text{TiO}_2$  electrode for DSSC because the adsorption energy distribution functions obtained in this work will offer the fundamental and informative data to fully understand the surface heterogeneity of the nanostructured  $\text{TiO}_2$  electrode.

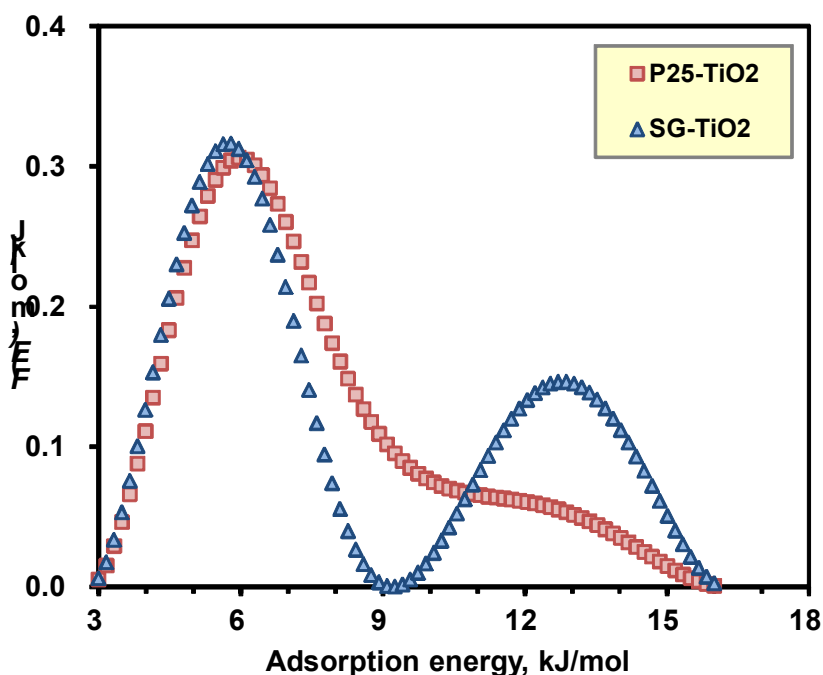


**Figure 3.10.** Adsorption energy distributions of SG- $\text{TiO}_2$  and P25- $\text{TiO}_2$  films.

Interfacial binding between the dye molecules (N719) and the surface of  $\text{TiO}_2$  was investigated by FT-IR spectra of the dye-anchored  $\text{TiO}_2$  films. In general, the efficiency of the charge injection process is highly dependent on bonding structure of the dye molecules adsorbed on the  $\text{TiO}_2$  film. In addition, the electron transfer in DSSC is strongly influenced by electrostatic and chemical interactions between  $\text{TiO}_2$  surface and the adsorbed dye molecules.<sup>88</sup>

**Figure 3.11** compares the FT-IR spectra of N719 dye adsorbed on  $\text{TiO}_2$  films (P25- $\text{TiO}_2$ , SG- $\text{TiO}_2$ ) and the signals of the dye powder. Absorption at  $2,105\text{ cm}^{-1}$  of N719 dye is attributed to the SCN stretch model of N-bonded SCN ligand.<sup>89,90</sup>

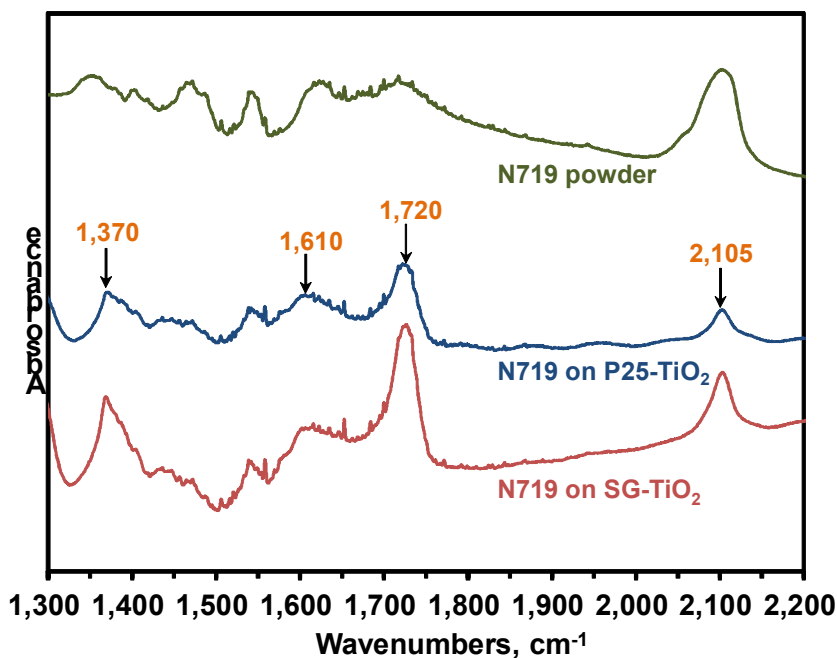


**Figure 3.11.** FT-IR spectra of N719 dye adsorbed on  $\text{TiO}_2$  films compared to the signals of the N719 dye powder.

The FT-IR spectra were observed at  $1,370\text{ cm}^{-1}$ ,  $1,610\text{ cm}^{-1}$ , and  $1,720\text{ cm}^{-1}$  when the

dye molecules were adsorbed on P25-TiO<sub>2</sub> and SG-TiO<sub>2</sub> films. The FT-IR spectra located at 1,370 cm<sup>-1</sup> (O-C-O symmetric stretch of the carboxyl group) and 1,610 cm<sup>-1</sup> (O-C-O asymmetric stretch of the carboxyl group) is consistent with the bidentate or bridging coordination.<sup>180</sup> Compared to the dye-anchored P25-TiO<sub>2</sub> films, the dye-anchored SG-TiO<sub>2</sub> films have strong absorptions at 1,720 cm<sup>-1</sup>, indicating the C=O stretch mode of the protonated carboxylic acid (i.e., ester-like linkage). Similar results were reported that the coordination of N719 dye on TiO<sub>2</sub> films occurs mainly by the contribution of unidentate (i.e., ester-like linkage) and partially by bidentate or bridging linkage.<sup>88-90</sup>

**Figure 3.12** shows the photocurrent-voltage curves of P25-TiO<sub>2</sub> and synthesized SG-TiO<sub>2</sub>. The fill factor (*FF*) and overall energy efficiency ( $\eta_{eff}$ ) were determined by the **Equations 2.1** and **2.2** which was described in detail elsewhere.<sup>22,37</sup>

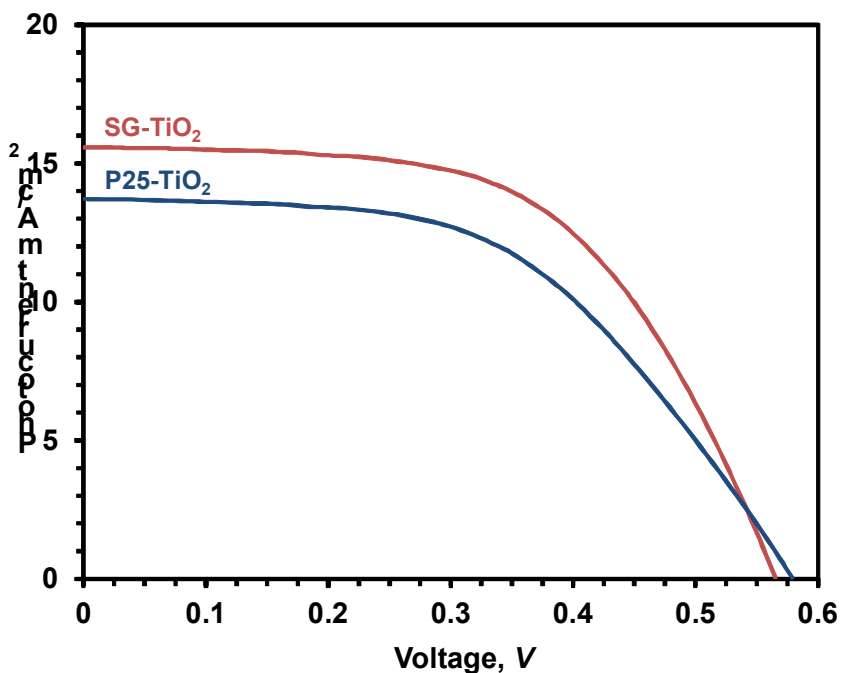


**Figure 3.12.** Photocurrent-voltage (*I-V*) curves of SG-TiO<sub>2</sub> and P25-TiO<sub>2</sub> films.

Here,  $I_{sc}$  is the short-circuit current density (mA/cm<sup>2</sup>),  $V_{oc}$  is the open-circuit voltage (V),



$P_{in}$  is the incident light power, and  $I_{max}$  (mA/cm<sup>2</sup>) and  $V_{max}$  (V) are the current density and voltage in the  $I$ - $V$  curve at the point of maximum power output. The determined  $I$ - $V$  curves are summarized in **Table 3.3**.

**Table 3.3.** Photovoltaic performance of dye-sensitized solar cell

	Film thickness, $\mu$ m	$V_{oc}$ , V	$I_{sc}$ , mA/cm <sup>2</sup>	Fill factor, $FF$	$\eta_{eff}$ , %
<b>P25-TiO<sub>2</sub> film</b>	4.7	0.58	13.6	0.53	4.1
<b>SG-TiO<sub>2</sub> film</b>	4.6	0.57	15.6	0.57	5.0

A dye-sensitized solar cell fabricated in this work gave an open-circuit voltage of 0.57 V and short-circuits current density of 15.6 mA/cm<sup>2</sup> for an incident light intensity of 100 mW/cm<sup>2</sup>. The power conversion efficiency of over 5.0 % was achieved using the single-phase anatase crystallites synthesized (SG-TiO<sub>2</sub>) in chapter 3. It was found that DSSC made of nanostructured SG-TiO<sub>2</sub> film showed better photo-energy conversion efficiency compared to those prepared using P25-TiO<sub>2</sub> film.

### 3.3.2 Adsorption Study of N719 Dye on SG-TiO<sub>2</sub> Electrode

The adsorption characteristics (i.e., equilibrium and kinetics) of N719 dye on the SG-TiO<sub>2</sub> were evaluated on the basis of adsorption equilibrium and kinetic studies. N719 dye has two bipyridyl ligands with two carboxyl groups at the 4 and 4' position of the bipyridyl group. It has been known that the carboxyl group interacts with SG-TiO<sub>2</sub> surfaces through chemical bond formation to the surface, chelating or bridging modes, or physical adsorption.<sup>91</sup> **Figure 3.13** shows the adsorption isotherms of N719 on SG-TiO<sub>2</sub> at three different temperatures (298.15, 313.15, and 333.15 K). The results show that the adsorption capacity increased with increasing temperature. The chemisorption usually requires activation energy which increases with increasing temperature. Finnie et al. have suggested from the vibrational spectroscopic study of the coordination of Ru (II) dye to the surface of nanocrystalline TiO<sub>2</sub> that the chemical bonding structure of dye molecule is a bidentate

chelate or bridging coordination to the SG-TiO<sub>2</sub> surface via two carboxylate groups per dye molecule.<sup>90</sup>

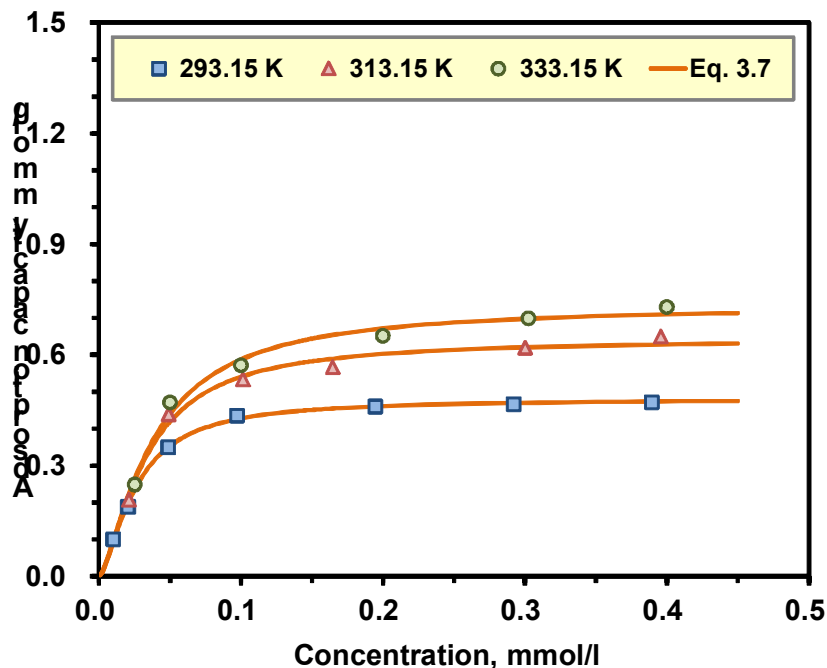


**Figure 3.13.** Adsorption isotherms of N719 on SG-TiO<sub>2</sub> particles at different temperatures.

The adsorption isotherm parameters, which can be obtained from the different model equations, are extensively used for the design of the feasible adsorption process. In the literature, the Langmuir isotherm has been widely applied to interpret the data obtained for the adsorption of liquid phase. It has shown a good agreement with a wide variety of experimental data for the adsorption of solutes from liquid solutions.<sup>92</sup> This isotherm is given by **Equation 3.5**:<sup>93</sup>

$$q = \frac{q_m b C}{1 + b C} \quad (\text{Eq. 3.5})$$

Where  $C$  is the concentration of adsorbate in solution at equilibrium (mol/l),  $q$  is the amount of adsorbate bonded to adsorbent in the case of reached equilibrium,  $q_m$  is the maximum amount of adsorbate bonded to adsorbent when a monolayer is formed, and  $b$  is the adsorption intensity or Langmuir coefficient. The basic assumption of Langmuir's theory is that the adsorption of one single adsorbate molecule takes place at specific active sites of an energetically homogeneous surface of the adsorbent. By contrast, Freundlich isotherm is an experimental model that can be applied to non-ideal adsorption on heterogeneous surfaces as well as for multi-layer adsorption.<sup>92</sup> It has been derived by assuming the heterogeneity of surface (exponentially decaying adsorption sites strength). It is expressed by the following equation.<sup>93</sup>

$$q = kC^{1/n} \quad (\text{Eq. 3.6})$$

where  $C$  and  $q$  have the same meanings as in Langmuir isotherm, while  $k$  and  $n$  are constants; number  $n$  being often lower than 1.

Both Freundlich and Langmuir concepts are combined in the postulation of Langmuir-Freundlich (named also "Sips' equation"): the interaction of one adsorbate molecule with one active site at heterogeneous surface possessing definite number of active sites is presumed.<sup>94,95</sup> This can be expressed by **Equation 3.7**.

$$q = \frac{q_m b C^{1/n}}{1 + b C^{1/n}} \quad (\text{Eq. 3.7})$$

Where  $q_m$  is the maximum amount of adsorbed species and  $n$  can be regarded as the parameter characterizing the system heterogeneity. If the value for  $n$  is less than one, it is a heterogeneous adsorbent, while values closer to or even one indicated that the adsorbent has relatively more homogeneous binding sites. Parameter  $b$  characterizes sorbate-sorbent interaction.

Among the well-known isotherms such as the Langmuir, Freundlich and Sips isotherm models, the adsorption equilibrium data of N719 on SG-TiO<sub>2</sub> were correlated by the Sips equation. The isotherms parameters were determined by using MATLAB R2008 software.

The object function,  $E$  (%), represents the average percent deviation between experimental and predicted results as follows in **Equation 3.8**.

$$E(\%) = \frac{100}{n} \sum_{k=1}^n \left[ \frac{|q_{\text{exp},k} - q_{\text{cal},k}|}{q_{\text{exp},k}} \right] \quad (\text{Eq. 3.8})$$

Where,  $n$  is the number of experimental data,  $q_{\text{exp},k}$  is the experimental adsorption capacity, and  $q_{\text{cal},k}$  the calculated adsorption capacity. The solid lines (**Figure 3.13**) are the predicted results with Sips isotherm parameters are shown in **Table 3.4**.

**Table 3.4.** Sips parameters of N719 adsorption on SG-TiO<sub>2</sub> for different temperatures

Temperature, K	pH	Parameters			
		$q_m$ , mmol/g	$b$ , l·mmol	$n$	$E$ , %
298.15	7	0.48	283	0.65	0.02
313.15	7	0.64	163	0.68	0.17
333.15	7	0.79	106	0.70	0.23

The isosteric enthalpy is a measure of the interaction between adsorbate molecules and adsorbent lattice atoms, and it may be used as a measure of the energetic heterogeneity of a solid surface. For the heterogeneous adsorption system, the isosteric enthalpy curve varies with the surface loading. It has been recognized that surface heterogeneity may come from the energetic, structural, and geometric heterogeneity.<sup>81</sup> The isosteric enthalpies of N719 dye adsorption were calculated by the Clausius-Clapeyron equation using the obtained Sips isotherm parameters and is shown in **Equation 3.9**.<sup>96</sup>

$$q_{st} = -R \left[ \frac{\partial \ln C}{\partial (1/T)} \right]_q \quad (\text{Eq. 3.9})$$

Where,  $C$  is the concentration,  $T$  is the temperature,  $R$  is the gas constant, and  $q_{st}$  is the isosteric enthalpy. The results showed that the isosteric enthalpies of adsorption with the surface loading increased slightly in the range from 2 kJ/mol to 12 kJ/mol (**Figure 3.14**).

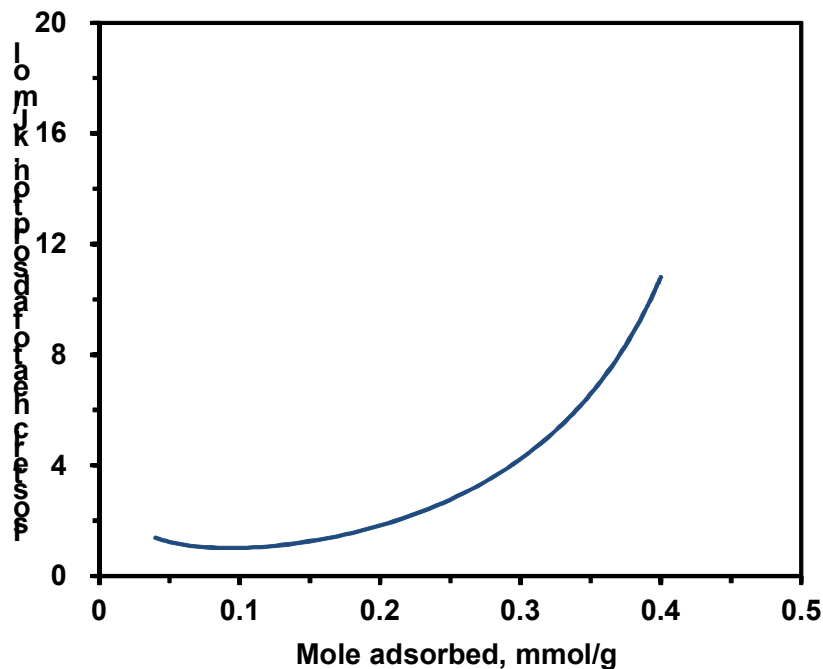


**Figure 3.14.** Isosteric heat of adsorption for N719 on SG-TiO<sub>2</sub> particles.

The kinetics of adsorption data was processed to understand the dynamics of adsorption process in terms of the order of rate constant. Two kinetic models were used to the adsorption kinetic data in order to investigate the behavior of adsorption process of N719 dye onto SG-TiO<sub>2</sub> particles. These models are the pseudo-first-order and pseudo-second-order models.<sup>98</sup> In this works, the adsorption kinetic experiments were carried out at different dye concentrations (0.05 and 0.5 mM). It was observed that the pseudo-first-order model explains the initial stages where rapid adsorption occurs but cannot be applied for the entire adsorption process. Thus, the kinetic data were analyzed with the pseudo-second-order model as given in **Equation 3.10**.<sup>97,98</sup>

$$\frac{dq}{dt} = k_2 (q_e - q)^2 \quad (\text{Eq. 3.10})$$

Integrating **Equation 3.10** for the boundary conditions of  $q=0$  to  $q=q_t$  at  $t=0$  to  $t=t$  gives the **Equation 3.11**.

$$\frac{t}{q_t} = \frac{1}{h} + \frac{t}{q_e} \quad (\text{Eq. 3.11})$$

The initial adsorption rate,  $h$ , of a second-order process as  $t \rightarrow 0$  is defined in **Equation 3.12**.

$$h = k_2 q_e^2 \quad (\text{Eq. 3.12})$$

Where,  $h$  (mg/g·min) is the initial adsorption rate,  $q_e$  (mg/g) is the adsorption capacity, and  $k_2$  (g/mg·min) is the second-order rate constant determined by the plot of  $t/q_t$  vs.  $t$ . In applying **Equation 3.11** and **3.12** to the experimental data, it is essential to have a precise knowledge of the equilibrium adsorption capacity,  $q_e$ .<sup>99</sup> The pseudo-second-order equation has also been interpreted as a special kind of Langmuir kinetics.<sup>100</sup> This line of interpretation assumes that i) the adsorbate concentration is constant in time and ii) the total number of binding sites depends on the amount of adsorbate adsorbed at equilibrium. One of the advantages of the pseudo-second order equation for estimating the  $q_e$  values is its small sensitivity for the influence of the random experimental errors.<sup>100</sup>

**Figure. 3.15a** shows the typical examples of the effect of initial concentrations (0.05 and 0.5 mM). It was noted that the correlation coefficients ( $R^2$ ) of the pseudo-second-order model for the linear plots of SG-TiO<sub>2</sub> were very close to 1 (**Figure 3.15b**). This result implies that adsorption kinetics can be successfully described by the pseudo-second-order model. As listed in **Table 3.5**, the determined rate constant,  $k_2$ , was 2.10 g/mmol·h for low concentration (0.05 mM) and 1.35 g/mmol·h for high concentration (0.5 mM). Contrary to our expectation, the adsorption kinetics was almost independent of the dye concentrations because of the very fine particles of SG-TiO<sub>2</sub>.

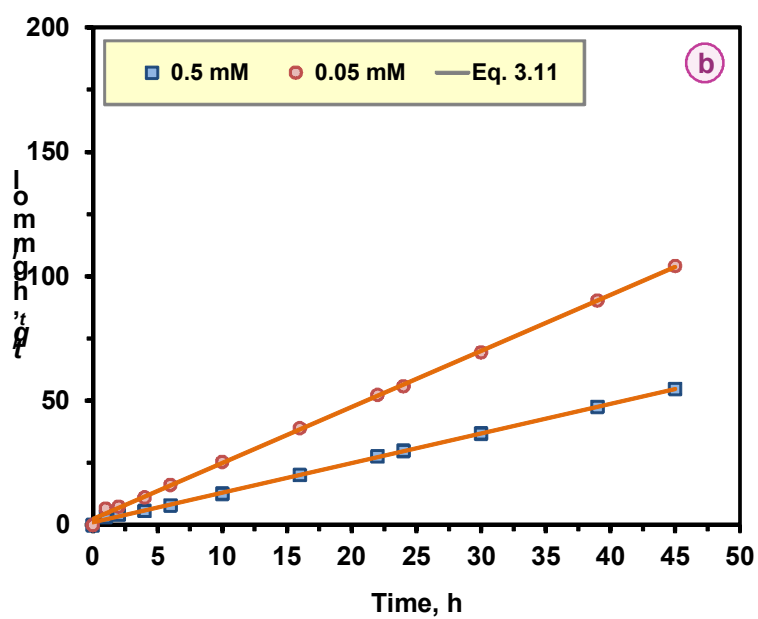
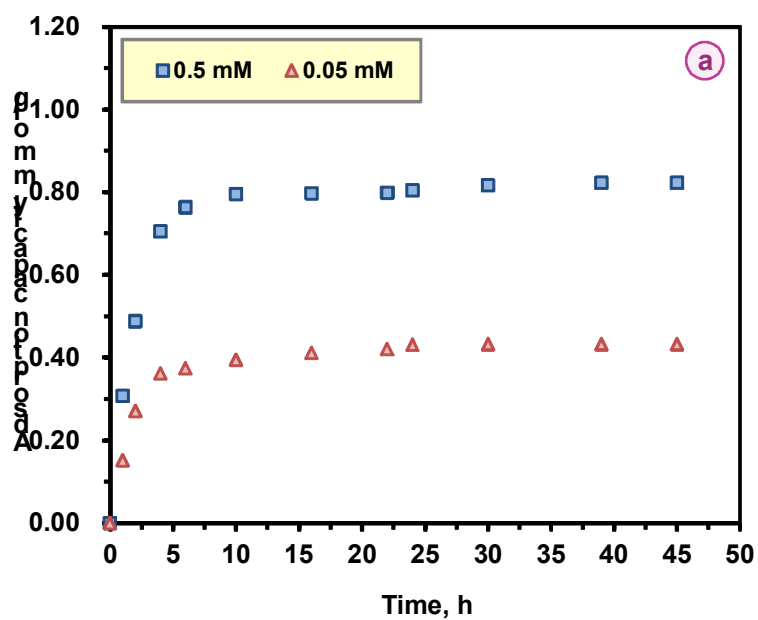


**Figure 3.15.** Adsorption kinetics of N719 on SG-TiO<sub>2</sub> particles depending on the concentrations (0.05 and 0.5 mM).

Also, the adsorption equilibrium time of N719 dye was present about more than 10 h.

**Table 3.5.** The pseudo-second-order kinetic parameters of N719 adsorption on SG-TiO<sub>2</sub>

Concentration, mM	Temperature, K	pH	Parameters			
			$q_e$ , mmol/g	$k_2$ , g/mmol·h	$h$ , g/mmol·h	$R^2$
0.05	333.15	7	0.44	2.10	0.41	0.99
0.5	333.15	7	0.83	1.35	0.95	0.99

To compare the influence of solution pH, the adsorption amount data were obtained in terms of pH (3, 4, 7, 10) at room temperature (298.15 K). As shown in **Figure 3.16a**, higher adsorption capacity was observed at pH 4. This result may come from the fact of the isoelectric point of SG-TiO<sub>2</sub> adsorbing N719 dye, which is around this pH. To verify this fact, zeta potential measurements of SG-TiO<sub>2</sub> before and after adsorption were measured in terms of solution pH (3-10). As shown in **Figure 3.16b**, the zeta potential values ranged approximately between +20 and -40 mV regardless of the adsorption of N719 dye on SG-TiO<sub>2</sub>. In addition, the isoelectric point of SG-TiO<sub>2</sub> was present around pH 3.5.

As a final work, an accurate knowledge of solar cell parameters from the experimental data is important for the design of solar cells and for the estimation of their performance. It has been established that the current-voltage curves of DSSC can be satisfactorily fitted to a 1-diode model for liquid electrolyte and a 2-diode model for polymer electrolyte.<sup>101</sup> The current-voltage relation using equivalent circuit and a 1-diode model (**Figure 2.11b**) under illumination is given **Equation 3.13**.<sup>73</sup>

$$I = I_{ph} - I_o \left\{ \exp \left[ \frac{q_c}{nk_B T} (V + IR) - 1 \right] \right\} - \frac{V + IR_s}{R_{sh}} \quad (\text{Eq. 3.13})$$

Where,  $I_{ph}$  is the photo-generated current,  $I_o$  is the diode saturation current (i.e., initial current),  $n$  is the diode quality factor (or ideality factor),  $R_s$  is the series resistance,  $R_{sh}$  is



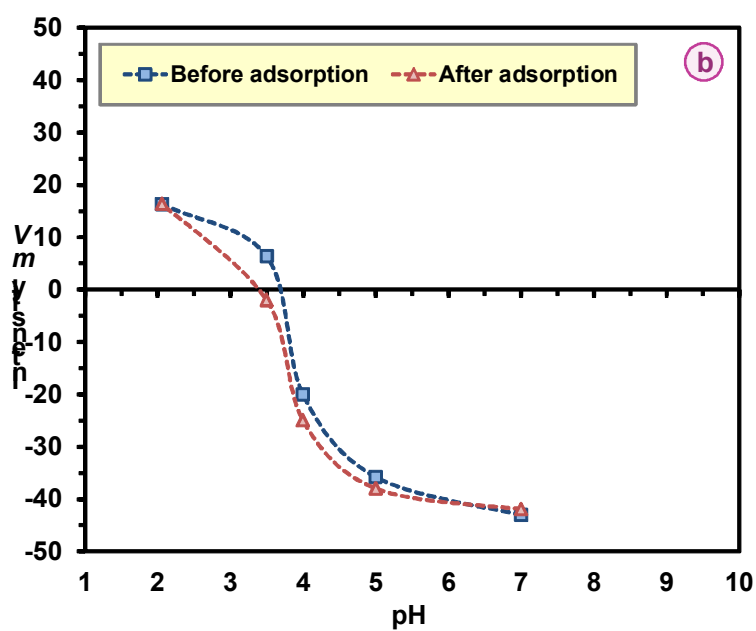
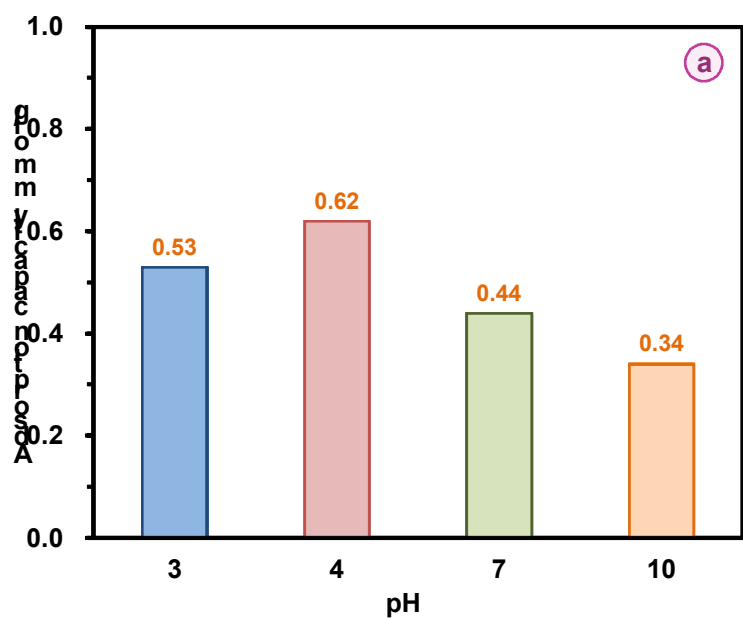


**Figure 3.16.** (a) Adsorption capacity of N719 with solution pH (b) zeta potential of SG-TiO<sub>2</sub> particles.

the parallel (shunt) resistance,  $q_c$  is the elementary electric charge ( $1.602 \times 10^{-19}$  C),  $k_B$  is the Boltzman constant ( $1.38 \times 10^{-23}$  J/K), and  $T$  is the temperature.

**Equation 3.13** cannot be solved analytically. To obtain five model parameters ( $I_{ph}$ ,  $I_o$ ,  $n$ ,  $R_s$ ,  $R_{sh}$ ), a nonlinear least-square optimization algorithm based on the Newton's method modified by introducing the so-called Levenberg parameter was used.<sup>102</sup> The objective function  $F$  with respect to the set of unknown parameters  $u$  is given by **Equation 3.14**.

$$F(u) = \sum_{i=1}^n [I_{i,exp} - I_{i,cal}(V_i, u)]^2 \quad (\text{Eq. 3.14})$$

Where,  $u$  is the unknown parameter ( $I_{ph}$ ,  $I_o$ ,  $n$ ,  $R_s$ ,  $R_{sh}$ ),  $I_{i,exp}$  and  $I_{i,cal}$  are the experimental and calculated current at  $i$ -th point, and  $n$  is the number of data points. **Figure 3.17** exhibits the flow chart for the calculation step of a nonlinear optimization procedure.

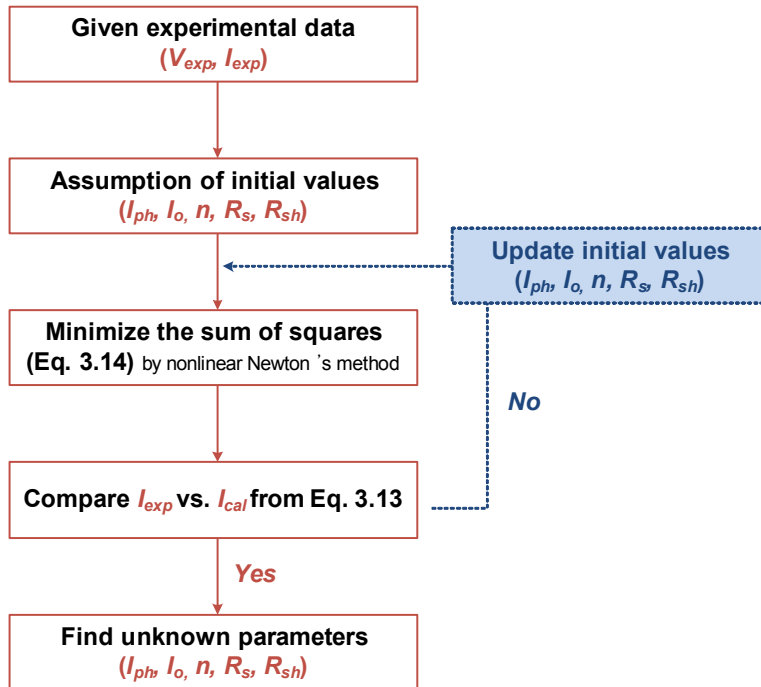


**Figure 3.17.** Flow chart for the calculation of 1-diode model.

To systematically study the influence of adsorption properties between dye molecules and  $\text{TiO}_2$  films on the power conversion efficiency of DSSC, the effect of adsorption quantity (of the dye) on the photovoltaic performance of DSSC was analyzed. **Figure 3.18** shows the influence of adsorption amount on the graphs of photocurrent-voltage ( $I$ - $V$ ) for nanocrystalline solar cell. The determined the short-circuit current ( $I_{sc}$ ), open-circuit voltage ( $V_{oc}$ ), fill factor ( $FF$ ), and overall conversion efficiency ( $\eta_{eff}$ ) of DSSCs are summarized in **Table 3.6**.

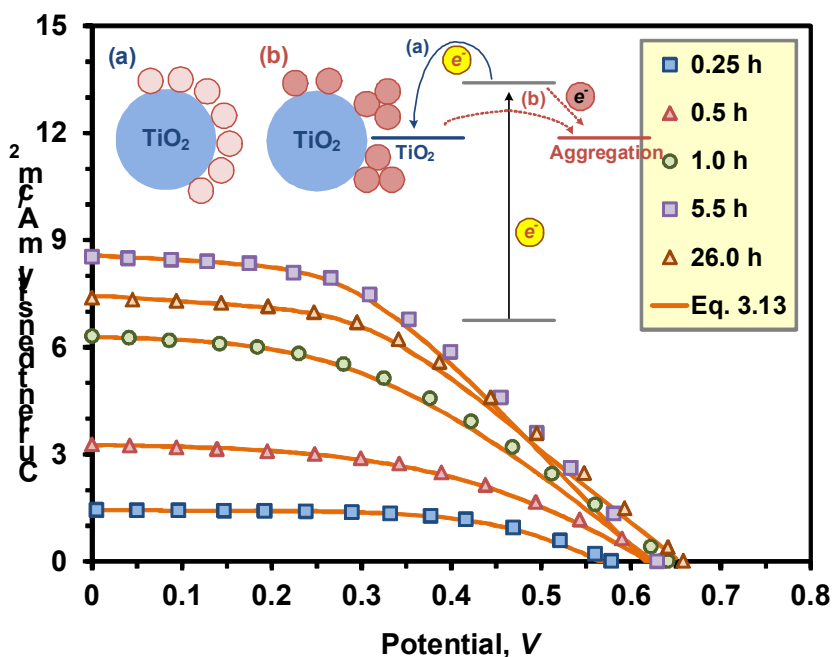


**Figure 3.18.**  $I$ - $V$  curves of SG- $\text{TiO}_2$  films depending on the N719 adsorption amount.

It is interesting to compare the amount of adsorbed dye with the photocurrent densities of corresponding DSSC. Before making the cell, the working electrodes were immersed in a 0.5 mM of N719 dye for different adsorption time (0.25, 0.5, 1.0, 5.5, and 26.0 h) to control the adsorption amount. As expected, it was noted that the order of the photocurrent

densities increased with the adsorption amount (i.e., adsorption time). The high adsorption capacity (i.e., increase in adsorption time up to 5.5 h) of SG-TiO<sub>2</sub> with the low charge transfer resistance may give rise to the superior  $I_{sc}$  of DSSC because of the monolayer adsorption [Figure 3.18(inside, a)]. However, the photocurrent density of SG-TiO<sub>2</sub> decreases with increasing immersion time (26.0 h). This result may explain how the agglomeration of dyes molecules adsorbed on SG-TiO<sub>2</sub> surfaces affected negatively on the charge transfer resistance.<sup>88,96,103,178,179</sup> To avoid this agglomeration of dye molecules [Figure 3.18(inside, b)], the dye adsorption should be conducted under a supercritical condition.<sup>103</sup> It can be concluded from this work that the conversion efficiency of the DSSC was highly dependent on the adsorption properties of N719 dye on TiO<sub>2</sub> films.

**Table 3.6.** Characteristics values of dye-sensitized solar cell depending on adsorption amount

Adsorption time, h	Adsorption amount, mol/cm <sup>2</sup>	Film thickness, $\mu$ m	$V_{oc}$ , V	$I_{sc}$ , mA/cm <sup>2</sup>	Fill factor, $FF$	$\eta_{eff}$ , %
0.25	$0.25 \times 10^{-8}$	4.6	0.58	1.4	59	0.5
0.5	$1.05 \times 10^{-8}$	4.6	0.62	3.3	47	1.0
1.0	$3.67 \times 10^{-8}$	4.6	0.63	6.3	42	1.7
5.5	$5.29 \times 10^{-8}$	4.6	0.62	8.5	45	2.4
26.0	$5.35 \times 10^{-8}$	4.6	0.66	7.3	45	2.2

The analysis of equivalent circuit using 1-diode model mentioned above is suitable to analyze the effects of interfacial resistance and back-electron-transfer. The decreased resistances in the SG-TiO<sub>2</sub> layer by adsorption quantity lead to the decrease of  $R_s$  values while the decrease in the back-electron-transfer rate yields an increase in the  $R_{sh}$  values because of a lower leakage current from SG-TiO<sub>2</sub> surface to electrolyte.

The solid lines (Light brown color) in Figure 3.18 is the predicted results using the parameters of 1-diode model listed in Tables 3.7. As shown in the Figure 3.18, a good agreement between the measured data and the predicted results was observed. Therefore, it

can be concluded from this work that the optimal conditions of dye adsorption properties should be carefully determined to increase the conversion efficiency of DSSC.

**Table 3.7.** Determination of 1-diode model parameters of dye-sensitized solar cell depending on the adsorption quantity

Adsorption amount, mol/cm <sup>2</sup>	$I_{ph}$ , A	$I_o$ , $\mu$ A	$n$	$R_s$ , $\Omega$	$R_{sh}$ , $\Omega$
$0.25 \times 10^{-8}$	$1.213 \times 10^{-3}$	$9.787 \times 10^{-5}$	2.353	$5.930 \times 10^1$	$2.288 \times 10^3$
$1.05 \times 10^{-8}$	$2.130 \times 10^{-3}$	$1.239 \times 10^{-6}$	4.571	$5.771 \times 10^1$	$4.664 \times 10^3$
$3.67 \times 10^{-8}$	$4.089 \times 10^{-3}$	$3.754 \times 10^{-7}$	2.569	$5.457 \times 10^1$	$7.548 \times 10^3$
$5.29 \times 10^{-8}$	$5.725 \times 10^{-3}$	$7.846 \times 10^{-11}$	1.296	$4.993 \times 10^1$	$8.106 \times 10^3$
$5.35 \times 10^{-8}$	$5.081 \times 10^{-3}$	$1.067 \times 10^{-11}$	1.231	$5.047 \times 10^1$	$7.974 \times 10^3$

### 3.4 Summary

The colloidal TiO<sub>2</sub> suspension was prepared by sol-gel method based on the hydrolysis of TTIP. The TiO<sub>2</sub> films of single-phase anatase crystallites were formed on the FTO glass for a working electrode of DSSC. The films were characterized by AED, AFM, BET, FE-SEM, FT-IR, HR-TEM, XPS, and XRD analysis. The contents of Ti and O of SG-TiO<sub>2</sub> are 27.01% and 52.23% corresponding to closely Ti<sup>4+</sup> state. The nanoparticle size of SG-TiO<sub>2</sub> is about 14 nm and the film thickness was ca. 4  $\mu$ m. According to the AFM image, the films have heterogeneous surface with a few separated islands. A dye-sensitized solar cell of SG-TiO<sub>2</sub> gave an open-circuit voltage of 0.57 V and short-circuits current density of 15.6 mA/cm<sup>2</sup> for an incident light intensity of 100 mW/cm<sup>2</sup>. It was found that DSSC made of SG-TiO<sub>2</sub> nanocrystalline films as photo-anodes achieved better photo-energy conversion efficiency compared to those prepared using commercially available P25-TiO<sub>2</sub> films. The power conversion efficiency of over 5.0% was achieved using the single-phase anatase SG-TiO<sub>2</sub> crystallites synthesized in this chapter.

The adsorption equilibrium and kinetic studies revealed that the adsorption of N719 on

SG-TiO<sub>2</sub> nanoparticles was dependent on temperature and pH. The maximum adsorption capacity was achieved at the isoelectric point of around pH 4. The adsorption isotherm data can be fitted well with the Sips isotherm, and the adsorption kinetic data were well described by the pseudo-second-order model. On the other hands, the photocurrent-voltage of DSSC in terms of adsorption quantity was evaluated by a 1-diode model. The energy conversion efficiency increased with the adsorption quantity. However, the efficiency decreased for the SG-TiO<sub>2</sub> cell with adsorption time of 26.0 h because of the high charge resistance caused by the agglomeration of adsorbed dye molecules. Moreover, the conversion efficiency is highly influenced by the adsorption state. It was also found that the equivalent circuit analysis using the 1-diode model for DSSC is very useful in evaluating the effects of adsorption quantity.

## Chapter 4. Photovoltaic Properties of TiO<sub>2</sub> Electrode Prepared by Mesoporous Silica Template

### 4.1 Introduction

The sensitized dyes which are attached to *n*-type semiconductor metal oxides in the DSSC generate electrons upon irradiation with visible light. Most of the electrons in the metal oxide electrode of the device flows by diffusion. This is a distinguished characteristic of DSSC as compared to others devices such as silicon based solar cells and thin film. Thus, quantity of dye molecules are adsorbed on a constant unit area is one of the most important factors determining the photo conversion efficiency of the DSSC.

In 1991, Gätzel et al. published the first concept of a DSSC using a visible light sensitized dye with nanocrystalline TiO<sub>2</sub> film and the photo conversion efficiency of DSSC has now reached approximately 10%.<sup>26</sup> The approximately 15  $\mu$ m thick electrode film made of nanocrystalline TiO<sub>2</sub> designed to adsorb a large amount of dye molecules are called mesoporous films.<sup>104</sup> The meaning and concept of mesopores were used in the early stages of research for DSSC research. However, most of the recently introduced mesoporous materials have ordered mesopores. Since the first mesoporous materials were introduced by Mobil company two decades ago,<sup>105</sup> many researchers have developed materials and currently, mesoporous metal oxide with ordered mesoporous and a high surface area are used for electronic devices and catalysis.<sup>106,107</sup> Among these method, the evaporation induced self assembly and spin coating methods using surfactants for the fabrication of mesoporous TiO<sub>2</sub> films have been applied in various fields.<sup>108,109</sup> But, these methods have crucial drawbacks for the fabrication of DSSC, because the thickness of the electrode film is not well controlled. It is necessary to obtain a suitable film thickness which is around 15  $\mu$ m for the high performance DSSC. To solve this problem, coating TiO<sub>2</sub> films by doctor blade or screen printing methods using a mixed paste consisting of a mesoporous powder and solvents is effective.<sup>110</sup>

In the addition, there are still many problems for highly performance of DSSC. Among

them, one of the most critical problems is the limitation of the nanocrystalline  $\text{TiO}_2$  film thickness to increase the adsorption amount of dye. This gives rise to other problems such as increase recombination rate and the diffusion length of the electrons.<sup>111-114</sup> Instead of controlling the thickness of the nanocrystalline  $\text{TiO}_2$  film, many previous experiments attempted the use of a multi-layer structure for the film. This is accomplished by using various size and types of  $\text{TiO}_2$  particles as light scattering layers fabricated to improve the photocurrent density by trapping long wavelength light in the  $\text{TiO}_2$  electrode.<sup>115,116</sup> It has been proved that adopted light scattering materials such as spheres,<sup>117</sup> hollows,<sup>118</sup> and inverse opals<sup>119</sup> remarkably improve the photo-conversion efficiency of DSSC, not only in theoretical simulations<sup>43</sup> but also in experimental research.<sup>119,120</sup> However, these materials can only play a significant role as a light scattering centers because they have restriction of dye adsorption. However, they cannot enhance photo conversion efficiency by adsorption of dye molecules. A multi functional material which can increase the adsorption amount of dye and also play a light scattering role is required to overcome the limitation of current materials to create a highly performed DSSC.

The synthesis of mesoporous  $\text{TiO}_2$  (i.e., nanoporous  $\text{TiO}_2$ ) particles has stimulated substantial research in the past decade.<sup>106,121</sup> A highly crystalline  $\text{TiO}_2$  particles with large surface area have enormous potential for applications.<sup>107,122</sup> Many researches have representatively synthesized mesoporous  $\text{TiO}_2$  materials.<sup>123,124</sup> Though they have plenty of merits in each case, hard templating called nano casting is quite a useful method for creating highly crystalline nanoporous  $\text{TiO}_2$  particles. The nanoporous  $\text{TiO}_2$  particles has controllable morphology determined by the morphology of the silica template. Thus, the nanoporous  $\text{TiO}_2$  particles has attractive characteristics for DSSC.

It has been reported that the efficiency of electron injection to the conduction band of  $\text{TiO}_2$  is highly dependent on the bonding structure of the dye adsorbed on the semiconductor  $\text{TiO}_2$ .<sup>13,125</sup> In addition, the electron transfer in DSSC is strongly influenced by the electrostatic and chemical interactions between the  $\text{TiO}_2$  surface and the adsorbed dye molecules.<sup>89</sup> A dye molecule of N719 used in this work has two bipyridyl ligands with two carboxyl groups at the 4 and 4' position of the bipyridyl group (**Figure 4.1a**). The possible anchoring modes for carboxylate group of dye on the anatase  $\text{TiO}_2$  ( $d_{101}$ ) surface are unidentate, bidentate, and bridging.<sup>89,90</sup> The carboxy groups can coordinate in



different ways to metal ions: simply by physical adsorption via hydrogen bonding (**Figure 4.1b**) or via chemical bond formation with a unidentate linkage, a bidentate (or chelating) linkage, or a bridging linkage (**Figure 4.1c**).

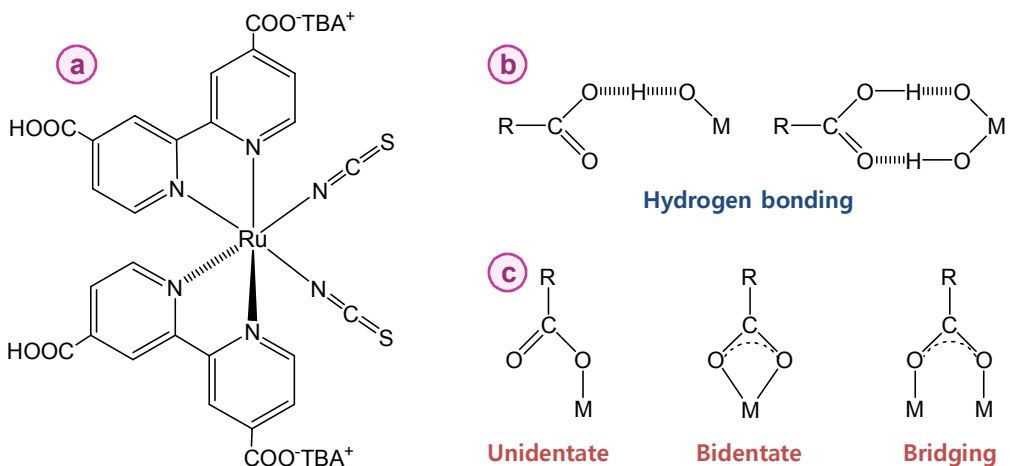


**Figure 4.1.** (a) Molecular structure of N719 (b) coordination types of physisorption (c) chemisorption.

A Ti ion can interact equally with the two oxygen atoms of the COO<sup>-</sup> group in the bidentate form. However, this disappears in the unidentate form since the ion interacts only with one of these oxygen atoms, resulting in an ester-type bond between the carboxylic acid group and the TiO<sub>2</sub> surface. In the bridging form, a metal ion interacts with one of the oxygen atoms, and the other metal ion interacts with the second oxygen atom. When one of the metal ions is replaced by a hydrogen atom of a water molecule, the system is in the pseudobridging configuration. The surface anchoring form plays an important role for the solar cell efficiency and it also has an influence on its stability. Unfortunately, systematic studies on the influence of the adsorption properties between N719 molecules and anatase TiO<sub>2</sub> (*d*<sub>101</sub>) surface on the energy conversion efficiency of DSSC are very limited.<sup>42</sup>

In this study a TiO<sub>2</sub> electrode using nanoporous TiO<sub>2</sub> powders (MK-TiO<sub>2</sub>, MS-TiO<sub>2</sub>, and MU-TiO<sub>2</sub>) was fabricated from different mesoporous silica template of KIT-6 (bicontinuous cubic, *Ia3d*), SBA-15 (2-D hexagonal, *P6mm*), and MSU-H (2-D hexagonal, *P6mm*) by nano casting method. The samples were characterized by AED, AFM, BET, FE-SEM, HR-TEM, and XRD. The bonding structures of N719 adsorbed on TiO<sub>2</sub> were investigated using FT-IR spectroscopy. The influence of the adsorption properties between N719 molecules and nanoporous TiO<sub>2</sub> film surfaces on the energy conversion efficiency of DSSC was also systematically investigated on the basis of photovoltaic performance calculated from the *I-V* curves. The nanoporous TiO<sub>2</sub> materials are expected to show superior adsorption properties in the DSSC, due to their high crystallinity and surface area. Finally, the multi layer (i.e., light scattering layer) nanoporous TiO<sub>2</sub> particles suggests high adsorption amount of dye due to the high surface area which is a representative characteristic of mesoporous materials.<sup>88</sup> It also has a light scattering effect due to its particle size which is around 200 nm spheres. This dual functionality of nanoporous TiO<sub>2</sub> particles suggests a new advance material for highly efficient DSSC.

#### 4.1.1 Mesoporous Materials

Mesoporous materials have been widely applied in many field such as catalysis, adsorption, separation, and biosensor technology owing to their high surface area and very large pore size. Depending on the predominant pore size, the porous materials are classified by the international union of pure and applied chemistry (IUPAC) into three classes:

- i ) Microporous material having pore sizes below 2.0 nm,
- ii) Mesoporous material with intermediate pore sizes between 2.0 and 50.0 nm,
- iii) Macroporous material with pore sizes exceeding 50.0 nm.

**Figure 4.2** shows the pore size distributions for different types of porous silica materials.<sup>126</sup> In 1992, M41S family (MCM-41, MCM-48, and MCM-50), pore size in the range of 2-10 nm, was discovered by Mobile corporation scientists.<sup>105</sup> M41S materials have been paid attention due to their very ordered pore structure, especially very narrow pore size distribution. According to the starting materials and varying synthesis condition,

different mesoporous silica oxide types are formed. Many mesoporous materials including KIT-6,<sup>127</sup> SBA-15,<sup>128</sup> and MSU-H<sup>129</sup> have been reported.

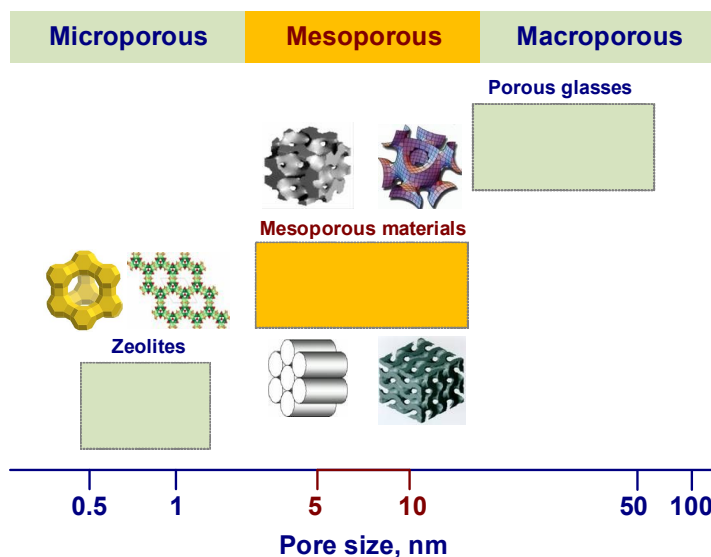


**Figure 4.2.** Pore size distributions for different types of porous silica materials.

**Figure 4.3** shows the synthesis process of common mesoporous silica. Inorganic structure is formed around the micelle of surfactant followed by thermal treatment.

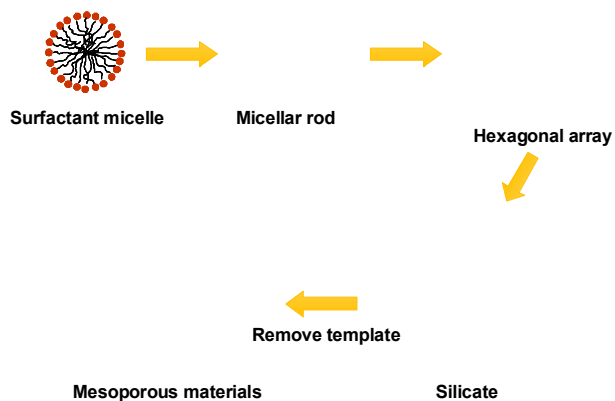


**Figure 4.3.** Synthesis process of common mesoporous silica.

The inorganic template is condensed by sol-gel process and the organic and inorganic substances are combined together by interaction. Finally, a well-allined porous materials can be obtained after thermal treatment or chemical extraction to remove the template. This method is called as liquid crystal templating mechanism. On the other hand, mesoporous silicates can also be synthesized by the self-assembly of surfactant as the structure directing agent. The synthesis is explained by cooperative templating mechanism and charge density matching model suggested by Stuky and Moniier group, respectively.<sup>130</sup>

In this article, three mesoporous materials such as KIT-6, SBA-15, and MSU-H were used to prepare TiO<sub>2</sub> particles. Similar to MCM-48, KIT-6 has *Ia3d* structure which is indicated by eight peaks by XRD as shown in **Figure 4.4a**.

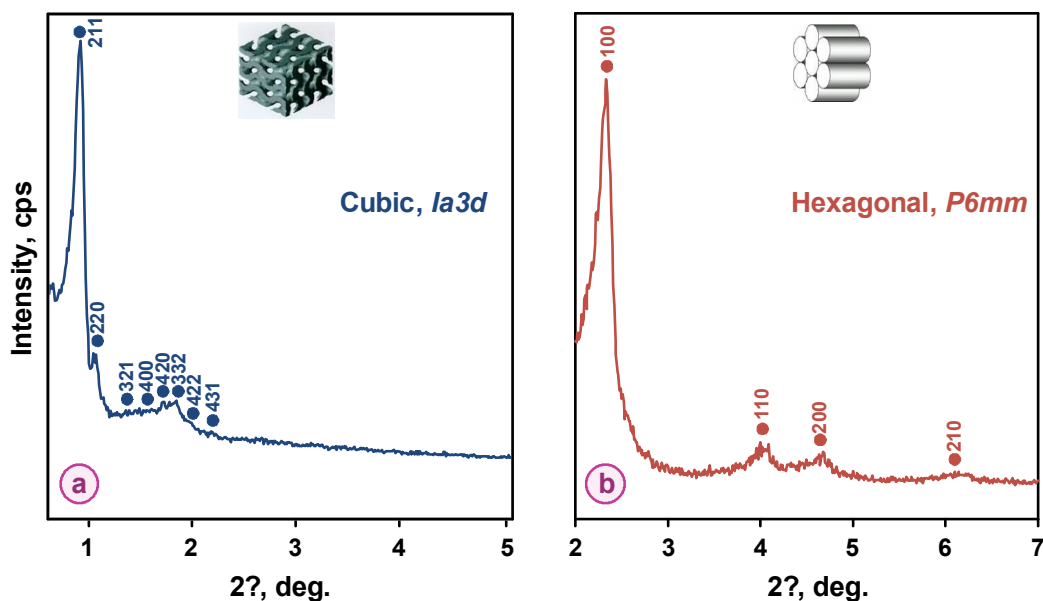


**Figure 4.4.** (a) XRD pattern of KIT-6, (b) SBA-15 and MSU-H.

The pore size of KIT-6 is 7-8 nm whereas that of MCM-48 was 2-3 nm respectively. It was observed that the XRD patterns are identical because of the same pore structure. However, the values of  $2\theta$  is different because the pore size and structure is different because of surfactant types and synthesis method. The XRD patterns of SBA-15 and

MSU-H are similar to MCM-41 [2D hexagonal ( $P6mm$ ) pore network] shown in **Figure 4.4b**. Since the synthetic method is different, the particle size, morphology and structural characteristics are different. **Table 4.1** summarizes the physical properties of various mesoporous silicates (KIT-6, SBA-15, and MSU-H) which were used in this work. The samples were characterized by XRD, BET, SEM, and TEM to obtain the informations about the crystallinity, pore size and volume and particle types. The obtained results are useful information to verified the target materials.

**Table 4.1.** Physical properties of various mesoporous silicate used in this works

	Surface area, m <sup>2</sup> /g	Pore volume, cm <sup>3</sup> /g	Pore size, nm	Particle size, $\mu$ m
<b>KIT-6</b>	615	0.95	7-8	Unknown
<b>MCM-41</b>	1,086	1.02	2-3	Unknown
<b>MCM-48</b>	912	0.88	2-3	Unknown
<b>MSU-H</b>	407	0.80	7-8	0.2-0.3
<b>SBA-15</b>	704	0.93	7-8	0.5-1.0

#### **4.1.2 Nanoporous TiO<sub>2</sub> Replicas from Mesoporous Silica**

After the discovery of M41S-family material by Mobil company in 1992, several new type of ordered mesoporous silicas (OMS) materials such as KIT-6, SBA-15, and MSU-H have been synthesized. Recently, these OMS have gained tremendous research interest due to their diverse applications including drug delivery system. In contrast to OMS, there are only very few reports on non-siliceous mesoporous materials, probably due to the complicated synthesis manipulations. Surfactant-templated synthesis and ligand assisted templating of non-siliceous mesoporous materials have many drawbacks. For example, damage to the mesostructure of metal oxide during the crystallization and the removal of the organic template by heat treatment. In addition, it is also very hard to control the soft-templated synthesis of mesoporous metal oxides in comparison to the OMS. Ryoo et

al. had established the novel approach to synthesize the mesoporous carbon (CMK-1) using mesoporous silica materials as a rigid template based on the replication method.<sup>131</sup> Several ordered non-siliceous mesoporous materials such as  $\text{CeO}_2$ ,  $\text{Co}_3\text{O}_4$ , and  $\text{Fe}_2\text{O}_3$  have been synthesized by taking advantage of this method. The synthesis method of various mesoporous spheres of metal oxides reported by Tang et al. makes it less attractive because of the multi step process and non ordered template.<sup>132</sup> However, to the best of my knowledge, there is no report about synthesis of ordered mesoporous  $\text{TiO}_2$  by this method. Herein, the ordered mesoporous  $\text{TiO}_2$  was synthesized by various mesoporous silica materials as rigid template.

$\text{TiO}_2$  is known to be used as a photocatalyst, gas sensor and photo electrode in DSSC. The increase in surface area can influence its activity positively. Thus, increasing surface area of  $\text{TiO}_2$  is regarded as of major importance particularly for catalytic performances. In the present study three different ordered mesoporous silica namely KIT-6, SBA-15, and MSU-H were taken as a rigid template to synthesize high surface area nanoporous  $\text{TiO}_2$ . Though SBA-15 and MSU-H has the same 2-D hexagonal structure, the particle size and shape are different. The synthesis method of MSU-H taken as template in the present work was modified by our research group in order to control the particle size by increasing the Na/Si ratio, known as salt effect. KIT-6 differs from SBA-15 and MSU-H by its 3-D cubic pore structure, irregular morphology, and larger particle size. The nanoporous  $\text{TiO}_2$ , obtained from mesoporous silica template, exhibits an inverse pore structure symmetry and a duplicate morphology of silica template. To increase the current density in DSSC, many works have been carried out to date. In this work, nanoporous  $\text{TiO}_2$  particles with high surface area and uniform nanochannels were synthesized for the modification of photo electrode structure.

## **4.2 Experimental**

### **4.2.1 Synthesis of Nanoporous $\text{TiO}_2$ Materials**

The methods of synthesis of silica materials such as KIT-6, SBA-15, and MSU-H are

available in else where.<sup>127-129</sup> **Figure 4.5** shows the preparation method of nanoporous TiO<sub>2</sub> particle. A triblock copolymer Pluronic P123 (EO<sub>20</sub>PO<sub>70</sub>EO<sub>20</sub>, Mw. 5,800 g/mol, Aldrich) was used as the structure directing agent for the silica materials. The tetraethylorthosilicate (i.e., TEOS, Aldrich) was used as the silica source for the KIT-6 and SBA-15 materials, and a sodium silicate solution (10 wt% of SiO<sub>2</sub>, Na/Si: 2.5) was used as the silica source for modified MSU-H material. After calcination, the mesoporous silica materials were used as templates for the synthesis of TiO<sub>2</sub> replica. In a typical nano replication (or nano casting), 0.75 g of Ti(OEt)<sub>4</sub> and 30 ml of water was mixed that resulted in a white precipitate. The precipitate centrifuged and was collected by decantation of supernatant solution and was dissolved with 1.0 g of HCl (35 wt%) at room temperature. The clear TiO<sub>2</sub> precursor sol was impregnated into 1.0 g of the mesoporous silica templates by the simple incipient wetness method, and the composites were dried at 433.15 K for 10 min. This impregnation drying process is repeated 9 times to maximize the amounts of TiO<sub>2</sub> precursor within the mesopores of silica templates. Subsequently, the samples were dried at 373.15 K for 24 h. The materials were heated to 723.15 K for 3 h under ambient conditions. After the removal of silica template using 1 M NaOH aqueous solution, nanoporous TiO<sub>2</sub> materials (i.e., MK-TiO<sub>2</sub>, MS-TiO<sub>2</sub>, and MU-TiO<sub>2</sub> replicas from KIT-6, SBA-15, and MSU-H) were obtained.

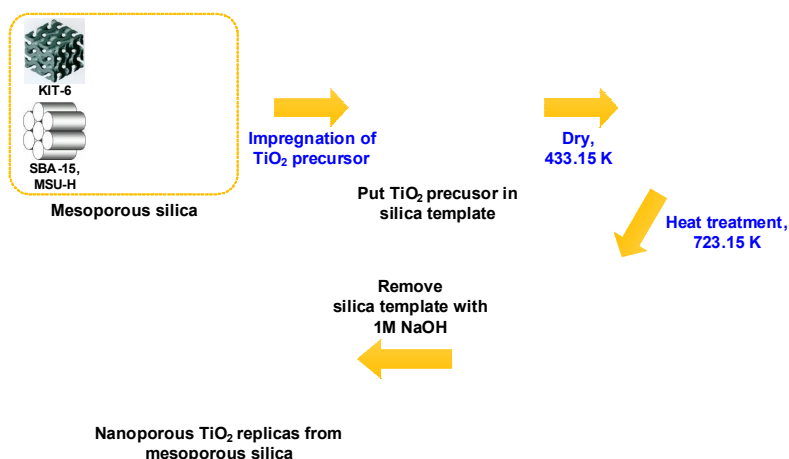


**Figure 4.5.** Synthesis process of nanoporous TiO<sub>2</sub> replicas from mesoporous silica.

#### 4.2.2 Fabrication of Nanoporous TiO<sub>2</sub> Electrode for Dye-Sensitized Solar Cell

**Figure 4.6** shows the schematic diagram for the fabrication of working electrode using nanoporous TiO<sub>2</sub> particle through the repetitive coating method. For the preparation of nanoporous TiO<sub>2</sub> thin film, TiO<sub>2</sub> slurry was prepared by the mixing 2 g nanoporous TiO<sub>2</sub> particles, 0.68 ml 10% [V/V] acetyl acetone, 1 g HPC, and 10.68 ml water for 12 h at 300 rpm using a paste mixer (PDM-300, Korea mixing technology Co.). Thus, a nanoporous TiO<sub>2</sub> film obtained by was coated onto the FTO glass (TEC 8: 10  $\Omega/\text{cm}^2$ , Pilkington Co.) by using a doctor blade coating (adhesive tape was used as spacer of ca. 65  $\mu\text{m}$  thickness). The nanoporous TiO<sub>2</sub> film was treated by heating at 773.15 K for 2 h. The nanoporous TiO<sub>2</sub> film formed on the FTO glass was 5-6  $\mu\text{m}$  thickness and 0.5 cm×0.5 cm in size. The adsorbed Na<sup>+</sup> metal ions resulted from the removal of mesoporous silica template in the synthesis process of nanoporous TiO<sub>2</sub> particles, will act as a resistance to the electrons in DSSC. Therefore, TiO<sub>2</sub> film was treated with the aqueous 0.1 M HCl solution for 4 h at 353.15 K for complete removal of Na<sup>+</sup> metal ions, which was followed by the dye adsorption. In addition, multi layer coating of the nanoporous TiO<sub>2</sub> film was examined for its influence on the enhancement of conversion efficiency of DSSC. The coated P25-TiO<sub>2</sub> films were re-coated by nanoporous TiO<sub>2</sub> slurry and calcined. Subsequently, the samples were treated with acid solution and adsorbed with dye molecule.

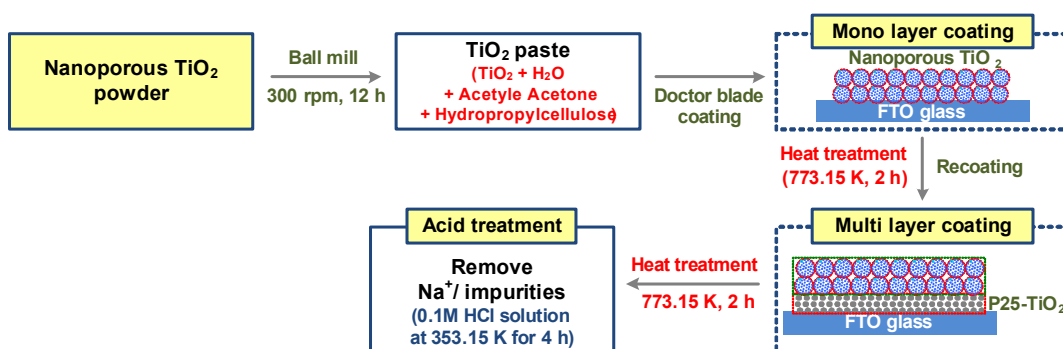


**Figure 4.6.** Manufacture process of nanoporous TiO<sub>2</sub> electrode.



To fabricate the DSSC, the prepared thin film electrode was immersed in the 0.3 mM N719 dye (Solaronix Co.) solution at 333.15 K for 12 h, rinsed with anhydrous ethanol and dried. Pt coated TEC 8 glass electrode was prepared as a counter electrode with an active area of 0.25 cm<sup>2</sup>. The Pt electrode was placed over the dye-adsorbed nanoporous TiO<sub>2</sub> electrode, and the edges of the cell were sealed with 2 mm wide stripers of 60 μm thick sealing sheet (SX 1170-60, Solaronix). Sealing was accomplished by hot-pressing the two electrodes together at 353.15 K. The redox electrolyte was filled into the cell through the small holes and the filling ports were sealed with a sealant glue (Amosil 4, Solaronix Co.). The composition of redox electrolyte was 0.3 M 1,2-dimethyl-3-propylimidazolium iodide (Solaronix Co.), 0.5 M LiI (Aldrich Co.), 0.05 M I<sub>2</sub> (Aldrich Co.), and 0.5 M 4-TBP (Aldrich Co.) with 3-MPN (Fluka Co.) as a solvent.

#### **4.2.3 Characterization of Nanoporous TiO<sub>2</sub> Electrode for Dye-Sensitized Solar Cell**

The crystallinity of the synthesized nanoporous TiO<sub>2</sub> was characterized by high resolution transmission electron microscope (HR-TEM; F20, Techai Co.) and an X-ray diffractometer (XRD; D/MAX-1200, Rigaku Co.) using a Cu  $k\alpha$  X-ray and Ni filter at 40 kV and 40 mA. The nanoporous TiO<sub>2</sub> electrode thickness and surface morphology were measured by field-emission scanning electron microscope (FE-SEM; S-4700, Hitachi Co.). The morphology of the nanoporous TiO<sub>2</sub> electrode was also examined in an atomic force microscope (AFM; CP-2, Veeco Co.) in the non-contact model. Nitrogen adsorption and desorption isotherms on nanoporous TiO<sub>2</sub> were measured at 77.15 K using an automatic analyzer (BET; ASAP 2010, Micromeritics Co.). Before the measurements, the samples were out gassed for 2 h in the degas port of the adsorption apparatus. The measurement of the adsorption-desorption isotherms required 1 day. The BET surface areas were determined from the adsorption of isotherms of nitrogen. In addition, the pore size distributions were also calculated by the density functional theory (DFT) method. The Adsorption equilibrium experiments were carried out by contacting a given amount of nanoporous TiO<sub>2</sub> electrode with 0.01-0.3 mM N719 dye solution in a shaking incubator at 333.15 K. The adsorption capacity ( $q$ ) of nanoporous TiO<sub>2</sub> electrode was measured by completely desorbing the adsorbed dye molecules from MK-TiO<sub>2</sub>, MS-TiO<sub>2</sub> and MU-TiO<sub>2</sub> electrode using 0.1 M NaOH solution/ethanol solution (50/50% [V/V]).

The resulting concentration was analyzed by UV/Vis spectrophotometer (UV-160A, Shimadzu Co.) at 528 nm. The fourier transform infrared spectrophotometer (FT-IR; DA-8, Bomem Co.) was used for the analysis of the bonding structure between dye molecules and nanoporous TiO<sub>2</sub> surface. The current-voltage ( $I$ - $V$ ) curves were measured using a source measure unit under irradiation of white light from a 1,000 W Xenon lamp (Solar simulation system; Thermo oriel instruments Co.). The incident light intensity and the active cell area were 100 mW/cm<sup>2</sup> and 0.25 cm<sup>2</sup>, respectively. The  $I$ - $V$  curves were used to calculate the short-circuit current ( $I_{sc}$ ), open-circuit voltage ( $V_{oc}$ ), fill factor ( $FF$ ), and overall conversion efficiency ( $\eta_{eff}$ ) of DSSC.

## 4.3 Results and Discussion

### 4.3.1 Characterization of Nanoporous TiO<sub>2</sub> Particles

The synthesized nanoporous TiO<sub>2</sub> materials (MK-TiO<sub>2</sub>, MS-TiO<sub>2</sub>, and MU-TiO<sub>2</sub>) were characterized by BET, TEM, and XRD analysis. It was confirmed that highly ordered TiO<sub>2</sub> materials with crystalline frameworks are successfully synthesized via the nano casting route from various mesoporous silica templates. **Figure 4.7** shows X-ray diffraction patterns for nanoporous TiO<sub>2</sub> particles from the KIT-6, SBA-15, MSU-H template. The well developed mesopore structure of TiO<sub>2</sub> was observed in small angle XRD patterns (inside figures). The nanoporous TiO<sub>2</sub> materials obtained from SBA-15 (**Figure 4.7b**) and MSU-H (**Figure 4.7c**) show one intense peak and two relatively weak peaks, which are characteristic of 2-D hexagonal ( $P6mm$ ) structure. The well resolved three peaks of ( $d_{211}$ ), ( $d_{220}$ ) and ( $d_{332}$ ) were observed, indicating the bicontinuous cubic  $Ia3d$  symmetry of KIT-6 (**Figure 4.7a**). The framework structures of nanoporous TiO<sub>2</sub> materials are highly crystalline with mainly anatase phases ( $d_{101}$ ,  $d_{004}$ ,  $d_{200}$ ,  $d_{105}$ , and  $d_{211}$ ) from wide angle XRD patterns (outside figures). The crystalline sizes of nanoporous TiO<sub>2</sub> frameworks were estimated to about 11 nm by using Scherrer's equation (**Eq. 3.2**).

**Figure 4.8** and **Figure 4.9** shows electron diffraction image and HR-TEM image of nanoporous TiO<sub>2</sub> particles respectively. The electron diffraction image of nanoporous TiO<sub>2</sub>

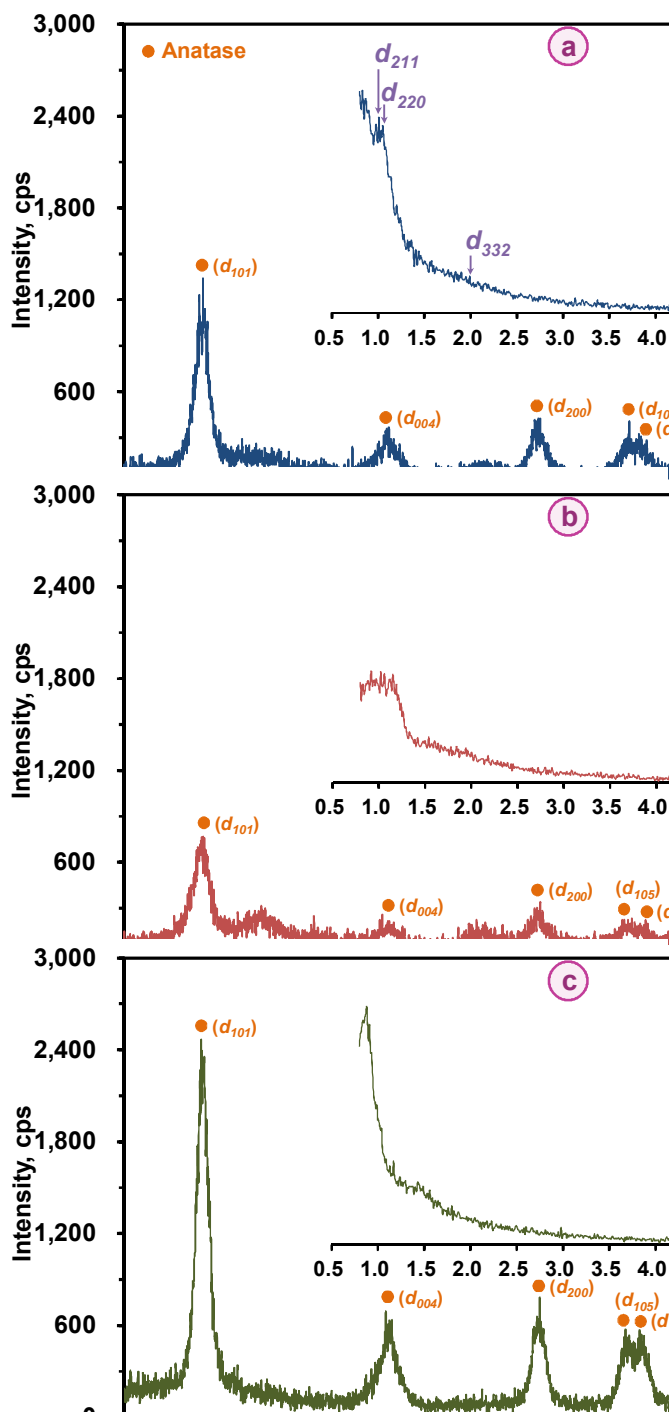


**Figure 4.7.** XRD patterns of nanoporous  $\text{TiO}_2$  particle: (a) MK- $\text{TiO}_2$ , (b) MS- $\text{TiO}_2$ , (c) MU- $\text{TiO}_2$ .

clear displays the Debye-Scherrer rings of anatase crystalline structure. The lattice fringes corresponding to the ( $d_{101}$ ,  $d_{004}$ , and  $d_{200}$ ) plane of anatase crystalline can be seen in the HR-TEM images. Compared to the P25-TiO<sub>2</sub>, the nanoporous TiO<sub>2</sub> synthesized via nano casting using various kinds of mesoporous silicas as the structure directing templates consists mainly of anatase phases as observed in the HR-TEM and XRD patterns.

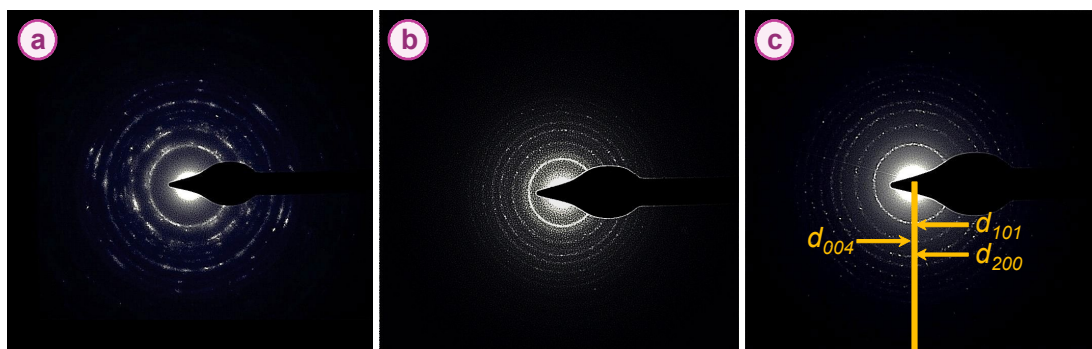


**Figure 4.8.** Electron diffraction image of nanoporous TiO<sub>2</sub> particle: (a) MK-TiO<sub>2</sub> (b) MS-TiO<sub>2</sub> (c) MU-TiO<sub>2</sub>.

The ordered meso structure was observed from the HR-TEM image of nanoporous TiO<sub>2</sub> in **Figure 4.9**. The anatase crystalline size prepared from KIT-6, SBA-15, and MSU-H was about 11 nm. The morphology and the mesopore structure of the synthesized nanoporous TiO<sub>2</sub> particles resemble the templates of KIT-6, SBA-15, and MSU-H.

**Table 4.2.** Textural properties of nanoporous TiO<sub>2</sub> replicas obtained from mesoporous silica

	$S_{BET}^a$ , m <sup>2</sup> /g	$V_t^b$ , cm <sup>3</sup> /g	$V_{DFT}^c$			APD <sup>d</sup> , nm	Particle size, $\mu$ m
			$V_{<2nm}$	$V_{<2-4nm}$	$V_{>4nm}$		
<b>MK-TiO<sub>2</sub></b>	388	0.488	0.118	0.074	0.105	0.4	unknown
<b>MS-TiO<sub>2</sub></b>	256	0.301	0.050	0.082	0.085	2.9	0.5-1.0
<b>MU-TiO<sub>2</sub></b>	160	0.444	0.024	0.042	0.116	4.8	0.2-0.3

<sup>a</sup>Specific BET surface area ( $P/P_0=0.1-0.2$ ), <sup>b</sup>Total pore volume at  $P/P_0=0.99$ , <sup>c</sup>DFT pore volume,

<sup>d</sup>Average pore width.

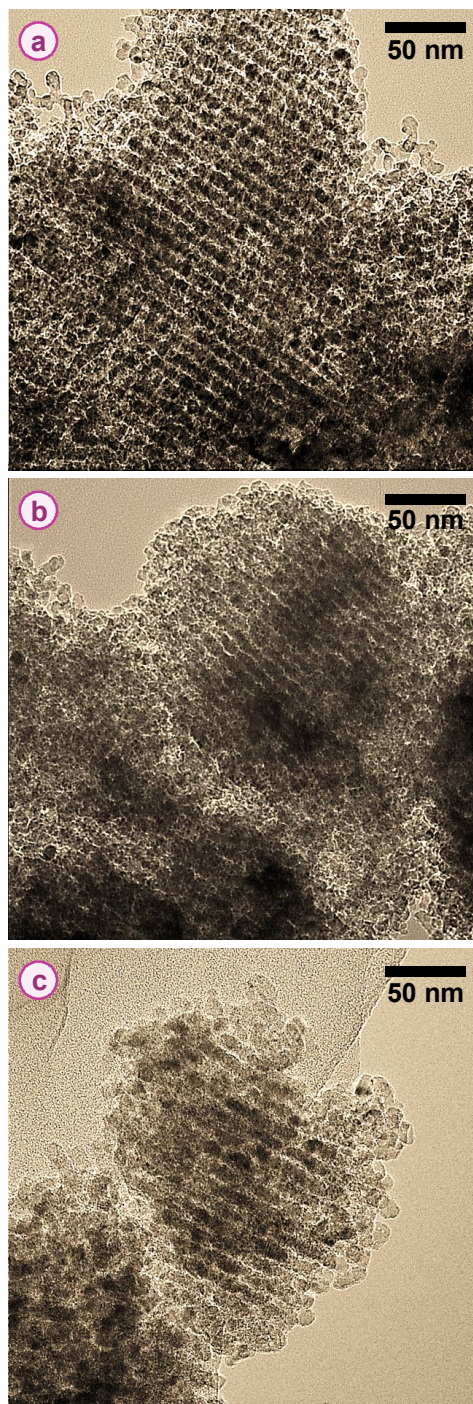


**Figure 4.9.** HR-TEM images of nanoporous  $\text{TiO}_2$  particle: (a) MK- $\text{TiO}_2$ , (b) MS- $\text{TiO}_2$ , (c) MU- $\text{TiO}_2$ .

The average particle size of nanoporous  $\text{TiO}_2$  measured by particle size analyzer (ELS-8000, Otsuka electronics Co.) are summarized in **Table 4.2**. The average particle size of MK- $\text{TiO}_2$  could not be obtained because of the irregular cubic morphology of KIT-6 template. However, the particle size of MS- $\text{TiO}_2$  and MU- $\text{TiO}_2$  were obtained because of the relatively uniform morphology of SBA-15 and MSU-H templates.

**Figure 4.10** shows the nitrogen absorption-desorption isotherms of the nanoporous  $\text{TiO}_2$  particles. The adsorption isotherm corresponds to the type IV isotherms with hysteresis loop according to the IUPAC. Well defined steps in the adsorption-desorption curves appear between the relative pressures,  $P/P_0$ , of 0.4-0.7.

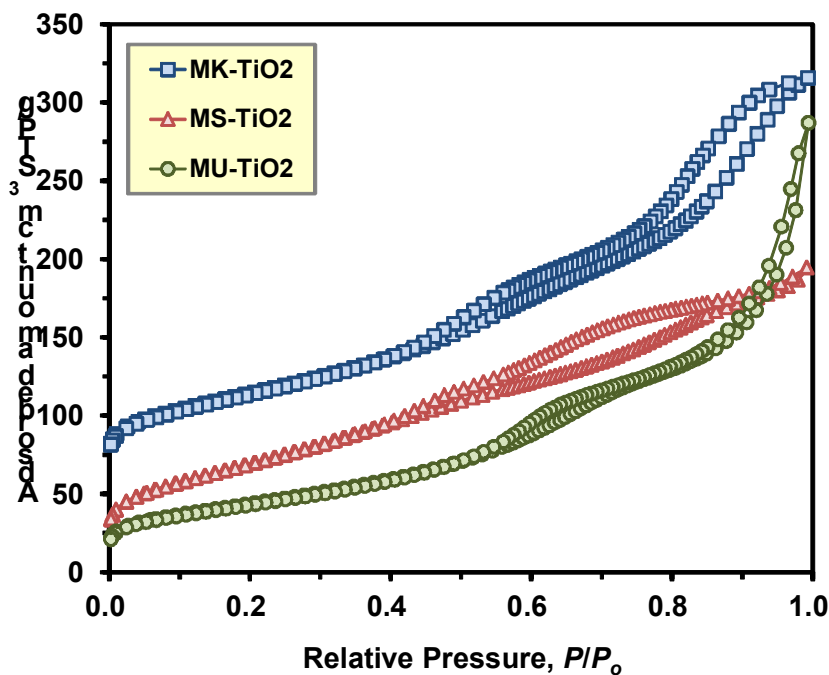


**Figure 4.10.**  $\text{N}_2$  adsorption and desorption isotherms for nanoporous  $\text{TiO}_2$  particles.

The important physical properties of nanoporous  $\text{TiO}_2$  are listed in **Table 4.2**. The BET surface area of MK- $\text{TiO}_2$ , MS- $\text{TiO}_2$ , and MU- $\text{TiO}_2$  are about  $388 \text{ m}^2/\text{g}$ ,  $256 \text{ m}^2/\text{g}$ , and  $160$

$\text{m}^2/\text{g}$ , respectively. In addition, the total pore volume and the average pore size of MK-TiO<sub>2</sub>, MS-TiO<sub>2</sub>, and MU-TiO<sub>2</sub> are in the range of 0.30-0.49  $\text{cm}^3/\text{g}$  and 0.4-4.8 nm when measured by using the DFT method.

**Figure 4.11** shows the pore size distributions of the nanoporous TiO<sub>2</sub> particles. These results indicate that various particle sizes of nanoporous TiO<sub>2</sub> with an ordered structure and high surface area can be successfully synthesized via direct replication route from the hard template.

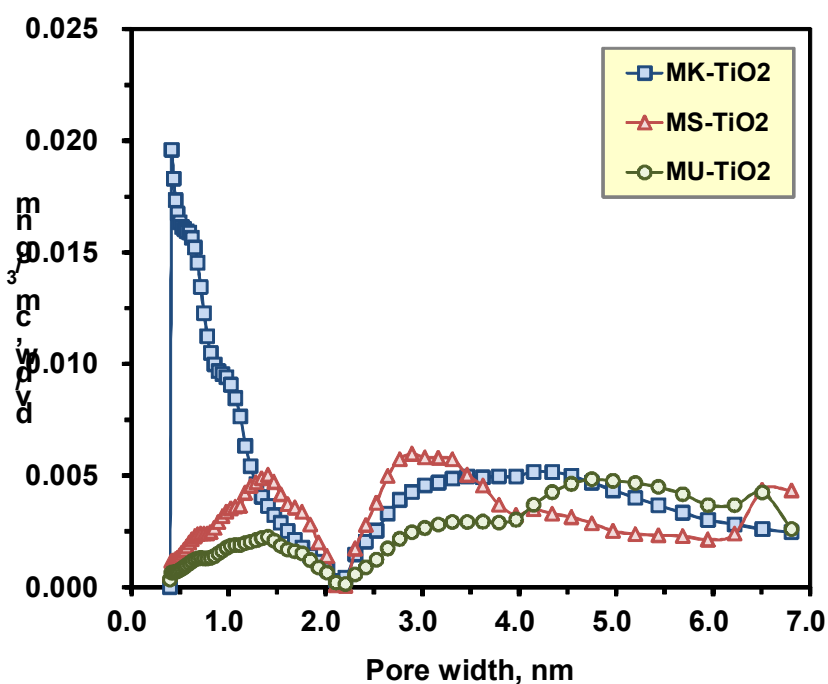


**Figure 4.11.** Pore size distributions of nanoporous TiO<sub>2</sub> particles.

On the other hand, it has been known that the shape and the intensity of the adsorption energy distribution curve are highly related to the physical property (i.e., geometrical heterogeneity) and chemical characteristics (i.e., energetic heterogeneity) of nanocrystalline TiO<sub>2</sub> for DSSC.<sup>61,87</sup> **Figure 4.12** compares the adsorption energy distributions

(AED) of nitrogen on nanoporous  $\text{TiO}_2$  thin films of MK- $\text{TiO}_2$ , MS- $\text{TiO}_2$ , and MU- $\text{TiO}_2$ . To calculate the AED from the low-pressure nitrogen adsorption isotherm data ( $P/P_o < 0.1$ ), the Flower-Guggenheim isotherm was adopted as a kernel function and the generalized nonlinear regularization.<sup>86,87</sup>

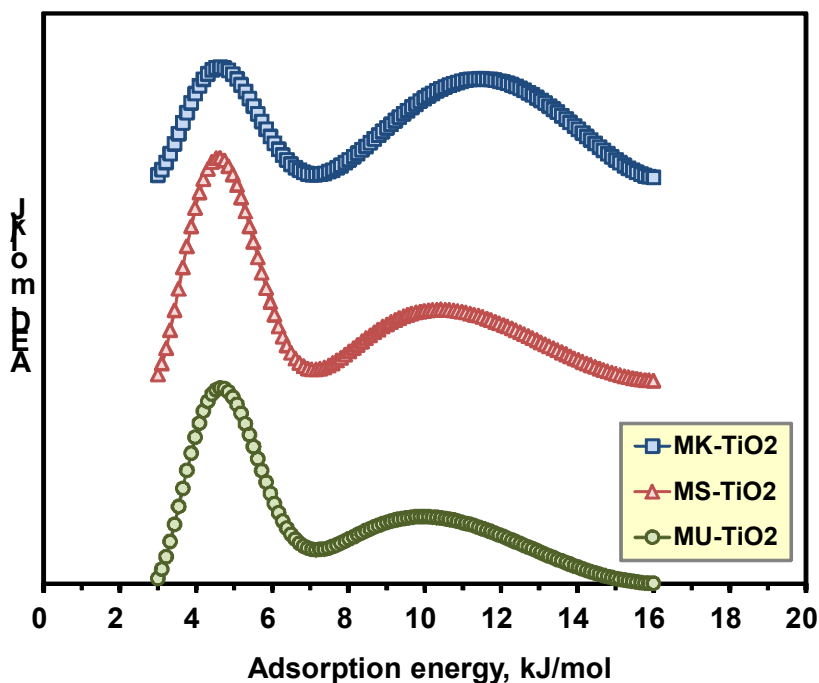


**Figure 4.12.** Adsorption energy distributions of nanoporous  $\text{TiO}_2$  particles.

As shown in **Figure 4.12**, all the AED curves showed two peaks indicating the existence of two energetically different adsorption sites. The first and second adsorption energy curves are distributed mainly in the range of 3-7 and 8-15 kJ/mol, respectively.

#### 4.3.2 Characterization of Nanoporous $\text{TiO}_2$ Electrode

The  $\text{TiO}_2$  thin films using the nanoporous  $\text{TiO}_2$  were prepared for the photo electrode in DSSCs. AFM and FE-SEM were used to examine the surface morphology of the  $\text{TiO}_2$



thin films. **Figure 4.13** shows the FE-SEM images. In case of P25-TiO<sub>2</sub> thin film (**Figure 4.13a**), the primary TiO<sub>2</sub> particles (i.e., anatase crystalline size) is homogenous and the particle size is around 25 nm. The P25-TiO<sub>2</sub> thin film consists of the sponge-like structure.<sup>13,38</sup>

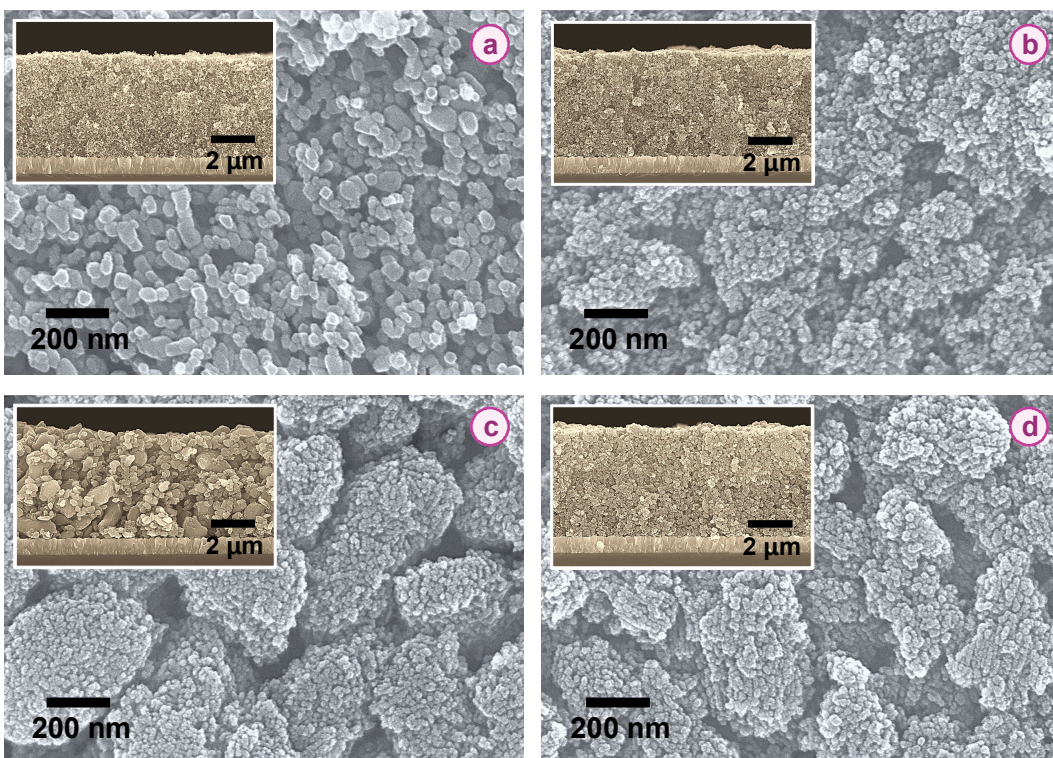


**Figure 4.13.** FE-SEM image of various TiO<sub>2</sub> thin films: (a) P25-TiO<sub>2</sub>, (b) MK-TiO<sub>2</sub>, (c) MS-TiO<sub>2</sub>, (d) MU-TiO<sub>2</sub>.

On the other hand, the primary particles of nanoporous TiO<sub>2</sub> thin film are about 5-10 nm, which correspond to the pore size of the silica template. MS-TiO<sub>2</sub> (**Figure 4.13c**) and MU-TiO<sub>2</sub> thin film (**Figure 4.13d**) have uniform structure with aggregated primary TiO<sub>2</sub> particles because of the nature of the used mesoporous silica templates. However, MK-TiO<sub>2</sub> (**Figure 4.13b**) thin film obtained from the irregular mesoporous template has heterogeneous surface morphology. The aggregated particle size of MK-TiO<sub>2</sub> is all different and this

particle size is still unknown. The spherical  $\text{TiO}_2$  aggregates of more than 200 nm are easily observed on the nanoporous  $\text{TiO}_2$  thin film for light scattering layer. The film thickness of the photoelectrode prepared using the nanoporous  $\text{TiO}_2$  replicas from mesoporous silica templates was approximately in the range of 5 to 6  $\mu\text{m}$  [(figure 4.13 (inlet))].

**Figure 4.14** illustrates the 3-D AFM images of the surface morphology of various  $\text{TiO}_2$  thin film. The surface of the electrode film made using the nanoporous  $\text{TiO}_2$  obtained the mesoporous template showed a rough surface compared with that of the P25- $\text{TiO}_2$  electrode. The surface of nanoporous  $\text{TiO}_2$  have heterogeneous surface with a few separated islands. The MK- $\text{TiO}_2$  films showed the highest surface roughness. In this works, the AFM images are equally observed in the FE-SEM images. The values of surface roughness are summarized in **Table 4.3**.

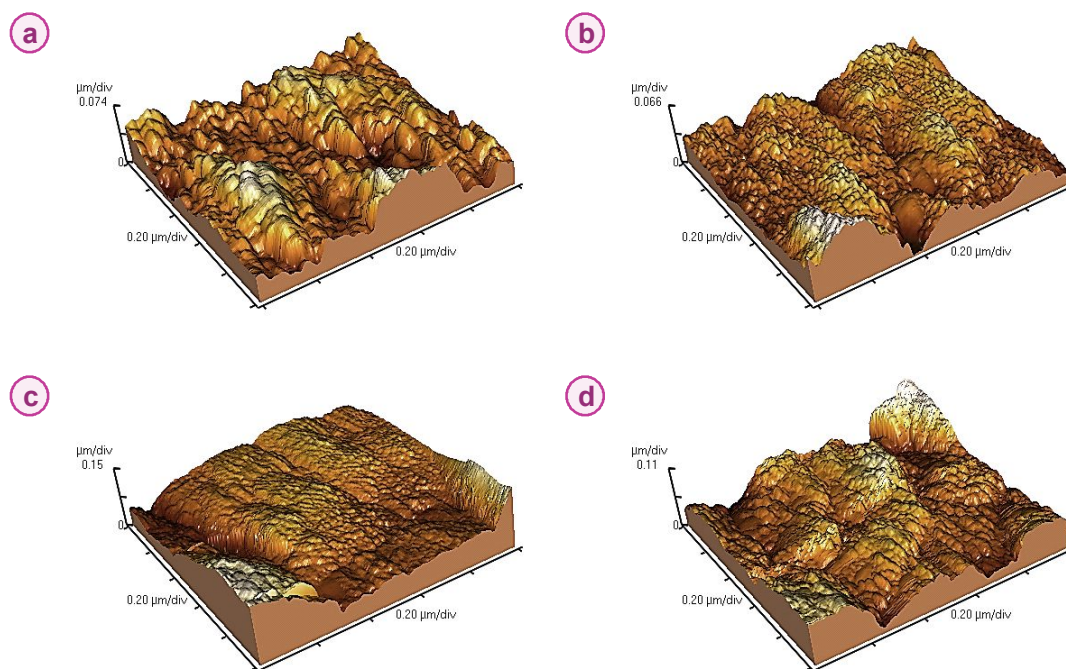


**Figure 4.14.** AFM image analysis of (a) P25- $\text{TiO}_2$ , (b) MK- $\text{TiO}_2$ , (c) MS- $\text{TiO}_2$ , (d) MU- $\text{TiO}_2$  film.

The amount of dye adsorbed is strongly related to the surface area and roughness of

the nanostructure TiO<sub>2</sub> electrode. If the TiO<sub>2</sub> electrode has a higher surface area and roughness, the amount of N719 dye adsorbed is drastically increased.<sup>1</sup>

**Table 4.3.** Surface characteristics of various TiO<sub>2</sub> films

Properties	Unit	P25-TiO <sub>2</sub> film	MK-TiO <sub>2</sub> film	MS-TiO <sub>2</sub> film	MU-TiO <sub>2</sub> film
Root mean square roughness ( $R_q$ )	nm	25.1	51.7	49.2	31.2
Mean roughness ( $R_a$ )	nm	20.3	40.9	38.2	24.6
Film thickness	$\mu\text{m}$	4.7	4.9	5.1	4.9
Adsorption amount of N719	mol/cm <sup>2</sup>	$4.982 \times 10^{-8}$	$22.459 \times 10^{-8}$	$20.243 \times 10^{-8}$	$25.571 \times 10^{-8}$

The N719 adsorption capacities of nanoporous TiO<sub>2</sub> thin film are over five times higher than P25-TiO<sub>2</sub> film. The surface area and surface roughness of nanoporous TiO<sub>2</sub> film are much larger than P25-TiO<sub>2</sub> film evident from results of BET (**Figure 3.8** and **4.10**) and AFM (**Figure 4.14**) analysis. However, the amount of N719 dye adsorption of the MK-TiO<sub>2</sub> electrode was smaller than that of MU-TiO<sub>2</sub> in spite of the big difference in the surface area between the three nanoporous TiO<sub>2</sub> electrode. Therefore, it is implied that there are other important properties responsible for high adsorption amount of N719 dye on TiO<sub>2</sub> electrode.

#### 4.3.3 Adsorption Properties of N719 on Nanoporous TiO<sub>2</sub> Thin Films

As stated in introduction section, the efficiency of the charge injection process is highly dependent on bonding structure of the dye molecules adsorbed on the semiconductor TiO<sub>2</sub>. In addition, the electron transfer in DSSC is strongly influenced by electrostatic and chemical interactions between TiO<sub>2</sub> surface and the adsorbed dye molecules. The photosensitizing molecule N719 used in this work has two bipyridyl ligands with two carboxyl groups at the 4 and 4' position of the bipyridyl groups. It has been known that the carboxyl groups can coordinate in two different ways with TiO<sub>2</sub> surface by physical adsorption via hydrogen bonding or via chemical bond formation with a unidentate (or

ester-like) linkage, a bidentate (or chelating) linkage, or a bridging linkage (see **Figure 4.1**). Recently, Leon et al.<sup>89,180</sup> suggested that coordination of the adsorption of Ru-bpy dyes on TiO<sub>2</sub> films occurs via bidentate or bridging linkage. Also, Finnie et al.<sup>90</sup> reported from the vibrational spectroscopic study that the chemical bonding structure of Ru(II) dye molecule is a bidentate chelate or bridging coordination to nanocrystalline TiO<sub>2</sub> surface via two carboxylate groups per dye molecule. In this work, interfacial binding between the dye molecules (N719) and the surface of TiO<sub>2</sub> replicas prepared from mesoporous silica templates (i.e., KIT-6, SBA-15, and MSU-H) was investigated by FT-IR spectra of the dye-anchored TiO<sub>2</sub> films.

**Figure 4.15** shows the FT-IR spectra of N719 adsorbed on nanoporous TiO<sub>2</sub> films (P25-TiO<sub>2</sub>, MK-TiO<sub>2</sub>, MS-TiO<sub>2</sub>, and MU-TiO<sub>2</sub>) compared with the signals of the dye powder.

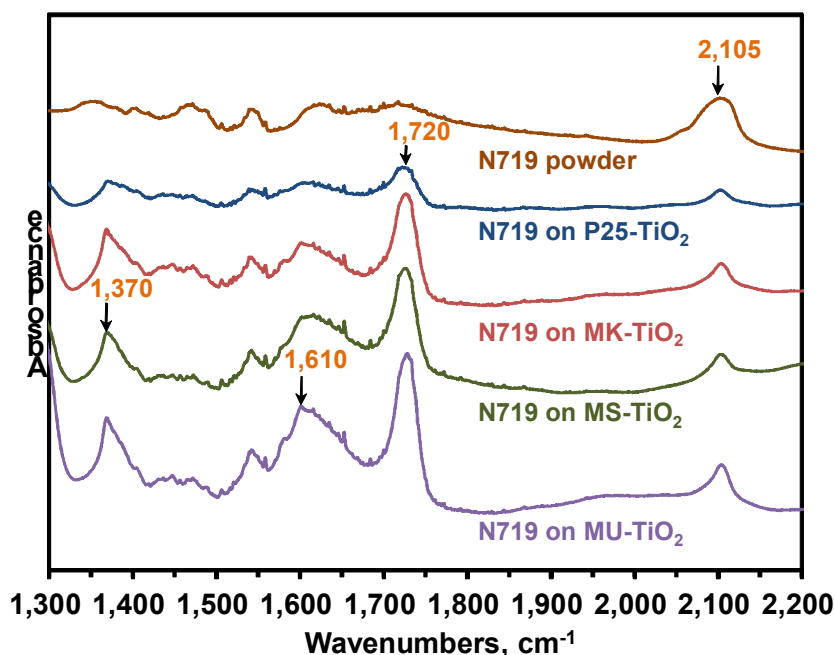


**Figure 4.15.** FT-IR spectra of N719 adsorbed on nanoporous TiO<sub>2</sub> film compared with the signals of the N719 dye powder.

Absorption at  $2,105\text{ cm}^{-1}$  of N719 powder is attributed to the SCN stretch model of N-bonded SCN ligand. When the dye anchored on P25-TiO<sub>2</sub>, MK-TiO<sub>2</sub>, MS-TiO<sub>2</sub>, and MU-TiO<sub>2</sub> films, the IR spectra have absorptions at  $1,370\text{ cm}^{-1}$ ,  $1,610\text{ cm}^{-1}$  and  $1,720\text{ cm}^{-1}$ . The IR spectra located at  $1,370\text{ cm}^{-1}$  (O-C-O symmetric stretch of the carboxyl group) and  $1,610\text{ cm}^{-1}$  (O-C-O asymmetric stretch of the carboxyl group) are consistent with the bidentate or bridging coordination.<sup>180</sup> Compared to the dye-anchored P25-TiO<sub>2</sub>, the dye-anchored nanoporous TiO<sub>2</sub> films have strong absorptions at  $1,720\text{ cm}^{-1}$ , indicating the C=O stretch mode of the protonated carboxylic acid (i.e., ester-like linkage). It can be concluded from this work that the coordination of N719 on TiO<sub>2</sub> films occurs mainly by the contribution of unidentate (i.e., ester-like linkage) and partially by bidentate or bridging linkage.

**Figure 4.16** shows the comparison of N719 adsorption isotherms and the corresponding Langmuir-Freundlich (LF) isotherm model<sup>133</sup> for three different nanoporous TiO<sub>2</sub> thin films.

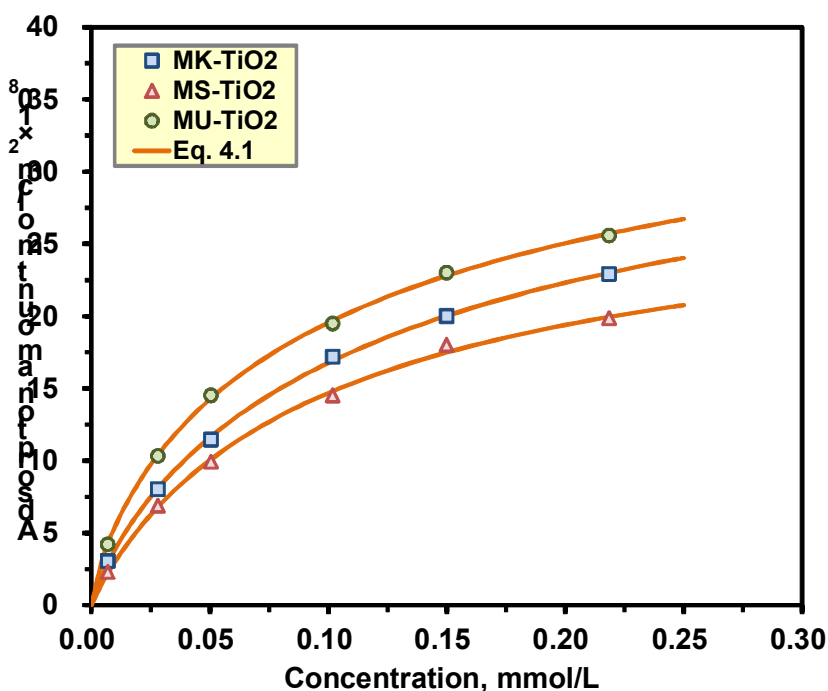


**Figure 4.16.** Adsorption equilibrium amount of N719 on nanoporous TiO<sub>2</sub> films at 333.15 K.

The LF equation and the determined isotherm parameters are listed in **Table 4.4**.

**Table 4.4.** Langmuir-Freundlich isotherm equation (a), adsorption energy distribution function (b), and Langmuir-Freundlich isotherm parameters (c).

(a) Langmuir-Freundlich isotherm equation			
$q = \frac{q_m (bC)^n}{1 + (bC)^n} \quad (\text{Eq. 4.1})$			
<p>where <math>q</math> is the adsorbed amount, <math>q_m</math> is the monolayer adsorption capacity, <math>b</math> (l/mmol) is the equilibrium constant, <math>C</math> is the solute equilibrium concentration and <math>n</math> is the system heterogeneity parameter.</p>			
(b) Adsorption energy distribution function			
$\theta(c) = \frac{n}{n_o} = \int_{E_{\min}}^{E_{\max}} \frac{\Phi_x \exp(E_{12}/RT)}{1 + \Phi_x \exp(E_{12}/RT)} F(E_{12}) dE_{12} \quad (\text{Eq. 4.2})$			
<p>where <math>\theta(c)</math> is the total fraction coverage of solute, <math>\Phi = \Phi(c, \theta)</math> is a model dependent function, <math>E_{12} = E_1 - E_2</math> is the energy difference between the solute and water, <math>F(E_{12})</math> is the energy distribution function, <math>T</math> is the absolute temperature, <math>R</math> is the gas constant; <math>\chi</math> is <math>c/c_{\text{sol}}</math>, where <math>c_{\text{sol}}</math> is the solubility of the solute in water.</p>			
(c) Langmuir-Freundlich isotherm equation parameters			
Parameters	MK-TiO <sub>2</sub>	MS-TiO <sub>2</sub>	MU-TiO <sub>2</sub>
$q_m$	38.4	29.9	41.5
$b$	7.39	9.62	8.61
$n$	0.84	0.94	0.77
$E^a$ , %	0.77	0.49	0.41

<sup>a</sup>Average percent error:  $E(\%) = \frac{100}{n} \sum_{k=1}^n \left[ \frac{|q_{\text{exp},k} - q_{\text{cal},k}|}{q_{\text{exp},k}} \right]$ .

The experimental results clearly show that MU-TiO<sub>2</sub> has a substantially higher adsorption capacity for N719 than that of MS-TiO<sub>2</sub> and MK-TiO<sub>2</sub>. The adsorption amount of N719 on three different nanoporous TiO<sub>2</sub> is in the following sequence: MU-TiO<sub>2</sub> > MK-TiO<sub>2</sub> > MS-TiO<sub>2</sub>. Contrary to our expectations however, there is no clear correlation between the adsorption amounts and the basic textural properties such as the BET surface area, the total pore volume and the average pore width. On the other hand, the molecular diameter of the N719 dye was reported to be about 1.76 nm which was based on the crystallographic data of N3 dye. Recently Chen et al. have also reported that the adsorption amount of organic

dyes [or Ru(II)-based complexes] on  $\text{TiO}_2$  depends on the molecular size of dyes employed.<sup>134</sup> Thus, in this work, to examine the relation between the pore volume and the N719 adsorption amount, the pore volumes were divided into three regions: i) volume of pore width below 2 nm ( $V_{<2 \text{ nm}}$ ), ii) volume of pore width between 2 and 4 nm ( $V_{2-4 \text{ nm}}$ ), and iii) volume of pore width greater than 4 nm ( $V_{>4 \text{ nm}}$ ).

As shown in **Figure 4.17**, a notable relationship was observed between the adsorption capacity of N719 and the volume of pore width greater than 4 nm ( $V_{>4 \text{ nm}}$ ), indicating that the dye adsorption has close connection with the molecular size and the proportion of pores having optimum size.

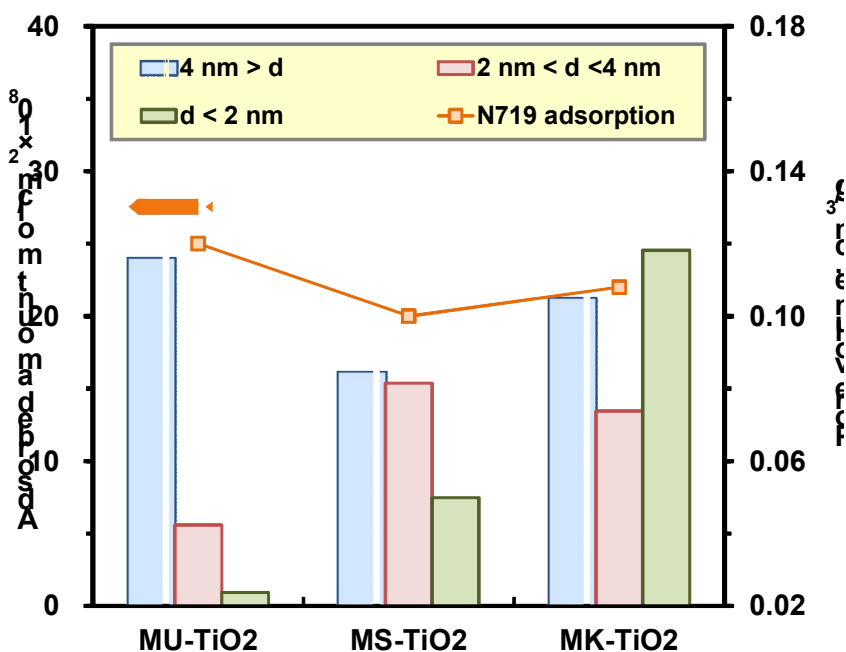


**Figure 4.17.** Pore volumes in comparison with N719 adsorption as a function of nanoporous  $\text{TiO}_2$  films.

In this work, the order of adsorption capacity of N719 was in good agreement with that of  $V_{>4 \text{ nm}}$ . It was found that the desirable pore widths required for achieving the highest N719 adsorption are about 2 times greater than the diameter of N719 molecules (1.76 nm).



Although MU-TiO<sub>2</sub> has the lowest BET surface area, the total pore volume and the largest average pore width, they reveal the highest N719 adsorption because of their largest amount of  $V_{>4 \text{ nm}}$ . Thus it is appropriate to explain that the N719 adsorption capacity is substantially dependent on the proportion of volume of pore width greater than 4 nm. The obtained result reveals that the pore volumes over a diameter of 4 nm may contribute to more adsorption than the micropore volumes below a width of 4 nm.

**Figure 4.18** shows the AEDs for N719 on three different nanoporous TiO<sub>2</sub> films. To calculate the energy distributions, the data below the monolayer coverage were determined from the LF equation and the generalized nonlinear regularization method which sets no assumption on position and shape of the solution (or the energy distribution function) (**Table 4.4**).<sup>64</sup>

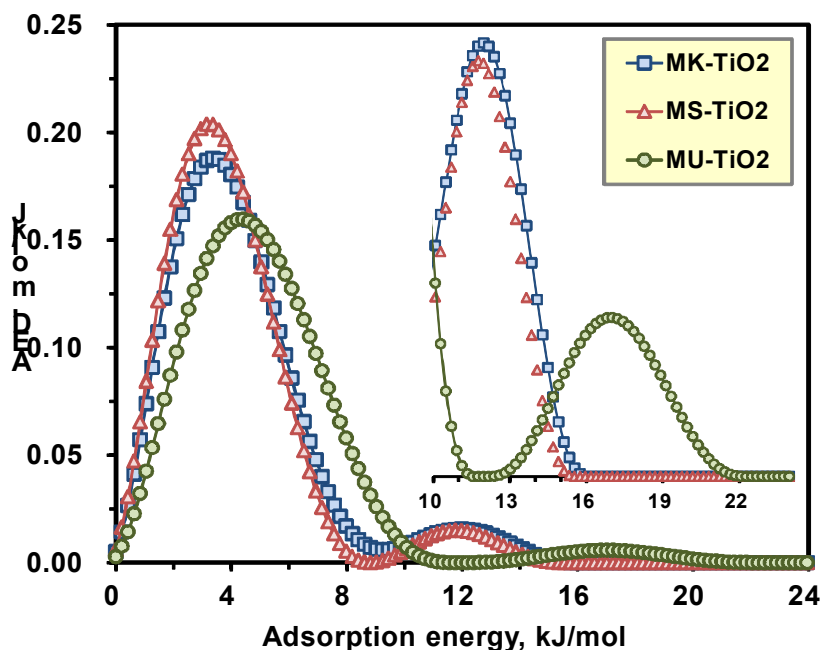


**Figure 4.18.** Adsorption energy distributions of N719 on nanoporous TiO<sub>2</sub> films.

The detailed procedures for determining the AEDs were described elsewhere.<sup>135</sup> As shown in **Figure 4.18**, similar shapes of AEDs were observed. All samples have two distinct AED



peaks, which may indicate that two different types of surface energy for N719 exist mainly on the surface of the adsorbent. In the cases of MK-TiO<sub>2</sub> and MS-TiO<sub>2</sub>, the lower AED peaks are located between 0 and 9.2 kJ/mol with the maximum at about 3.15 (MS-TiO<sub>2</sub>) and 3.36 (MK-TiO<sub>2</sub>) kJ/mol, whereas the higher AED peaks appeared between 9.2 and 16.0 kJ/mol with the maximum at about 11.76 (MS-TiO<sub>2</sub>) and 11.97 (MK-TiO<sub>2</sub>) kJ/mol. In contrast, the AED for the MU-TiO<sub>2</sub> differ slightly from the case of MK-TiO<sub>2</sub> and MS-TiO<sub>2</sub>. The AED peak shape, height, and location of MU-TiO<sub>2</sub> are greatly broader, lower, and shifted toward relatively higher adsorption energy. The main and shoulder (or small) AED curves are in the range of 0-11.6 and 12.4-22.1 kJ/mol, where the pronounced maxima were located at 4.4 and 17.0 kJ/mol, respectively.

To evaluate the photovoltaic performance of nanoporous TiO<sub>2</sub> thin film, photo-current-voltage (*I-V*) curves were measured using a source measure unit under irradiation of white light from a 1,000 W Xenon lamp. The incident light intensity and the active cell area were 100 mW/cm<sup>2</sup> and 0.25 cm<sup>2</sup>, respectively.

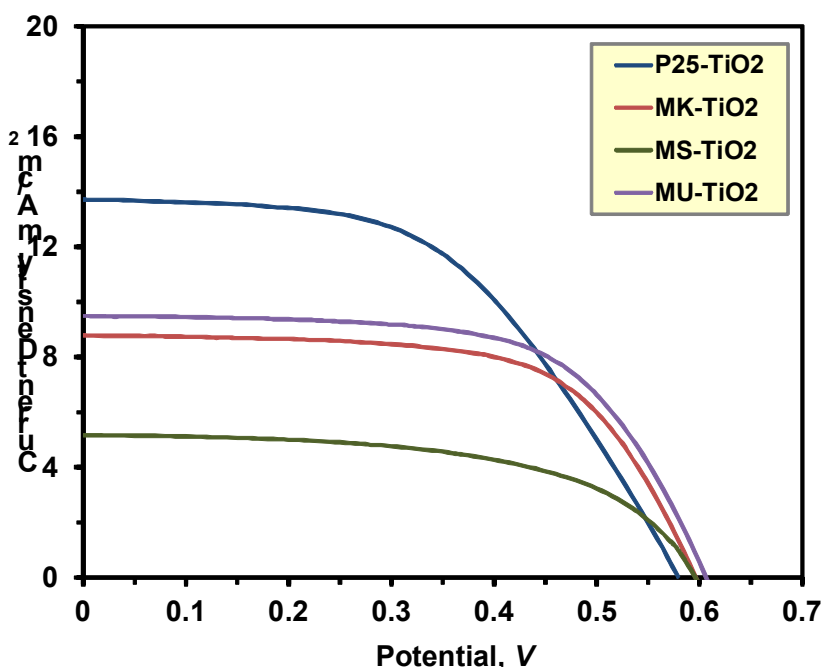


**Figure 4.19.** *I-V* curves of nanoporous TiO<sub>2</sub> films.

**Figure 4.19** shows the photo-current-voltage ( $I$ - $V$ ) curves for nanoporous TiO<sub>2</sub> films and the short-circuit current ( $I_{sc}$ ), open-circuit voltage ( $V_{oc}$ ), fill factor ( $FF$ ), and overall conversion efficiency ( $\eta_{eff}$ ) of DSSC are listed in **Table 4.5**.

**Table 4.5.** Photovoltaic performance of dye-sensitized solar cell using nanoporous TiO<sub>2</sub> films.

	Film thickness, $\mu\text{m}$	$V_{oc}$ , V	$I_{sc}$ , $\text{mA}/\text{cm}^2$	Fill factor, $FF$	$\eta_{eff}$ , %
<b>P25-TiO<sub>2</sub> film</b>	4.7	0.58	13.6	0.53	4.1
<b>MK-TiO<sub>2</sub> film</b>	4.9	0.59	8.8	0.64	3.3
<b>MS-TiO<sub>2</sub> film</b>	5.1	0.59	5.2	0.57	1.7
<b>MU-TiO<sub>2</sub> film</b>	4.9	0.60	9.5	0.64	3.6

Contrary to our expectation, the conversion efficiencies of nanoporous TiO<sub>2</sub> (MK-TiO<sub>2</sub>, MS-TiO<sub>2</sub>, and MU-TiO<sub>2</sub>) were lower than the commercial TiO<sub>2</sub> (P25-TiO<sub>2</sub>) film although they have an extremely high surface area and uniform nanochannels. The result is attributed to the restriction of electron transport in MK-TiO<sub>2</sub>, MS-TiO<sub>2</sub>, and MU-TiO<sub>2</sub> mainly because of the electron recombination and the electron loss, which is related to the dispersion property of nanoporous materials. It was found that the chemical dispersion of P25-TiO<sub>2</sub> was better than that of the synthesized nanoporous TiO<sub>2</sub> materials. Thus, search for appropriate conditions will be continued for the modification of MK-TiO<sub>2</sub>, MS-TiO<sub>2</sub>, and MU-TiO<sub>2</sub> to increase the dispersion property. On the other hand, it was observed that the overall conversion efficiency ( $\eta_{eff}$ ) was in the following order: MU-TiO<sub>2</sub> film (3.6%) > MK-TiO<sub>2</sub> film (3.3%) > MS-TiO<sub>2</sub> film (1.7%). This trend is identical to that of the N719 adsorption on nanoporous TiO<sub>2</sub>. Therefore, it is reasonable to conclude that the overall photovoltaic performance was substantially dependent on the adsorption amount of N719.

#### 4.3.4 Improvement of Photovoltaic Performance for Dye-Sensitized Solar Cell

As previously stated, it was found that the high surface area and the uniform structure

of nanoporous  $\text{TiO}_2$  did not help the enhancement of the overall conversion efficiency. Especially, the surface area of  $\text{TiO}_2$  electrode was independent of the current density in DSSC. This result may come from the fact that the diffusion in photoelectron transfer on nanoporous  $\text{TiO}_2$  semiconductor is restricted. In this work, it was attempted to fabricate a dual functional nanoporous  $\text{TiO}_2$  which has a high adsorption amount of dye by the high surface area and a light scattering effect by its particle size of more than 200 nm spheres.<sup>186-188</sup> For high efficiency DSSC are prepared by the multi-layer (or light scattering layer) coating of nanoporous  $\text{TiO}_2$  particles on P25- $\text{TiO}_2$  electrode.

**Figure 4.20** shows FE-SEM image of cross-section in multi-layer coating films,<sup>136,137</sup> showing no crack and some gap. The P25- $\text{TiO}_2$  film is a mono layer and various nanoporous film are multi layer. The thickness of mono layer films is ca. 8  $\mu\text{m}$  and that of multi-layer film is ca. 9  $\mu\text{m}$ .

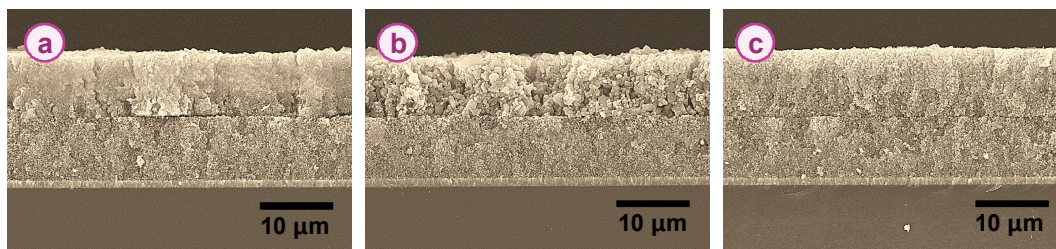


**Figure 4.20.** FE-SEM image for multi-layer coating: (a) P25- $\text{TiO}_2$ /MK- $\text{TiO}_2$ , (b) P25- $\text{TiO}_2$ /MS- $\text{TiO}_2$ , (c) P25- $\text{TiO}_2$ /MU- $\text{TiO}_2$ .

Moreover, the aggregated particle size in P25- $\text{TiO}_2$  film is around 25 nm (**Figure 3.6**) and that in the nanoporous  $\text{TiO}_2$  films are more than 200 nm (**Figure 4.13**). Especially, In P25- $\text{TiO}_2$ /MU- $\text{TiO}_2$  films (**Figure 4.20c**), there was no gap between each layer because the shape of aggregated P25- $\text{TiO}_2$  particles and aggregated MU- $\text{TiO}_2$  particles were similar.

The multi layer coatings of nanoporous  $\text{TiO}_2$  were also used for the fabrication of DSSC. **Figure 4.21** shows current-voltage characteristics of DSSC for multi-layer coating of P25- $\text{TiO}_2$ /nanoporous  $\text{TiO}_2$  electrode. The representative photoelectric values ( $V_{oc}$ ,  $I_{sc}$ ,  $FF$ , and  $\eta_{eff}$ ) are also listed in **Table 4.6**. From the results of photovoltaic performance, it was

confirmed that the multi-layer coating is very useful method for the highly efficient DSSC. Surprisingly, the energy conversion efficiency of multi-layer coated nanoporous  $\text{TiO}_2$  samples on P25- $\text{TiO}_2$  (i.e., P25- $\text{TiO}_2$ /MK- $\text{TiO}_2$ , P25- $\text{TiO}_2$ /MS- $\text{TiO}_2$ , and P25- $\text{TiO}_2$ /MU- $\text{TiO}_2$ ) ended up to be 0.9-1.1 times higher than that of the P25- $\text{TiO}_2$ /P25- $\text{TiO}_2$  film (Table 4.6).

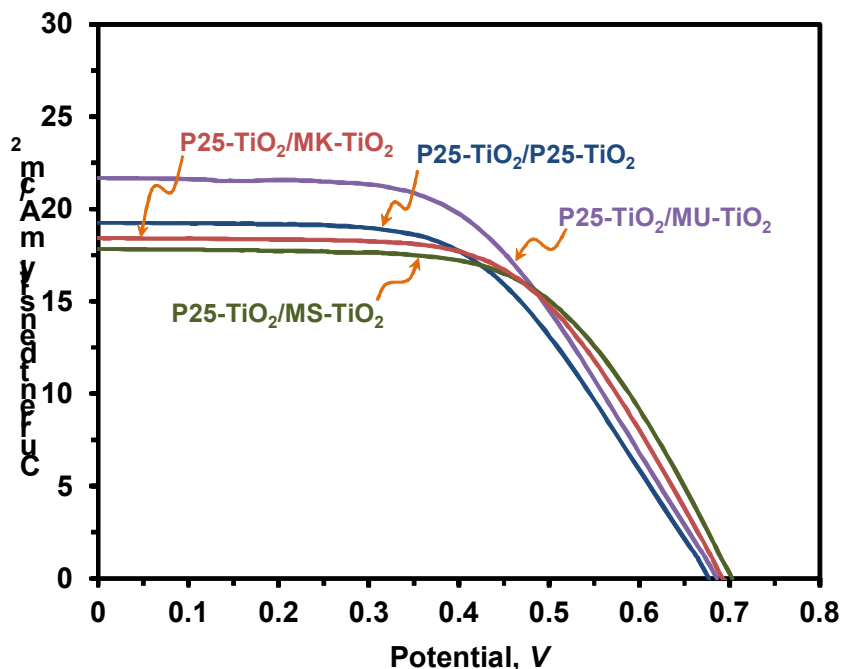


**Figure 4.21.** *I-V* curves of nanoporous  $\text{TiO}_2$  films by using multi-layer coating.

Although nanoporous  $\text{TiO}_2$  films by the multi-layer coating method used in this work overcome the problem of photoelectron transfer in DSSC, it should be noted that nanoporous  $\text{TiO}_2$  films are not transparent because of the larger  $\text{TiO}_2$  particle size. For the industrial application, more fine  $\text{TiO}_2$  particles with high transparency are needed to achieve the high energy conversion efficiency in DSSCs. If mono-dispersed nanosize and mesoporous silica template are obtained, it is possible to get nanoporous  $\text{TiO}_2$  particle.

**Table 4.6.** Photovoltaic performance for various TiO<sub>2</sub> electrode of dye-sensitized solar cell with multi-layer coating.

	Film thickness, $\mu\text{m}$	$V_{oc}$ , V	$I_{sc}$ , $\text{mA}/\text{cm}^2$	Fill factor, $FF$	$\eta_{eff}$ , %
<b>P25-TiO<sub>2</sub>/P25-TiO<sub>2</sub> film</b>	17.2	0.68	19.3	0.55	7.2
<b>P25-TiO<sub>2</sub>/MK-TiO<sub>2</sub> film</b>	17.1	0.69	18.7	0.60	7.7
<b>P25-TiO<sub>2</sub>/MS-TiO<sub>2</sub> film</b>	17.0	0.70	17.8	0.61	7.6
<b>P25-TiO<sub>2</sub>/MU-TiO<sub>2</sub> film</b>	17.1	0.69	21.7	0.54	8.0

#### 4.4 Summary

A novel nanoporous TiO<sub>2</sub> (MK-TiO<sub>2</sub>, MS-TiO<sub>2</sub>, and MU-TiO<sub>2</sub>) particles were successfully synthesized by the nano casting method using the mesoporous templates including KIT-6 (bicontinuous cubic,  $Ia3d$ ), SBA-15 (2-D hexagonal,  $P6mm$ ) and MSU-H (2-D hexagonal,  $P6mm$ ) and used as the electrode for DSSC. The nanoporous TiO<sub>2</sub> electrode were prepared and characterized by AED, AFM, BET, FE-SEM, FT-IR, HR-TEM and XRD for DSSC. Unlike the commercial P25-TiO<sub>2</sub>, MK-TiO<sub>2</sub>, MS-TiO<sub>2</sub>, and MU-TiO<sub>2</sub> electrode consist mainly of anatase phase. It was found that the nanoporous TiO<sub>2</sub> particles have high surface area and ordered pore network. The adsorption bonding structure of N719 on nanoporous TiO<sub>2</sub> films is caused by unidentate and bidentate linkage. The photovoltaic performance of nanoporous TiO<sub>2</sub> electrodes were evaluated from the overall conversion efficiency ( $\eta_{eff}$ ), fill factor ( $FF$ ), open-circuit voltage ( $V_{oc}$ ) and short-circuit current ( $I_{sc}$ ) from the  $I$ - $V$  curves measured. The overall conversion efficiency ( $\eta_{eff}$ ) was in the following order: MU-TiO<sub>2</sub> film (3.6%) > MK-TiO<sub>2</sub> film (3.3%) > MS-TiO<sub>2</sub> film (1.7%). The results of adsorption properties obtained in this work can be concluded that the photoelectric performance is strongly dependent on the adsorption amount of dye molecules and the pore size distributions of MK-TiO<sub>2</sub>, MS-TiO<sub>2</sub>, and MU-TiO<sub>2</sub>. Contrary to expectation, the photovoltaic conversion efficiencies of nanoporous TiO<sub>2</sub> electrode compared to P-25 were low although they showed the higher dye adsorption capacities. The result implies that the excessively generated electron could be acting as a resistance of the

electron diffusion and many recombination could occur. For overcoming these problems, nanoporous  $\text{TiO}_2$  thin film was fabricated by multi-layer method. It was found that the multi-layer electrode gave higher efficiency in DSSC because of nanoporous  $\text{TiO}_2$  has the light scattering effect. In addition, the energy conversion efficiency of multi-layer coated nanoporous  $\text{TiO}_2$  samples on P25- $\text{TiO}_2$  (i.e., P25- $\text{TiO}_2$ /MK- $\text{TiO}_2$ , P25- $\text{TiO}_2$ /MS- $\text{TiO}_2$ , and P25- $\text{TiO}_2$ /MU- $\text{TiO}_2$ ) ended up to be 0.9-1.1 times higher than that of the P25- $\text{TiO}_2$ /P25- $\text{TiO}_2$  film.

## Chapter 5. Enhanced Photovoltaic Properties of TiO<sub>2</sub> Electrode Prepared by Polycondensation in Sol Reaction

### 5.1 Introduction

Currently, the researches is being conducted only on materials such as TiO<sub>2</sub> with high specific area, highly ordered morphology and porosity, highly efficient dye molecules and various counter electrodes. Research on the electrolytes is also focused on the development of high efficiency solid materials.<sup>138,139</sup> However, very little work is being done on structure of DSSC. For photovoltaic cells in DSSC, ruthenium (II) complexes containing polypyridyl ligands dye adsorbed on TiO<sub>2</sub> porous film is excited by visible light. It has been reported that the efficiency of the electron injection process to the conduction band of TiO<sub>2</sub> is highly dependent on structural properties of the semiconductor TiO<sub>2</sub> film.<sup>140</sup> In addition, the electron transfer in DSSC is strongly influenced by physical and chemical properties of TiO<sub>2</sub>.<sup>141</sup> For this reason, nanosized TiO<sub>2</sub> particles have received great attention for use as a photo electrode in DSSC systems. To develop a porous geometry, the TiO<sub>2</sub> photo electrode having nanosized TiO<sub>2</sub> colloids are generally sintered on a transparent conducting substrate.<sup>61,142</sup> Various preparation methods such as soft chemistry, hydrothermal, and the sol-gel process have been suggested for nanosized TiO<sub>2</sub> colloids.<sup>143-145</sup> It has been also reported that the sol-gel process has many advantages for the fabrication of thin film in DSSC. The function of nanocrystalline TiO<sub>2</sub> thin films fabricated from TiO<sub>2</sub> colloidal sol has been found to be strongly dependent on the sol preparation process. Such synthetic procedures have been shown to control a wide range of material properties of the resulting films, including particle size and crystallographic phase, film porosity, surface structure, film roughness, electron transport properties, and optical light scattering.<sup>20</sup> Recently, the synthesis of TiO<sub>2</sub> colloidal paste for making of photo electrode in DSSC attracted much attention from all over the world.<sup>146</sup> However, there is no report on the systematic controls of microstructured TiO<sub>2</sub> thin film to induce a high efficiency in DSSC. Moreover, systematic studies on the influence of the adsorption properties between N719 molecules

and TiO<sub>2</sub> surface on the energy conversion efficiency of DSSC are very limited.<sup>66</sup>

Therefore, this work systematically examined the relationship between the photovoltaic performance and the morphological characteristics of TiO<sub>2</sub> nanoparticles. TiO<sub>2</sub> electrode with different textural and crystalline structures were fabricated using TiO<sub>2</sub> colloidal sol prepared from titanium-tetraisopropoxide used as a starting material by applying the sol-gel method under different aging conditions.<sup>147</sup> The adsorption properties of N719 dye on TiO<sub>2</sub> electrode were investigated by adsorption equilibrium isotherm, isosteric enthalpies of dye adsorption,<sup>81</sup> and adsorption energy distributions.<sup>81,82,84</sup> It was found that the aging process among the sol preparation steps is the most important step in controlling the physical, chemical properties of TiO<sub>2</sub> electrode on photo electrode of DSSC.

### 5.1.1 Sol-Gel Process for Synthesis of TiO<sub>2</sub>

TiO<sub>2</sub> has been widely used as gas sensors,<sup>148</sup> photocatalyst,<sup>149</sup> biomembrane,<sup>150</sup> hydrothermal catalyst,<sup>151</sup> pigment,<sup>152</sup> environmental process<sup>153</sup> and dye-sensitized solar cells.<sup>154,155</sup> The physical and chemical characteristics of TiO<sub>2</sub> can be controlled by its particle size, morphology, and crystalline phase. Nanosized TiO<sub>2</sub> (< 100 nm) has attracted substantial interests due to their unusual optical<sup>156</sup>, electrical<sup>157</sup>, and catalytic properties. In this chapter, the ultrafine TiO<sub>2</sub> particles for TiO<sub>2</sub> electrode in DSSC were synthesized and characterized. TiO<sub>2</sub> can be synthesized by several different methods: i) inert gas condensation,<sup>158</sup> ii) flame spray pyrolysis,<sup>159</sup> iii) hydrothermal,<sup>160</sup> and vi) sol-gel.<sup>161</sup>

In this work, the sol-gel method was used. Sols are defined as the colloidal particles dispersed in a liquid.<sup>162</sup> In general, colloid means solid particles with diameter of 1-100 nm. A gel is defined as interconnected, rigid network particles with pores of submicrometer dimension and exists in polymeric chains. The sol-gel process has successfully applied for the preparation of ceramic powders, monolith, thin films, and fibers. **Figure 5.1** shows the typically sol-gel process. The sol-gel process has several advantages listed below:

- |                                       |  |
|---------------------------------------|--|
| i) Particle growth in molecular level | ii) Homogeneous product with high purity |
| iii) High surface area                | vi) Low chemical reaction temperature    |

This method is a procedure for the preparation of oxide particles usually from



homogeneous solutions of alkoxides in organic media through their hydrolysis with as a solute, although it was originally developed for the preparation of a gel from a obtained sol. The products of this method are normally amorphous spheres.<sup>163</sup> However, sol-gel processing provides good chemical homogeneity and the possibility of deriving unique metastable structures at low reaction temperatures. Typically, sol-gel method requires further heat treatment to induce crystallization of amorphous precipitates. The calcination process frequently gives rise to particle agglomeration and grain growth and may phase transformation. Hydrothermal treatment represents an alternative to calcinations for promoting crystallization under milder temperatures.<sup>164</sup>

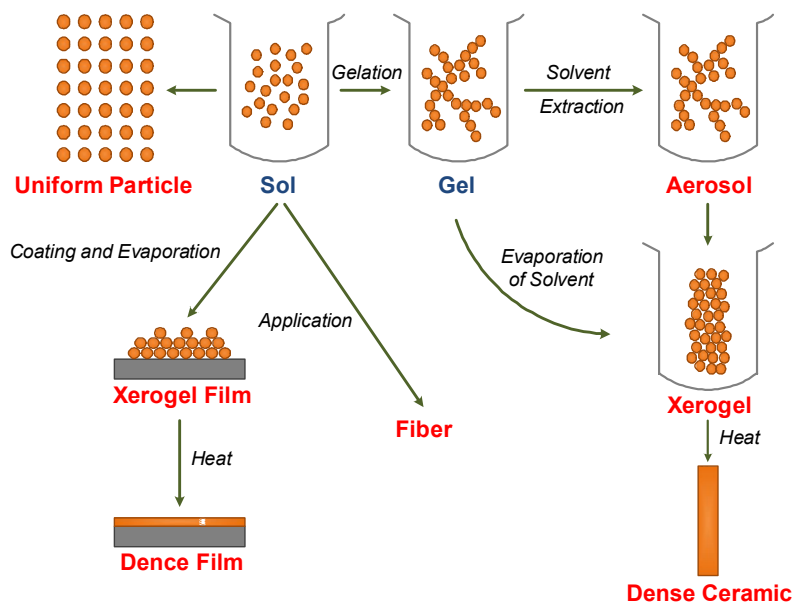
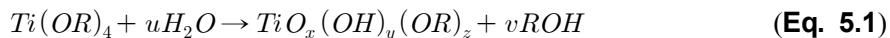


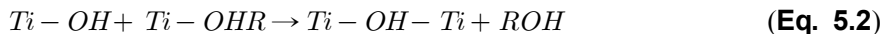
**Figure 5.1.** Typical sol-gel process.

Sol-gel chemistry is based on the hydrolysis and polycondensation of metal alkoxides. During hydrolysis and polymerization, the reaction precipitates the hydrous  $\text{TiO}_2$  alkoxide groups ( $\text{RO-}$ ), bridging oxygens and probably a small amount of water as shown in **Equation 5.1**.

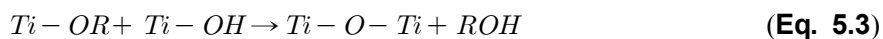


After hydroxy groups (-OH) are generated, propagation occurs through a polycondensation process. Two complete mechanisms have been considered and are shown in **Equation 5.2** and **5.3** respectively.

i ) Formation of hydroxy bridges through the elimination of solvent molecules via olation



ii) Formation of oxygen bridging through the elimination of H<sub>2</sub>O or ROH via oxolation.



Where, R is alkyl group (C<sub>n</sub>H<sub>2n+1</sub>-). These reactions can be involved in the transformation of a metal alkoxide into an oxide network. The structure and morphology of the resulting network strongly depend on the relative contributions of each of them. In sol-gel method, type of metal alkoxide, amount of water, type of peptizing agent, acid to alkoxide ratio are found to be the main parameters that affects the physical properties of TiO<sub>2</sub> powders. The above mentioned parameters are usually varied according to the experimental scheme for preparation of TiO<sub>2</sub> powders. Suh et al.<sup>165</sup> studied the effect of aging conditions on the pore structural properties of TiO<sub>2</sub> aerogels. Aging conditions had no significant effect on the surface area of the calcined product. On the contrary, the pore volume and pore size were shown to increase with the extent of aging time.

The sol-gel processing of TiO<sub>2</sub> is usually performed by the hydrolysis and polycondensation of titanium alkoxide in the presence of an acid catalyst. The acid catalyst plays a very important role in the sol-gel process. The uncharged precipitates in the sol-gel reaction are peptized by adding the acid catalyst. They become positively charged through proton adsorption. The charged particles repel each other, thus developing stable sols. In generally, HCl, HNO<sub>3</sub> and CH<sub>3</sub>COOH have been widely used as acid catalysts.

TiO<sub>2</sub> could be used as a catalyst or dye-sensitized solar cell electrode in the form of powder or film at high temperature of over 773.15 K. Physical properties of TiO<sub>2</sub> such as surface area and pore size could be detrimentally changed at high temperature because of

phase transformation. Therefore, it is essential to understand and control the phase transformation of  $\text{TiO}_2$  for good application affecting the performance at high temperature.

## 5.2 Experimental

### 5.2.1 Synthesis of $\text{TiO}_2$ Sols and $\text{TiO}_2$ Particles

**Figure 5.2** shows an experimental apparatus for the synthesis of  $\text{TiO}_2$  sol. The reaction between titanium tetra-isopropoxide (TTIP; Junsei Chemical Co. > 98%) as a starting material and distilled water ( $\text{H}_2\text{O}$ ) was performed under the stirring condition of 1,000 rpm and temperatures of 313.15 K and 365.15 K.

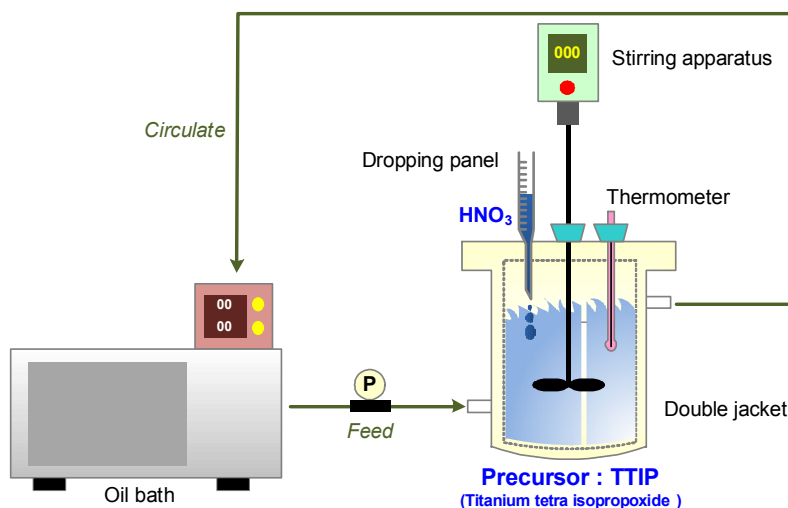


**Figure 5.2.** Experimental apparatus for synthesis of  $\text{TiO}_2$  sol.

The amount of water was fixed at 100  $\text{H}_2\text{O}/\text{Ti}$  molar ratio.<sup>147</sup> The first chemical reaction was a hydrolysis between TTIP and water. It was too fast to control the reaction rate. On the other hand, after the initial hydrolysis, the reaction was easily controlled because of the slow polycondensation rate. The characteristic of  $\text{TiO}_2$  sol particles was controlled by

optimizing the time and temperature of aging and is shown in **Figure 5.3**.

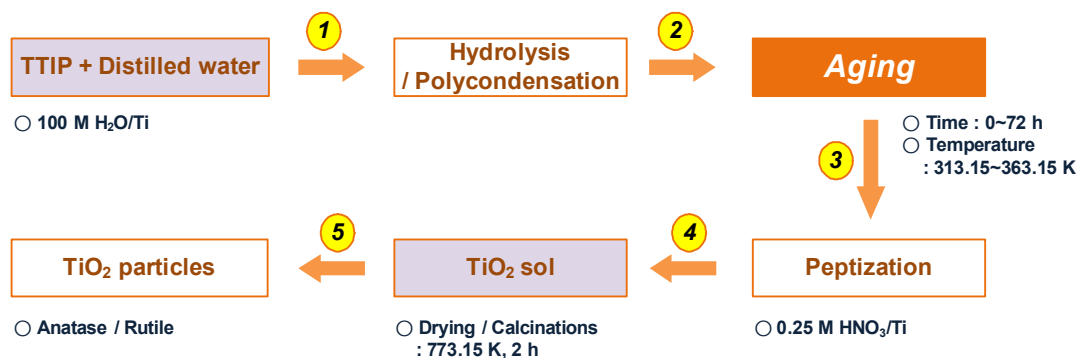


**Figure 5.3.** Experimental flowchart for synthesis of TiO<sub>2</sub>.

The initial fast reaction between the water and TTIP reached the equilibrium temperature within 30 min. The reaction after 30 min was named “aging”. In this work, the aging refers to slow polycondensation in synthesis reaction of TiO<sub>2</sub> sol. The effect of aging was investigated according to the variation of aging times (0, 24, and 72 h) under the condition of two different aging temperatures of 313.15 K and 363.15 K. The characteristics of TiO<sub>2</sub> sol particles were measured by the effect of the aging time under the condition of aging temperatures with 313.15 K and 363.15 K. After the aging, TiO<sub>2</sub> solution was transformed into a solution phase like paste, and a peptizing agent acidic or basic electrolyte was added to peptize the solution effectively. Although various electrolytes such as HCl, HNO<sub>3</sub> and NH<sub>4</sub>OH were available for peptizing agent, this experiment was performed under the condition of nitric acid (HNO<sub>3</sub>; Aldrich Co. 60%) as an inorganic acid to derive the ionic repulsive force required at the condition of low concentration. An acidic electrolyte was added to the solution with TiO<sub>2</sub> aggregated particles (determined by aging) to induce the repulsive force between inter particles and to prevent continuous aggregation.

Based on the particle size analysis (PSA) report and according to the concentration of peptizing agent (HNO<sub>3</sub>) (**Figure 5.4**), the particle of TiO<sub>2</sub> sol were well dispersed in a narrow range of about 0.15 to 0.3 HNO<sub>3</sub>/Ti molar ratio. The amount of the HNO<sub>3</sub> was

optimized at 0.25  $\text{HNO}_3/\text{Ti}$  molar ratio determined by the PSA experiment. The hydrous  $\text{TiO}_2$  sol was dried at 353.15 K for 1 day and calcined at 773.15 K for 1 h by 275.15 K/min at the final temperature to obtain a  $\text{TiO}_2$  thin film electrode.

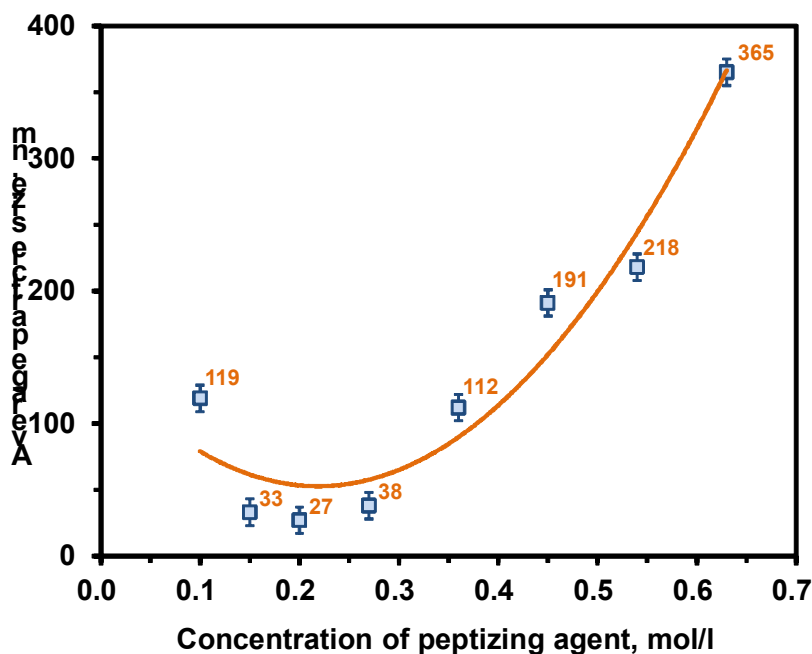


**Figure 5.4.** Average particle size of  $\text{TiO}_2$  sol particles according to concentration of peptization agent ( $\text{HNO}_3$ ).

### 5.2.2 Fabrication of $\text{TiO}_2$ Electrode

As mentioned before,  $\text{TiO}_2$  sol was obtained under the variation of aging times (0, 24, and 72 h) at two different aging temperatures (313.15 K and 363.15 K). The obtained  $\text{TiO}_2$  sol was dried at 353.15 K for 1 day to make a  $\text{TiO}_2$  paste. A  $\text{TiO}_2$  thin film electrode was prepared under the different mixing ratio of the dried  $\text{TiO}_2$  sol particles (5-25 wt%) and HPC binder (10-25 wt%) for optimized composition of  $\text{TiO}_2$  paste. For the fabrication of  $\text{TiO}_2$  thin film,  $\text{TiO}_2$  paste was prepared by adding 2 g dried  $\text{TiO}_2$  sol particles, 1 ml 10% [V/V] acetyl acetone, 2 g hydroxypropyl cellulose (HPC; Aldrich Co.,

Mw. 80,000), and 10 ml distilled water for 20 min at a stirring speed of 1,350 rpm using a paste mixer (PDM-300, Korea mixing technology Co.). TiO<sub>2</sub> film was then fabricated by coating twice a precursor paste onto the FTO glass plates (TEC 8: 10  $\Omega/\text{cm}^2$ , Pilkington Co.) using the screen printing method. The TiO<sub>2</sub> film was treated by heating at 773.15 K for 1 h. The TiO<sub>2</sub> film formed on the FTO glass is 7-14  $\mu\text{m}$  in thickness and 0.5 cm $\times$ 0.5 cm in square size.

### **5.2.3 Fabrication of Dye-Sensitized Solar Cells**

To fabricate the DSSC, the prepared TiO<sub>2</sub> thin film electrode was immersed in the 0.3 mM N719 dye (Solaronix Co.) solution at 333.15 K for 12 h and rinsed with anhydrous ethanol and dried. A Pt coated onto the FTO glass plates (TEC 8: 10  $\Omega/\text{cm}^2$ , Pilkington Co.) electrode was prepared as a counter electrode with an active area of 0.25 cm<sup>2</sup>. The Pt electrode was placed over the dye adsorbed TiO<sub>2</sub> thin film, and the edges of the cell were sealed with 2 mm wide stripers of 60  $\mu\text{m}$  thick sealing sheet (SX 1170-60, Solaronix Co.). Sealing was accomplished by hot-pressing the two electrodes together at 393.15 K. The redox electrolyte filled into the cell through the small holes and the filling ports were sealed with a sealant glue (Amosil 4, Solaronix Co.). The redox electrolyte was composed of 0.3 M 1,2-dimethyl-3-propylimidazolium iodide (Solaronix Co.), 0.5 M LiI (Aldrich Co.), 0.05 M I<sub>2</sub> (Aldrich Co.), and 0.5 M 4-TBP (Aldrich Co.) in 3-MPN (Fluka Co.) as a solvent.

### **5.2.4 Characterization of TiO<sub>2</sub> Sol Particles and TiO<sub>2</sub> Electrode**

To investigate the properties of TiO<sub>2</sub> sol particles caused by aging conditions, the particle size distribution, turbidity, and isoelectric point (IEP) of TiO<sub>2</sub> sol were measured by particle size analyser (ELS-8000, Otsuka electronics Co.), turbidity meter (2100N turbidimeter, Hach Co.), and zeta potential analyser (Zetasizer 3000, Malvern instrument Co.), respectively. The prepared TiO<sub>2</sub> sol particles (0.1 g) were dispersed in 0.1 M KCl solution and the suspension was treated in an ultrasonic bath for 1 h for the measurement of zeta potential. The pH of this suspension was then adjusted to desired values using diluted HCl and KOH solution. To probe the particle size and formation process of TiO<sub>2</sub> sol particle, the dried TiO<sub>2</sub> sol powders were investigated by high resolution transmission

electron microscopy (HR-TEM; F20, Techai Co.). Nitrogen adsorption isotherms on TiO<sub>2</sub> sol particles and TiO<sub>2</sub> electrode were measured at 77.15 K using an automatic analyzer (nanoPOROSITY, Mirae SI Co.). Before the measurements, the samples were out gassed for 2 h in the degas port of the adsorption apparatus. The measurement of the adsorption isotherms required 1 day. The BET specific surface areas were determined by nitrogen adsorption. In addition, the pore size distributions were also calculated by the Barrett, Joyner, and Halenda (BJH) method. The thermal curve of TiO<sub>2</sub> sol particles were analysed by thermal gravity analysis (TGA; STA 1640, Stanton redcroft Co.). The fourier transform infrared spectrophotometer (FT-IR; FT/IR-410, Jasco Co.) was used to analyze micro-structure changes in TiO<sub>2</sub> sol particles cause by aging conditions. The crystallinity of the manufactured TiO<sub>2</sub> sol particles and TiO<sub>2</sub> electrode were characterized by an X-ray diffraction (XRD; D/MAX- 1200, Rigaku Co.) using a Cu  $k\alpha$  X-ray and Ni filter at 35 kV and 15 mA. The morphology of calcined TiO<sub>2</sub> particles and TiO<sub>2</sub> electrode prepared from TiO<sub>2</sub> sol were measured by field-emission scanning electron microscopy (FE-SEM; S-4700, Hitachi Co.). Finally, the surface morphology of the TiO<sub>2</sub> thin film electrode was also examined on an atomic force microscope (AFM; XE-100, Park systems Co.) in the non-contact mode.

### **5.2.5 Adsorption and Photovoltaic Properties of TiO<sub>2</sub> Electrode**

Adsorption equilibrium experiments were carried out by contacting a given amount of TiO<sub>2</sub> thin film electrode with N719 dye solution of 0.01-0.5 mM in a shaking incubator at 303.15-333.15 K for 12 h. The pH of N719 dye solution was adjusted by 0.1 M HCl and 0.1 M NaOH solution. The adsorption capacity of TiO<sub>2</sub> film was measured by completely desorbing the adsorbed dye molecules from TiO<sub>2</sub> film using 0.1 M NaOH solution/ethanol (50/50 vol%). The concentration of N719 dye solution was analyzed by UV spectrophotometer (UV-160A, Shimadzu Co.) at 522 nm. The adsorption properties of N719 dye on TiO<sub>2</sub> electrode were evaluated by adsorption equilibrium isotherm,<sup>166</sup> isosteric enthalpies of adsorption, and adsorption energy distributions. The capacities of fabricated DSSC and the current-voltage ( $I$ - $V$ ) curves were measured using a source measure unit under irradiation of white light from a 1,000 W Xenon lamp (Solar simulation system; Thermo oriel instruments Co.). The incident light intensity and the active cell area were

100 mW/cm<sup>2</sup> and 0.25 cm<sup>2</sup>, respectively. The  $I$ - $V$  curves were used to calculate the short-circuit current ( $I_{sc}$ ), open-circuit voltage ( $V_{oc}$ ), fill factor ( $FF$ ), and overall conversion efficiency ( $\eta_{eff}$ ) of DSSCs. The electrochemical impedance spectroscopy (EIS) measurements were performed using the AC impedance (CHI 660A, CH instrumental Co.) over the frequency ranging from 1 to 10<sup>6</sup> Hz with amplitudes of  $\pm 5$  mV over the  $V_{oc}$ .

## 5.3 Results and Discussion

### 5.3.1 Physicochemical Properties of TiO<sub>2</sub> Sol Particles by Aging

Figure 5.5 shows the turbidity and photograph (inlet) of synthesized TiO<sub>2</sub> sol samples according to aging time and temperature.

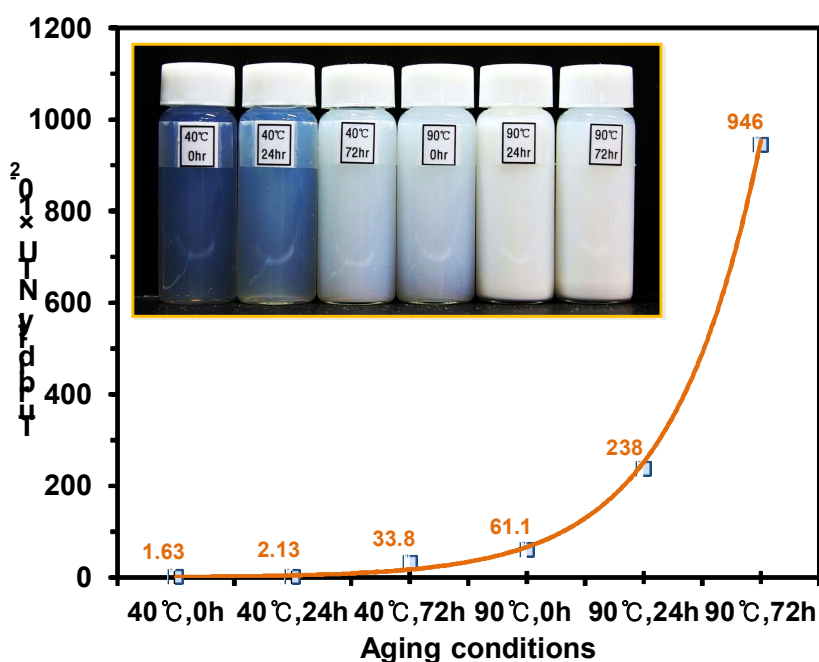


**Figure 5.5.** Turbidity and photograph (inlet) of TiO<sub>2</sub> sol samples according to aging conditions.



In the case of  $\text{TiO}_2$  sol sample of 0 h at 313.15 K, the turbidity of  $\text{TiO}_2$  sol was the lowest and the color of  $\text{TiO}_2$  sol was highly transparent. In contrast,  $\text{TiO}_2$  sol sample of 72 h at 363.15 K, the turbidity of  $\text{TiO}_2$  sol was increased and the color of  $\text{TiO}_2$  sol was opaque more than in the case of 0 h at 313.15 K. The aging time and temperature increased, the turbidity of  $\text{TiO}_2$  sol increased. The increase of turbidity are clearly related with the particle size of  $\text{TiO}_2$  sol.<sup>163,16</sup>

**Figure 5.6** shows the particle size distribution of  $\text{TiO}_2$  sol particles prepared under different aging times (0, 24, and 72 h) at two temperatures (313.15 and 363.15 K).

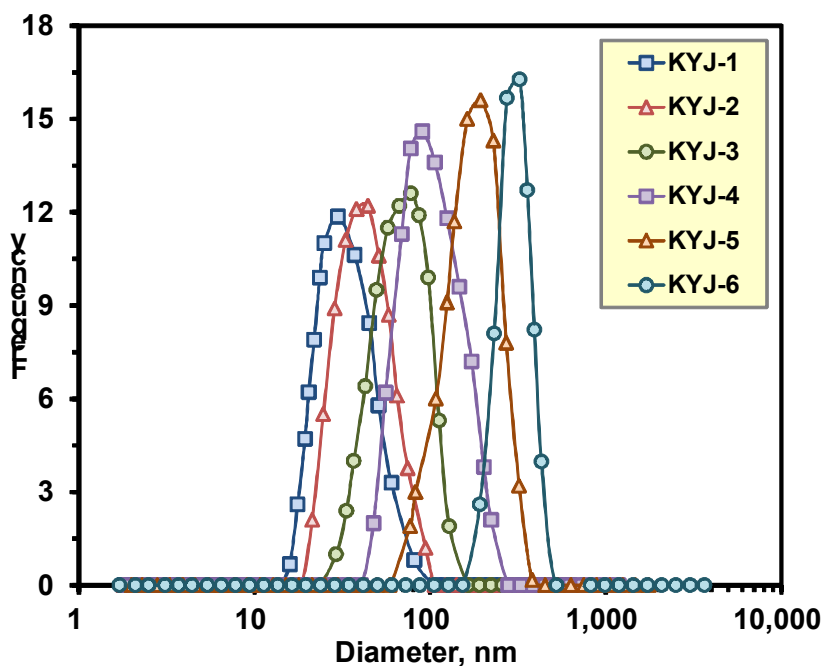


**Figure 5.6.** Particle size distributions of  $\text{TiO}_2$  sol particles according to the different aging conditions.

In this chapter, KYJ-1, KYJ-2, KYJ-3, KYJ-4, KYJ-5, and KYJ-6 are prepared  $\text{TiO}_2$  sol particles under different aging conditions (313.15 K-0 h, 313.15 K-24 h, 313.15 K-72 h, 363.15 K-0 h, 363.15 K-24 h, and 363.15 K-72 h). All samples clearly showed homogeneous particle size distribution.  $\text{TiO}_2$  sol prepared under lower aging temperature

and shorter aging time showed small particle size and narrow particle size distribution.

On the other hand, TiO<sub>2</sub> sol prepared under higher aging temperature and longer aging time resulted in large particle size and with a wide particle size distribution. It can be concluded from this work that aging temperatures as well as aging times are promoting the aggregation of particles.<sup>167</sup> The average particle size of the six TiO<sub>2</sub> sol prepared under different aging conditions are in the following sequence: KYJ-6 > KYJ-5 > KYJ-4 > KYJ-3 > KYJ-2 > KYJ-1. The average particle size and turbidity of six TiO<sub>2</sub> sol are summarized in **Table 5.1**. This result clearly indicates that the aging time and temperature are important process variables in controlling the particle size.<sup>168</sup> Also, the results of particle size analysis was corresponded to result of TiO<sub>2</sub> sol turbidity.

**Table 5.1.** Turbidity and average particle size of six TiO<sub>2</sub> sol according to different aging conditions

Sample No.	Aging temperature, K	Aging time, h	Turbidity, NTU	Average particle size, nm
KYJ-1	313.15	0	163	19
KYJ-2		24	213	44
KYJ-3		72	338	78
KYJ-4	363.15	0	611	90
KYJ-5		24	23,800	193
KYJ-6		72	94,600	323

To investigate the change in surface characteristic of TiO<sub>2</sub> sol particles, the zeta potential of TiO<sub>2</sub> sol particles were analyzed. In general, the zeta potential is a surface potential of thickness of electric double layer which formed on TiO<sub>2</sub> sol surface. **Figure 5.7a** and **b** shows the zeta potential vs. pH curves of synthesized TiO<sub>2</sub> sol particles prepared under different aging conditions. Increasing the aging time and temperature, the isoelectric point (IEP) of TiO<sub>2</sub> sol particles decreased down to 4.5 from 6.3 because of the

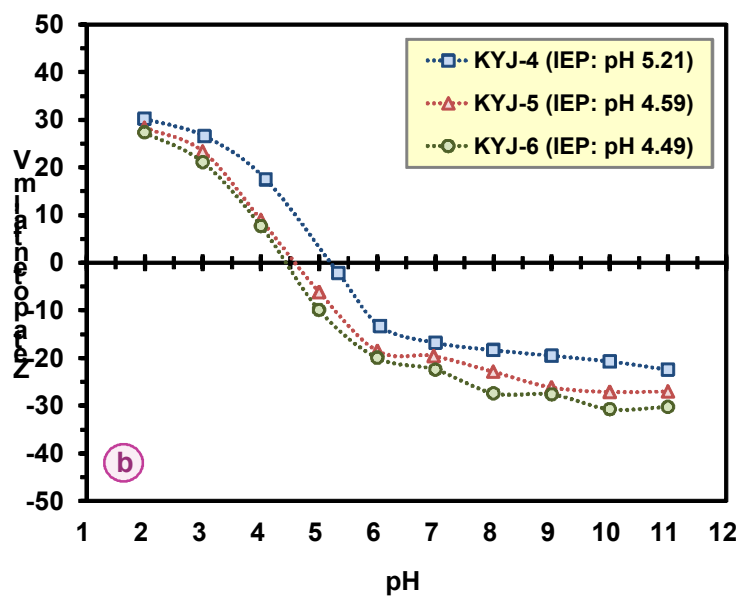
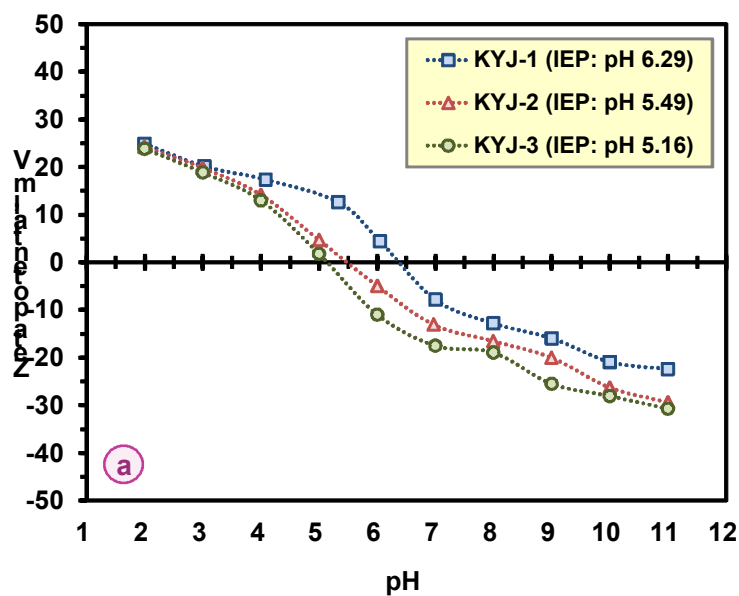


**Figure 5.7.** Zeta potential curves of TiO<sub>2</sub> sol particle with various aging time at (a) 313.15 K (b) 363.15 K.

acidification of aged TiO<sub>2</sub> sol particles with lower surface hydroxy groups by polycondensation:  $\text{Ti-OH} + \text{OH-Ti} \rightarrow \text{Ti-O-Ti} + \text{H}_2\text{O}$ .<sup>169</sup> As shown in **Table 5.1**, the TiO<sub>2</sub> sol particle size increased with the progression of aging. The results come from the aggregation of polycrystalline phase of TiO<sub>2</sub> sol particles because of the lower electrophoretic mobility and the reduction of zeta potential. The IEP of the six TiO<sub>2</sub> sol particles prepared under different aging conditions are in the following sequence: KYJ-1 (pH 6.29) > KYJ-2 (pH 5.49) > KYJ-4 (5.21) > KYJ-3 (5.16) > KYJ-5 (4.59) > KYJ-6 (4.49).

**Figures 5.8** show HR-TEM images of TiO<sub>2</sub> sol particles prepared under different aging times at two temperatures. **Figures 5.8 (a-c)** present the sizes and shapes of sol particles according to the aging times (0, 24, and 72 h) at lower 313.15 K. At 0 h, TiO<sub>2</sub> sol particles are in 3-5 nm range. These can be considered as primary particles. On the other hand, after 24 h, sol particles are aggregated to large particles. Finally, after 72 h, particles are necked and aggregated to the structure of a bunch of grapes. **Figures 5.8 (d-f)** show the aggregated particles under the aging temperature of higher 363.15 K. At 0 h, many sol particles are aggregated to polycrystalline aggregate than in the case of **Figure 5.8c**.<sup>167</sup> After 72 h and at 363.15 K, the average particle size aggregated is about 50 nm showing the formation of continuous necking of primary particles. This result implies that aging temperatures rather than aging times are promoting the aggregation of particles. However, the biggest particles were obtained at 363.15 K for 72 h (**Figure 5.8f**). Moreover, the viscosity was also higher than that of sample prepared at 313.15 K for 0 h (**Figure 5.8a**). Thus, it is evident from this results that the aging time and temperature are important process variables in controlling the particle size.

**Figure 5.9** shows the N<sub>2</sub> adsorption curve of TiO<sub>2</sub> sol particles prepared under different aging times at two temperatures of at 313.15 K and 363.15 K. The feature of all adsorption-desorption results except the sample of KYJ-1 corresponds to type IV isotherms of mesoporous material in the International Union of Pure and Applied Chemistry (IUPAC) classification.<sup>170</sup> When the relative pressure  $P/P_0$  increases, the capillary condensation occurs, resulting in a gradual increase in adsorption at middle-high relative pressure. Subsequently, an exponential increase in adsorption occurs at high relative pressure. The pore size is in the range over 2-50 nm.

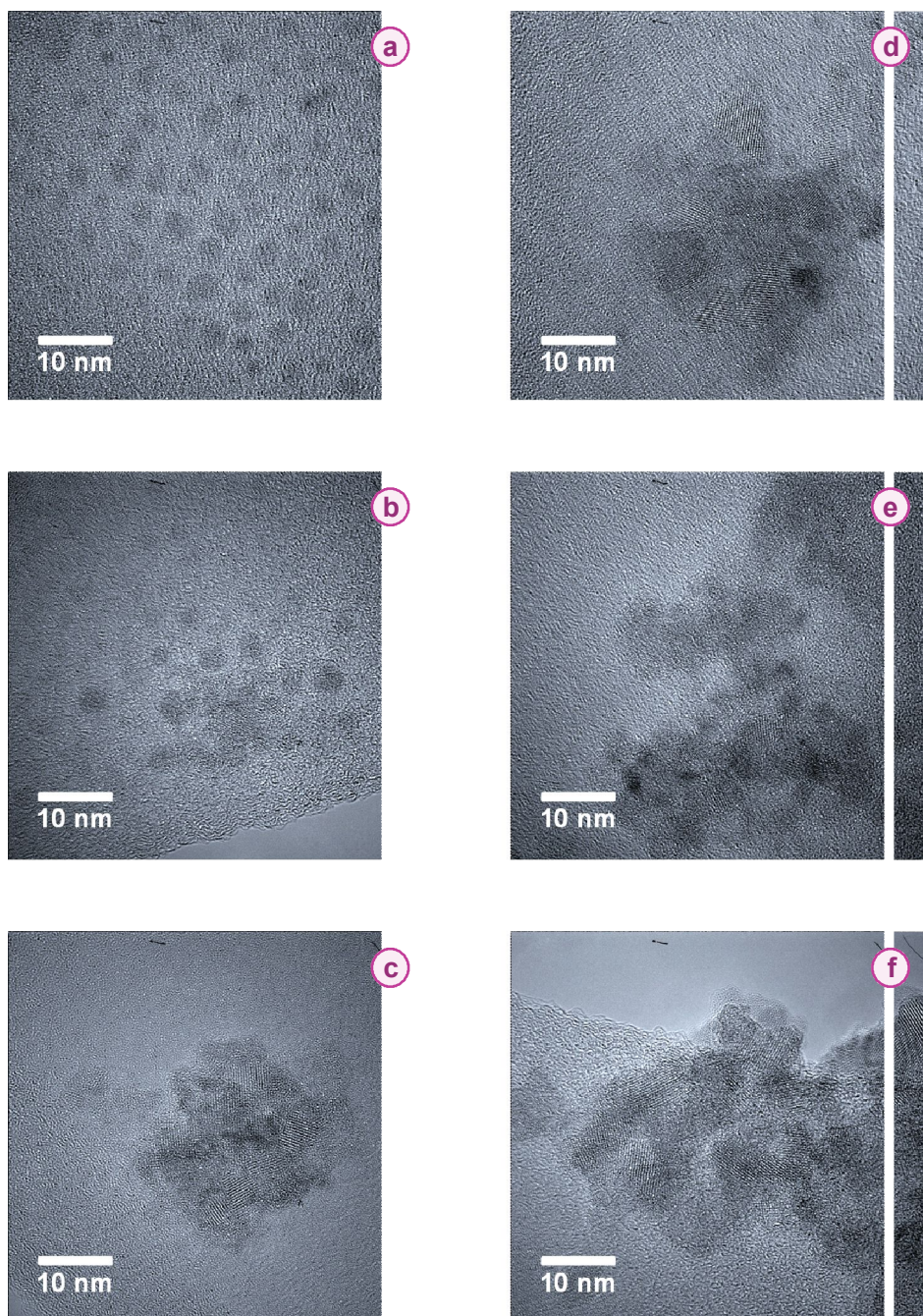


**Figure 5.8.** HR-TEM image of TiO<sub>2</sub> sol particles according to the aging times [0 h (a, d), 24 h (b, e) and 72 h (c, f)] at 313.15 K (left side) and at 363.15 K (right side).

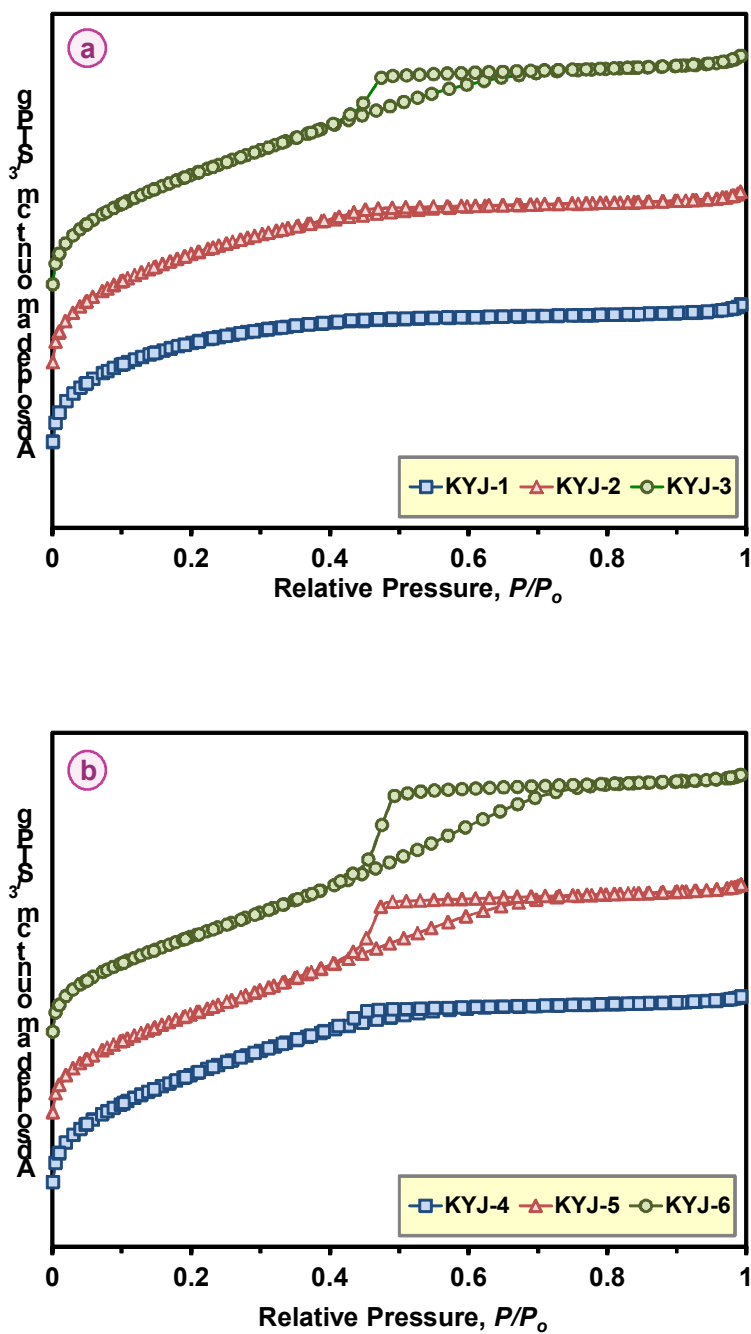


**Figure 5.9.**  $N_2$  adsorption and desorption isotherm of  $TiO_2$  sol particles with various aging time at 313.15 K (a) and 363.15 K (b).

The curve for KYJ-1 was found to be the type I of microporous material in IUPAC classification, which shows high adsorption capability. The steep rise at a very low relative pressure range evidently indicates the presence of micropores. However, the widening of knee of all isotherms with increasing aging conditions implies a reduction of the micropores. On the whole, the N<sub>2</sub> adsorption and desorption isotherms were clearly changed to type IV from type I as aging time and temperature increased. As the aging progressed, the size of hysteresis loop at middle-high relative pressure became larger. The change of pore structure of TiO<sub>2</sub> sol particles were observed in more detail in **Figure 5.10**. The pore size distribution of TiO<sub>2</sub> sol particles were calculated by BJH method from desorption branches. As the aging time and temperature were increased, the average pore size and total pore volume of TiO<sub>2</sub> sol particles were increased as shown in **Figure 5.10**. It is explained by the change of the particle size of TiO<sub>2</sub> sol.

The specific surface area, average pore size and total pore volume of KYJ-series were measured from the nitrogen adsorption isotherms (see **Table 5.2**).

**Table 5.2.** Physical properties of six TiO<sub>2</sub> sol particles according to different aging conditions

Sample No.	Aging temperature, K	Aging time, h	Surface area <sup>a</sup> , m <sup>2</sup> /g	Total pore volume <sup>b</sup> , cm <sup>3</sup> /g	Average pore size <sup>c</sup> , nm
KYJ-1	313.15	0	237	0.071	2.50
KYJ-2		24	234	0.097	2.53
KYJ-3		72	231	0.112	3.06
KYJ-4	363.15	0	220	0.094	2.71
KYJ-5		24	190	0.127	3.07
KYJ-6		72	180	0.148	3.25

<sup>a</sup>Specific BET surface area ( $P/P_0=0.1-0.2$ ), <sup>b,c</sup>Average pore size and total pore volume ( $P/P_0=0.99$ ) calculated by BJH method.

With increasing aging time and temperatures, the surface area of the TiO<sub>2</sub> sol particles decreased in the range of 237 to 180 m<sup>2</sup>/g. However, the average pore size and total pore

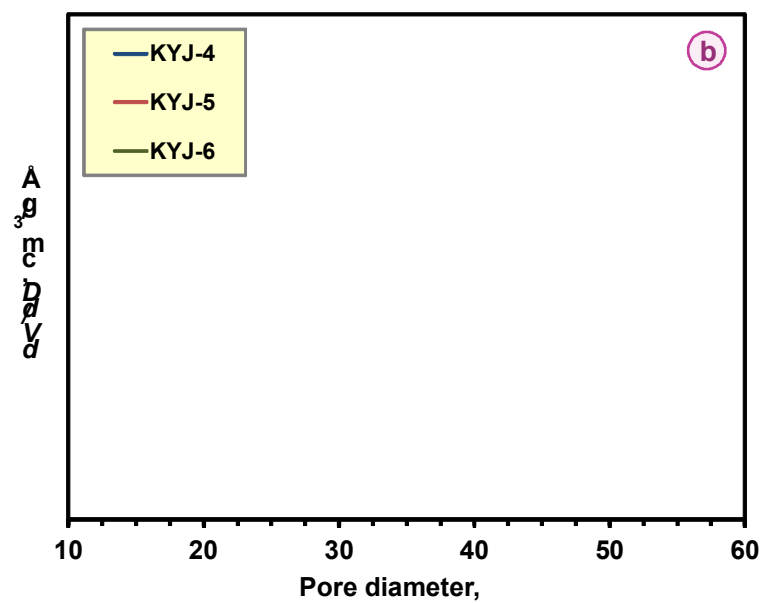
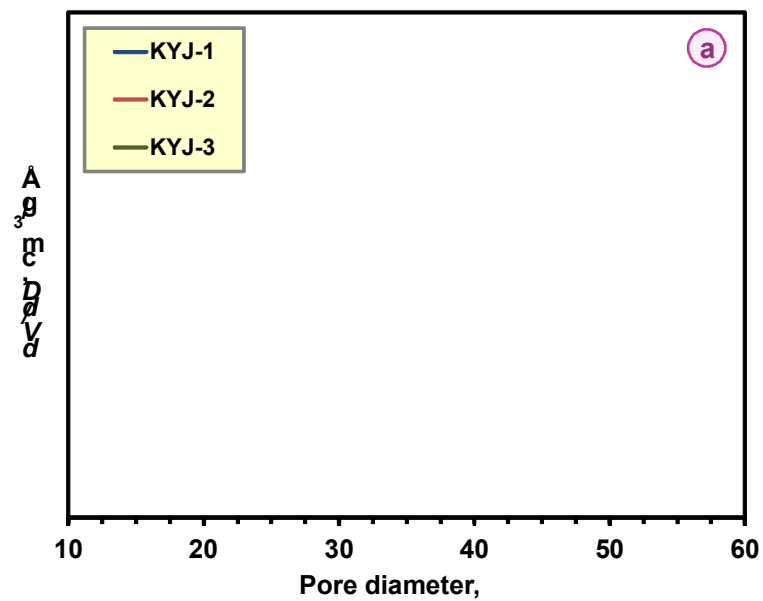


**Figure 5.10.** BJH pore size distribution of TiO<sub>2</sub> sol particles with various aging time at 313.15 K (a) and 363.15 K (b).



volume were increased as aging progressed, because the aggregation and necking size of  $\text{TiO}_2$  sol particle expanded with increasing of the aging time and temperature. From the above results, the aging time and temperature highly affected the microstructure shape of  $\text{TiO}_2$  sol.

Also, the above results could be confirmed by the thermal stability of  $\text{TiO}_2$  sol particles by thermal gravity analysis. **Figure 5.11** shows the TGA curves of  $\text{TiO}_2$  sol particles prepared under different aging times at two different temperatures of at 313.15 K and 363.15 K. The TGA curves were performed in the range of 293.15-1,073.15 K, with a heating rate of 275.15 K/min at air atmosphere. Typically, 0.1 g of  $\text{TiO}_2$  sol sample was analyzed. As seen from the **Figure 5.11**, heating the  $\text{TiO}_2$  sol particles prepared at a different aging conditions leads to two mass-loss domains.<sup>171</sup> The initial, large mass loss below 423.15 K is attributed to the elimination of incorporated water (adsorbed water).<sup>172</sup> The sharp mass loss at 523.15 K is attributed to the elimination of tightly bound hydroxyl species (structure water) accompanied by  $\text{TiO}_2$  crystallization. The feature of all TGA curves of  $\text{TiO}_2$  sol samples were similar. The total loss of weight were only different because the removal of amount of adsorbed water was different. The total loss of weight of the six  $\text{TiO}_2$  sol samples prepared under different aging conditions are in the following sequence: KYJ-1 (22.4%) > KYJ-2 (20.6%) > KYJ-3 (18.1%) > KYJ-4 (17.7%) > KYJ-5 (15.6%) > KYJ-6 (14.2%). The results comes from the decreasing in the amount of adsorbed water on the surface of  $\text{TiO}_2$  sol particles because of the smaller surface area formed through the progressing of aging.

**Figure 5.12** shows the result of FT-infrared spectra (FT-IR) for different aging temperatures of 313.15 K and 363.15 K. The type and the amount of bonding group existing in the  $\text{TiO}_2$  sol particles were analyzed using the KBr method (FT-IR) in the range of 400 to 4,000  $\text{cm}^{-1}$  wavelength number. In general, the characteristic absorption peaks of Ti-O-bending vibration and Ti-OH stretching vibration in the  $\text{TiO}_2$  sol particles appear at 500  $\text{cm}^{-1}$  and 1,630  $\text{cm}^{-1}$ . As expected, the unique vibration peak of Ti-O bending and Ti-OH stretching was observed as shown in **Figure 5.12**, and the intensity of Ti-O- absorption peak near 500  $\text{cm}^{-1}$  increased with the progression of aging. In the result of FT-IR as shown **Figure 5.12a**, Ti-OH groups are largely formed with the progression of aging, and then they turn into Ti-O-Ti bond (oxolation) from Ti-OH bonds (olation) by po-

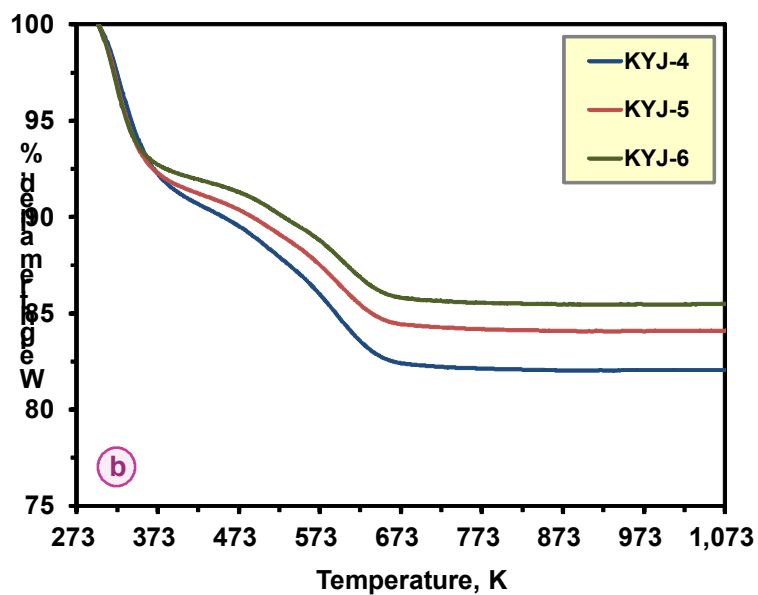
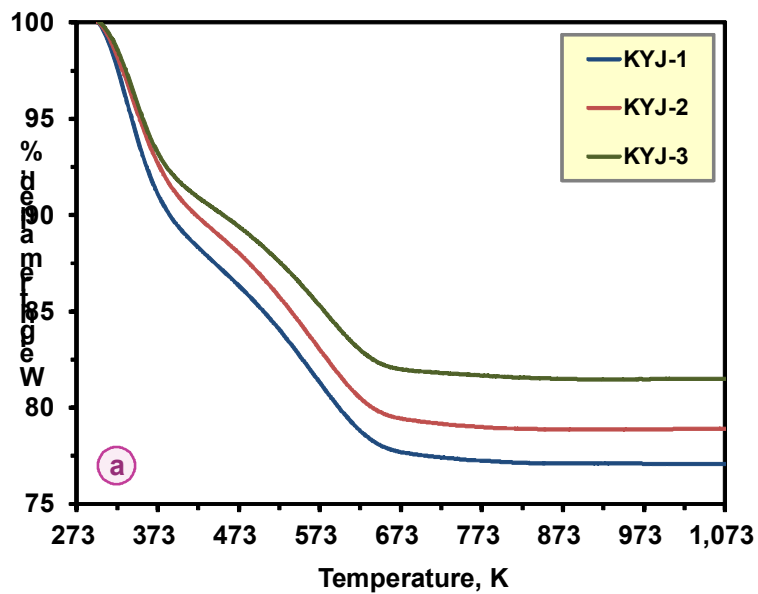


**Figure 5.11.** TGA curves of TiO<sub>2</sub> sol particles with various aging time at (a) 313.15 K (b) at 363.15 K.

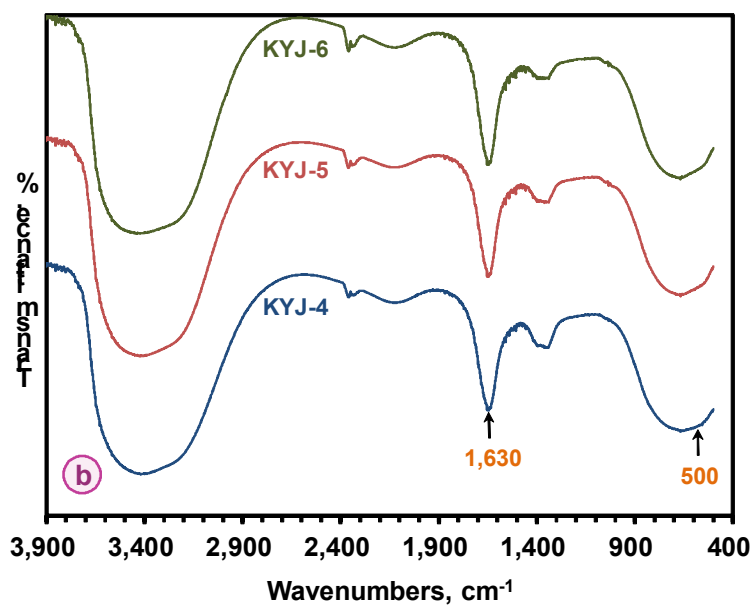
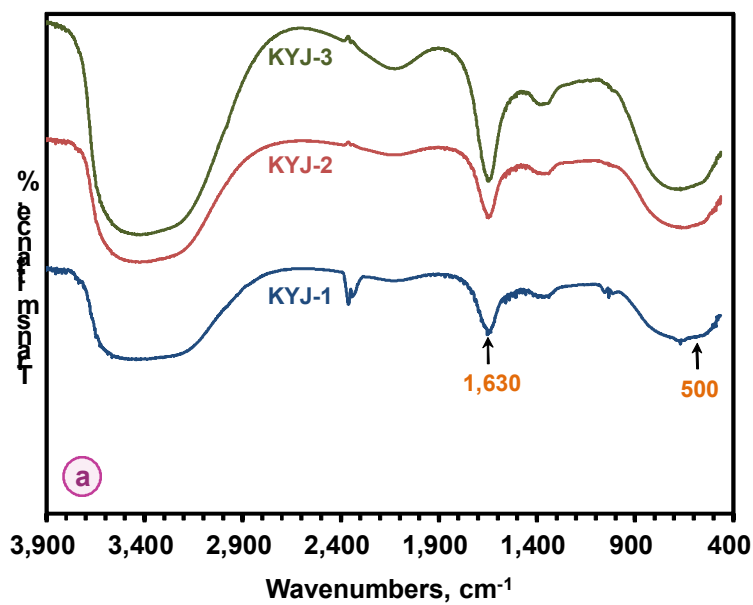


**Figure 5.12.** FT-IR spectra of TiO<sub>2</sub> sol particles with various aging time at (a) 313.15 K (b) 363.15 K.

lymerization/condensation as follows:  $\text{Ti-OH} + \text{Ti-OH} \rightarrow \text{Ti-O-Ti} + \text{H}_2\text{O}$ . On the other hand, all the chemical bonds reach the equilibrium state in the case of the aging of 72 h. Even though there is no noticeably change after fast polycondensation, the particles can be aggregated by slow polycondensation according to the aging.

The crystallinity of  $\text{TiO}_2$  sol particles and calcined  $\text{TiO}_2$  particles was analyzed by XRD. **Figures 5.13** show the XRD patterns of  $\text{TiO}_2$  sol particles prepared under different aging times at two different temperatures of at 313.15 K and 363.15 K. Before calcination, all samples mainly had the brookite crystalline phase. With increasing aging times at 313.15 K, an increment in the brookite crystalline phase was observed. The brookite peak intensity ( $25^\circ$ ) of  $\text{TiO}_2$  sol prepared at 72 h and 363.15 K (**Figure 5.13b**) is higher than that of  $\text{TiO}_2$  sol prepared at 72 h and 313.15 K (**Figure 5.13a**). It may be safe to conclude that the crystallinity increased with the aging temperatures and times.

In addition, the XRD patterns of calcined  $\text{TiO}_2$  sol particles (Calcined temperature: 773.15 K) prepared under different aging conditions were investigated. Numerous changes were observed with the aging times for the sample of 313.15 K (**Figure 5.14a**). With increasing aging times,  $\text{TiO}_2$  particles having rutile crystalline phase as ( $d_{110}$ ) were changed into anatase crystalline phase as ( $d_{101}$ ). For the sample of KYJ-3, a greater amount of rutile phase changed to an anatase crystalline phase with the small existence of brookite crystalline phase ( $d_{121}$ ) and also small rutile crystalline phase as ( $d_{110}$ ). However, the samples of KYJ-5 and KYJ-6 were mostly observed a anatase crystalline phases (**Figure 5.14b**). As a result, crystalline phases are affected by particle size even at the calcinations of 773.15 K as shown in **Figure 5.14**. Therefore, the big particle sizes which had the small surface area showed the slow transition of the crystalline phase (crystalline phase transition: anatase  $\rightarrow$  rutile) by the effect of Ostwald Ripening.<sup>181-183</sup>

To confirm the morphology of calcined  $\text{TiO}_2$  powder according to aging effect, it was investigated by FE-SEM. **Figure 5.15** shows the FE-SEM images of calcined  $\text{TiO}_2$  powder's morphology. In the case of the samples of different aging temperature (a, d) for 0 h, rutile phase with big particle size ( $>50$  nm) was observed after the calcination of  $\text{TiO}_2$  sol powders. In addition, many aggregated  $\text{TiO}_2$  particles were observed. On the other hand, in the case of 24 h (b, e) and 72 h (c, f), the anatase phase with small particle size (av. 20 nm) was mostly noticed.

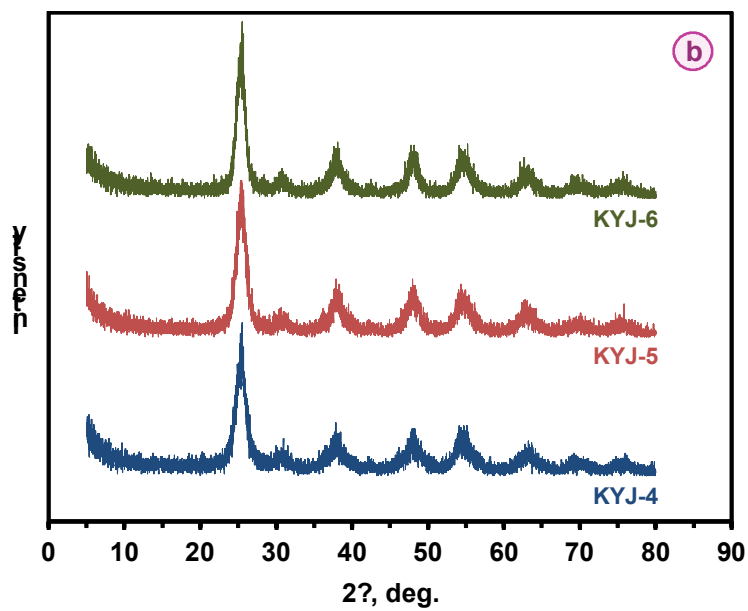
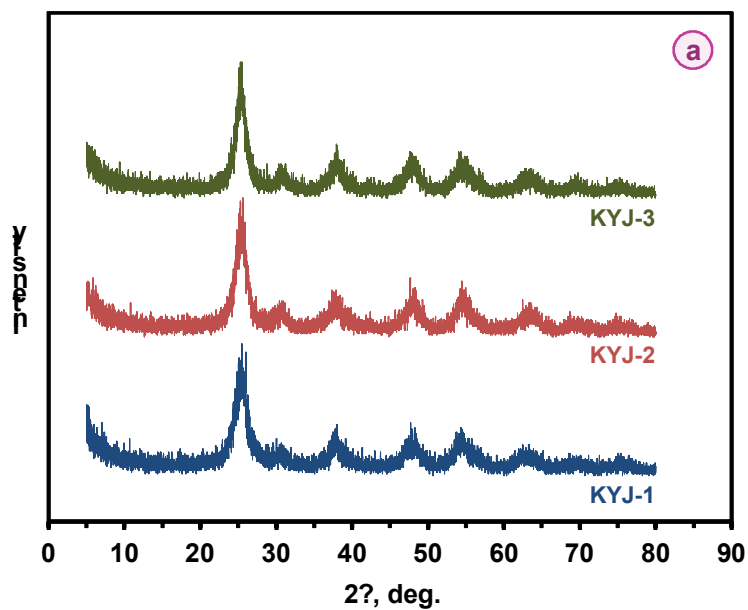


**Figure 5.13.** XRD patterns of TiO<sub>2</sub> sol particles with various aging time at 313.15 K (a) and at 363.15 K (b).

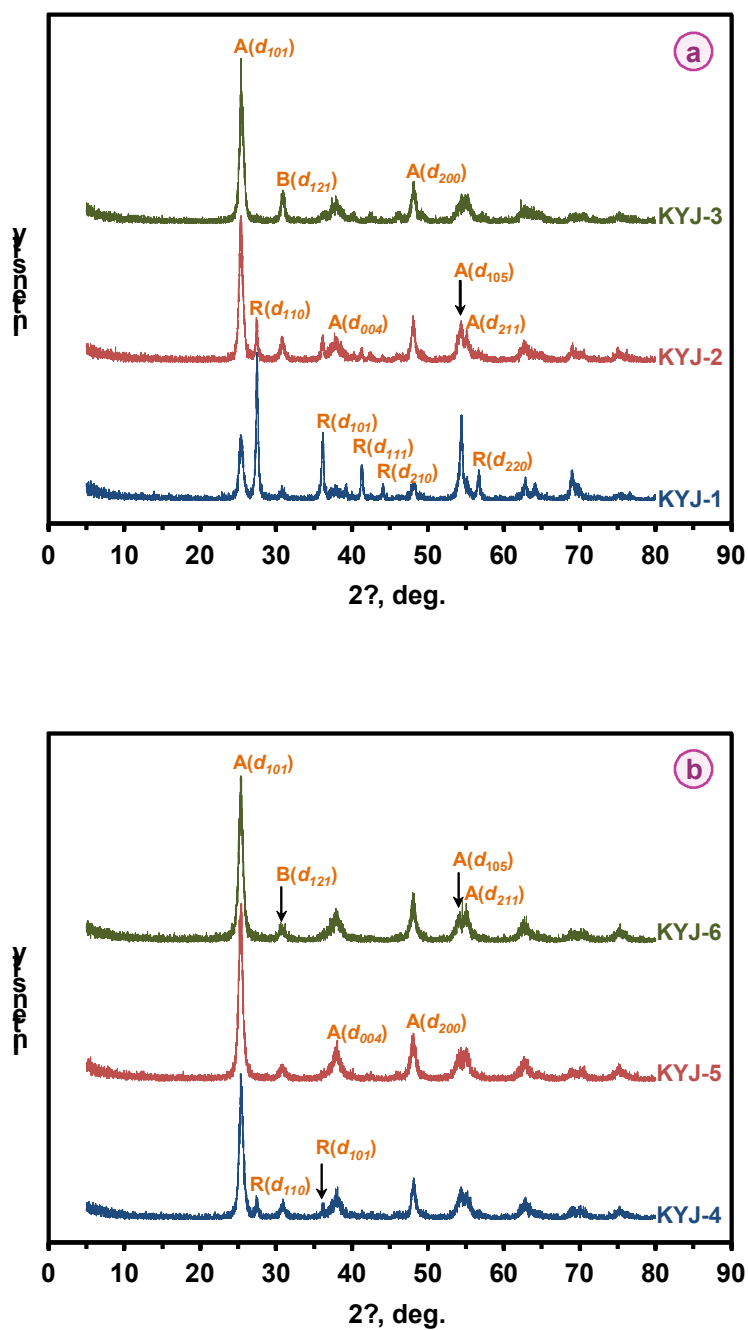


**Figure 5.14.** XRD patterns of calcined  $\text{TiO}_2$  sol particles with various aging time at 313.15 K (a) and at 363.15 K (b).

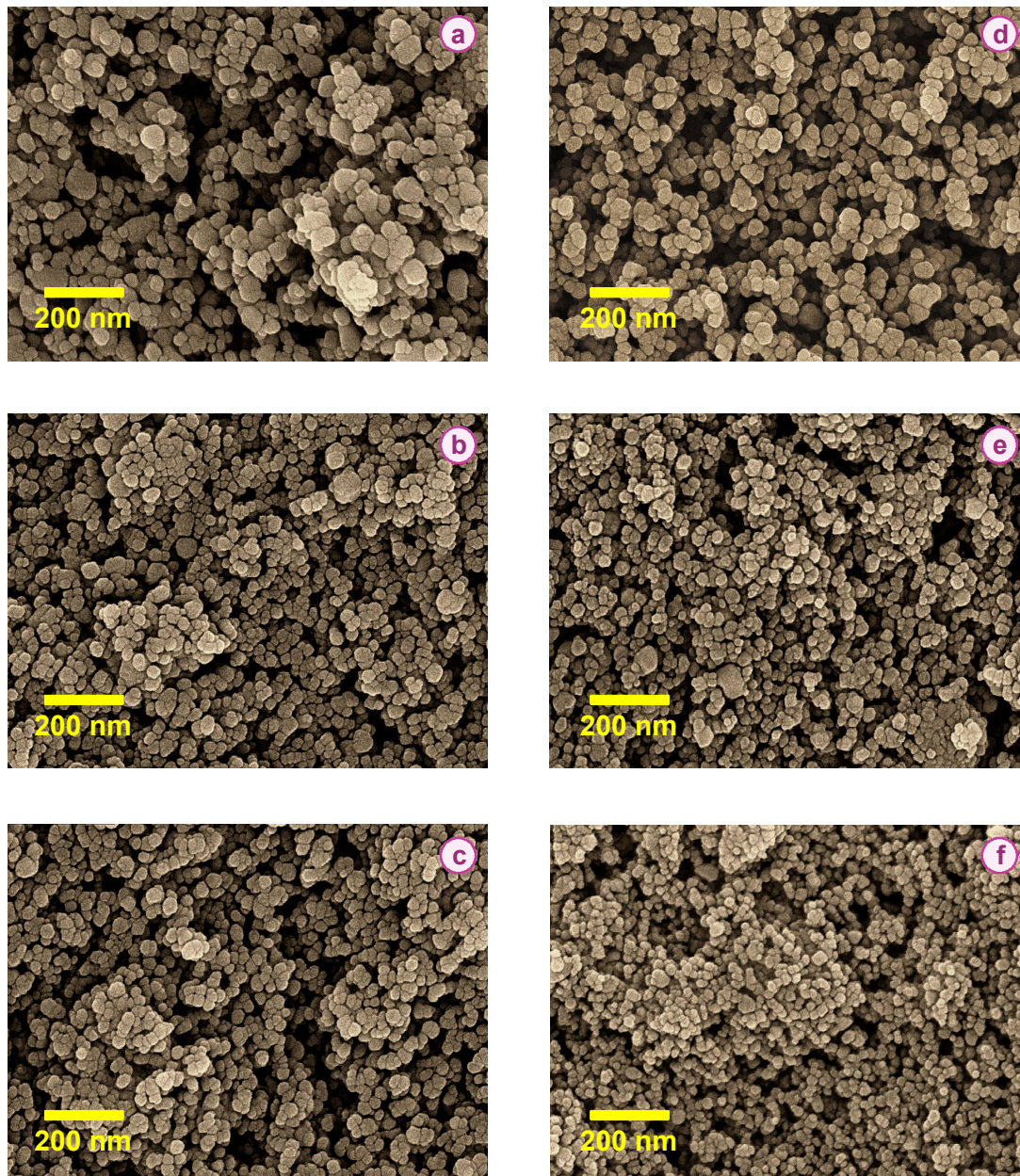


**Figure 5.15.** FE-SEM images of calcined  $\text{TiO}_2$  powder's morphology according to the different aging conditions: 0 h (a, d); 24 h (b, e); 72 h (c, f) at 313.15 K (left side) and at 363.15 K (right side).

Especially, in the case of 72 h (f) at 363.15 K, the TiO<sub>2</sub> powder has well-dispersive particle and small particle. At this time, the particle sizes of the six calcined TiO<sub>2</sub> samples prepared under different aging conditions are in the following sequence: KYJ-1 > KYJ-4 > KYJ-2 > KYJ-3 > KYJ-5 > KYJ-6.

### 5.3.2 Structure Properties of TiO<sub>2</sub> Electrode by Aging

The properties of the nanocrystalline TiO<sub>2</sub> thin film fabricated from synthesized TiO<sub>2</sub> sol were investigated to fabricate the DSSC. The TiO<sub>2</sub> paste of optimal condition for fabrication of TiO<sub>2</sub> electrode was chosen based on the experimental results using the KYJ-6 sample. The optimal amount of the dried KYJ-6 powder was determined in the range of (5-25%) and 10% of HPC as a binder. The results of conversion efficiency are listed in **Table 5.3**.

**Table 5.3.** Photocurrent-voltage of TiO<sub>2</sub> thin films electrode depending on KYJ-6 powder content in TiO<sub>2</sub> paste

TiO <sub>2</sub> content in the TiO <sub>2</sub> paste	Film thickness, $\mu\text{m}$	$I_{sc}$ , $\text{mA}/\text{cm}^2$	$V_{oc}$ , $\text{V}$	Fill factor, $FF$	$\eta_{eff}$ , %
5% KYJ-6 powder	7.0	5.6	0.62	0.63	2.2
10% KYJ-6 powder	7.0	8.5	0.63	0.63	3.4
15% KYJ-6 powder	7.0	11.8	0.63	0.62	4.6
20% KYJ-6 powder	7.0	14.2	0.64	0.57	5.2
25% KYJ-6 powder	7.0	8.2	0.63	0.63	3.2

Although the highest efficiency (5.2%) for 20% KYJ-6 sample was obtained, the fill factor was lower compared with the other samples. Thus, the TiO<sub>2</sub> contents were reduced from 20% to 18%. To determine the optimal amount of binder, the contents of HPC were adjusted in the range of 10-25% for the sample of 18% KYJ-6 sample. As shown in **Table 5.4**, a higher conversion efficiency of 7.3% was obtained when the contents of TiO<sub>2</sub> and



HPC were 18% and 15%, respectively. Thus, all TiO<sub>2</sub> electrodes prepared from six TiO<sub>2</sub> sols were fabricated by optimized TiO<sub>2</sub> paste in this chapter.

**Table 5.4.** Photocurrent-voltage of TiO<sub>2</sub> thin films electrode depending on the concentration of HPC binder in TiO<sub>2</sub> paste

HPC concentration in the TiO <sub>2</sub> paste	Film thickness, $\mu\text{m}$	$I_{sc}$ , $\text{mA}/\text{cm}^2$	$V_{oc}$ , $\text{V}$	Fill factor, $FF$	$\eta_{eff}$ , %
<b>10% Hydroxypropylcellulose</b>	7.0	16.3	0.67	0.59	6.5
<b>15% Hydroxypropylcellulose</b>	7.0	15.6	0.71	0.66	7.3
<b>20% Hydroxypropylcellulose</b>	7.0	14.0	0.65	0.66	6.0
<b>25% Hydroxypropylcellulose</b>	7.0	10.2	0.63	0.66	4.2

To investigate the effect of aging conditions on the crystallinity of the prepared samples, XRD was used. As shown in **Figure 5.16**, the XRD patterns of the TiO<sub>2</sub> films prepared under different aging conditions reveal that the main crystal phase of all the prepared samples was anatase ( $d_{101}$ ,  $d_{004}$ ,  $d_{200}$ ,  $d_{105}$ , and  $d_{211}$ ) although they have also rutile ( $d_{110}$ ,  $d_{111}$ , and  $d_{210}$ ) and brookite ( $d_{121}$ ) crystalline phase to some extent. In addition, TiO<sub>2</sub> films having partly rutile crystalline phase are obviously changed into pure anatase crystalline phase with increasing aging times irrespective of their aging temperature. The anatase crystalline phase as ( $d_{101}$ ) was very important adsorption site between TiO<sub>2</sub> and N719 dye molecular. As the size of anatase crystalline phase as ( $d_{101}$ ) increased, dye adsorption amount increased and adsorption bonding strength of between TiO<sub>2</sub> and N719 dye molecular also increased.<sup>66,146</sup> The KYJ-1F, KYJ-2F, KYJ-3F, KYJ-4F, KYJ-5F, and KYJ-6F are prepared TiO<sub>2</sub> thin film from TiO<sub>2</sub> sol according to different aging conditions (313.15 K-0 h, 313.15 K-24 h, 313.15 K-72 h, 363.15 K-0 h, 363.15 K-24 h, and 363.15 K-72 h) in this chapter.

The approximate anatase crystallite size of TiO<sub>2</sub> film samples were calculated by using Scherrer's equation (**Equation 3.2**). The ratio of anatase crystalline phase ( $F_A$ ) was calculated by using the anatase constant equation and given by **Equation 5.4**.<sup>173</sup>

$$F_A (\%) = \frac{1}{1 + 1.26 I_R / I_A} \quad (\text{Eq. 5.4})$$

Where  $I_A$  and  $I_R$  the X-ray diffraction intensities at  $2\theta = 25.3^\circ$  for anatase main peak ( $d_{101}$ ) and  $27.5^\circ$  for rutile main peak ( $d_{110}$ ), respectively.

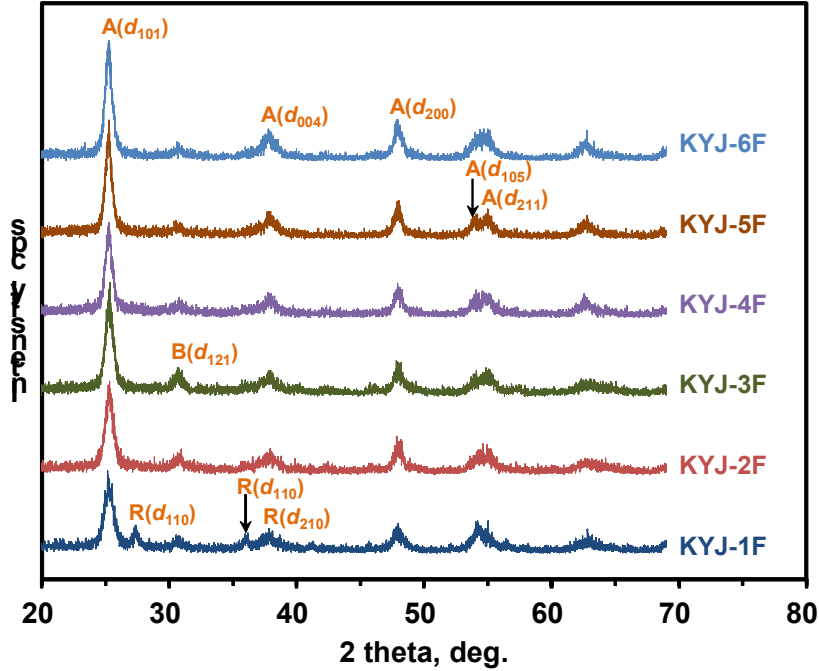


**Figure 5.16.** XRD patterns of prepared  $\text{TiO}_2$  film from  $\text{TiO}_2$  sol according to the different aging conditions.

**Table 5.5** lists the physical properties obtained from XRD characterization for the  $\text{TiO}_2$  films prepared at different aging conditions. It is found that the crystallinity and their crystallite size of anatase phase as ( $d_{101}$ ) continually increased with aging times. The crystallite size, which is varied between 11 and 20 nm as listed in **Table 5.5**, is also dependent on the aging temperature. The  $\text{TiO}_2$  films prepared at 363.15 K have relatively larger sizes compared to that of the  $\text{TiO}_2$  films prepared at 313.15 K. Except the KYJ-1F

and KYJ-4F, no rutile phase (or peak) was observed. This result indicates that the aging time as well as the aging temperature can be a critical factor affecting the crystal phase of TiO<sub>2</sub> film.

**Table 5.5.** Physical properties of TiO<sub>2</sub> film with different aging conditions

Sample No.	Aging temperature, K	Aging time, h	Size of anatase crystalline phase as ( $d_{101}$ ), nm	Anatase ratio, %	Fractal dimension, $D$
KYJ-1F	313.15	0	11	71	2.489
KYJ-2F		24	14	100	2.514
KYJ-3F		72	15	100	2.526
KYJ-4F	363.15	0	17	91	2.490
KYJ-5F		24	18	100	2.519
KYJ-6F		72	20	100	2.514

In order to quantitatively characterize the degree of geometrical nonuniformity (or surface irregularities) for the prepared TiO<sub>2</sub> particles, fractal dimension (or fractal geometry)  $D$ , which showed values varying between 2 and 3, is used. For perfectly smooth surface the value is  $D=2$  while totally irregular (or rough) surface has a fractal dimension of 3. In this study, the surface fractal dimension of the prepared TiO<sub>2</sub> particles were calculated by using Avnir and Jaroniec equation based on the Frenkel-Halsey-Hill model and nitrogen adsorption isotherm data. The Avnir-Jaroniec equation is shown in **Equation 5.5** and **5.6** respectively.<sup>174,175</sup>

$$\ln(x) = K - (3 - D)\ln(A) \quad (\text{Eq. 5.5})$$

Where

$$A = -\Delta G = RT \ln\left(\frac{P_o}{P}\right) \quad (\text{Eq. 5.6})$$

Here  $x$  is the amount adsorbed,  $K$  is constant and  $A$  corresponds to the adsorption

potential.  $R$  is the universal gas constant,  $T$  is the absolute temperature and  $P_o$  and  $P$  are the saturation and equilibrium pressures during the gas adsorption respectively. **Table 5.5** lists the calculated results of the surface fractal dimensions for the prepared TiO<sub>2</sub> films from TiO<sub>2</sub> sol. As shown in **Table 5.5**, the prepared films had fractal dimensions ranging from 2.489 to 2.526, which suggested the existence of irregular surface. In addition, the fractal dimensions are reasonably correlated with the aging conditions. In other words, the surface roughnesses (or irregularity) of TiO<sub>2</sub> films increase with aging time and anatase ratio. It is also found that the size of anatase crystalline phase and the ratio of anatase increase as the surface geometry of TiO<sub>2</sub> film become more irregular (or roughen).

The 3-dimensional AFM images are also used to get some further insight into the morphological changes brought about by aging time and aging temperature on the surface of TiO<sub>2</sub> film. The images are recorded at the scan rate of 0.3 Hz on 3  $\mu\text{m}$  × 3  $\mu\text{m}$  planar in non- contact mode and shown in **Figure 5.17**. It is observed that the surface of the prepared films became rougher as the aging time and aging temperature increased. The AFM images also clearly show that the KYJ-6F has more uniformly coated surface without void and aggregated particles compared to that of other samples. **Table 5.6** also lists the Rms ( $R_q$ ) and mean ( $R_a$ ) roughness value of TiO<sub>2</sub> film. The surface roughness values for TiO<sub>2</sub> film are observed to decrease in the sequence of KYJ-6F > KYJ-5F > KYJ-3F > KYJ-2F > KYJ-4F > KYJ-1F, which is the similar as that of the size of anatase crystalline phase.

**Table 5.6.** Surface roughness of TiO<sub>2</sub> thin film with different aging conditions

Sample No.	Aging temperature, K	Aging time, h	Root mean square roughness ( $R_q$ ), nm	Mean roughness ( $R_a$ ), nm
<b>KYJ-1F</b>	313.15	0	9.36	7.18
<b>KYJ-2F</b>		24	10.21	7.97
<b>KYJ-3F</b>		72	11.16	8.93
<b>KYJ-4F</b>	363.15	0	9.65	7.72
<b>KYJ-5F</b>		24	12.78	9.73
<b>KYJ-6F</b>		72	14.26	11.03

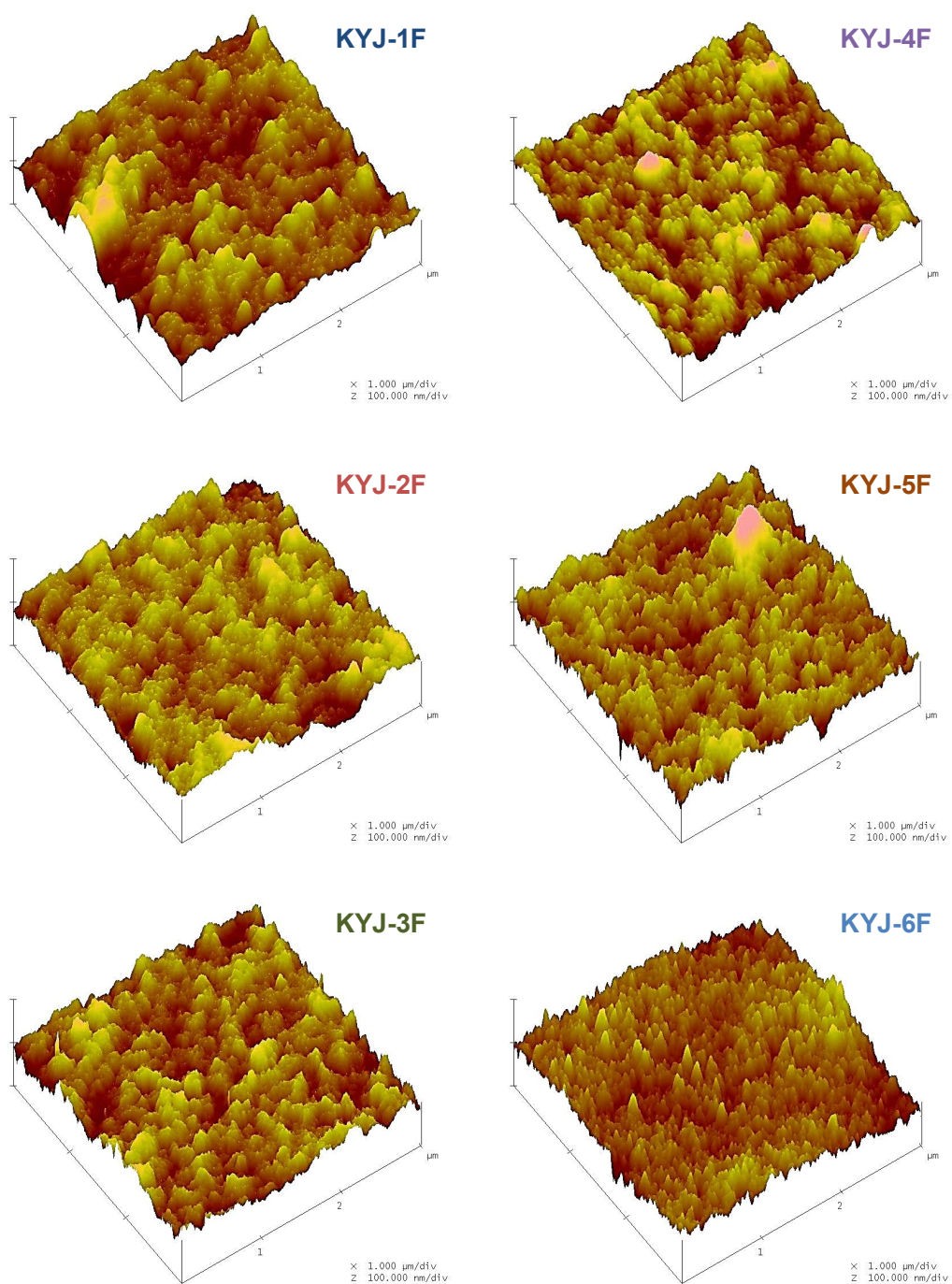


**Figure 5.17.** 3-dimensional AFM images of  $\text{TiO}_2$  thin film according to different aging conditions.

The TiO<sub>2</sub> thin films having some rutile phase (KYJ-1F and KYJ-4F) represent relatively lower surface roughness values compared to that of the films having pure anatase phase. This result can be explained by the transition degree of TiO<sub>2</sub> crystalline phase. Our previous study<sup>168</sup> has shown that the phase transformation from anatase to rutile is partially dependent on the particle size. In other words, the TiO<sub>2</sub> sols with larger particle size represent relatively slower transition of the crystalline phase. Therefore, the TiO<sub>2</sub> thin film samples with some rutile phase (KYJ-1F and KYJ-4F) have low surface roughness. Commonly, if the TiO<sub>2</sub> thin film has a highly surface roughness, the highly amount of N719 dye adsorbed is drastically increased.<sup>1,31</sup>

**Figure 5.18** shows the FE-SEM surface images of TiO<sub>2</sub> thin film. It can be seen that some of rutile phase with larger particle size (>30 nm) is observed after fabrication of TiO<sub>2</sub> film in case of the samples prepared at aging temperatures of 313.15 and 363.15 K for 0 h (KYJ-1F and KYJ-4F) and a lot of aggregated TiO<sub>2</sub> particles are also observed. However, the TiO<sub>2</sub> particles prepared at aging time of 24 h (KYJ-2F and KYJ-5F) and 72 h (KYJ-3F and KYJ-6F) exhibit the mostly anatase phase with small particle size (average: <20 nm). Especially in the case of KYJ-5F (24 h) and KYJ-6F (72h) prepared at aging temperature of 363.15 K, well-ordered surface and highly dispersive pore structures are observed. For higher adsorption capacity of N719 dye on TiO<sub>2</sub> film, the TiO<sub>2</sub> particles consisted higher anatase crystalline phase because, TiO<sub>2</sub> particle size of the anatase crystalline phase was smaller than that of the rutile crystalline phase.<sup>1,31</sup>

In general, N719 dye adsorption is substantially dependent on the specific surface area of TiO<sub>2</sub> thin film. It has been reported that the higher the TiO<sub>2</sub> thin film surface area which could support the larger available adsorption site, the larger the N719 dye adsorption onto TiO<sub>2</sub> thin film.<sup>31</sup> **Table 5.7** lists the BET specific surface area, average pore size and total pore volume of TiO<sub>2</sub> thin films prepared at different aging conditions. The reasonable correlation between the textural properties and the aging conditions are observed. As listed in **Table 5.7**, the surface area and total pore volume of TiO<sub>2</sub> particles are increased with increasing aging time and temperature, while the average pore size has decreased. In other words, longer aging time at the same aging temperature resulted in higher surface area and total pore volume and narrower average pore size. The TiO<sub>2</sub> films having pure (100%) anatase phase have relatively higher BET surface area and pore volume than that of the



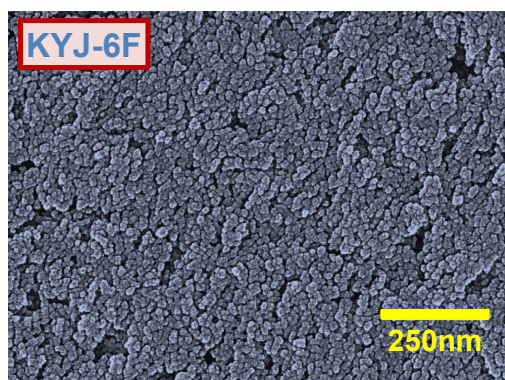
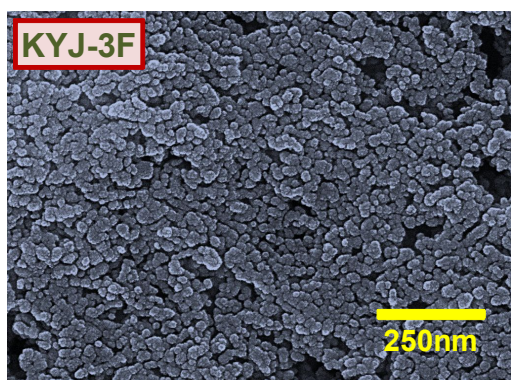
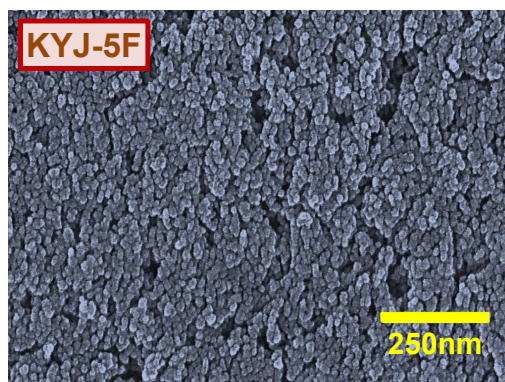
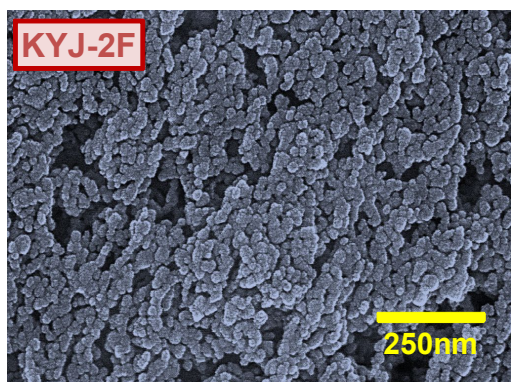
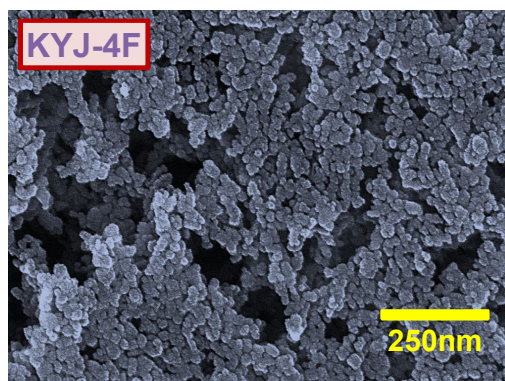
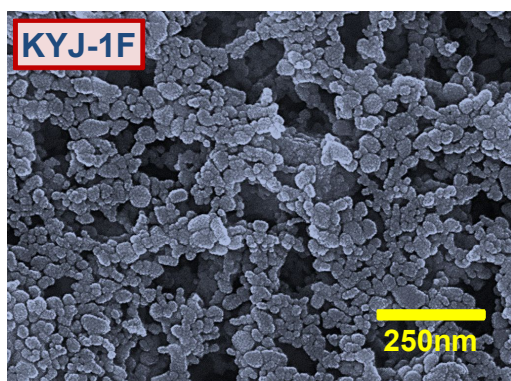


**Figure 5.18.** FE-SEM surface images of  $\text{TiO}_2$  thin film according to different aging conditions.

TiO<sub>2</sub> films consisting of both anatase and rutile structures (i.e., KYJ-1F and KYJ-4F). Moreover, in the case of the films representing the same structure, the larger the crystallite size, the greater the BET surface area and pore volume are (see **Tables 5.5** and **5.7**). Thus it seems reasonable to conclude that the textural and crystalline properties of TiO<sub>2</sub> film are highly dependent on the aging time and temperature.

**Table 5.7.** Textural properties of TiO<sub>2</sub> thin film prepared according to the different aging conditions

Sample No.	Aging temperature, K	Aging time, h	Surface area <sup>a</sup> , m <sup>2</sup> /g	Total pore volume <sup>b</sup> , cm <sup>3</sup> /g	Average pore size <sup>c</sup> , nm
KYJ-1F	313.15	0	41.2	0.103	8.57
KYJ-2F		24	46.7	0.118	6.55
KYJ-3F		72	54.6	0.125	7.66
KYJ-4F	363.15	0	44.2	0.111	8.18
KYJ-5F		24	63.4	0.133	6.35
KYJ-6F		72	69.5	0.138	6.24

<sup>a</sup>Specific BET surface area ( $P/P_0=0.1-0.2$ ), <sup>b,c</sup>Average pore size and total pore volume ( $P/P_0=0.99$ ) calculated by BJH method.

**Figure 5.19** shows photographs of the photo electrode layers manufactured by synthesized TiO<sub>2</sub> sol under different aging conditions.

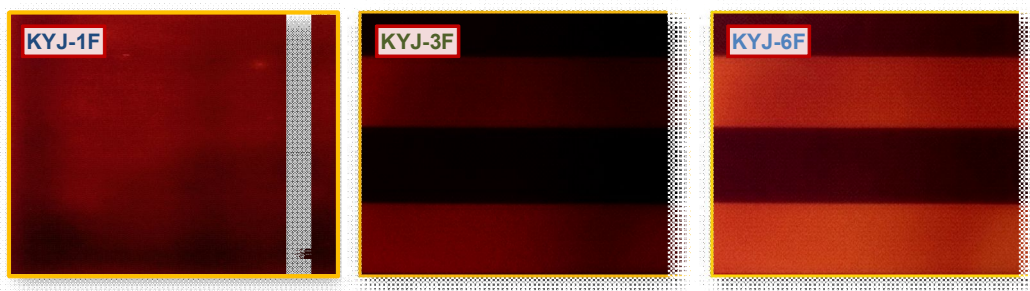


**Figure 5.19.** Photographs of photo electrode layers with a background of stripe.



The high transparency is one of the important factors for supporting the many application areas of the DSSC.<sup>52</sup> As shown in **Figure 5.19**, the KYJ-6F was transparent. We can see the clear stripes of the background because the KYJ-6F consisted of the small TiO<sub>2</sub> particles which were well dispersed. On the other hands, the KYJ-3F was semi-transparent with slightly stripes of background. However, the KYJ-1F was opaque and completely purple and we cannot see any stripes of background. The KYJ-1F consisted of the big TiO<sub>2</sub> particle which was aggregated. It has been reported that aggregated particles can diffuse visible light effectively.<sup>176</sup> Hence, the KYJ-1F was able to diffuse visible light. This is the reason why the layer of KYJ-1F was opaque. From this result, the transparency of the photo electrode can be changed by the aging conditions. It can be concluded that the aging conditions are controlling the various properties of TiO<sub>2</sub> film: particle size, surface area, roughness, crystalline phase, and transparency.

### **5.3.3 Adsorption Properties of TiO<sub>2</sub> Electrode by Aging**

It has been known that the performance of DSSC is closely related with the adsorption equilibrium amount of dye on TiO<sub>2</sub>. Thus it is appropriate to investigate the adsorption conditions optimized for improving their cell performance. In particular, the adsorption equilibrium amount of N719 dye on TiO<sub>2</sub> film is highly dependent on the BET surface area, crystalline size, and crystalline phase. In the current work, the N719 dye adsorption isotherms are obtained at different temperatures and different pHs. To analyze the experimental isotherm data, Langmuir (**Equation 3.5**) and Langmuir-Freundlich (**Equation 4.1**) isotherm equations were used.

Our previous work has shown that the photovoltaic performance of the dye-sensitized solar cells (DSSC) is closely related with the textural properties of TiO<sub>2</sub> and its adsorption equilibrium amount of dye as well as the coordination of dye adsorbed in TiO<sub>2</sub> film.<sup>66,88,168</sup> Therefore, it is necessary to systematically examine the effect of aging conditions on the adsorption characteristics (i.e., equilibrium and kinetics) of the dye in the TiO<sub>2</sub> film. In this study, dye N719 which has two bipyridyl ligands with two carboxyl groups at the 4 and 4' position of the bipyridyl group is used as model adsorbate. The adsorption equilibrium isotherm data (symbols) of dye N719 in the six different TiO<sub>2</sub> film samples at three

different temperatures (303.15, 318.15 and 333.15 K) are shown in **Figures 5.20** and **5.21** and their calculated Langmuir and Langmuir-Freundlich (LF) isotherm parameters are listed in **Table 5.8** and **Table 5.9**, respectively.

**Table 5.8.** Langmuir isotherm parameters of N719 dye on various TiO<sub>2</sub> films at three different temperatures

Sample No.	Temperature, K	$q_m$	$b$	$E^a$ , %
<b>KYJ-1F</b>	303	23.96	5.214	0.956
	318	24.02	10.25	1.411
	333	30.98	13.73	1.859
<b>KYJ-2F</b>	303	44.47	6.716	0.922
	318	50.37	12.10	1.615
	333	54.57	15.09	4.916
<b>KYJ-3F</b>	303	50.16	6.754	5.578
	318	56.69	12.39	2.094
	333	60.73	15.19	4.011
<b>KYJ-4F</b>	303	34.49	5.927	1.983
	318	35.00	11.32	1.965
	333	41.04	14.23	2.481
<b>KYJ-5F</b>	303	65.46	8.401	3.158
	318	67.61	12.42	3.000
	333	69.78	15.69	5.083
<b>KYJ-6F</b>	303	73.72	9.120	3.945
	318	75.76	12.64	2.850
	333	76.33	16.47	4.972

$$^a \text{Average percent error: } E(\%) = \frac{100}{n} \sum_{i=1}^n \left[ \frac{|q_{cal,i} - q_{exp,i}|}{q_{cal,i}} \right] .$$

As shown in these figures, all N719 dye adsorption equilibrium isotherms are concave to the concentration axis, revealing the class L (or Langmuir type) curves based on the Giles

classification and favorable systems.<sup>177</sup>

**Table 5.9.** Langmuir-Freundlich isotherm parameters of N719 dye on various TiO<sub>2</sub> films at three different temperatures

Sample No.	Temperature, K	$q_m$	$b$	$n$	$E^a$ , %
<b>KYJ-1F</b>	303	24.04	5.18	0.998	0.347
	318	24.25	10.03	0.990	0.753
	333	31.38	13.32	0.984	1.336
<b>KYJ-2F</b>	303	45.55	6.38	0.985	0.845
	318	51.55	11.46	0.974	1.039
	333	56.34	13.93	0.970	3.641
<b>KYJ-3F</b>	303	51.30	6.43	0.983	4.885
	318	58.35	11.57	0.967	2.258
	333	62.21	14.34	0.968	4.798
<b>KYJ-4F</b>	303	34.64	5.87	0.997	1.857
	318	35.40	11.03	0.988	1.362
	333	41.65	13.74	0.981	2.033
<b>KYJ-5F</b>	303	66.89	8.00	0.981	0.704
	318	69.78	11.52	0.964	2.741
	333	72.87	14.12	0.944	2.780
<b>KYJ-6F</b>	303	74.82	8.84	0.978	0.884
	318	78.45	11.63	0.960	3.881
	333	79.74	14.80	0.941	4.980

Moreover the adsorption equilibrium amount of N719 increases with the temperature, indicating an endothermic process. This result can be attributed to an increase in the mobility of N719 dye onto TiO<sub>2</sub> film at higher temperatures and to the chemical interactions the N719 dye and the surface of TiO<sub>2</sub> film. It was also found that between the adsorption equilibrium amount and textural properties of TiO<sub>2</sub> film were clearly correlated. The obtained adsorption equilibrium amount of N719 dye in the TiO<sub>2</sub> film samples are in

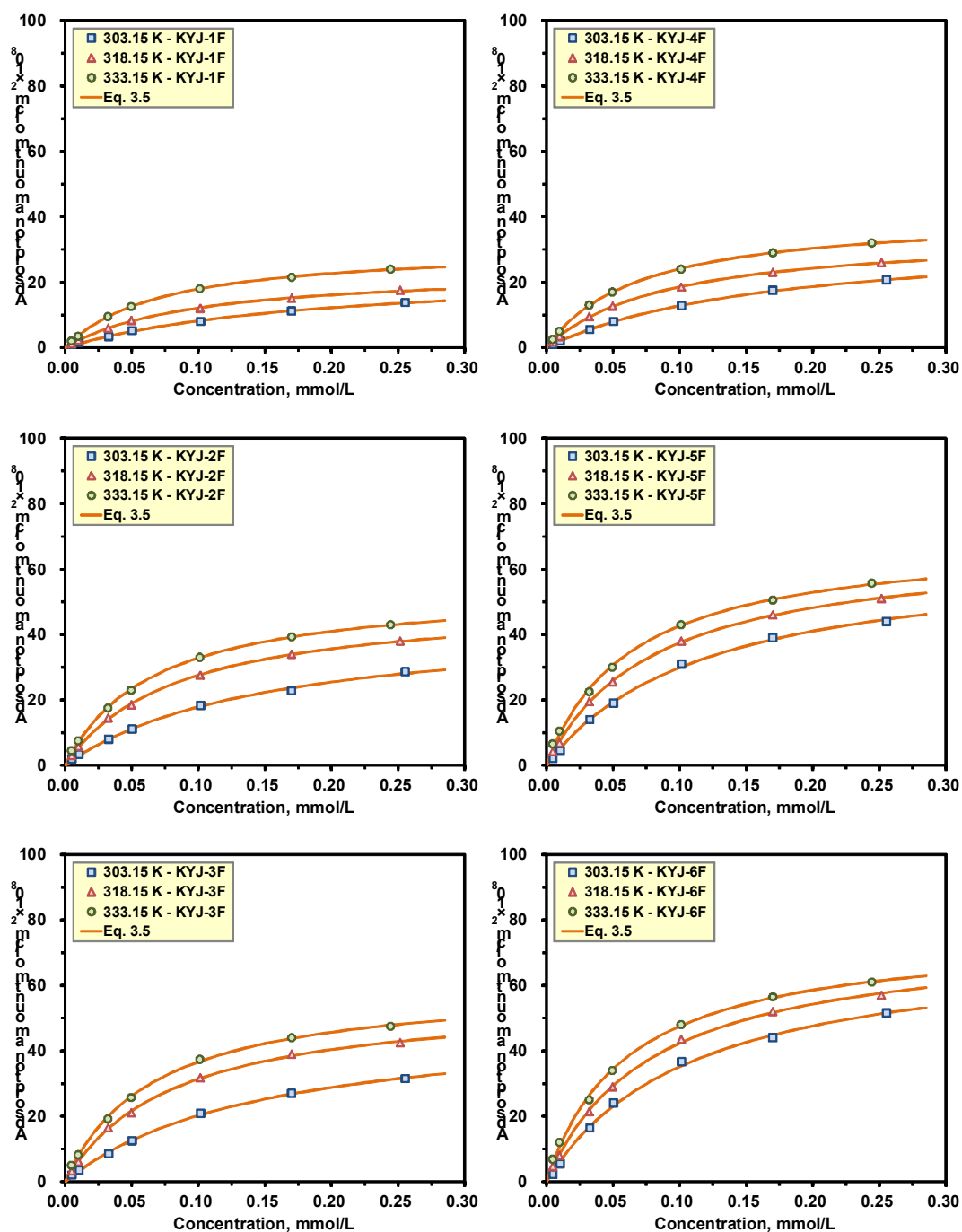


**Figure 5.20.** Adsorption isotherms of N719 on KYJ-TiO<sub>2</sub> film series at three different temperatures (Langmuir equation).

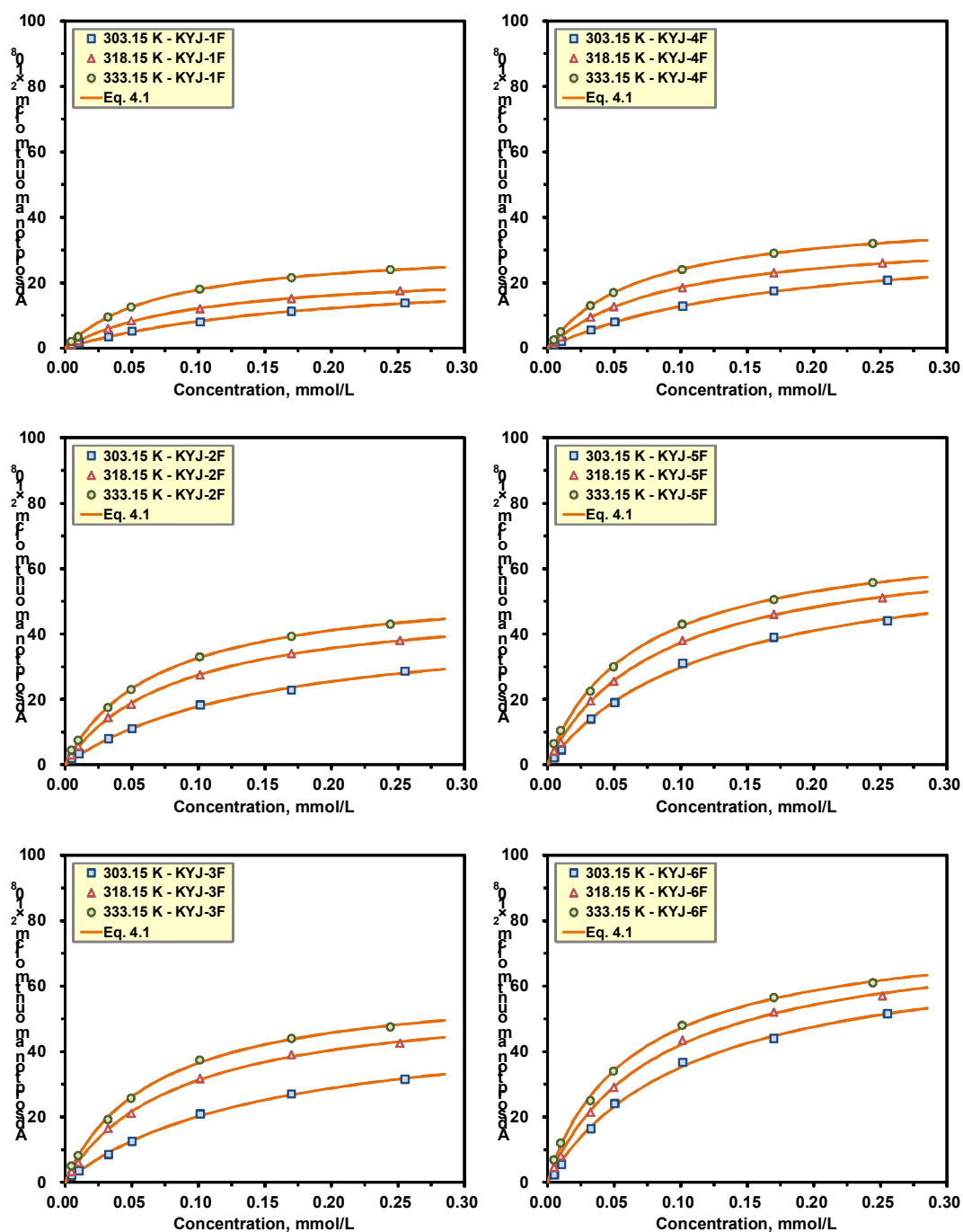


**Figure 5.21.** Adsorption isotherms of N719 on KYJ-TiO<sub>2</sub> film series at three different temperatures (Langmuir-Freundlich equation).

the order of KYJ-6F > KYJ-5F > KYJ-3F > KYJ-2F > KYJ-4F > KYJ-1F, which is identical with that of the BET surface area and the total pore volume. In addition, the adsorption capacities of N719 dye are closely related with the anatase ratio, the surface roughness, the fractal dimension and the size of anatase crystalline phase. As shown in **Figure 5.16** and **Table 5.5**, it is apparent that the higher the anatase ratio and the larger the anatase crystalline phase size, the greater adsorption equilibrium amount. In other words, TiO<sub>2</sub> films having anatase ratio of 100 % exhibits higher adsorption equilibrium amount of N719 dye than that of TiO<sub>2</sub> films having anatase ratio of 91 and 71%. In the case of TiO<sub>2</sub> films having the same anatase ratio (100%), the adsorption equilibrium amount increase with the anatase crystalline phase size. The values of the surface roughness (or fractal dimension) for TiO<sub>2</sub> film also increased with the aging time irrespective of the aging temperature (**Table 5.6**).

On the other hand, the solid lines in **Figure 5.20** and **5.21** are the fitting results. As can be seen, the Langmuir and LF isotherms are found to adequately represent the N719 adsorption isotherm data. It is found that these isotherm parameters  $q_m$  and  $b$  increase with temperature and are observed to increase in the order of KYJ-1F < KYJ-4F < KYJ-2F < KYJ-3F < KYJ-5F < KYJ-6F, which is correctly identical with that of the BET surface area and pore volume (see **Table 5.8**).

Moreover, the heterogeneity parameter  $n$  (LF isotherm) decreases with increasing temperature for all samples, implying the greater surface heterogeneity at higher temperatures (see **Table 5.9**). The heterogeneity parameter also is in the order KYJ-1F > KYJ-4F > KYJ-2F > KYJ-3F > KYJ-5F > KYJ-6F, which is the same as that of the BET surface area and pore volume. These results indicate that the TiO<sub>2</sub> film having the higher BET surface area and pore volume represent the stronger adsorption interaction for N719 dye and these textural properties as well as the crystallinity of the TiO<sub>2</sub> film also plays a key role in the N719 dye adsorption.

In general, the initial pH of the solution plays a key role in the adsorption process, since it could affect the surface charge of the adsorbent and the ionic and structural properties of adsorbate (or N719 dye) as well as the interaction between the adsorbate and the adsorbent. To examine the effect of solution pH on the dye adsorption, the adsorption equilibrium isotherm of dye N719 are also obtained for the six different TiO<sub>2</sub> films at

three different pH values (pH 3, 5, and 7) under the same condition of 333.15 K.

**Table 5.10.** Langmuir isotherm parameters of N719 dye on various TiO<sub>2</sub> films in terms of pH at 333.15 K

Sample No.	pH	$q_m$	$b$	$E^a$ , %
<b>KYJ-1F</b>	3	29.62	60.03	1.917
	5	26.70	46.79	0.730
	7	20.18	35.32	1.306
<b>KYJ-2F</b>	3	43.39	66.79	4.157
	5	38.78	62.62	2.588
	7	26.30	55.11	3.052
<b>KYJ-3F</b>	3	57.66	69.52	1.210
	5	52.63	64.35	2.034
	7	39.54	55.96	3.672
<b>KYJ-4F</b>	3	42.90	61.32	3.618
	5	38.15	59.34	2.246
	7	25.70	45.63	3.922
<b>KYJ-5F</b>	3	58.30	81.50	2.778
	5	52.75	78.94	1.686
	7	39.94	65.72	1.452
<b>KYJ-6F</b>	3	76.39	86.74	1.604
	5	69.49	79.79	2.321
	7	49.25	67.35	0.925

**Figures 5.22 and 5.23** show their adsorption isotherms plotted as adsorbed equilibrium amount versus aqueous phase equilibrium concentration. This result also clearly proves that the N719 dye adsorption is highly dependent on the solution pH as well as the textural and crystalline properties of TiO<sub>2</sub> films and the system temperature. The adsorption equilibrium amount increases with decreasing the initial pH for all the samples studied, suggesting that the N719 dye adsorption is more favorable at acidic condition.

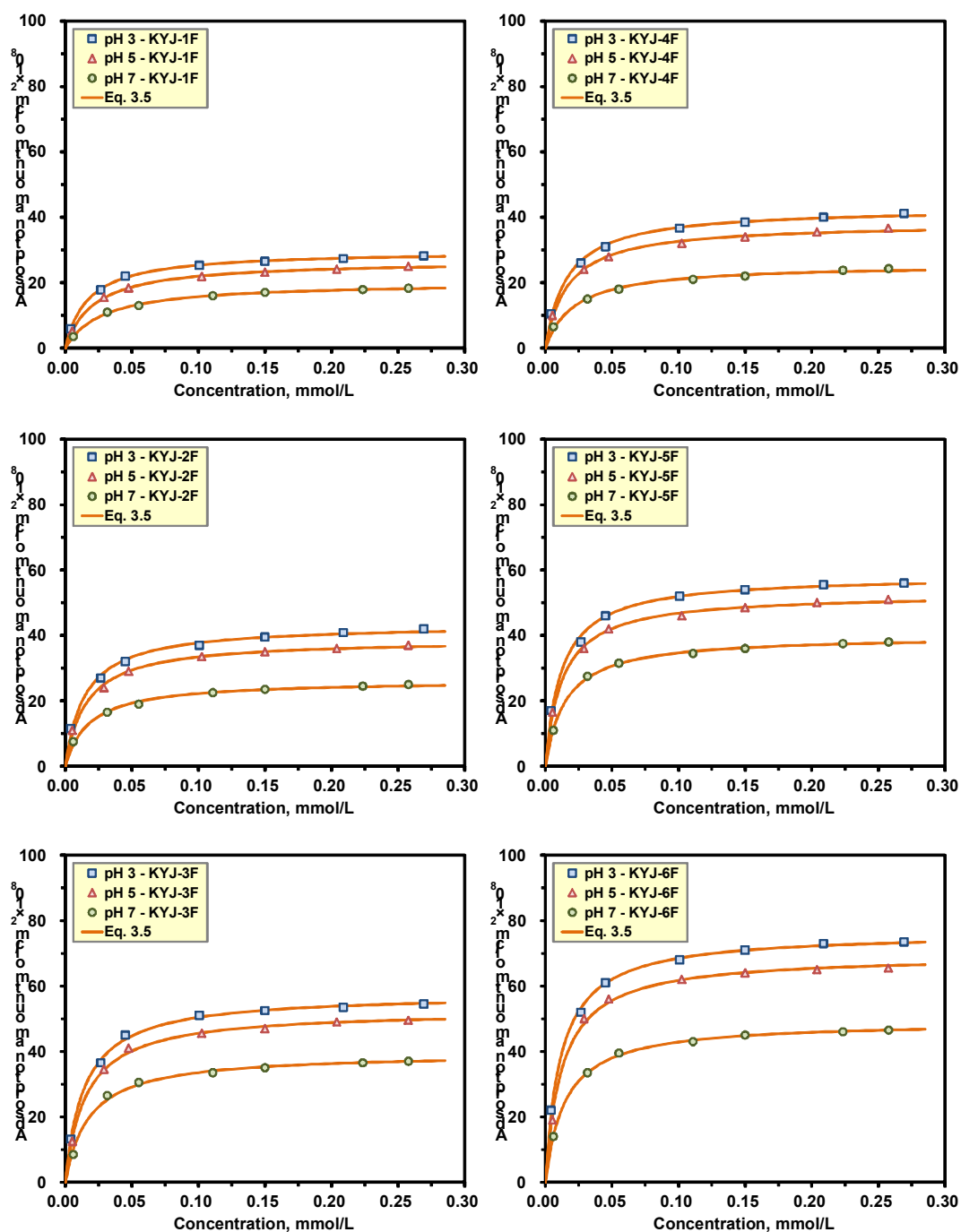


**Figure 5.22.** Adsorption isotherms of N719 on KYJ-TiO<sub>2</sub> film series at three different pH (Langmuir equation).



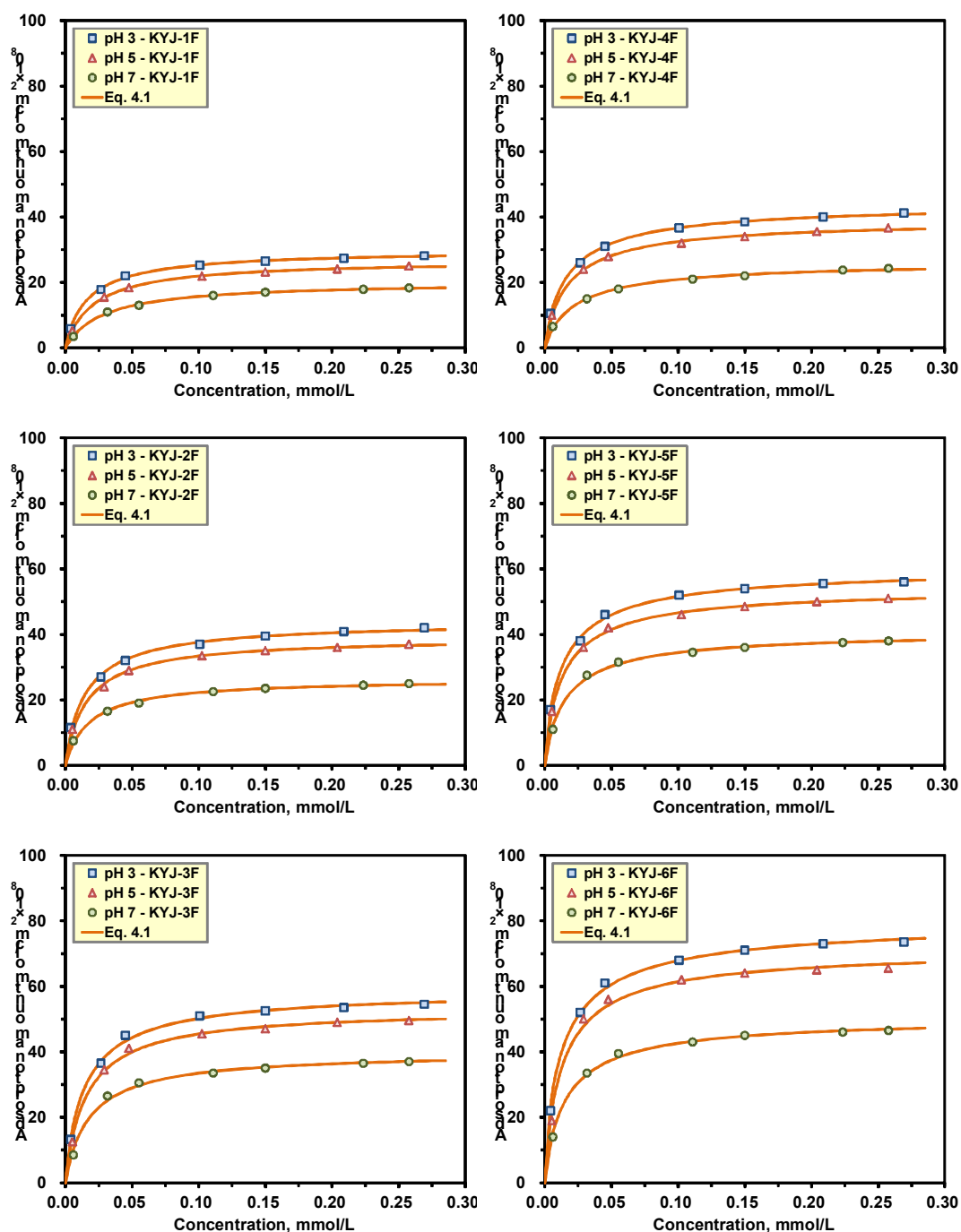


**Figure 5.23.** Adsorption isotherms of N719 on KYJ-TiO<sub>2</sub> film series at three different pH (Langmuir-Freundlich equation).

**Table 5.11.** Langmuir-Freundlich isotherm parameters of N719 dye on various TiO<sub>2</sub> films in terms of pH at 333.15 K

Sample No.	pH	$q_m$	$b$	$n$	$E^a$ , %
<b>KYJ-1F</b>	3	30.12	58.41	0.943	1.067
	5	26.96	45.86	0.971	0.711
	7	20.31	34.83	0.983	1.305
<b>KYJ-2F</b>	3	44.18	64.60	0.936	2.839
	5	39.13	61.48	0.969	1.840
	7	26.52	54.07	0.974	1.146
<b>KYJ-3F</b>	3	58.92	66.91	0.921	2.376
	5	53.22	62.93	0.961	2.517
	7	39.94	54.72	0.968	4.067
<b>KYJ-4F</b>	3	44.27	57.69	0.898	1.498
	5	39.34	55.54	0.905	0.900
	7	26.57	42.31	0.910	2.249
<b>KYJ-5F</b>	3	60.66	75.49	0.860	1.278
	5	54.34	74.36	0.894	0.936
	7	41.05	61.97	0.908	2.315
<b>KYJ-6F</b>	3	80.60	77.57	0.817	1.419
	5	71.57	75.51	0.890	1.345
	7	50.75	63.30	0.898	2.170

This result is related with the electrostatic interactions between the N719 dye exhibiting a negative charge in ethanol solution and the surface of TiO<sub>2</sub> film representing a positive charge in acidic condition. Thus the higher N719 dye adsorption is achieved at lower pHs. Langmuir and Langmuir-Freundlich (LF) isotherm were also used to correlate the N719 dye adsorption equilibrium isotherm data and their determined parameters were listed in **Tables 5.10** and **5.11**, respectively. As shown in these figures and tables, the adsorption of N719 dye in TiO<sub>2</sub> films is well represented by the Langmuir and LF isotherm model equations. In addition the isotherm parameters determined represent similar tendencies, which are

observed from the temperature effect on the N719 dye adsorption. In other words, the isotherm parameters  $q_m$  and  $b$  decrease with increasing pHs irrespective of the model equation, but the heterogeneity parameter  $n$  increase with pHs. This result reveals that the degree of heterogeneity increased at lower pHs and larger BET surface area and pore volume.

To further investigate the adsorption processes and the adsorbed state of N719 dye in TiO<sub>2</sub> films prepared at different conditions, several thermodynamic functions [i.e., the adsorption free energy ( $\Delta G^\circ$ ), enthalpy ( $\Delta H^\circ$ ) and entropy ( $\Delta S^\circ$ )] are calculated using the Langmuir isotherm constant and the Van't Hoff equation. **Table 5.12** lists the model equations used in this study. These parameters give valuable information about the adsorption mechanism existed between the N719 (adsorbate) and the TiO<sub>2</sub> film (adsorbent).

**Table 5.12.** Thermodynamic parameters

<b>(a) Adsorption free energy (<math>\Delta G^\circ</math>)</b>	
$\Delta G^\circ = -RT \ln b$	<b>(Eq. 5.7)</b>
where $b$ is the Langmuir equation constant, $R$ is the gas constant and $T$ is the temperature.	
<b>(b) Van't Hoff equation</b>	
$\ln b = \frac{\Delta S^\circ}{R} - \frac{\Delta H^\circ}{RT}$	<b>(Eq. 5.8)</b>
where $b$ is the Langmuir equation constant, $R$ is the gas constant, $T$ is the temperature, $\Delta H^\circ$ is the adsorption enthalpy and $\Delta S^\circ$ is the adsorption entropy.	

**Table 5.13** shows the thermodynamic parameters determined for N719 dye adsorption on the six different TiO<sub>2</sub> films. The obtained thermodynamic values can be classified into two main groups: i) negative values of adsorption free energy ( $\Delta G^\circ$ ) and ii) positive values of enthalpy ( $\Delta H^\circ$ ) and entropy ( $\Delta S^\circ$ ). As shown in **Table 5.13**, the adsorption free energy values ( $\Delta G^\circ$ ) are negative for all cases and become gradually lower (or smaller) as the temperature increases. Thus it is reasonable to suggest that the N719 dye adsorption for TiO<sub>2</sub> film is spontaneous process closing to the physisorption region (-20 to 0 kJ/mol) rather than the chemisorption region (-80 to -400 kJ/mol) and favorable process thermo-

dynamically leading to a corresponding increase in the adsorption equilibrium amount at higher temperatures.

**Table 5.13.** Thermodynamic parameters of N719 dye (Gibbs energy, enthalpy and entropy)

Sample No.	$\Delta G^\circ$			$\Delta H^\circ$ , KJ/mol·K	$\Delta S^\circ$ , J/mol·K
	303.15 K	318.15 K	333.15 K		
<b>KYJ-1F</b>	-4.162	-6.156	-7.256	27.25	104.06
<b>KYJ-2F</b>	-4.800	-6.595	-7.517	22.80	91.49
<b>KYJ-3F</b>	-4.814	-6.657	-7.536	22.55	90.79
<b>KYJ-4F</b>	-4.485	-6.419	-7.354	24.68	96.70
<b>KYJ-5F</b>	-5.364	-6.664	-7.625	17.54	75.72
<b>KYJ-6F</b>	-5.571	-6.710	-7.760	16.56	73.04

In addition, the adsorption enthalpy ( $\Delta H^\circ$ ) and entropy ( $\Delta S^\circ$ ) values are positive for the whole adsorption tests, reflecting the endothermic process of N719 dye adsorption and the increased degree of freedom (or randomness) between N719 dye and TiO<sub>2</sub> film, respectively. It is also noted that the thermodynamic values are gradually increased (or decreased) with increasing the aging time under the same aging temperature. Moreover, the TiO<sub>2</sub> films prepared at 363.15 K have relatively lower (or higher for  $\Delta G^\circ$ ) thermodynamic values than that of the TiO<sub>2</sub> films prepared at 313.15 K. Also the entropy ( $\Delta S^\circ$ ) values are increased with increasing the enthalpy ( $\Delta H^\circ$ ) values. The magnitudes of adsorption enthalpy and entropy are in the order of KYJ-1F > KYJ-4F > KYJ-2F > KYJ-3F > KYJ-5F > KYJ-6F, which is identical with that of the BET surface area and the pore volume. On the whole, the TiO<sub>2</sub> films having pure anatase phase have lower adsorption enthalpy and entropy values compared to that of the TiO<sub>2</sub> films composing both anatase and rutile phase. It is also interesting to note that the larger the anatase crystalline phase size, the smaller is the adsorption enthalpy and entropy. This result implies that the interaction between N719 dye and TiO<sub>2</sub> film is highly dependent on the textural and

anatase crystalline phase.

Adsorption energy distribution (AED) function has been also used to characterize porous solid surfaces having complex porous structure and chemical composition.

**Table 5.14.** AED parameters of N719 dye on various TiO<sub>2</sub> films in terms of pH

Sample No.	pH	Peak location, kJ/mol	Peak width, kJ/mol	Peak max, kJ/mol	Peak height, mol/kJ
<b>KYJ-1F</b>	3	2.94-15.34	12.40	9.24	0.176
	5	2.10-14.50	12.40	8.61	0.180
	7	1.05-13.66	12.61	7.77	0.179
<b>KYJ-2F</b>	3	0-18.49	18.49	9.45	0.125
	5	1.89-17.44	15.55	9.24	0.146
	7	1.05-15.97	14.92	8.82	0.153
<b>KYJ-3F</b>	3	4.41-15.13	10.72	9.66	0.197
	5	4.20-14.71	10.51	9.45	0.207
	7	3.99-14.08	10.09	9.24	0.214
<b>KYJ-4F</b>	3	0.84-17.65	16.81	9.45	0.137
	5	0-16.18	16.18	9.45	0.153
	7	0-14.50	14.50	8.40	0.164
<b>KYJ-5F</b>	3	3.15-18.07	14.92	9.87	0.150
	5	2.73-16.39	13.66	9.87	0.164
	7	3.99-14.92	10.93	9.66	0.195
<b>KYJ-6F</b>	3	3.78-16.81	13.03	10.29	0.169
	5	5.04-15.34	10.30	10.08	0.207
	7	4.20-14.50	10.30	9.45	0.211

This function can substantially provides valuable information on the interactions between the probe molecule and the solid surface. In this work, Langmuir-Freundlich (LF) equation and the generalized nonlinear regularization method were used to calculate the AED function, which were summarized in **Table 4.4** (see **Equation 4.2**).

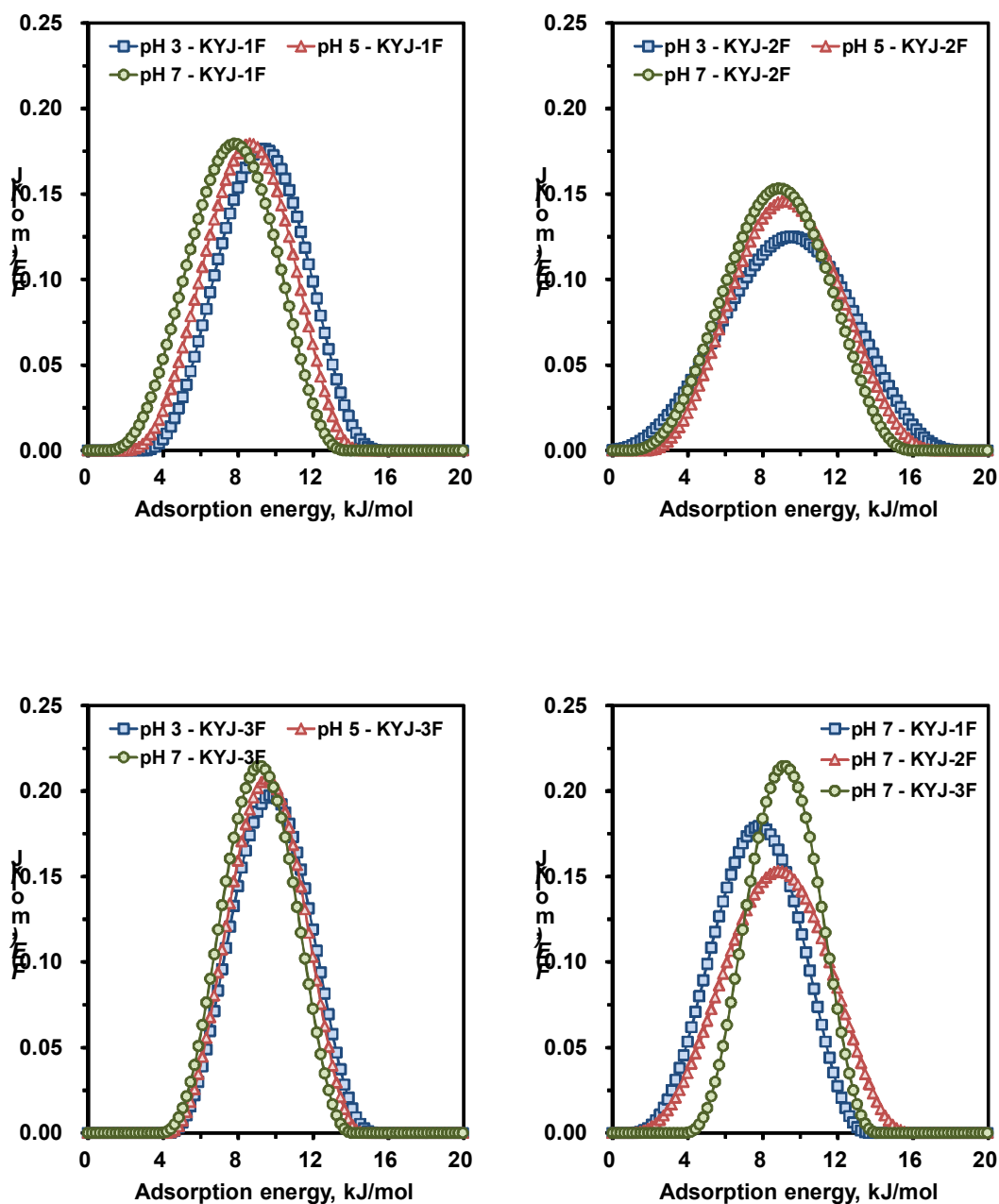


**Figure 5.24.** Calculated adsorption energy distribution curves for KYJ-1F, KYJ-2F and KYJ-3F at three different pHs.

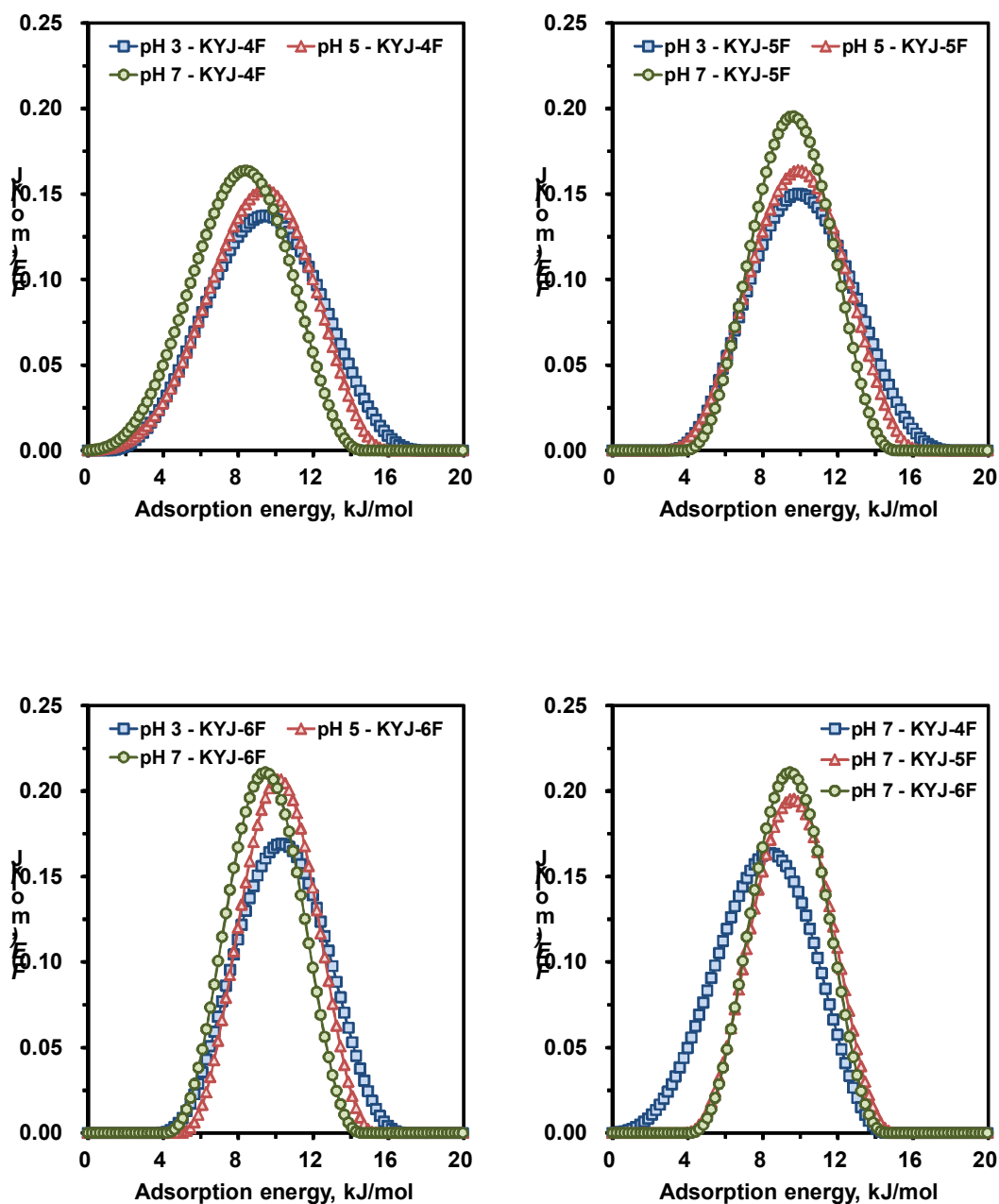


**Figure 5.25.** Calculated adsorption energy distribution curves for KYJ-4F, KYJ-5F and KYJ-6F at three different pHs.

In particular, the AED functions are calculated using the data points below the monolayer coverage which were determined from the LF equation. Detailed explanation for calculating the AED function can be found in elsewhere.<sup>81,82,84</sup>

**Figures 5.24**, and **5.25** and **Table 5.14** show the variation of the AED curves for N719 dye on TiO<sub>2</sub> films prepared at different aging conditions in different pH values. The calculated AED functions represent only one peak for all of the TiO<sub>2</sub> films, supporting the presence of one type of surface energy on the TiO<sub>2</sub> samples. Furthermore, the peak height and shape of AED curves became gradually lower and broader and the peak location also was shifted toward the upper energy when the pH was decreasing from 7 to 3 except for the AED pattern of the KYJ-1F. For example, the pronounced peak maximum (or the peak width) of the AED function for KYJ-6F sample were about 9.45 (10.3), 10.1 (10.3), and 10.3 (13.0) kJ/mol, for pH 7, pH 5, and pH 3 respectively. In addition the peak height values of the same sample and for the same pHs are 0.211, 0.207 and 0.169 mol/kJ respectively. The peak maximum of the AED function is shifted about 0.8 kJ/mol to the higher energy as increase the pH values. This results clearly indicate that the adsorption interactions between the N719 dye and the surface of TiO<sub>2</sub> films are enhanced with the decreasing the pHs.

The characteristics of the AED function are also well correlate with the degree of surface heterogeneity of the TiO<sub>2</sub> films. As increasing the LF parameter ( $n$ ) value, the peak width and the peak height of AED curves became narrow and high, respectively. The shifting of the curves toward the relatively lower energies with increasing the heterogeneity parameter  $n$  is also observed. This result also implies that the interaction between the N179 dye molecules and the TiO<sub>2</sub> film increased with the surface heterogeneity.

**Figure 5.24** (lower right side) and **Figure 5.25** (lower right side) compare the calculated AED curves for N719 dye on different TiO<sub>2</sub> films in the same value of pH (pH 7). Contrary to our expectations, there is no clear correlation between the AED peaks and the TiO<sub>2</sub> films. With the increase of BET surface area and pore volume, the peak maximum values and the peak width of AED curves are also increased and narrowed, respectively.

The variations of the AED curves for N719 dye on the same TiO<sub>2</sub> films investigated at three different temperatures are also shown in **Figures 5.26** and **5.27** and **Table 5.15**. The AED peak shape and patterns are generally similar to that of the AED curves obtained at



three different pHs.

**Table 5.15.** AED parameters of N719 dye on various TiO<sub>2</sub> films in terms of temperature

Sample No.	Temperature, K	Peak location, kJ/mol	Peak width, kJ/mol	Peak max, kJ/mol	Peak height, mol/kJ
<b>KYJ-1F</b>	303.15	0-7.14	7.14	2.94	0.227
	318.15	0-9.03	9.03	3.78	0.223
	333.15	0-10.50	10.50	4.62	0.198
<b>KYJ-2F</b>	303.15	0-7.56	7.56	3.15	0.238
	318.15	0-9.45	9.45	3.99	0.218
	333.15	0-11.13	11.13	4.83	0.192
<b>KYJ-3F</b>	303.15	0-7.56	7.56	3.15	0.241
	318.15	0-9.66	9.66	4.20	0.213
	333.15	0-11.13	11.13	5.04	0.191
<b>KYJ-4F</b>	303.15	0-7.35	7.35	3.15	0.236
	318.15	0-9.45	9.45	3.99	0.218
	333.15	0-10.71	10.71	4.83	0.195
<b>KYJ-5F</b>	303.15	0-7.98	7.98	3.36	0.242
	318.15	0-9.66	9.66	4.20	0.213
	333.15	0-11.13	11.13	4.83	0.193
<b>KYJ-6F</b>	303.15	0-8.19	8.19	3.78	0.237
	318.15	0-9.66	9.66	4.62	0.213
	333.15	0-11.55	11.55	5.04	0.188

The higher the system temperature, the broader and lower is the AED curve. In addition, a gradual shift of the distribution peak location toward higher adsorption energies was observed as the system temperature increased. In other words, by increasing system temperature from 303.15 to 333.15 K, the AED peak height of KYJ-6F for N719 dye decreased from 0.237 to 0.188 mol/kJ; conversely, the AED peak width increased from 8.1-

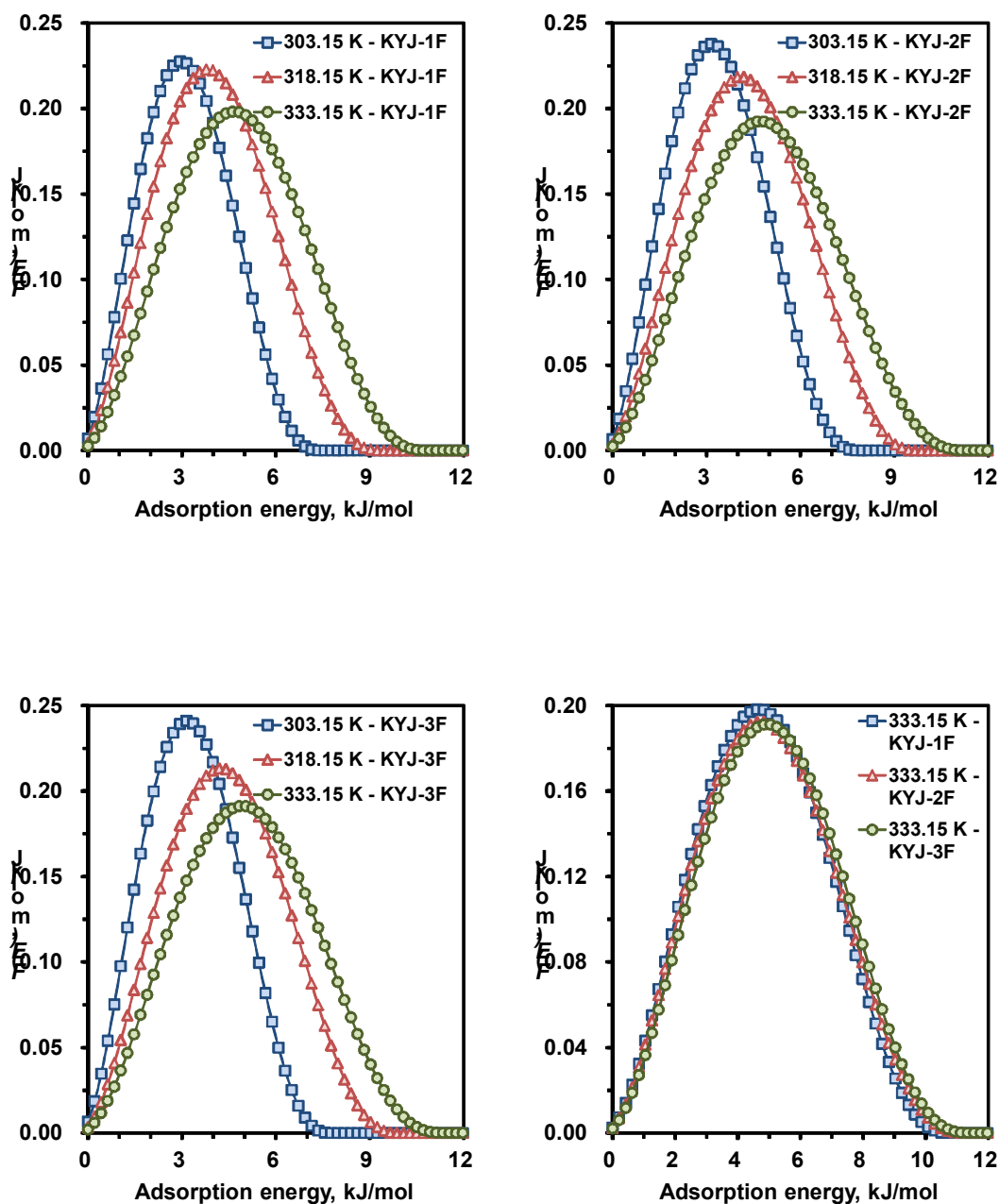


**Figure 5.26.** Calculated adsorption energy distribution curves for KYJ-1F, KYJ-2F and KYJ-3F at three different temperatures.

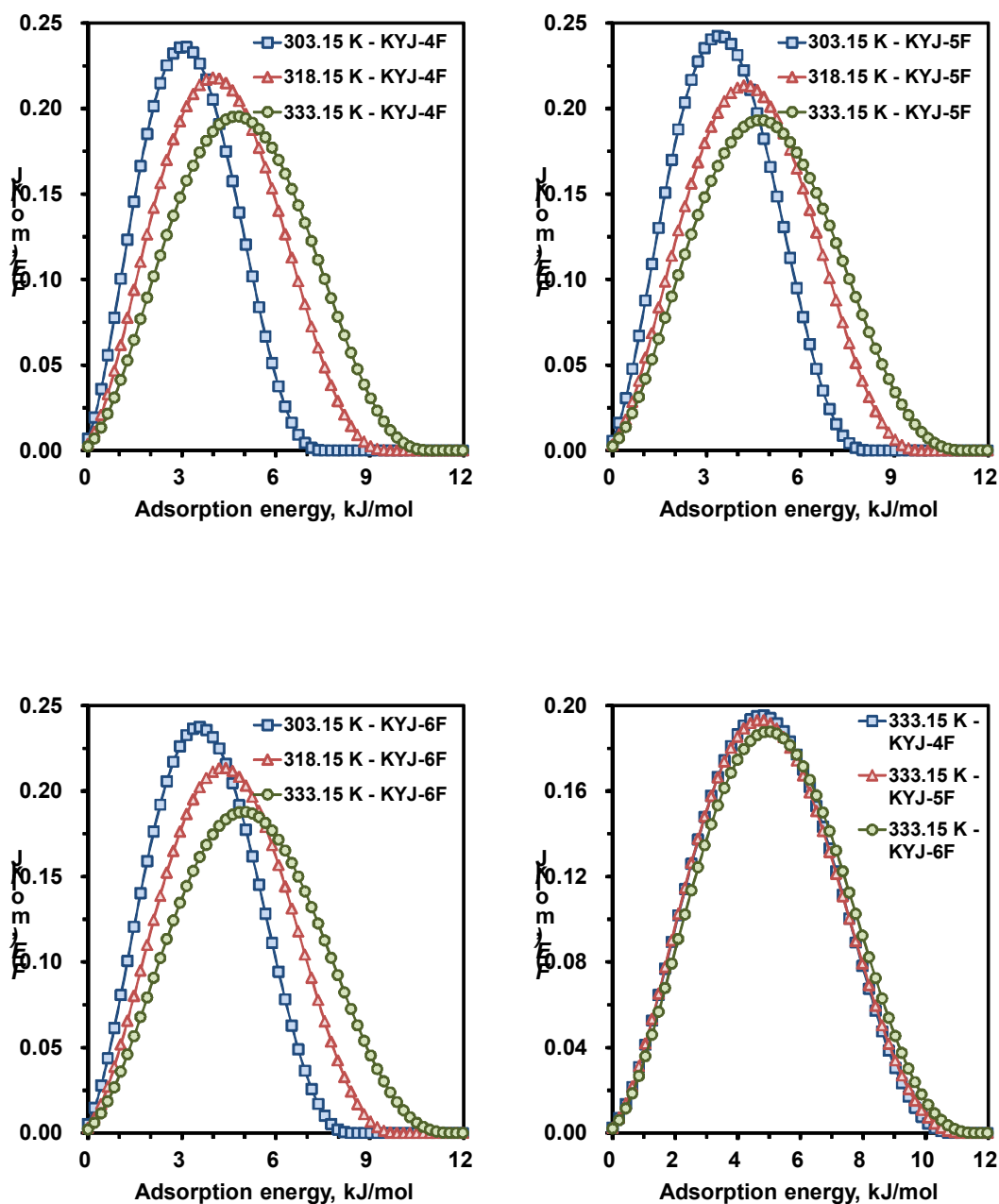


**Figure 5.27.** Calculated adsorption energy distribution curves for KYJ-4F, KYJ-5F and KYJ-6F at three different temperatures.

9 to 11.55 kJ/mol. In addition, the pronounced maximum of the AED curve for KYJ-6F sample are 3.78 (303.15 K), 4.62 (318.15 K), and 5.04 (333.15 K) kJ/mol, respectively. On the other hand, **Figure 5.26** (lower right side) and **Figure 5.27** (lower right side) compare the calculated AED functions for N719 dye on TiO<sub>2</sub> films aged at the same temperature (333.15 K). As can be seen, the AED curves have a close relation with the textural properties of TiO<sub>2</sub> films, although the difference between the peak width and the peak height of the AED curves is small. It is evident that the increase in adsorption energy may be mainly attributed to both the increase of surface area and pore volume and the difference in the size of anatase crystalline phase and the ratio of anatase-rutile. The larger the BET surface area (or pore volume), the lower and broader are the AED curves. The peak maxima also are shifted toward higher adsorption energy when those values increased. Moreover, the similar tendency is also observed for heterogeneity parameter  $n$ . The AED curves become gradually lower and broader with decreasing the parameter  $n$ . In addition, the peak maximum value of AED curves was increased with decreasing the parameter  $n$ .

#### **5.3.4 Photovoltaic Performance of TiO<sub>2</sub> Electrode by Aging**

To investigate the influence of aging conditions on the photovoltaic performance of TiO<sub>2</sub> thin films, several key factors such as the current density ( $I_{sc}$ ), open circuit voltage ( $V_{oc}$ ), fill factor ( $FF$ ), and energy conversion efficiency ( $\eta_{eff}$ ) are measured and compared in **Figure 5.28** and **Table 5.16**. Based on the adsorption isotherm result, the TiO<sub>2</sub> thin films were immersed in a solution containing 0.3 mM N719 dye at pH 3 and 333.15 K for 12 h to make the optimized DSSC. As can be seen, the photovoltaic performances are closely related with the textural properties and the crystallinity of TiO<sub>2</sub> films. On the whole the TiO<sub>2</sub> films prepared at 363.15 K have relatively higher energy conversion efficiency and the current density than that of the TiO<sub>2</sub> films prepared at 313.15 K. In addition, the longer the aging time at the same aging temperature, the higher photovoltaic the performance is. It is also found that the TiO<sub>2</sub> films exhibiting 100% anatase phase have relatively higher photovoltaic performance than that of the TiO<sub>2</sub> films consisting of both anatase and rutile phase.

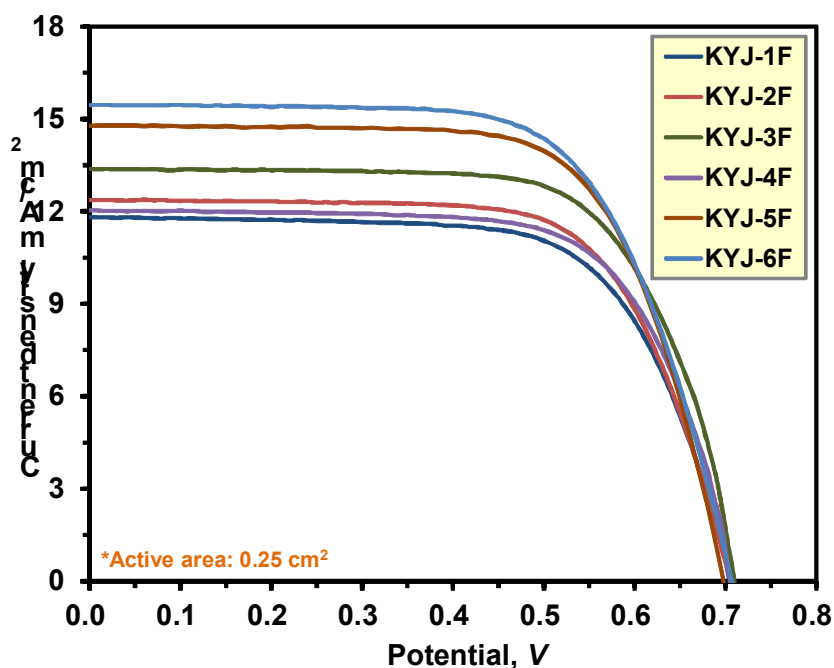


**Figure 5.28.** *I-V* curves of KYJ-TiO<sub>2</sub> film series under different aging conditions.

Moreover, in the case of the TiO<sub>2</sub> films exhibiting the same crystallite phase, the larger crystallite size, the surface area, the pore volume, the higher photovoltaic performance is.

**Table 5.16.** Photovoltaic performance of DSSC for KYJ-TiO<sub>2</sub> film series under different aging conditions

Sample No.	Aging temperature, K	Aging time, h	Film thickness, $\mu\text{m}$	$I_{sc}$ , $\text{mA}/\text{cm}^2$	$V_{oc}$ , V	Fill factor, FF	$\eta_{eff}$ , %
KYJ-1F	313.15	0	7.0	11.8	0.71	0.67	5.6
KYJ-2F		24	7.0	12.9	0.71	0.68	6.0
KYJ-3F		72	7.0	13.4	0.70	0.69	6.6
KYJ-4F	363.15	0	7.0	12.0	0.71	0.69	5.9
KYJ-5F		24	7.0	14.8	0.71	0.68	7.1
KYJ-6F		72	7.0	15.6	0.71	0.66	7.3

**Figure 5.29** shows the Nyquist plots of TiO<sub>2</sub> thin film based DSSC which are prepared at different aging temperature and aging time.

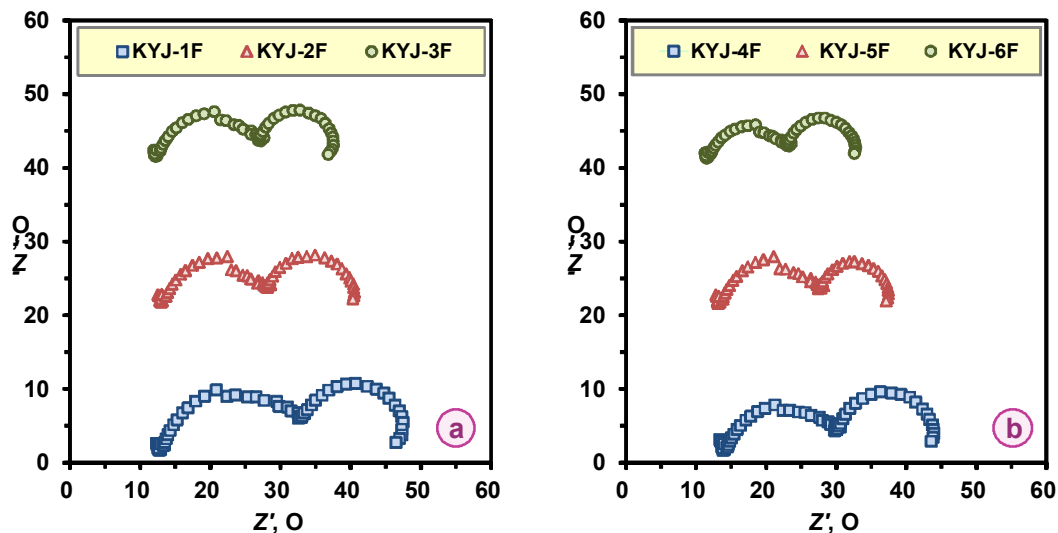


**Figure 5.29.** Nyquist plots of KYJ-TiO<sub>2</sub> film series with various aging time at (a) 313.15 K (b) 363.15 K.

As can be seen, a large semicircle at low frequencies and a small one at high frequencies are observed for all solar cells. In general, the frequency responses can be classified into three regions: i) high frequency range ( $10^3$ - $10^6$  Hz) corresponding to charge transfer processes occurring at the Pt/electrolyte interface, ii) intermediate frequency range ( $1$ - $10^3$  Hz) representing the resistance occurred at the TiO<sub>2</sub>/dye/electrolyte interface, and iii) low frequency range ( $0.1$ - $1$  Hz) relating with the Nernst diffusion within the electrolyte. As shown in **Figure 5.29**, the resistance occurred at the TiO<sub>2</sub>/dye/electrolyte interface decreased with increasing aging time and temperature, implying that the electron transport in the rutile layer (KYJ-1F and KYJ-1F) is slower than in the anatase layer (KYJ-2F, KYJ-3F, KYJ-5F and KYJ-6F).<sup>77</sup> In addition, the larger the anatase crystallite size and the surface area and pore volume, the lower is the resistance. The **KYJ-4F-6F** thin films based DSSC which are prepared at higher temperature (363.15 K) represent relatively lower resistance compared to that of **KYJ-1F-3F** thin films based DSSC (see **Figure 5.29a**).

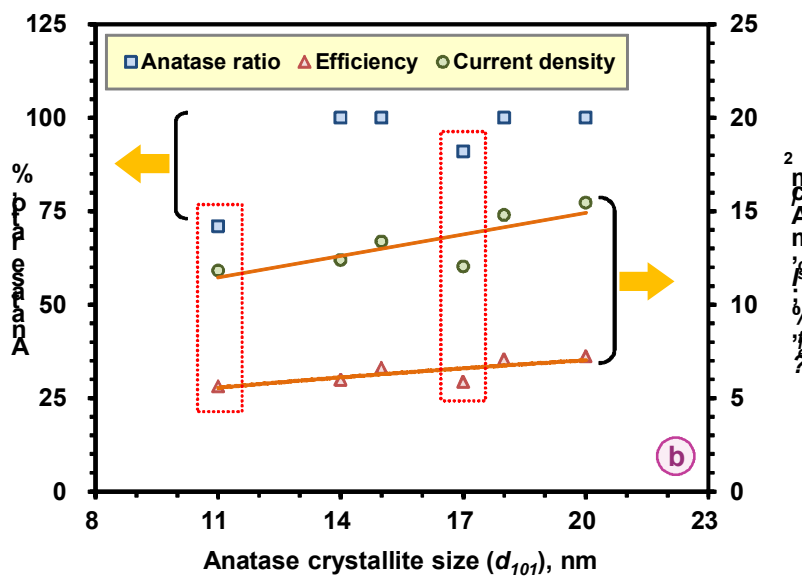
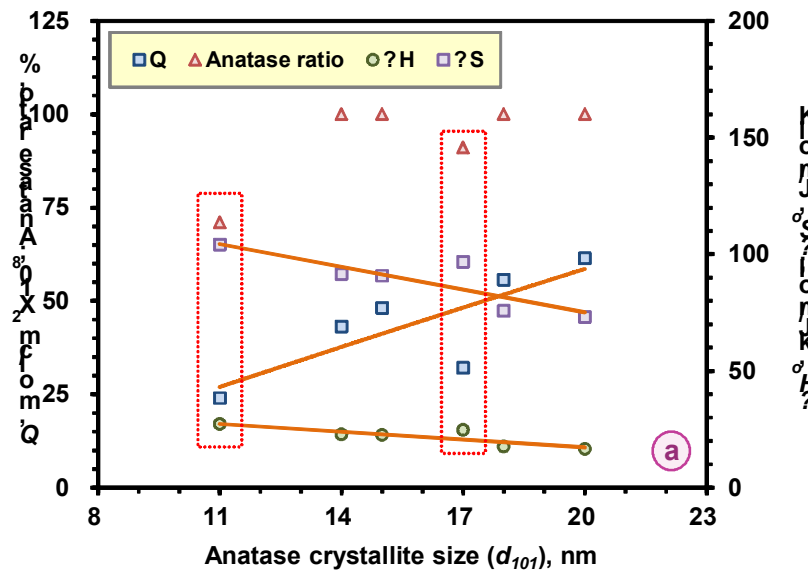


**Figure 5.30.** (a) Correlation plot between crystallite size-adsorption (b) crystallite size-photovoltaic properties.

**Figure 5.30** clearly demonstrates that the photovoltaic performance has a close connection with the anatase crystallite size, N719 dye adsorption amount ( $Q$ ) and thermodynamic parameters ( $\Delta H^\circ$  and  $\Delta S^\circ$ ). It is evident that the larger crystallite sizes are more favorable for enhancing the photovoltaic properties ( $\eta_{eff}$  and  $I_{sc}$ ) and the N719 dye adsorption amount irrespective of their composition ratio. On the whole, the  $\eta_{eff}$  and the  $I_{sc}$  of the  $\text{TiO}_2$  film increased linearly with the crystallite size although the  $\text{TiO}_2$  film consisting of both anatase and rutile phase give slightly lower  $\eta_{eff}$  and the  $I_{sc}$  than that of the  $\text{TiO}_2$  film having pure anatase phase. In addition, the  $\text{TiO}_2$  film (KYJ-4F) having relatively higher anatase phase (91%) exhibit slightly higher photovoltaic performance than that of the film (KYJ-1F) representing lower anatase phase (71%), which is attribute to its higher N719 dye adsorption amount and lower  $\Delta H^\circ$  and  $\Delta S^\circ$  (see **Figure 5.30a** dotted square). Moreover, the pure anatase (100%) phase films exhibit much higher photovoltaic performance compared to that of the anatase-rutile mixture phase films, which is closely related with the N719 dye adsorption characteristics. In other words, the greater the N719 dye adsorption amount and the lower the adsorption enthalpy and the adsorption entropy, the higher the  $\eta_{eff}$  and the  $I_{sc}$ .

The optimal condition for the highest efficiency of DSSC was chosen based on the experimental results. The optimal time and temperature under our experimental conditions was 72 h and 363.15 K for the synthesis of  $\text{TiO}_2$  sol. After preparation of the  $\text{TiO}_2$  electrode,  $\text{TiO}_2$  particles mostly showed anatase phase, the average particle size was in the range of 15-20 nm, and the layer of  $\text{TiO}_2$  electrode was high transparency.

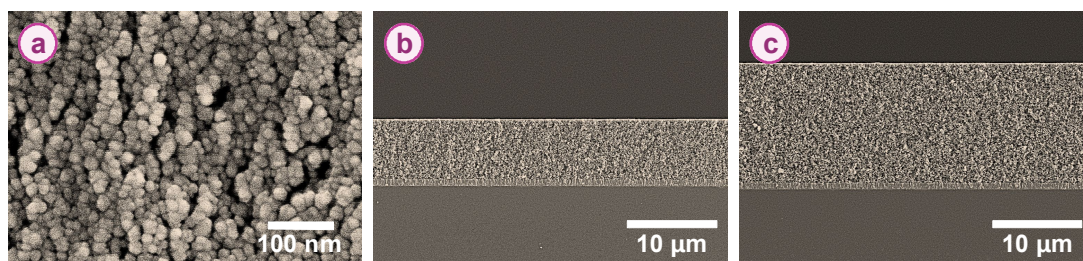


**Figure 5.31.** FE-SEM image of KYJ-6F: (a) surface, (b) thickness, and (c) thickness of repetitive dry coating.



**Figure 5.31** shows the FE-SEM image of  $\text{TiO}_2$  thin film prepared from the  $\text{TiO}_2$  sol obtained under the optimal aging conditions (i.e., 72 h, 363.15 K). As shown in **Figure 5.31a**, the KYJ-6F showed small aggregated and homogeneously dispersed particles. The average particle size was about 20 nm and the thickness of thin film was about 7  $\mu\text{m}$  (see **Figure 5.31b**). For the manufacturing of highly efficient DSSC, the  $\text{TiO}_2$  film as coated four times by using the repetitive dry coating method.<sup>136</sup> **Figure 5.31c** shows the FE-SEM image of KYJ-6F. The thickness of  $\text{TiO}_2$  thin film is about 14  $\mu\text{m}$ . On the basis of the results obtained under our experimental conditions, the maximum energy conversion efficiency was set at 10.2% (**Figure 5.32**) for the  $\text{TiO}_2$  thin films prepared from the  $\text{TiO}_2$  sol synthesized under the optimal aging conditions.

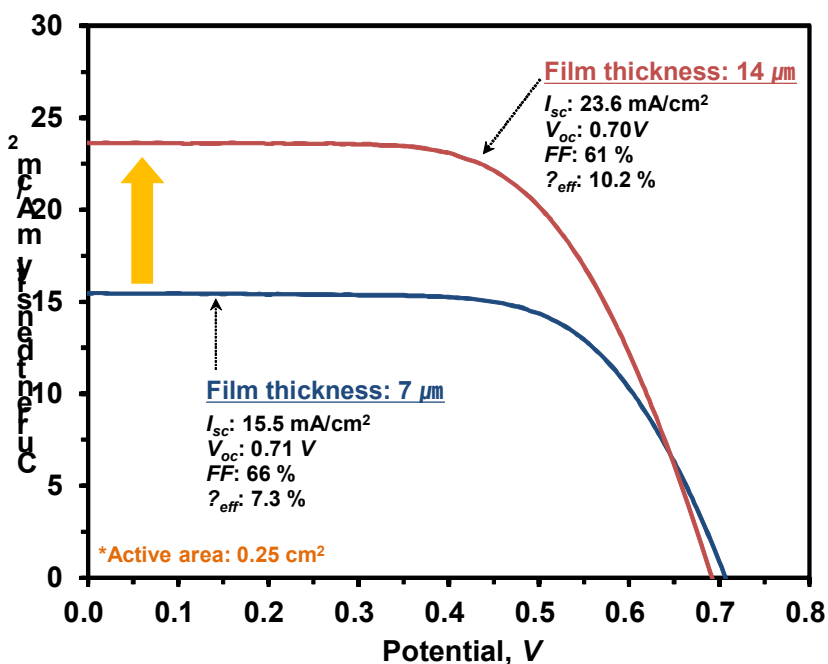


**Figure 5.32.**  $I$ - $V$  curves of  $\text{TiO}_2$  thin film with repetitive dry coating method fabricated using  $\text{TiO}_2$  sol prepared under optimal aging conditions of 363.15 K and 72 h.

## 5.4 Summary

TiO<sub>2</sub> sol was prepared through the aging process accompanied by hydrolysis/polycondensation. The aging step in the TiO<sub>2</sub> sol preparation is the most important in controlling the size and microstructure of TiO<sub>2</sub> sol particles. The samples were analyzed by BET, FE-SEM, FT-IR, HR-TEM, PSA, TGA, Turbidity, XRD, and Zeta potential analysis. It was also observed surprisingly that the physical and chemical properties of the TiO<sub>2</sub> sol particles was not changed even after the calcinations of TiO<sub>2</sub> sol.

TiO<sub>2</sub> electrode with different textural and crystalline phase properties are fabricated to systematically investigate the effects of aging conditions (time and temperature) on the performance of DSSC. It has also successfully demonstrated the relationship between the crystallite size, crystalline phase (anatase and rutile), N719 dye adsorption properties and photovoltaic performance. Results showed that the aging time and aging temperature are important factors dominating the textural and crystal structure and crystallinity of TiO<sub>2</sub> particles. The BET surface area, pore volume and crystallite size increases with aging time and aging temperature. Adsorption equilibrium isotherms are obtained for N719 dye on the TiO<sub>2</sub> films prepared at different aging conditions at temperatures ranging from 303.15 to 333.15 K and at pHs ranging from 3 to 7, respectively. The N719 adsorption equilibrium amount increase with increasing temperature and conversely decreasing pH, which indicate that the endothermic and acidic conditions are more effective in enhancing the N719 adsorption capacity. In addition, the greater the surface area, pore volume and crystallite size, the larger the N719 dye adsorption is. The TiO<sub>2</sub> films having pure anatase phase represent higher N719 dye adsorption amount than that of the TiO<sub>2</sub> films composing of both anatase and rutile phase. The Langmuir and LF isotherm equation models are found to successfully describe the adsorption isotherm data. The surface heterogeneity of TiO<sub>2</sub> films was compared in terms of the adsorption energy distribution functions and the heterogeneity parameter. The AED curves relatively became lower, broader and toward higher energy as decreased the heterogeneity parameter  $n$  and conversely increased the surface area and pore volume.

A reasonable correlation between the crystallite size, the N719 dye adsorption amount and the photovoltaic performance ( $I_{sc}$  and  $\eta_{eff}$ ) was established. The short circuit current

( $I_{sc}$ ) and overall conversion efficiency ( $\eta_{eff}$ ) are highly dependent on the crystallite size and the N719 dye adsorption properties (i.e., adsorption equilibrium amount, adsorption enthalpy and entropy). It is evident that the  $TiO_2$  film having pure anatase phase, high surface area including pore volume, large crystallite size is desirable for enhancing the photovoltaic performance. Finally, DSSC fabricated by the KYJ-6 (72 h, 363.15 K) sol particles (18%) and HPC binder (15%) with a repetitive dry coating method, has a high conversion efficiency of 10.2% with high transparency.

## Chapter 6. Overall Conclusions

For high energy conversion efficiency of DSSC, the synthesis and characterization of various  $\text{TiO}_2$  nano-particles, and their adsorption and photovoltaic properties were investigated in this research. Based on the experimental and theoretical studies, the following conclusions were obtained.

The colloidal  $\text{TiO}_2$  suspension was prepared by sol-gel method based on the hydrolysis of TTIP. The  $\text{TiO}_2$  films of single-phase anatase crystallites were formed on the FTO glass for a working electrode of DSSC. The contents of Ti and O of prepared SG- $\text{TiO}_2$  are 27.01% and 52.23% corresponding to closely  $\text{Ti}^{4+}$  state respectively. The nanoparticle size of SG- $\text{TiO}_2$  is about 14 nm and the film thickness is ca. 4  $\mu\text{m}$ . A dye-sensitized solar cell of SG- $\text{TiO}_2$  gave an open-circuit voltage of 0.57 V and short-circuits current density of 15.6  $\text{mA}/\text{cm}^2$  for an incident light intensity of 100  $\text{mW}/\text{cm}^2$ . It was found that DSSC made of SG- $\text{TiO}_2$  nanocrystalline films as photo-anodes achieved better photo-energy conversion efficiency compared to those prepared using commercially available P25- $\text{TiO}_2$  films. The power conversion efficiency of over 5.0% (without mask) was achieved using the single-phase anatase SG- $\text{TiO}_2$  crystallites synthesized in this work. The adsorption equilibrium and kinetic studies revealed that the adsorption of N719 on SG- $\text{TiO}_2$  nanoparticles was temperature dependent and also pH dependent. The maximum adsorption capacity was achieved at the isoelectric point of around pH 4. The adsorption isotherm data can be fitted well with the Sips isotherm, and the adsorption kinetic data were well described by the pseudo-second-order model. On the other hands, the photocurrent-voltage of DSSC in terms of adsorption quantity was evaluated by a 1-diode model which is very useful in evaluating the effects of adsorption quantity. The energy conversion efficiency increased with the adsorption quantity is highly influenced by the adsorption state.

A highly ordered nanoporous  $\text{TiO}_2$  (MK- $\text{TiO}_2$ , MS- $\text{TiO}_2$ , and MU- $\text{TiO}_2$ ) particles were successfully synthesized by the nano casting method using the mesoporous templates

including KIT-6 (bicontinuous cubic), SBA-15 (2-D hexagonal) and MSU-H (2-D hexagonal). The nanoporous TiO<sub>2</sub> electrode of DSSC were prepared and characterized by AED, AFM, BET, FE-SEM, FT-IR, HR-TEM and XRD. Unlike the commercial P25-TiO<sub>2</sub>, MK-TiO<sub>2</sub>, MS-TiO<sub>2</sub>, and MU-TiO<sub>2</sub> have anatase phase, high surface area, and ordered pore network. The adsorption bonding structure of N719 on nanoporous TiO<sub>2</sub> films is caused by unidentate and bidentate linkage. The overall conversion efficiency (without mask) is in the following order: MU-TiO<sub>2</sub> film (3.6%) > MK-TiO<sub>2</sub> film (3.3%) > MS-TiO<sub>2</sub> film (1.7%). From the results of adsorption properties obtained from this work, the photoelectric performance is strongly dependent on the adsorption amount of dye molecules and the pore size distributions of MK-TiO<sub>2</sub>, MS-TiO<sub>2</sub>, and MU-TiO<sub>2</sub>. Contrary to expectation, the photovoltaic conversion efficiencies of nanoporous TiO<sub>2</sub> electrode compared to P-25 were low although they showed the higher dye adsorption capacities. The result implies that the excessively generated electron can be acted as a resistance of the electron diffusion and many recombination could occur. For overcoming these problem, nanoporous TiO<sub>2</sub> thin film was fabricated by multi-layer method. It was found that the multi-layer electrode give higher efficiency in DSSC because nanoporous TiO<sub>2</sub> has the light scattering effect. In addition, the energy conversion efficiency of multi-layer coated nanoporous TiO<sub>2</sub> samples on P25-TiO<sub>2</sub> (i.e., P25-TiO<sub>2</sub>/MK-TiO<sub>2</sub>, P25-TiO<sub>2</sub>/MS-TiO<sub>2</sub>, and P25-TiO<sub>2</sub>/MU-TiO<sub>2</sub>) ended up to be 0.9-1.1 times higher than that of the P25-TiO<sub>2</sub>/P25-TiO<sub>2</sub> film.

To improve the performance of DSSC, TiO<sub>2</sub> sol was synthesized under different aging conditions by modified sol-gel method. The TiO<sub>2</sub> sol was prepared through the aging process accompanied by hydrolysis/polycondensation. It found from the analysis of BET, FE-SEM, FT-IR, HR-TEM, PSA, TGA, Turbidity, XRD, and Zeta potential analysis that the aging step in the TiO<sub>2</sub> sol preparation is the most important in controlling the size and structure of TiO<sub>2</sub> particles. It was also observed surprisingly that the physical and chemical properties of the TiO<sub>2</sub> particles were not changed even after the calcinations of TiO<sub>2</sub> sol. TiO<sub>2</sub> electrode with different textural and crystalline phase properties are fabricated to systematically investigate the effects of aging conditions (time and temperature) on the performance of DSSC. The BET surface area, pore volume and crystallite size increases with aging time and temperature which are important factors for the textural and crystal structure and crystallinity of TiO<sub>2</sub> particles. The TiO<sub>2</sub> films having pure anatase phase

represent higher N719 dye adsorption amount than that of the  $\text{TiO}_2$  films composing of both anatase and rutile phase. The Langmuir and LF isotherm equation models are found to successfully describe the adsorption isotherm data. The surface heterogeneity of  $\text{TiO}_2$  films was compared in terms of the adsorption energy distribution functions and the heterogeneity parameter. The AED curves relatively became lower, broader and toward higher energy as decreased the heterogeneity parameter  $n$  and conversely increased the surface area and pore volume. A reasonable correlation between the crystallite size, the N719 dye adsorption amount and the photovoltaic performance ( $I_{sc}$  and  $\eta_{eff}$ ) was established. The short circuit current ( $I_{sc}$ ) and overall conversion efficiency ( $\eta_{eff}$ ) are highly dependent on the crystallite size and the N719 dye adsorption properties (i.e., adsorption equilibrium amount, adsorption enthalpy and entropy). It is evident that the  $\text{TiO}_2$  film having pure anatase phase, high surface area including pore volume, large crystallite size is desirable for enhancing the photovoltaic performance. Finally, DSSC fabricated by the KYJ-6 (72 h, 363.15 K) sol particles (18%) and HPC binder (15%) with a repetitive dry coating method, has a high conversion efficiency of 10.2% (without mask) with high transparency.

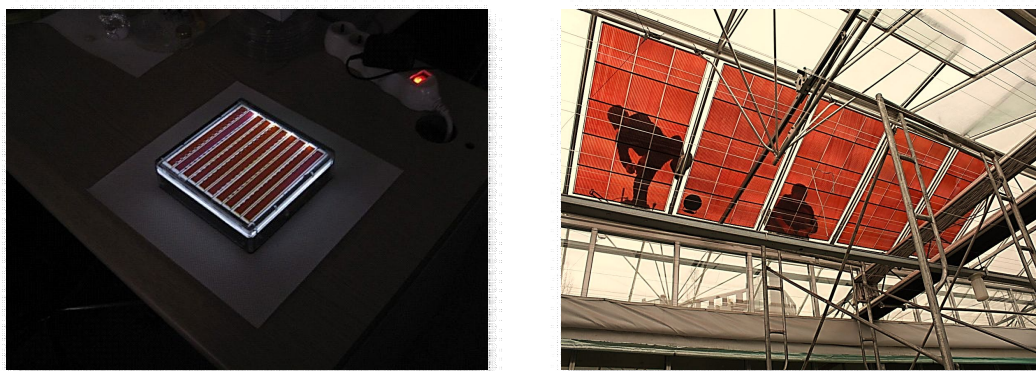


**Figure 6.1.** Commercial applications of the photo electrode: i ) LED emission tile (left side), ii ) greenhouse (right side)

The experimental and theoretical results for the adsorption and photovoltaic properties of nanocrystalline  $\text{TiO}_2$  electrode for high conversion efficiency in DSSC can be successfully

applied for commercial manufacture processes. **Figure 6.1** shows commercial applications of prototype DSSC fabricated by Acrosol Co., Ltd company using the  $\text{TiO}_2$  paste obtained in this work. DSSC module (module size: 15 cm×15 cm, current and voltage: 250 mA and 3V) using the photo electrode has been applied to the LED emission tile. DSSC panels (panel size: 165 cm×100 cm, maximum power: 40 W) installed on the roof of a greenhouse in Gwangju Institute of Science and Technology.

Unfortunately, the commercial application of DSSC has been very limited because of low stability and low conversion efficiency. Much works for the coating technology of  $\text{TiO}_2$  thin film and mass production of  $\text{TiO}_2$  paste are required for high photovoltaic performance in DSSC.

## Literature Cited

- [1] Luque, A.; Hegedus, S. *Handbook of Photovoltaic Science and Engineering*, John Wiley & Sons: Chichester, **2003**.
- [2] Sørensen, B. *Renewable Energy*, Academic Press: London, **1979**.
- [3] Kazmerski, L. L. *Renew. Sust. Energ. Rev.*, **1997**, 1(1), 71.
- [4] *Photovoltaics: Current Status And A Strategy For European Industrial And Market Development To The Year 2010*, AGORES: Bruxelles, **2010**.
- [5] Alsema, E. A.; Nieuwlaar, E. *Energy Policy*, **2000**, 28(14), 999.
- [6] Oliver, M.; Jackson, T. *Energy Policy*, **2000**, 28(14), 1011.
- [7] Fthenakis, V. M. *Energy Policy*, **2000**, 28(14), 1051.
- [8] Green, M. A. *Prog. Photovolt. Res. Appl.*, **2001**, 9, 287.
- [9] Shah, A.; Torres, P.; Tscharnner, R.; Wyrsh, N.; Keppner, H. *Science*, **1999**, 285(5427), 692.
- [10] Goetzberger, A.; Hebling, C. *Sol. Energy Mater. Sol. Cells*, **2000**, 62, 1.
- [11] Green, M. A. *Prog. Photovolt. Res. Appl.*, **2000**, 8(1), 127.
- [12] McEvoy, A. J.; Grätzel, M. *Sol. Energy Mater. Sol. Cells*, **1994**, 32(3), 221.
- [13] O'Regan B.; Grätzel M. *Nature*, **1991**, 353, 737.
- [14] Nazeeruddin, M. K.; Kay, A.; Rodicio, I.; Humphry-Baker, R.; Müller, E.; Liska, P.; Vlachopoulos, N.; Grätzel, M. J. *Am. Chem. Soc.*, **1993**, 115, 6382.
- [15] Brabec, C. J.; Sacriciftci, N. S.; Hummelen, J. C. *Adv. Funct. Mater.*, **2001**, 11(1), 15.
- [16] Green, M. A.; Emery, K.; Hishikawa, Y.; Warta, W. *Prog. Photovolt. Res. Appl.*, **2009**, 17, 320.
- [17] Green, M. A.; Emery, K.; Bücher, K.; King, D. L.; Igari, S. *Prog. Photovolt. Res. Appl.*, **1998**, 6, 265.
- [18] Green, M. A.; Emery, K.; Bücher, K.; King, D. L.; Igari, S. *Prog. Photovolt. Res. Appl.*, **1999**, 7, 321.



- [19] Arakawa, H. Recent Advances in Research and Development for Dye-Sensitized Solar Cells II, CMC Publishing: Tokyo, **2007**.
- [20] Barbe, C. J.; Arendse, F.; Comte, P.; Jirousek, M.; Lenzmann, F.; Shklover, V.; Grätzel, M. *J. Am. Ceram. Soc.* **1997**, 80, 3167.
- [21] Arakawa, H. *Catalysts and Catalysis*, **2002**, 44, 190.
- [22] Grätzel, M. *J. Photochem. Photobiol. C-Photochem. Rev.*, **2003**, 4, 145.
- [23] Hara, K.; Sato, T.; Katoh, R.; Furube, A.; Ohga, Y.; Shinpo, A.; Suga, S.; Sayama, K.; Sugihara, H.; Arakawa, H., *J. Phys. Chem. B*, **2002**, 107(2), 597.
- [24] Hayase, S.; Sumino, H.; Murai, S.; Mikoshiba, T. *IEICE Technical Report*, **2001**, 101.
- [25] Ding, I. K.; Tétreault, N.; Brillet, J.; Hardin, B. E.; Smith, E. H.; Rosenthal, S. J.; Sauvage, F.; Grätzel, M.; McGehee, M. D. *Adv. Funct. Mater.*, **2009**, 19, 1.
- [26] Chiba, Y.; Islam, A.; Watanabe, Y.; Komiya, R.; Koide, N. Han, L. *Jpn. J. Appl. Phys.*, **2006**, 45, 638.
- [27] Yanagida, M.; Onozawa-Komatsuzaki, N.; Kurashige, M.; Sayama, K.; Sugihara, H. *Sol. Energy Mater. Sol. Cells*, **2010**, 94(2), 297.
- [28] Weintraub, B.; Wei, Y.; Wang, Z. L. *Angew. Chem. Int. Ed.*, **2009**, 48, 1.
- [29] Hwang, K. J.; Lee, J. W.; Park, J. Y.; Kim, S. I. *J. Nanosci. Nanotechnol.*, **2011**, 11(2), 1522.
- [30] Arakawa, H. *Proceedings of WCPEC-4*, 2006, 179.
- [31] Kawakita, M.; Kawakita, J.; Uchikoshi, T.; Sakka, Y. *J. Mater. Res.*, **2009**, 24, 1417.
- [32] Gerischer, H.; Tributsch, H. *Ber. Bunsen-Ges. Phys. Chem.*, **1968**, 72 ,437.
- [33] Anderson, S.; Constable, E. C.; Dare-Edwards, M. P.; Goodenough, J. B.; Hamnett, A.; Seddon, K. R.; Wright, R. D. *Nature*, **1979**, 280, 571.
- [34] Smestad, G. *Sol. Energy Mater. Sol. Cells*, **1994**, 32, 273.
- [35] Hagfeldt, A.; Grätzel, M. *Chem. Rev.*, **1995**, 95(1), 49.
- [36] Gutschner, M.; Nowak, S. Potential and Implementation of Building-Integrated Photovoltaics on the Local Level - Case Studies and Comparison of Urban and Rural Areas in Switzerland, 16<sup>th</sup> European Photovoltaic Solar Energy Conference: Glasgow, **2001**.
- [37] Kalyanasundaram, K.; Grätzel, M. *Coord. Chem. Rev.*, **1998**, 77, 347.
- [38] Grätzel, M. *Prog. Photovolt. Res.*, **2000**, 8, 171.
- [39] Levine, I. N. Physical Chemistry, International Student Edition, McGraw-Hill: Tokyo,

**1978.**

- [40] Matthews, D.; Infelta, P.; Grätzel, M. *Sol. Energy Mater. Sol. Cells*, **1996**, 44, 119.
- [41] Cahen, D.; Hodes, G. *J. Phys. Chem. B*, **2000**, 104, 2053.
- [42] Hagfeldt A.; Grätzel M. *Acc. Chem. Res.*, **2000**, 33(5), 269.
- [43] Pichot, F.; Gregg, B. A. *J. Phys. Chem. B*, **2000**, 104, 6.
- [44] Ferber, J.; Luther, J. *Sol. Energy Mater. Sol. Cells*, **1998**, 53, 29.
- [45] Zaban, A.; Meier, A.; Gregg, B. A. *J. Phys. Chem. B*, **1997**, 101, 7985.
- [46] Green, M. A. *Solar Cells, Operating Principles, Technology, and System Applications*, Prentice-Hall: New jersey, **1982**.
- [47] Park, N. G. *J. Ind. Eng. Chem.*, **2004**, 15(3), 265.
- [48] Huang, S. Y.; Schlichthorl, G.; Nozik, A. J.; Grätzel, M.; Frank, A. J. *J. Phys. Chem. B*, **1997**, 101, 2576.
- [49] Grätzel, M. *Curr. Opin. Colloid Interface Sci.*, **1999**, 4, 314.
- [50] Wang, P.; Zakeeruddin, S. M.; Comte, P.; Charvet, R.; Humphry-Baker, R.; Grätzel, M. *J. Phys. Chem. B*, **2003**, 107(51), 14336.
- [51] Ito, S.; Murakami, T. N.; Comte, P.; Liska, P. Grätzel, C.; Nazeeruddin, M. K.; Grätzel, M. *Thin Solid Films*, **2008**, 516, 4613.
- [52] Ito S.; Nazeeruddin, M. K.; Liska, P.; Comte, P.; Charvet, R.; Pechy, P.; Jirousek, M.; Kay, A.; Zakeeruddin. S. M.; Grätzel, M. *Prog. Photovolt: Res. Appl.*, **2007**, 15, 603.
- [53] Kaven, L.; O'Regan, B.; Kay, A.; Grätzel, M. *J. Electroanal. Chem.*, **1993**, 346, 291.
- [54] Hagfeldt, A.; Didriksson, B.; Palmqvist, T.; Lindström, H.; Södergren, S.; Rensmo, H.; Lindquist, S. E. *Sol. Energy Mater. Sol. Cells*, **1994**, 31, 481.
- [55] Wolfbauer, G.; Bond, A. M.; Eklund, J. C.; MacFarlane, D.R. *Sol. Energy Mater. Sol. Cells*, **2001**, 70, 85.
- [55] Ferber, J.; Kern, R.; Chmiel, G.; Hinsch, A.; Kroon, J.; Luther, J.; Meyer, A.; Meyer, T.; Niepmann, R.; Van Roosmalen, J.; Uhlendorf, I. Investigation of the Long-Term Stability of Dye-Sensitized Solar Cells, Proceedings of the 12<sup>th</sup> Workshop on Quantum Solar Energy Conversion: Südtirol, **2000**.
- [56] Rijnberg, J.; Kroon, J. M.; Wienke, J.; Hinsch, A.; Van Roosmalen, J. A. M.; Sinke, W. C.; Scholtens, B. J. R.; De Vries, J. G.; De Koster, C. G.; Duchateau, A. L. L.;

- Maes, I. C. H.; Henderickx, H. J. W. Long Term Stability of Nano crystalline Dye-Sensitized Solar Cells, 2<sup>nd</sup> World Conference and Exhibition on Photovoltaic Solar Energy Conversion: Vienna, **1998**.
- [57] Kay, A.; Grätzel, M. *Sol. Energy Mater. Sol. Cells*, **1996**, 44, 99.
- [58] Papageorgiou, N.; Athanassov, Y.; Armand, M.; Bonhote, P.; Pettersson, H.; Azam, A.; Gratzel, M. *J. Electrochem. Soc.*, **1996**, 143, 3099.
- [59] Gordon, R. G. *MRS Bulletin*, **2000**, 52.
- [60] Lasnier, A.; Ang, T. G., Photovoltaic Engineering Handbook, Adam hilger: New york, **1990**.
- [61] Hwang, K. J.; Yoo, S. J.; Jung, S. H.; Park, D. W.; Kim, S. I. Lee, J. W. *Bull. Korean Chem. Soc.*, **2009**, 30(1), 172.
- [62] Park, D. W.; Choi, Y. K.; Hwang, K. J.; Lee, J. W.; Park, J. K.; Jang, H. D.; Park, H. S.; Yoo, S. J. *Adv. Powder Tech.*, **2011**, doi:10.1016/j.appt.2010.11.003.
- [63] Stanley, A.; Verity, B.; Matthews, D. *Sol. Energy Mater. Sol. Cells*, **1998**, 52, 141.
- [64] Lee, J. W.; Hwang, K. J.; Shim, W. G.; Park, K. H.; Gu, H. B.; Kwun, K. H. *Korean J. Chem. Eng.*, **2007**, 24(5), 847.
- [65] Kawakita, J. *Science & Technology Trends*, **2010**, 35, 70.
- [66] Hwang, K. J.; Jung, S. H.; Park, D. W.; Yoo, S. J.; Lee, J. W. *Curr. Appl. Phys.*, **2010**, 10, S184.
- [67] Lee, J. W.; Hwang, K. J.; Shim, W. G.; Moon, I. S. *Sep. Sci. Technol.*, **2006**, 41(16), 3655.
- [68] Kalavathy, M. H.; Karthikeyan, T. S.; Miranda, L. R. *J. Colloid Interface Sci.*, **2005**, 292, 354.
- [69] Ghouti, M. A.; Khraisheh, M. A. M.; Ahmad, M. A. M.; Allen, S. *J. Colloid Interface Sci.*, **2005**, 287, 6.
- [70] Hao, S.; Wu, J.; Fan, L.; Huang, Y.; Lin, J.; Wei, Y. *Sol. Energy*, **2004**, 76, 745.
- [71] Zhang, Z.; Zakeeruddin, S. M.; O'Regan, B. C.; Humphry-Baker, R.; Grätzel, M. *J. Phys. Chem. B*, **2005**, 109, 2818.
- [72] Anta, J. A.; Casanueva, F.; Oskam, G. *J. Phys. Chem. B*, **2006**, 110, 5372.
- [73] Ouennoughi, Z.; Chegaar, M. *Solid-State Electronics*, **1999**, 43, 1985.
- [74] Lee, J. W.; Hwang, K. J.; Park, D. W.; Park, K. H.; Shim, W. G.; Kim, S. C. *J.*

- Nanosci. Nanotechnol.*, **2007**, 7(11), 3717.
- [75] Moudler, J. F.; Stickle, W. F.; Sobol, P. E.; Bomben, K. D. Handbook of X-ray Photoelectron Spectroscopy, Perkin-Elmer: Eden prairie, **1992**.
- [76] Scherrer, P. *Math. Phys.* **1918**, 2, 98.
- [77] Park, N. G.; Van de Lagemaat, J. Frank, A. J. *J. Phys. Chem. B*, **2000**, 104, 8989.
- [78] Yang, P. D.; Zhao, D. Y.; Mar golese, D. I.; Chmelka, B. F.; Stucky, G. D. *Chem. Mater.* **1999**, 11, 2813.
- [79] Yu, Y. H.; Gao, Z. *Chem. Commun.* **2000**, 1755.
- [80] Park, D. W.; Park, K. H.; Lee, J. W.; Hwang, K. J.; Choi, Y. K. *J. Nanosci. Nanotechnol.*, **2007**, 7(11), 3722.
- [81] Rudzinski, W.; Everett, D. H. Adsorption of Gases on Heterogeneous Surfaces, Academic Press: London, **1992**.
- [82] Jaroniec, M.; Madey, R. Physical Adsorption on Heterogeneous Solids, Elsevier: Amsterdam, **1988**.
- [83] Puziy, A. M.; Matynia, T.; Gawdzik, B. *Langmuir*, **1999**, 15, 6016.
- [84] Szombathely, M. V.; Brauer, P.; Jaroniec, M. J. *Comput. Chem.*, **1992**, 13, 17.
- [85] Roth, T. M.; Weese, J.; Honerkamp, J. *Comput. Phys. Commun.*, **2001**, 139, 279.
- [86] Lee, J. W.; Kwang, H. C.; Shim, W. G.; Kim, C.; Moon, H. *J. Nanosci. Nanotechnol.*, **2006**, 6(11), 3577.
- [87] Shim, W. G.; Kang, H. C.; Kim, S. C.; Lee, J. W.; Moon, H. *J. Nanosci. Nanotechnol.*, **2006**, 6(11), 3583
- [88] Hwang, K. J.; Yoo, S. J.; Kim, S. S.; Kim, J. M.; Shim, W. G.; Kim, S. I.; Lee, J. W. *J. Nanosci. Nanotechnol.* **2008**, 8(10), 4976.
- [89] Leon, C. P.; Kador, L.; Peng B.; Thelakkat, M. *J. Phys. Chem. B* **2006**, 110(17), 8723.
- [90] Finnie, K. S.; Bartlett, J. R.; Woolfrey, J. L. *Langmuir*, **1998**, 14, 2744.
- [91] Murakoshi, K.; Kano, G.; Wada, Y.; Yanagida, S.; Miyazaki, H.; Matsumoto, M.; Murasawa, S. *J. Electroanal. Chem.*, **1995**, 396, 27.
- [92] Ghiaci, M.; Abbaspur, A.; Kia, R.; Seyden-Azad, F. *Sep. Purif. Technol.*, **2004**, 40, 217.
- [93] Damjanović, L.; Rakić, V.; Rac, V.; Stošić, D.; Auroux, A. *J. Hazard. Mater.*, **2010**,

- [94] Nevskaya, D. M.; Santianes, A.; Munoz, V. *Carbon*, **1999**, 37, 1065.
- [95] Do, D. D. Adsorption Analysis: Equilibria and Kinetics, Imperial College Press: London, **1998**.
- [96] Rouquerol, G.; Rouquerol, J.; Sing, K. Adsorption by Powders and Porous Solids, Academic Press: London, **1999**.
- [97] Rahchamani, J.; Mousavi, H. Z.; Behzad, M. *Desalination*, **2011**, 267, 256.
- [98] Ho, Y. S.; McKay, G. *Water Res.*, **2000**, 24, 735.
- [99] Ho, Y. S.; Ng, J. C. Y.; McKay, G. *Sep. Sci. Technol.*, **2001**, 36, 241.
- [100] Gupta, S. S.; Bhattacharyya, K. G. *Adv. Colloid Interface Sci.*, **2011**, 162, 39.
- [101] Nogueira, A. F.; Paoli, M. A. D.; Montanari, I.; Monkhouse, R.; Nelson, J.; Durrant, J. R. *J. Phys. Chem. B*, **2001**, 105, 7517.
- [102] Riggs, J. B. An Introduction to Numerical Methods for Chemical Engineers, Texas Tech. Uni. Press: Lubbock, **1998**.
- [103] Katoh, R.; Furube, A.; Barzykin, A. V.; Arakawa, H.; Tachiya, M. *Coordinat. Chem. Rev.*, **2004**, 248, 1195.
- [104] Grätzel, M. *Nature*, **2001**, 414, 338.
- [105] Kresge, C. T.; Leonowicz, M. E.; Roth, W. J.; Vartulli, J. C.; Beck, J. S. *Nature*, **1992**, 359, 710.
- [106] Yang, P.; Zhao, D.; Margolese, D. I.; Chmelka, B. F.; Stucky, G. D. *Nature*, **1998**, 396, 152.
- [107] Yang, P.; Zhao, D.; Margolese, D. I.; Chmelka, B. F.; Stucky, G. D. *Chem. Mater.*, **1999**, 11, 2813.
- [108] Brinker, C. J.; Lu, Y.; Sellinger, A.; Honyou, F. *Adv. Mater.*, **1999**, 11, 579.
- [109] Soler-Illia, G. J. de A. A.; Louis, A.; Sanchez, C. *Chem. Mater.*, **2002**, 14, 750.
- [110] Deb, S. K. *Sol. Energy Mater. Sol. Cells*, **2005**, 88, 1.
- [111] Huang, S. Y.; Schlichthörl, G.; Nozik, A. J.; Grätzel, M.; Frank, A. J. *J. Phys. Chem. B*, **1997**, 101(14), 2576.
- [112] Nissfolk, J.; Fredin, K.; Hagfeldt, A.; Boschloo, G. *J. Phys. Chem. B*, **2006**, 110, 17715.
- [113] Fisher, A. C.; Peter, L. M.; Ponomarev, E. A.; Walker, A. B.; Wijayantha, K. G. U.

- J. Phys. Chem. B*, **2000**, 104(5), 949.
- [114] Van De Lagemaat, J.; Park, N. G.; Frank, A. J. *J. Phys. Chem. B*, **2000**, 104, 2044.
- [115] Wang, Z. S.; Kawauchi, H.; Kashima, T.; Arakawa, H. *Coord. Chem. Rev.*, **2004**, 248, 1381.
- [116] Agrios, A. G.; Cesar, I.; Comte, P.; Nazeeruddin, M. K.; Grätzel, M. *Chem. Mater.*, **2006**, 18, 5395.
- [117] Yang, L.; Lin, Y.; Jia, J.; Xiao, X.; Li, X.; Zhou, X. *J. Power Sources*, **2008**, 182, 370.
- [118] Koo, H. J.; Kim, Y. J.; Lee, Y. H.; Lee, W. I.; Kim, K.; Park, N. G. *Adv. Mater.*, **2008**, 20, 195.
- [119] Mihi, A.; Calvo, M. E.; Anta, J. A.; Miguez, H. *J. Phys. Chem. C*, **2008**, 112, 13.
- [120] Hore, S.; Nitz, P.; Vetter, C.; Prah, C.; Niggemann, M.; Kern, R. *Chem. Commun.* **2005**, 15, 2011.
- [121] Wu, C. W.; Ohsuna, T.; Kuwabara, M.; Kuroda, K. *J. Am. Chem. Soc.*, **2006**, 128, 4544.
- [122] Tian, B. Z.; Liu, X. Y.; Tu, B.; Yu, C. Z.; Fan, J.; Wang, L. M.; Xie, S. H.; Stucky, G. D.; Zhao, D. Y. *Nat. Mater.*, **2003**, 2, 159.
- [123] Lee, J.; Orilall, M. C.; Warren, S. C.; Kamperman, M.; DiSalvo, F. J.; Wiesner, U. *Nat. Mater.*, **2008**, 7, 222.
- [124] Kim, S. S.; Lee, H. I.; Shon, J. K.; Hur, J. Y.; Kang, M. S.; Park, S. S.; Kong, S. S.; Yu, J. A.; Seo, M.; Li, D.; Thakur, S. S.; Kim, J. M. *Chem. Lett.*, **2008**, 37(2), 140
- [125] Park, N. G.; Mascarenhas, J. A.; Frank, A. J. *J. Phys. Chem. B*, **1999**, 103, 3308.
- [126] Behrens, P. *Adv. Mater.*, **1993**, 5(2), 127.
- [127] Kleitz, F.; Choi, S. H.; Ryoo, R. *Chem. Commun.*, **2003**, 2136.
- [128] Zhao, D.; Feng, J.; Huo, Q.; Melosh, N.; Fredrickson, G. H.; Chemlka, B. F.; Stucky, G. D. *Science*, **1998**, 279, 548.
- [129] Kim, S. S.; Karkamkar, A.; Pinnavaia, T. J. *J. Phys. Chem.*, **2001**, 105(32), 7663.
- [130] Friouzi, A.; Kumar, D.; Bull, L. M.; Besier, T.; Sieger, P.; Huo, Q.; Walker, S. A.; Zasadzinski, J. A.; Glinka, C.; Nicol, J. *Science*, **1995**, 267, 1138.
- [131] Ryoo, R.; Joo, S. H.; Jun, S. *J. Phys. Chem. B*, **1999**, 103, 7743.

- [132] Dong, A. G.; Ren, N.; Tang, Y.; Wang, Y. J.; Zhang, H.; Hua, W. M.; Gao, Z. *J. Am. Chem. Soc.*, **2003**, 125(17), 4976.
- [133] Umpleby, R. J.; Baxter, S. C.; Chen, Y.; Shah, R. N.; Shimizu, K. D. *Anal. Chem.*, **2001**, 73(19), 4584.
- [134] Chen, K. F.; Hsu, Y. C.; Wu, Q.; Sun, S. S. *Org. Lett.*, **2009**, 11(2), 377.
- [135] László, K.; Podkościelny, P.; Dąbrowski, A. *Appl. Surf. Sci.*, **2009**, 252, 5752.
- [136] Ito, S.; Kitamura, T.; Wada, Y.; Yanagida, S. *Sol. Energy Mater. Sol. Cells*, **2003**, 76(1), 3.
- [137] Hauch, A.; Georg, A.; Krasovec, U. O.; Orel, B. *J. Electrochem. Soc.*, **2002**, 149, H159.
- [138] Biancardo M.; West K.; Krebs F. C. *J. Photochem. Photobiol. A-Chem.*, **2007**, 187, 395.
- [139] Biancardo M.; West K.; Krebs C. F. *Sol. Energy Mater. Sol. Cells*, **2006**, 90, 2575.
- [140] Wang, H.; Liu, Y.; Xu, H.; Dong, X.; Shen, H.; Wang, Y.; Yang, H. *Renewable Energy*, **2009**, 34, 1635.
- [141] O'Regan, B. C.; Bakker, K.; Kroeze, J.; Smit, H.; Sommeling, P.; Durrant, J. R. *J. Phys. Chem. B*, **2006**, 110, 17155.
- [142] Kang, M. G.; Ryu, K. S.; Chang, S. H.; Park, N. G.; Hong, J. S.; Kim, K. J. *Bull. Korean Chem. Soc.*, **2004**, 25(5), 742.
- [143] Yin, H.; Wada, Y.; Kitamura, T.; Sumida, T.; Hasegawa, Y.; Yanagida, S. *J. Mater. Chem.*, **2002**, 12, 378.
- [144] Park, S. D.; Cho, Y. H.; Kim, W. W.; Kim, S. J. *J. Solid State Chem.*, **1999**, 146, 230.
- [145] Wang, C. C.; Ying, J. Y. *Chem. Mater.*, **1999**, 11, 3113.
- [146] Jung, H. S.; Lee, S. W.; Kim, J. Y.; Hung, K. S.; Lee, Y. C.; Ko, K. H. *J. Colloid Interface Sci.*, **2004**, 279, 479.
- [147] Yoldas, B. E. *Amer. Ceram. Soc. Bull.*, **1975**, 54(3), 289.
- [148] Xu, Y.; Yao, K.; Zhou, X.; Cao, Q. *Sens. Actuator B-Chem.*, **1993**, 14, 492.
- [149] Sclafani, A.; Herrmann, J. M. *J. Phys. Chem.*, **1996**, 100, 13655.
- [150] Szaniawski, A. R.; Spencer, H. G. *Biotechnol. Prog.*, **1996**, 12, 403.
- [151] Weissman, J. G.; Ko, E. I.; Kaytal, S. *Appl. Catal. A*, **1993**, 94, 45.

- [152] Phani, G.; Tulloch, G.; Vittorio, D.; Skryabin, I. *Renew. Energy*, **2001**, 22, 303.
- [153] Tan, J.; Yunfang, H.; Wenxiang, H.; Xiuzeng, C.; Xiansong, F. *Dyes Pigment.*, **2002**, 52, 215.
- [154] Balek, V.; Mitsuhashi, T.; Bountseva, I.; Beckman, I.; Málek, Z.; Šubrt, J. *J. Therm. Anal. Calorim.*, **2002**, 69(1), 93.
- [155] Constable, E. C.; Harverson, P.; Ramsden, J. J. *Chem. Commun.*, **1997**, 17, 1683.
- [156] Kim, H. J.; Odoul, S.; Lee, C. H.; Kweon, Y. G. *Surf. Coat. Technol.*, **2001**, 140, 293.
- [157] Jang, H. D.; Friedlander, S. K. *Aerosol Sci. Technol.*, **1998**, 29, 81.
- [158] Bickmore, C. R.; Waldner, K. F.; Baranwal, R.; Hinklin, T.; Treadwell, D. R.; Laine, R. M. *J. Eur. Ceram. Soc.*, **1998**, 18, 287.
- [159] Aruna, S. T.; Tirosh, S.; Zaban, A. *J. Mater. Chem.*, **2000**, 10, 2388.
- [160] Gopal, M.; Chan, W. J.; Dejonghe, L. C. *J. Mater. Sci.*, **1997**, 92, 6001.
- [161] Sugimoto, T.; Zhou, X. P.; Muramatsu, A. *J. Colloid Interface Sci.*, **2003**, 259, 43.
- [162] Hench, L. L.; West, J. K. *Chem. Rev.*, **1990**, 33.
- [163] Wang, C. C.; Ying, J. Y. *Chem. Mat.*, **1999**, 11, 3113.
- [164] Yoldas, B. E. *J. Non-Cryst. Solids*, **1984**, 63, 145.
- [165] Suh, D. J.; Park, T. J. *J. Mater. Sci. Letters*, **1997**, 16, 490.
- [166] Sips, R. J. *Chem. Phys.*, **1948**, 16, 490.
- [167] Brinker, C. J.; Scherer, G. W. *Sol-Gel Science*, Academic press: San Diego, **1990**.
- [168] Hwang, K. J.; Lee, J. W.; Yoon, H. S.; Jang, H. D.; Kim, J. G.; Yang, J. S.; Yoo, S. J. *Bull. Korean Chem. Soc.*, **2009**, 30(10), 2365.
- [169] Liao, D. L.; Wu, G. S.; Liao, B. Q. *Colloid Surf. A-Physicochem. Eng. Asp.*, **2009**, 348, 270.
- [170] Webb, P. A.; Orr, C. *Analytical Methods in Fine Particle Technology*, Micromeritics Instrument Corporation: Georgia, **1997**.
- [171] Jiang, K.; Zakutayev, A.; Stowers, J.; Anderson, M. D.; Tate, J.; McIntyre, D. H.; Johnson, D. C.; Keszler, D. A. *Solid State Sci.*, **2009**, 11, 1692.
- [172] Ge, L.; Xu, M.; Sun, M.; Fang, H. *Mater. Res. Bull.*, **2006**, 41, 1596.
- [173] Spurr, R. A.; Myers, H. *Anal. Chem.*, **1957**, 29, 760.
- [174] Jaroniec, M. *Langmuir*, **1995**, 11, 2316.



- [175] Jaroniec, M.; Gadkaree, K. P.; Choma, J. *Colloid Surfaces A*, **1996**, 118, 203.
- [176] Rothenberger, G.; Comte, P.; Grätzel, M. *Sol. Energy Mater. Sol. Cells*, **1999**, 58, 321.
- [177] Avom, J.; Mbadcam, J. K.; Noubactep, C.; Germain, P. *Carbon*, **1997**, 35(3), 365.
- [178] Lee, C. R.; Kim, H. S.; Jang, I. H.; Im, J. H.; Park, N. G. *ACS Appl. Mater. Interfaces*, **2011**, dx.doi.org/10.1021/am2001696.
- [179] Keis, K.; Lindgren, J.; Lindquist, S. E.; Hagfeldt, A. *Langmuir*, **2000**, 16, 4688.
- [180] León, C. P.; Kador, L.; Peng, B.; Thelakkat, M. *Phys. Status Solidi A*, **2011**, 208(1), 59.
- [181] Ratke, L.; Voorhees, P. W. *Growth and Coarsening: Ostwald Ripening in Material Processing*, Springer: Berlin, **2002**.
- [182] Wilson, G. J.; Matijasevich, A. S.; Mitchell, D. R.; Schulz, J. C.; Will, G. D. *Langmuir*, **2006**, 22(5), 2016.
- [183] Yang, H. G.; Zeng, H. C. *J. Phys. Chem. B*, **2004**, 108(11), 3492.
- [184] Park, M. W.; Chun, K. Y.; Lee, J. S.; Kwak, D. J.; Sung, Y. M.; Hyun, Y. T. *Electron. Mater. Lett.*, **2009**, 5(3), 109.
- [185] Wang, H. H.; Su, C.; Chen, H. S.; Liu, Y. C.; Hsu, Y. W.; Hsu, N. M.; Li, W. R. *J. Nanomater.*, **2011**, doi:10.1155/2011/547103.
- [186] Yu, I. G.; Kim, Y. J.; Kim, H. J.; Lee, C.; Lee, W. I. *J. Mater. Chem.*, **2011**, 21, 32.
- [187] Kim, Y. J.; Lee, M. H.; Kim, H. J.; Lim, G.; Choi, Y. S.; Park, N. G.; Kim, K., Lee, W. I. *Adv. Mater.*, **2009**, 21, 3668.
- [188] Kim, Y. J.; Kim, H. J.; Lee, M. H.; Lim, G. I.; Song, H. Y.; Choi, Y. S.; Park, N. G.; Lee, C.; Lee, W. I. *J. Nanosci. Nanotechnol.*, **2010**, 10(1), 340.

## **Abstract in English**

# **Photovoltaic Characterization of Nanocrystalline TiO<sub>2</sub> Electrode Controlled by Aging Process for High Efficient Dye-Sensitized Solar Cells**

**Kyung-Jun Hwang**

Advisor : Prof. Jae-Wook Lee, Ph.D.

Department of Chemical Engineering,

Graduate School of Chosun University

The world economy has been rapidly growing, coupled with the dramatic demand for energy. The consumption of oil and natural gas is expected to reach 65% among the sources of energy by 2010, which suggests that dangerous energy system like the oil shock still exists. For the past several years, energy consumption has tremendously increased. It is causing another problem such as global warming and environmental regulations (due to the energy derived from fossil fuels). Currently, many countries are exploring a variety of eco-friendly policies and a research on various kinds of renewable energies such as nuclear energy, photovoltaic, hydraulic power, tidal energy, and geothermal energy in gathering pace and momentum.

Solar cell as an alternative renewable energy source is the electricity generated from sun light directly by photovoltaic effect. Prof. Grätzel and his co-workers developed dye-sensitized solar cells (DSSC) in the laboratory of Photonics and Interfaces at EPFL Switzerland in 1991. Compared to silicon solar cell, DSSC has attracted much attention from industrial fields because of the high energy conversion efficiency and low fabrication cost. For the enhancement of energy conversion efficiency, many researchers focused their research on the nanocrystalline TiO<sub>2</sub> electrode, dye development, electrolyte, electron diffusion, sealing technology

and conductivity substrate.

In this study, the development of various  $\text{TiO}_2$  electrode and the photovoltaic characterization were systematically investigated for the fabrication of highly efficient DSSC. The nanocrystalline  $\text{TiO}_2$  electrode in DSSC plays an important role in photoelectron transfer and current generation. Nanocrystalline  $\text{TiO}_2$  particles (SG- $\text{TiO}_2$ ) as a key part in DSSC, were synthesized by typical sol-gel method. The synthesized SG- $\text{TiO}_2$  particles are single-phase anatase nanocrystallites with particle size of av. 15 nm. The sample was prepared by the SG- $\text{TiO}_2$  electrode for the fabrication of the DSSC. The SG- $\text{TiO}_2$  electrode including commercial P25- $\text{TiO}_2$  electrode were characterized by AED, AFM, BET, FE-SEM, FT-IR, HR-TEM, XPS, and XRD analysis. It was found that DSSC made of SG- $\text{TiO}_2$  electrode as photo-anodes achieved better photo-energy conversion efficiency compared to those prepared using commercially available P25- $\text{TiO}_2$  electrode. The influences of adsorption properties on the energy conversion efficiency of DSSC are investigated. For this, adsorption equilibrium and kinetics of N719 dye on the SG- $\text{TiO}_2$  electrode were examined in terms of temperature, adsorption time and pH. Especially, dye adsorption was highly influenced by the temperature and adsorption time which affected the energy conversion efficiency. The experimental data of *I-V* curves were successfully analyzed by employing the 1-Diode model.

To increase the adsorption amount and understand the structural characteristics of photo electrode, nanoporous  $\text{TiO}_2$  particles were synthesized using mesoporous templates (KIT-6, SBA-15 and MSU-H) with a uniform pore structure. The prepared nanoporous  $\text{TiO}_2$  (MK- $\text{TiO}_2$ , MS- $\text{TiO}_2$  and MU- $\text{TiO}_2$ ) electrodes were characterized by AED, AFM, BET, FE-SEM, FT-IR, HR-TEM and XRD for DSSC. It was found that the nanoporous  $\text{TiO}_2$  particles have high surface area and ordered pore network. The nanoporous  $\text{TiO}_2$  electrode showed high adsorption amount for N719 dye. Specially, uniform pore size of the 4 nm or more had a strong effect on N719 dye adsorption of nanoporous  $\text{TiO}_2$  electrode. The adsorption bonding structure of N719 dye on nanoporous  $\text{TiO}_2$  electrode is caused by unidentate and bidentate linkage. The results of adsorption properties obtained in this work was found that the photoelectric performance is strongly dependent on the adsorption amount of dye

molecules and the pore size distributions of MK-TiO<sub>2</sub>, MS-TiO<sub>2</sub>, and MU-TiO<sub>2</sub>. Contrary to expectation, the photovoltaic conversion efficiencies of nanoporous TiO<sub>2</sub> electrode compared to commercial P25-TiO<sub>2</sub> electrode were low although they showed the higher dye adsorption capacities. The results implies that the excessively generated electron can act as a resistance to the electron diffusion and many recombination can occur. To overcome the problem, nanoporous TiO<sub>2</sub> electrode was coated on a layer of the P25-TiO<sub>2</sub> electrode by multi-layer method. It was found that the multi-layer electrode gave higher efficiency in DSSC because nanoporous TiO<sub>2</sub> has light scattering effect (aggregated particle size of the nanoporous TiO<sub>2</sub>: > av. 200 nm).

The highly efficient DSSC was fabricated by using the nanocrystalline TiO<sub>2</sub> electrode prepared by slow polycondensation in sol reaction. The TiO<sub>2</sub> sol was obtained by hydrolysis/polycondensation using titanium-tetraisopropoxide (TTIP) as a starting material. Here, the slow polycondensation in sol reaction refers to "aging". The aging conditions were adjusted to control the particle size and microstructure of TiO<sub>2</sub> sol particle and calcined TiO<sub>2</sub> particle. A TiO<sub>2</sub> electrode (KYJ-TiO<sub>2</sub>) on photo electrode of DSSC was fabricated using TiO<sub>2</sub> sol. The effect of aging conditions (aging times and temperatures) on physical and chemical properties of KYJ-TiO<sub>2</sub> electrode was systematically investigated. Results showed that the crystallinity, particle size, roughness, surface area, and transparency of KYJ-TiO<sub>2</sub> electrode can be successfully controlled by the adjustment of aging conditions in synthesis process of TiO<sub>2</sub> sol. The adsorption properties (adsorption equilibrium isotherm, isosteric enthalpies of dye adsorption, and adsorption energy distributions) of N719 dye molecules on the prepared KYJ-TiO<sub>2</sub> electrode were also investigated. It was found that physical and chemical properties of KYJ-TiO<sub>2</sub> electrode greatly affected the photovoltaic factors (short-circuit current and overall conversion efficiency) on DSSC. Therefore, DSSC fabricated by the optimized TiO<sub>2</sub> sol has high transparency and high energy conversion efficiency of 10.2% (without mask). The systematic studies of the influence of photovoltaic characterization of nano- crystalline TiO<sub>2</sub> electrode obtained from this study can be successfully applied for economical DSSC module fabrication.

## Research Activities

### *Personal:*

Name : **Kyung-Jun Hwang**  
Date of birth : November'10, 1980  
Gender / Martial status : Male / Married  
Nationality : Korea  
Mailing Address : Department of Chemical Engineering, Chosun University,  
375 Seosuk-dong, Dong-gu, Gwangju 501-759, Korea  
E-mail Address : kjaction@naver.com

### *Work Experience:*

October 2008 : **DYESOL Co.**, Queanbeyan, Australia  
Technical Training, Prototype DSSC module  
December 2008-December 2010 : **Acrosol Co.**, Mokpo-si, Korea  
Manager, Research and Development Division (DSSC)

### *Area of Interest:*

#### ◎ **Dye-Sensitized Solar Cells** (2006-Present)

1. Synthesis and Characterization of  $\text{TiO}_2$  (Sol, Film, Powder, and Fiber)
2. Adsorption Characterization of Dye on  $\text{TiO}_2$  electrode
3. Development of Prototype DSSC (DSSC Module and DSSC Panel)

#### ◎ **Adsorption and Separation Technologies** (2005-Present)

1. Synthesis and Characterization of Porous Materials  
(Metal-Organic Frameworks, Mesoporous Silica, Carbon Nano Fiber, and Natural Adsorbent)
2. Liquid and Gas-Phase Adsorption  
(Removal of VOCs, Water Vapors,  $\text{CO}_2$ , Dyes, and Radioactive substance)
3. Optimization of Adsorption Process

#### ◎ **Sol-Gel Technologies** (2007-Present)

1. Synthesis and Application of Ceramic materials ( $\text{TiO}_2$  sol,  $\text{Al}_2\text{O}_3$  sol, and Core-Shell Structure)
2. Optimization of Sol-Gel Process (Control of Material Property and Process Scale-Up)

© **Water and Wastewater Treatments** (2005-2007)

1. Photocatalysis (Removal of Dyes and Fabrication of Photocatalyst Tile)
2. Dissolved Air Flotation (Removal of Algae and Trihalomethane)

**List of International Scientific Journals (SCI/SCIE):**

1. J. W. Lee, **K. J. Hwang**, W. G. Shim, I. S. Moon, **Thermodynamic and Kinetic Behaviors of Trinitrotoluene Adsorption on Powdered Activated Carbons**, *Separation Science and Technology (Sep. Sci. Technol.)*, 41(16) (2006) 3655-3672. I/F: 1.028 ISSN: 0149-6395
2. Jae-Wook Lee, **Kyung-Jun Hwang**, Wang-Geun Shim, Kyung-Hee Park, Hal-Bon Gu, Kyu-Hyuk Kwun, **Energetic Surface Heterogeneity of Nanocrystalline Dye-Sensitized Solar Cells**, *Korean Journal of Chemical Engineering*, 24(5) (2007), 847-850. I/F: 0.893 ISSN: 0256-1115
3. Jae-Wook Lee, **Kyung-Jun Hwang**, Dong-Won Park, Kyung-Hee Park, Wang-Geun Shim, Sang-Chai Kim, **Photocurrent-Voltage of a Dye-Sensitized Nanocrystalline TiO<sub>2</sub> Solar Cells Influenced by N719 Dye Adsorption Properties**, *Journal of Nanoscience and Nanotechnology*, 7(11), 3717-3721 (2007) I/F: 1.435 ISSN: 1533-4880
4. Dong-Won Park, Kyung-Hee Park, Jae-Wook Lee, **Kyung-Jun Hwang**, Yong-Kook Choi, **Hydrochloric Acid Treatment of TiO<sub>2</sub> Electrode for Quasi-solid-state Dye-Sensitized Solar Cells**, *Journal of Nanoscience and Nanotechnology*, 7(11), 3722-3726 (2007) I/F: 1.435 ISSN: 1533-4880
5. S. H. Roh, D. H. Kwak, H. J. Jung, **K. J. Hwang**, I. H. Baek, Y. N. Chun, S. I. Kim, J. W. Lee, **Simultaneous Removal of Algae and Their Secondary Algal Metabolites from Water by Hybrid System of DAF and PAC Adsorption**, *Separation Science and Technology*, 43(1) (2008) 113-131 I/F: 1.028 ISSN: 0149-6395
6. Seung-Joon Yoo, Se-Il Lee, Dong-Heui Kwak, Kwang-Gil Kim, **Kyung-Jun Hwang**, Jae-Wook Lee, Un-Yeon Hwang, Hyung-Sang Park, Jong-Ok Kim, **Photocatalytic Degradation of Methylene Blue and Acetaldehyde by TiO<sub>2</sub>/Glaze Coated Porous Red Clay Tile**, *Korean Journal of Chemical Engineering*, 25(5) (2008) 1232-1238 I/F: 0.893 ISSN: 0256-1115
7. **Kyung-Jun Hwang**, Seung-Joon Yoo, Sung-Soo Kim, Ji-Man Kim, Wang-Geun Shim, Sun-Il Kim, Jae-Wook Lee, **Photovoltaic Performance of Nanoporous TiO<sub>2</sub> Replicas Synthesized from Mesoporous Materials for Dye-Sensitized Solar Cells**, *Journal of Nanoscience and Nanotechnology*, 8(10), 4976-4981 (2008) I/F: 1.435 ISSN: 1533-4880
8. **Kyung-Jun Hwang**, Seung-Joon Yoo, Sung-Hoon Jung, Dong-Won Park, Sun-Il Kim, Jae-Wook Lee, **Synthesis and Characterization of Nanostructured Titania Films for Dye-Sensitized Solar Cells**, *Bulletin of The Korean Chemical Society*, 30(1), 172-176 (2009) I/F: 0.936 ISSN: 0253-2964
9. **Kyung-Jun Hwang**, Jae-Wook Lee, Ho-Sung Yoon, Hee-Dong Jang, Jin-Geol Kim,, Jin-Suk

- Yang, Seung-Joon Yoo, **Photoelectric Characteristics of Nanocrystalline TiO<sub>2</sub> Film Prepared from TiO<sub>2</sub> Colloid Sol for Dye-Sensitized Solar Cell**, *Bulletin of The Korean Chemical Society*, 30(10), 2365-2369 (2009) I/F: 0.936 ISSN: 0253-2964
10. **Kyung-Jun Hwang**, Sung-Hoon Jung, Dong-Won Park, Seung-Joon Yoo, Jae-Wook Lee, **Heterogeneous Ruthenium Dye Adsorption on Nanostructured TiO<sub>2</sub> Films for Dye-Sensitized Solar Cells**, *Current Applied Physics*, 10, S184-S187 (2010) I/F: 1.586 ISSN: 1567-1739
  11. **Kyung-Jun Hwang**, Wang-Geun Shim, Sung-Hoon Jung, Seung-Joon Yoo, Jae-Wook Lee, **Analysis of Adsorption Properties of N719 Dye Molecules on Nanoporous TiO<sub>2</sub> Surface for Dye-Sensitized Solar Cell**, *Applied Surface Science*, 256, 5428-5433 (2010) I/F: 1.616 ISSN: 0169-4332
  12. **Kyung-Jun Hwang**, Jae-Wook Lee, Ju-Young Park, Sun-Il Kim, **Influence of TiO<sub>2</sub> Nanofiber Additives for High Efficient Dye-Sensitized Solar Cells**, *Journal of Nanoscience and Nanotechnology*, 11(2), 1522-1524 (2011) I/F: 1.435 ISSN: 1533-4880
  13. Yeon-Hum Yun, **Kyung-Jun Hwang**, Young-Jung Wee, Soon-Do Yoon, **Synthesis, Physical Properties, and Characterization of Starch-Based Blend Films by Adding Nano-Sized TiO<sub>2</sub>/Poly(methyl metacrylate-co-acrylamide)**, *Journal of Applied Polymer Science*, 120(3), 1850-1858 (2011) I/F: 1.203 ISSN: 0021-8995
  14. Dong-Won Park, Yong-Kook Choi, **Kyung-Jun Hwang**, Jae-Wook Lee, Jai-Koo Park, Hee-Dong Jang, Hyung-Sang Park, Seung-Joon Yoo, **Nanocrystalline TiO<sub>2</sub> Films Treated with Acid and Base Catalysts for Dye-Sensitized Solar Cells**, *Advanced Powder Technology*, doi:10.1016/j.appt.2010.11.003 (2011) I/F: 0.636 ISSN: 0921-8831, **Article in press**.
  15. **Kyung-Jun Hwang**, Jae-Wook Lee, Wang-Geum Shim, Hee-Dong Jang, Se-Il Lee, Seung-Joon Yoo, **Adsorption and Photocatalysis of Nanocrystalline TiO<sub>2</sub> Particles Prepared by Sol-Gel Method for Methylene Blue Degradation**, *Advanced Powder Technology*, doi:10.1016/j.appt.2011.05.010 (2011) I/F: 0.636 ISSN: 0921-8831, **Article in press**.
  16. Wang-Geun Shim, **Kyung-Jun Hwang**, Jong-Tae Chung, Young-Soon Baek, Seung-Joon Yoo, Sang-Chai Kim, Hee Moon, and Jae-Wook Lee, **Adsorption and Thermodesorption Characteristics of Benzene in Nanoporous Metal Organic Framework MOF-5**, *Advanced Powder Technology*, (2011) I/F: 0.636 ISSN: 0921-8831, **Article in press**.

### **List of Domestic Scientific Journals:**

1. Jae-Wook Lee, **Kyung-Jun Hwang**, Sung-Hee Roh, Sun-Il Kim, **Influence of Nanostructured TiO<sub>2</sub> Electrode Fabricated with Acid-treated Paste on the Photovoltaic Efficiency of Dye-Sensitized Solar Cells**, *Journal of Industrial and Engineering Chemistry*, 18(4), 356- 360 (2007) ISSN: 1225-0112.

2. Sung-Hoon Jung, **Kyung-Jun Hwang**, Sung-Won Kang, Hyung-Gon Jeong, Sun-Il Kim, Jae-Wook Lee, **Efficiency Variation of Dye-Sensitized Solar Cell Influenced by Phosphor Additives**, *Journal of Industrial and Engineering Chemistry*, 20(2), 227-233 (2009) ISSN: 1225-0112.
3. Ji-Eun Jeong, Ji-Eun Shin, **Kyung-Jun Hwang**, Jae-Wook Lee, Sun-Il Kim, **Changes in the Components and Acceptability of Cucumber-Hot Pepper Pickles during Storage**, *Korean Journal of Food and Cookery Science*, 25(3), 345-349 (2009) ISSN: 1225-701X.
4. **Kyung-Jun Hwang**, Sung-Hoon Jung, Seung-Joon Yoo, Sun-Il Kim, Jae-Wook Lee, **Preparation of Al<sub>2</sub>O<sub>3</sub>-coated TiO<sub>2</sub> Electrode for Recombination Blocking of Photoelectron in Dye-Sensitized Solar Cells**, *Applied Chemistry for Engineering*, 21(2), 162-168 (2010) ISSN: 1225-0112.

### ***List of Korean Patent:***

1. Seung-Joon Yoo, Jae-Wook Lee, Sun-Il Kim, **Kyung-Jun Hwang**, **Synthesis of Titanium Dioxide by Aging and Peptization Method for Photoelectrode of Dye-Sensitized Solar Cells**, 10-2008-0006060, Applied (2008)
2. Jae-Wook Lee, Hyung-Gon Jeong, Sun-Il Kim, Seung-Joon Yoo, **Kyung-Jun Hwang**, **Photoelectrodes for High Efficient Dye-Sensitized Solar Cells and Method for Manufacturing Thereof**, 10-2009-0015283, Applied (2009) / 10-0996445, Registration (2010)
3. Sun-Il Kim, Jae-Wook Lee, Ju-Young Park, **Kyung-Jun Hwang**, Hyung-Gon Jeong, **Photoelectrode of Dye-Sensitized Solar Cell Containing Titanium Oxide Nanofiber and Method for Manufacturing Thereof**, 10-2009-0095890, Applied (2009)
4. Hyung-Gon Jeong, Sung-Won Kang, **Kyung-Jun Hwang**, Jae-Wook Lee, **Photoelectrode of Dye-Sensitized Solar Cell and Method for Producing of the Photoelectrode of Dye-Sensitized Solar Cell**, 10-2010- 0074219, Applied (2010)
5. Jae-Wook Lee, Seung-Joon Yoo, Sun-Il Kim, **Kyung-Jun Hwang**, Kyung-Hee Park, **Composition for Photoelectrode of Dye-Sensitized Solar Cell and Dye-Sensitized Solar Cell using Thereof**, 10-2011-0040176, Applied (2011)

### ***List of Participation in International Conferences:***

1. Jae-Wook Lee, **Kyung-Jun Hwang**, Wang-Geun Shim, **Influence of Adsorption Properties of Ru(II) Dye on Energy Conversion Efficiency of Dye-Sensitized Solar Cells**, 2006 Korea/Romania Joint Workshop for Molecular Science and Engineering, P.278, Romanian Academy, Romania (2006)
2. Kyung-Hee Park, **Kyung-Jun Hwang**, Jae-Wook Lee, Sung-Young Cho, Seung-Jai Kim, Hal-Bon Gu, **Influence of Acetic Acid on the Photovoltaic Performance of Ru(II) Dye Sensitized Nanocrystalline TiO<sub>2</sub> Solar Cells**, *AIChE Annual Meeting*, Technical Sessions, P.229,



San francisco Hilton, USA (2006)

3. **Kyung-Jun Hwang**, Dong-Won Park, Kyung-Hee Park, Wang-Geun Shim, Sang-Chai Kim, Jae-Wook Lee, **Influence of Ru(II) Dye Adsorption Properties on Performance of Nano-Structured TiO<sub>2</sub> Solar Cell**, 2006 *International Conference on Nanoscience and Nanotechnology*, PM2-058, P.97, Korea Institute of Industrial Technology (KITECH), Gwangju, Korea (2006)
4. Kyung-Hee Park, **Kyung-Jun Hwang**, Jae-Wook Lee, Hal-Bon Gu, **Characterization of Mesoporous TiO<sub>2</sub> Nanocrystalline Films for Performance of Dye-Sensitized Solar Cell**, 2006 *International Conference on Nanoscience and Nanotechnology*, PM2-005, P.132, Korea Institute of Industrial Technology (KITECH), Gwangju, Korea (2006)
5. Dong-Won Park, Kyung-Hee Park, **Kyung-Jun Hwang**, Jae-Wook Lee, Yong-Kook Choi, **Influence of Acid Treatment of TiO<sub>2</sub> Photoelectrode in a Quasi Solid-State Dye-Sensitized Solar Cell**, 2006 *International Conference on Nanoscience and Nanotechnology*, PM2-024 P.78, Korea Institute of Industrial Technology (KITECH), Gwangju, Korea (2006)
6. Jae-Wook Lee, **Kyung-Jun Hwang**, Kyung-Hee Park, Wang-Geun Shim, Sang-Chai Kim, **Synthesis and Characterization of Nanostructured Titania Films for Dye-Sensitized Solar Cells**, FOA-9 (*Fundamentals of Adsorption*), P.434, Giardini Naxos, Sicily, Italy (2007)
7. **Kyung-Jun Hwang**, Seung-Joon Yoo, Sung-Soo Kim, Ji-Man Kim, Jae-Wook Lee, **Influence of Structural and Adsorption Properties of TiO<sub>2</sub> Electrode on Photovoltaic Efficiency of Dye-Sensitized Solar Cells**, *The 2<sup>nd</sup> KOREA-JAPAN Bilateral Joint Workshop on Dye-Sensitized and Organic Solar Cell*, P-6, P.60, KIST, Seoul, Korea (2007)
8. K. H. Park, H. G. Jeong, S. J. Moon, **K. J. Hwang**, J. W. Lee, H. Li, H. B. Gu,, **Influence of Fluorescence Additives in TiO<sub>2</sub> Photoelectrode on Ru(II) Dye-Sensitized Solar Cells**, *Nano Europe Fair and Conference*, P-53, St Gallen, Switzerland (2007)
9. **K. J. Hwang**, S. J. Yoo, D. W. Park, Y. K. Choi, J. W. Lee, **Influence of Acid and Base Catalysts on the Formation of TiO<sub>2</sub> Nanocrystalline Films for Performance of Dye-Sensitized Solar Cells**, *The 5<sup>th</sup> International Conference on Separation Science and Technology*, S3-41, P.185, Beijing university of chemical technology, China (2007)
10. Dong-Won Park, **Kyung-Jun Hwang**, Jae-Wook Lee, Yong-Kook Choi, **Equilibrium and Dynamics of Liquid-Phase Trinitrotoluene Adsorption on Granular Activated Carbon**, *The 9<sup>th</sup> Asian Conference on Analytical Sciences and The 39<sup>th</sup> Convention of the Korean Society of Analytical Sciences*, P-EN-TUE-38, P.342, Ramada Plaza Jeju, Jeju Island, Korea (2007)
11. **Kyung-Jun Hwang**, Seung-Joon Yoo, Sung-Soo Kim, Ji-Man Kim, Jae-Wook Lee, **Analysis of Bonding Structure between Dye Molecule and Mesostructured TiO<sub>2</sub> Surface for Dye-Sensitized Solar Cells**, 2007 *International Conference on Nanoscience and Nanotechnology*, PM2-046 P.296, Kimdaejeung convention center, Gwangju, Korea (2007)

12. **Kyung-Jun Hwang**, Seung-Joon Yoo, Sung-Hee Roh, Sun-Il Kim, Jae-Wook Lee, **Influence of Aging Time and Temperature on Physical and Chemical Properties of Microstructure TiO<sub>2</sub> for Dye-Sensitized Solar Cells**, *2007 Korea-Japan Symposium on Frontier Photoscience*, PO24, P.235, Hyundai hotel, Gyeongju, Korea (2007)
13. **Kyung-Jun Hwang**, Sung-Hoon Jung, Seung-Jun Yoo, Sun-Il Kim, Jae-Wook Lee, **Heterogeneous Ruthenium Dye Adsorption on Nanostructured Titania Films for Dye Sensitized Solar Cells**, *Renewable Energy 2008*, P-PV-090, P.270, BEXCO & Nurimaru, Busan, Korea (2008)
14. Sung-Hoon Jung, **Kyung-Jun Hwang**, Seung-Jun Yoo, Sun-Il Kim, Jae-Wook Lee, **Influence of Physical and Chemical Properties on the Performance of Dye-Sensitized Solar Cells**, *8<sup>th</sup> International Conference on Separation Science and Technology*, JP-11, P.291, Nihon University, Nagano, Japan (2008)
15. **Kyung-Jun Hwang**, Sung-Hoon Jung, Jae-Wook Lee, Sun-Il Kim, Dong-Won Park, Seung-Jun Yoo, **Design of High Efficient Dye-Sensitized Solar Cells Using Nanostructured TiO<sub>2</sub> Particles Prepared under Different Aging Conditions**, *2008 International Conference on Nanoscience and Nanotechnology*, P1-44, P.74, Chonnam University, Gwangju, Korea (2008)
16. Sung-Hoon Jung, **Kyung-Jun Hwang**, Yong-Kook Choi, Sun-Il Kim, Dong-Won Park, Jae-Wook Lee, **Nanocrystalline TiO<sub>2</sub> Films Treated with Acid and Base Catalyst for High Efficient Dye-Sensitized Solar Cells**, *2008 International Conference on Nanoscience and Nanotechnology*, P2-84, P.306, Chonnam University, Gwangju, Korea (2008)
17. **Kyung-Jun Hwang**, Sung-Hoon Jung, Yu-Ran Jin, Seung-Jun Yoo, Jae-Wook Lee, **Absorption and Photoelectric Characteristics of Nanocrystalline TiO<sub>2</sub> Film Prepared from TiO<sub>2</sub> Colloid Sol for Dye-Sensitized Solar Cells**, *3<sup>rd</sup> International Conference on the Industrialization of DSC*, PMO008, P-42, Nara Prefectural New Public Hall, Nara, Japan (2009)
18. Sung-Hoon Jung, Seung-Joon Yoo, **Kyung-Jun Hwang**, Hyung-Gon Jeong, Sun-Il Kim, Jae-Wook Lee, **Al<sub>2</sub>O<sub>3</sub>-Coated TiO<sub>2</sub> Thin Film using Synthesized Bohemite Sol for High Efficient Dye-Sensitized Solar Cells**, *3<sup>rd</sup> International Conference on the Industrialization of DSC*, AFV014, P-81, Nara Prefectural New Public Hall, Nara, Japan (2009)
19. Sung-Won Kang, Hyung-Gon Jeong, Jae-Wook Lee, **Kyung-Jun Hwang**, Kyung-Hee Park, En-Mei Jin, **Photoluminescence Characteristics of TiO<sub>2</sub>-Paste Including Nanophosphors in Dye-Sensitized Solar Cells**, *3<sup>rd</sup> International Conference on the Industrialization of DSC*, ICV010, P-72, Nara Prefectural New Public Hall, Nara, Japan (2009)
20. **Kyung-Jun Hwang**, Sung-Hoon Jung, Seung-Joon Yoo, Sun-Il Kim, Jae-Wook Lee, **Adsorption of Dye Molecules on Al<sub>2</sub>O<sub>3</sub>-Coated TiO<sub>2</sub> Thin Film for High Efficient Dye-Sensitized Solar Cells**, *Seventh International Symposium (Surface Heterogeneity Effects in Adsorption and Catalysis on Solids)*, P-163, Maria Curie-Sklodowska University, Lublin, Poland (2009)
21. **Kyung-Jun Hwang**, Sun-Il Kim, Jae-Wook Lee, **Heterogeneous Adsorption of Dye Molecules**

- on Nanostructured Titania Films for Dye-Sensitized Solar Cells, *Seventh International Symposium (Surface Heterogeneity Effects in Adsorption and Catalysis on Solids)*, P-180, Maria Curie-Sklodowska University, Lublin, Poland (2009)
22. Sung-Hee Roh, Kyung-Jun Hwang, Sun-Il Kim, Jae-Wook Lee, **Analysis of Thermodynamic Properties of N719 Dye Molecules on Nanocrystalline TiO<sub>2</sub> Surface**, *2009 International Conference on Nanoscience and Nanotechnology*, CMC-5, P.131, Mokpo National University, Muan, Korea (2009)
  23. Kyung-Jun Hwang, Seung-Joon Yoo, Wang-Geun Shim, Sun-Il Kim, Jae-Wook Lee, **Photovoltaic Efficiency of Dye-Sensitized Solar Cells Depending on Different Physical and Chemical Properties of TiO<sub>2</sub> Thin Film**, *18<sup>th</sup> International Conference on Photochemical Conversion and Storage of Solar Energy*, P3-24, P.235, Korea University, Seoul, Korea (2010)
  24. Kyung-Jun Hwang, Seung-Joon Yoo, Jae-Wook Lee, **Preparation, Characterization and Photocatalytic Activity of Synthesized TiO<sub>2</sub> for Methylene Blue Degradation**, *The 6<sup>th</sup> International Conference on Separation Science and Technology*, P.126, International Conference Center at Central South University, Changsha, Hunan, China (2010)
  25. Do-Young Choi, Kyung-Jun Hwang, Chan Kim, Jae-Wook Lee, **Adsorption of Carbon Dioxide on Activated Hollow Carbon Fiber Prepared from Natural Kapok**, *The 6<sup>th</sup> International Conference on Separation Science and Technology*, P.105, International Conference Center at Central South University, Changsha, Hunan, China (2010)
  26. Kyung-Jun Hwang, Seung-Joon Yoo, Wang-Geun Shim, Jae-Wook Lee, **Adsorption and Photocatalysis of TiO<sub>2</sub> Prepared by Sol-Gel Method for Methylene Blue Degradation**, *2010 International Conference on Nanoscience and Nanotechnology*, P1EP-15, P.407, GIST, Gwangju, Korea (2010)
  27. Jae-Wook Lee, Kyung-Jun Hwang, Sang-Chai Kim, Hee Moon, Wang-Geun Shim, **Adsorption of Aromatic Hydrocarbons in Nanoporous Metal Organic Framework MOF-5**, *2010 International Conference on Nanoscience and Nanotechnology*, P1M-38, P.149, GIST, Gwangju, Korea (2010)

### **Award:**

- April 2007 : **Best Poster Presentation Prize**  
*Influence of Adsorption Properties on the Performance of Dye-Sensitized Nanocrystalline TiO<sub>2</sub> Solar Cells*, Korean Institute of Chemical Engineers Spring Meeting, Lotte Hotel Ulsan, Korea
- October 2008 : **Best Poster Presentation Prize**

*Effects of Surface Characterization of TiO<sub>2</sub> Particles on the Performance of Dye-Sensitized Solar Cells*, Korean Institute of Chemical Engineers Fall Meeting, BEXCO, Korea

April 2010 : **Best Poster Presentation Prize**

*Photoelectric Characteristics of Nanocrystalline TiO<sub>2</sub> Film Prepared from TiO<sub>2</sub> Colloid Sol for Dye-Sensitized Solar Cells*, Korean Institute of Chemical Engineers Spring Meeting, EXCO, Korea

April 2010 : **Best Poster Presentation Prize**

*Preparation and Adsorption Properties of Kapok-derived Activated Hollow Carbon Fibers*, Korean Institute of Chemical Engineers Spring Meeting, EXCO, Korea

***Table of Research Results (2006-Present):***

Research Area	SCI(SCIE) Journal	Domestic Journal	International Conference	Domestic Conference	Korean Patent
<i>Dye-Sensitized Solar Cell</i>	10	3	22	22	5
<i>Adsorption Sci. and Tech.</i>	2	-	2	10	-
<i>Material Sci. and Tech.</i>	1	-	-	12	-
<i>Water Treatment</i>	2	-	-	3	-
<i>Photocatalysis</i>	1	-	3	4	-
<i>Food and Cookery Sci.</i>	-	1	-	-	-
<b>Total</b>	<b>16</b>	<b>4</b>	<b>27</b>	<b>51</b>	<b>5</b>